

**THE DENSITY OF STATES IN  
THE TWO-DIMENSIONAL ELECTRON GAS  
AND QUANTUM DOTS**

A Dissertation

Presented to the Faculty of the Graduate School

of Cornell University

in Partial Fulfillment of the Requirements for the Degree of

Doctor of Philosophy

by

Raymond Cameron Ashoori

January 1991

© Raymond Cameron Ashoori 1990

ALL RIGHTS RESERVED

# **THE DENSITY OF STATES IN THE TWO-DIMENSIONAL ELECTRON GAS AND QUANTUM DOTS**

Raymond Cameron Ashoori, Ph.D.

Cornell University 1991

The density of states (DOS) in both the two-dimensional (2d) electron gas and arrays of “quantum dots” is studied using capacitive and tunneling techniques. A capacitance bridge described in this thesis, is used to make high sensitivity capacitance measurements on GaAs samples produced using molecular beam epitaxy.

We have made quantitative determinations of the “thermodynamic” DOS of Landau levels in a 2d system whose electronic density can be varied by means of a gate bias. A novel technique which, by taking advantage of two normalization conditions based on knowledge of the Landau level degeneracy and level spacing, allows extraction of the DOS from capacitance data using no sample parameters. The method yields the DOS as a function of Fermi energy in the 2d electron gas. We find that Lorentzian lineshapes give an excellent fit to the Landau level structure. Further, the widths of these lines are independent of the strength of the magnetic field. In high fields, the exchange enhanced spin splitting is observed and the exchange energy is determined.

The “single-particle” DOS is measured in the same samples. Zero bias tunneling of electrons between a quantum well and an  $n^+$  substrate is studied with excitation voltages smaller than  $k_B T$ . At low temperatures and only with magnetic field applied perpendicular to the plane of the electron gas in the well, the tunneling rate develops a novel temperature dependent suppression. The data are interpreted in terms of a magnetic field induced energy gap, at the Fermi level, in the single-particle spectrum of electrons in the well.

We laterally confine electrons in a quantum well into arrays of quantum dots using a technique which requires only slight ( $300\text{\AA}$ ) surface corrugation of the sample. Electron beam lithography and reactive ion etching techniques are used to produce this corrugation. These samples are studied using a capacitance method which has allowed us to determine the lateral area of dots. Further, on the femto-Farad scale, quasi-periodic capacitance fluctuations are observed. We show, through comparisons with simulated results, that these fluctuations arise as due to an almost regular spectrum for adding single electrons to the dots which develops as a consequence of the Coulomb blockade.

## Table of Contents

<b>I Introduction</b> .....	1
1.1 The Two-Dimensional Density of States .....	2
1.2 Quantum Dot Systems .....	7
References .....	13
<b>II Computerized Capacitance Bridge</b> .....	14
2.1 Introduction .....	14
2.2 Rough Schematic .....	15
2.3 Theory of Operation .....	17
2.4 Evaluation of Sample Impedance .....	20
2.5 Implementation of Bridge .....	21
2.6 Special Features .....	24
References .....	27
<b>III Quantitative Measurement of the Two-Dimensional Thermodynamic Density of States</b> .....	28
3.1 Introduction .....	28
3.2 Sample Design .....	33
3.3 Measurements .....	36
3.4 Analysis Procedure .....	42
3.5 Low Field Landau Level Fitting .....	60
3.6 High Fields .....	75
3.7 Observations Regarding the Spatial Extent of States .....	85
3.8 Summary .....	101
Appendix A) Explanation of $\eta$ term .....	102
Appendix B) Details of the DOS Calculation .....	105

Appendix C) Comparison of Abscissas on DOS Plots.....	114
References.....	116

## **IV Equilibrium Tunneling from the Two-Dimensional**

<b>Electron Gas</b> .....	119
4.1 Introduction.....	119
4.2 Samples and Method.....	120
4.3 Extraction of Tunneling Conductance from Capacitance Data.....	123
4.4 Sample Characterization.....	130
4.5 Tunneling in the Presence of Magnetic Field.....	131
4.6 Average Conductance.....	138
4.7 Low Density Tunneling Suppression in the Absence of Magnetic Field.....	143
4.8 Low Density Region with Magnetic Field Applied.....	153
4.9 Speculations Regarding Possible Causes for the Suppression Effects.....	155
4.10 Summary.....	161
References.....	162

<b>V Creation of Quantum Dots</b> .....	164
5.1 Introduction.....	164
5.2 Physics of the Confinement Technique.....	168
5.3 Device Fabrication Sequence.....	172
5.4 Measurement of Dot Area.....	179
References.....	191

## **VI Observation of the Single Electron Addition**

<b>Spectrum of Quantum Dots</b> .....	193
6.1 Introduction.....	193
6.2 Equilibrium State of Quantum Dots.....	195
6.3 Spectrum of One Electron Additions to a Quantum Dot.....	198

6.4 Capacitance Fluctuations Expected in an Array of Quantum Dots .....	203
6.5 Comparison of Simulation to Observed Capacitance Spectra.....	221
6.6 Capacitance Spectra in Magnetic Field.....	230
6.7 Tunneling Rate Measurements.....	236
6.8 Shape of the Relaxation Peak.....	242
6.9 Summary .....	248
References.....	251
 <b>VII Computer Simulation of Quantum Dot Capacitance.....</b>	 252
References.....	256

## List of Figures

2.1 Rough schematic of automated bridge .....	16
2.2 Illustration of inner workings of bridge .....	22
3.1 Layer structure of samples used in DOS determination.....	32
3.2 Band structure of samples.....	34
3.3 Capacitance and loss tangent of sample <b>B</b> vs. frequency .....	38
3.4 Low and high frequency capacitances in zero field.....	40
3.5 Low and high frequency capacitances in field .....	41
3.6 DOS in sample <b>B</b> at 2 Tesla.....	52
3.7 Lever arm from sample <b>B</b> at 2 Tesla.....	55
3.8 Zero field DOS in sample <b>B</b> .....	57
3.9 Thermal broadening of Landau levels.....	59
3.10 Fits to DOS in sample <b>A</b> at 4 Tesla .....	63
3.11 Fits to DOS in sample <b>A</b> at 3 Tesla .....	66
3.12 Fits to DOS in sample <b>B</b> at 2 Tesla .....	67
3.13 Fits to DOS in sample <b>A</b> at 2 Tesla .....	69
3.14 Fits to DOS in sample <b>C</b> at 4 Tesla .....	70
3.15 Widths of Landau levels as a function of density.....	72
3.16 Illustration DOS determination method at 8.5 Tesla.....	78
3.17 DOS at 8.5 Tesla fit with Lorentzian lineshapes.....	80
3.18 DOS at 8.5 Tesla fit with Gaussian lineshapes .....	81
3.19 Sample model for low in-plane conductivity.....	88
3.20 Capacitance and loss tangent with broadening.....	90
3.21 Broadening parameter as a function of temperature.....	93
3.22 Broadening parameter at 8.5 Tesla as a function of Fermi Energy .....	96
3.23 Broadening parameter at 4 Tesla as a function of Fermi Energy .....	98
3.24 Pictorial description of $\eta$ term .....	103



3.25 Values of $C_{geom}$ vs. $\eta$ .....	108
4.1 Essential structure of samples .....	121
4.2 Figure illustrating equilibration of well and substrate charge densities ..	124
4.3 Tunneling suppression in sample <b>A</b> at 4 Tesla .....	132
4.4 Tunneling suppression in sample <b>A</b> at 2 Tesla .....	135
4.5 Tunneling suppression in sample <b>A</b> at 8.5 Tesla.....	136
4.6 Tunneling suppression in sample <b>B</b> at 4 Tesla .....	137
4.7 Summary plot of tunneling suppression with fits.....	141
4.8 Tunneling conductivity in zero field .....	145
4.9 Sample model for low densities .....	146
4.10 Fraction of well area occupied with electrons .....	150
4.11 Low density tunneling suppression .....	152
4.12 Low density tunneling suppression as a function of temperature.....	154
4.13 Low density tunneling conductivity at 290 mK for different fields .....	156
5.1 Layer structure of samples used to make quantum dots .....	169
5.2 Basic schematic of quantum dot sample .....	170
5.3 Band structure under a pillar .....	171
5.4 Band structure between pillars .....	173
5.5 Electron micrograph of patterns used to produce dots .....	176
5.6 Electron micrograph of pillars after etching.....	178
5.7 Electron micrograph of completed sample .....	180
5.8 Low and high frequency capacitances for a broad area sample.....	182
5.9 Low and high frequency capacitances for dot sample.....	183
5.10 Illustration of model used to determine dot area.....	185
5.11 Dot area determined from data for different samples.....	187
5.12 Dot area from data compared to simulation .....	188
6.1 Illustration of Coulomb effects in quantum dots .....	197
6.2 Single electron addition spectrum for quantum dots .....	201
6.3 Capacitance from model compared with measured capacitance.....	209
6.4 Illustration of the convolution function for lock-in measurements.....	213
6.5 Fluctuations due to $n^{\text{th}}$ electron addition to dot array .....	216
6.6 Simulated capacitance spectrum at low gate biases .....	217

6.7 Simulated capacitance spectrum at high gate biases .....	218
6.8 Simulated capacitance spectrum for random electron additions.....	222
6.9 Capacitance fluctuation data at 615 Hz.....	224
6.10 Fluctuation data from sample conductance at 1.7 kHz .....	228
6.11 Fluctuation data from sample capacitance at 1.7 kHz.....	229
6.12 Simulated capacitance spectrum for magnetic field applied.....	232
6.13 Conductance fluctuation data in magnetic field at high bias.....	234
6.14 Conductance fluctuation data in magnetic field at low bias .....	235
6.15 Relaxation peak frequency as a function of amplitude .....	241
6.16 Capacitance and loss tangent vs. frequency for quantum dots.....	244
6.17 Broadening parameter as a function of amplitude.....	245
6.18 High frequency capacitance as a function of amplitude.....	247
6.19 Capacitance vs. frequency curves for different amplitudes.....	249
7.1 DOS from computer model and Hansen's data.....	254

# Chapter I

## Introduction

This thesis deals with the behavior of electrons in dimensions less than three. Specifically, it uses measures of the electronic density of states (DOS) to study these systems. The thesis is roughly divided into two parts. The first part deals with the two-dimensional (2d) electron gas in GaAs. The 2d electron gas forming at an inversion layer at the silicon-silicon dioxide interface has been studied heavily since the 1960's. It is a statement of the wealth of physics contained by semiconductor 2d systems that new and exciting results, such as the quantum Hall effect<sup>1</sup> (circa 1980), are still being discovered in them. Most present experiments are being done in much higher mobility materials such as in the GaAs/AlGaAs system. The second part of the thesis deals with a newer, less studied mesoscopic system, an array of very small electron packets. Only very recently has it become technologically feasible to produce feature sizes small enough in semiconductor systems to do these experiments. Such packets have become known as "quantum dots". One salient feature in the study of these "dots" is the production of a system so small that the energies associated with the addition of one electron to the system are so large, either due to a quantum level spacing or electrostatic effects in the system, as to be experimentally observable.

## 1.1 The Two-Dimensional Density of States

Since the early magnetoconductance work of Fowler et. al.,<sup>2</sup> which first demonstrated that the electronic density of states in a deeply inverted silicon surface was two-dimensional, there has been much interest in the effects of a perpendicularly applied magnetic field on the 2d electron gas. The reason for this is clear: because of the confinement, there is no dispersion in the direction of the magnetic field so that a magnetic field applied perpendicular to the plane of the electron gas creates highly degenerate electron energy levels. In a single particle picture and with no disorder in the 2d electron gas, the magnetic field essentially places electrons in identical harmonic oscillator potential wells of number equal to the number of magnetic flux quanta passing through the 2d system. The quantum energy levels, equally spaced in energy, in these harmonic oscillator potential wells are known as “Landau levels”. Depending on the magnetic field strength, these levels can have enormous degeneracy. For example, the highest magnetic field strength used in the data presented in this thesis is 8.5 T. At this field strength, a spin degenerate Landau level contains  $4.1 \times 10^{11}$  states per square centimeter. Both the energy spacing of these levels and their degeneracy increase linearly with the applied field. Thus for a given density of electrons in the 2d gas, the position of the Fermi energy moves between different Landau levels as the magnetic field strength is varied.

In the absence of a magnetic field, the DOS in two dimensions is a constant, dependent only on fundamental constants and the effective mass of the confined electrons. In the single particle picture with no scattering of electrons, the addition of a magnetic field perpendicular to the plane of the 2d electron gas produces a series of Dirac delta functions in the DOS spectrum.

Of course, the DOS spectrum does not involve true delta functions: instead, one expects that these levels should contain some broadening. For one thing, the electrons in the 2d gas have a finite scattering time for elastic collisions with impurities. Moreover, changes in the DOS spectrum created by the magnetic field modify scattering times as the density of final states into which electrons can scatter and lengths for screening impurities are changed. This suggests that even in a single particle picture a self consistent approach is needed to understand the DOS theoretically. Further, particle exchange and many body effects may also change the character of these levels.

One intriguing consequence of confinement of the electron gas into two dimensions is the quantum Hall effect (QHE). Ordinarily, in most bulk metals and semiconductors, the Hall resistance is linear in the magnetic field. For the 2d electron gas, though, plateaus in the Hall resistance appear, quantized to values of  $\nu h/e^2$ . The integer,  $\nu$ , is equal to the number of filled Landau levels. The plateaus occur when the Fermi energy is located in the region between Landau levels. A key question is: How does DOS spectrum relate to the formation of these plateaus?

Basic theories<sup>3,4</sup> of the quantum Hall effect rely on the existence of a nonzero DOS between Landau levels in the DOS spectrum. Given that the Hall plateaus occur with the Fermi level between Landau levels, these states are required to “pin” the Fermi level in the region between Landau levels over some range in magnetic field to give the plateaus the observed width. Further, crucial to theories is the idea that these states existing between Landau levels are localized; electrical conduction cannot occur through them. One may expect that information about the shape of the DOS peaks will lead to clues about the

nature of the electronic states and what allows them to produce such bizarre phenomena as quantum Hall plateaus.

### *Density of States Measurement*

In the last few years there have been attempts, both experimentally as well as theoretically, to determine the shapes of Landau level DOS peaks. Most of the experimental studies have been either largely qualitative in nature or restricted to low magnetic fields, interpreting peaks in the specific heat, capacitance, or magnetization of the 2d electron gas as the magnetic field strength is varied as reflecting an underlying energy spectrum of the Landau level DOS. The early capacitance work of Kaplit and Zemel<sup>5</sup> on a MOSFET structure demonstrated the sensitivity of capacitance measurements to the DOS in an inversion layer.

In chapter 3, we present a technique which allows us to do precision quantitative spectroscopy of these levels now *as a function of Fermi energy* of the 2d electron gas. This technique has permitted a systematic study of the DOS at various magnetic field strengths and over a wide range of electron densities in three samples. Through characterizing Landau levels this way we have determined that both their shapes and the dependence of their level widths on magnetic field strength are different from that previously thought. Specifically, we observe that Landau level DOS peaks are well characterized by Lorentzian lineshapes whose level widths, although dependent on the electronic density of the 2d electron gas, are independent of magnetic field strength.

A measure, other than the DOS, of the “nature” of electronic states is their spatial extent or “localization length”. In a pioneering theoretical work, Abrahams et. al.<sup>6</sup> predicted, using scaling theory, that in two dimensions electrons are localized by an arbitrarily small amount of disorder, and at zero

temperature the electronic conduction thus drops to zero. When a magnetic field is applied, the localization length of electrons is thought<sup>7</sup> to oscillate in electronic energy as this energy is moved from Landau level to Landau level. The localization length is thought to become very large in a region near the DOS peak, usually called the band of “extended states”, and much shorter in the region between Landau levels, called the band of “localized states”. This variation in localization length is thought to be ultimately responsible for the Hall resistance plateaus of the quantum Hall effect.

Chapter 3 also develops a method, integrated with the capacitance technique used to determine the DOS, which probes the localization length of states in the region between Landau levels. The results show evidence of the localization length smoothly decreasing and achieving a minimum length at a position nearly half way between Landau levels, supporting some of these basic ideas on the localization length.

### *Two different Densities of States*

In a many body system of electrons it is typically not simple or even possible to describe the system in terms of an independent electron model. The behavior of the system is discussed in terms of an antisymmetrized many body wavefunction for the system of identical particles. Often one speaks of “quasi-particle” excitations that have the appearance of a single particle, but contain some amount of “dressing” due to Coulomb, phonon, and other interactions.

An interesting feature of tunneling is that an exponential decrease in probability for several particles tunneling together compared to that of a single particle makes it very unlikely that any electrons dressing a particular electron can accompany it during tunneling. Electrons must shed their dressing before

they can tunnel. The electronic system typically gains or loses energy during this process. The tunneling of an electron into or out of the system may force the system into a nonequilibrium state. This state of affairs requires the definition of two different densities of states, one for a system which has been allowed to relax back to equilibrium after a tunneling event, and the other which describes the nonequilibrium situation.

The thermodynamic DOS,<sup>8</sup>  $\partial n / \partial \mu$ , is the change in the particle density of a system for a change in chemical potential after a time period longer than the system's internal equilibration time. The means by which the system moves between the initial state with one chemical potential to the final state with another affects only the time scale for changing states and is irrelevant to the value of the thermodynamic DOS. In the audio frequency capacitance measurements described above potentials are changed so slowly that the 2d electron gas system evolves reversibly during the course of a measurement; those experiments determine thermodynamic DOS.

The single-particle or tunneling DOS is instead measured when the system of particles does not have sufficient time to rearrange during the sudden subtraction or addition of a single electron, as is the case with tunneling measurements. The time an electron spends underneath a heterostructure tunnel barrier such as those used in the experiments described in this thesis is thought to be around  $10^{-13}$  seconds.<sup>9</sup> Tunneling currents in our experiments depend on the single particle DOS. If energy is required to “undress” an electron in the 2d electron gas so that it can tunnel out, we expect the tunneling DOS may be smaller than the thermodynamic DOS.

The tunneling conductance thus reflects the single-particle DOS.<sup>10</sup> In chapter 4, we report results from a novel type of tunneling measurement which



we call “Equilibrium Tunneling”. We measure the tunneling of particles between a two dimensional electron gas and a three dimensional electron gas. These two electron gases are kept in quasi-equilibrium during the experiments, with voltages no larger than  $k_B T$  applied across the tunnel barrier. This allows for measurement of the single-particle DOS at the Fermi energy in the quantum well to an energy resolution of order  $k_B T$ . Capacitive coupling allows us to do these small signal measurements which contrast with earlier, more standard I-V measurements, in which difficulties associated with making electrical contact to a 2d layer did not allow an examination of tunneling at voltages across the tunnel barrier smaller than the bandwidth of states in the 2d gas. These prior experiments thus had little energy resolution of features in the single particle DOS. Our tunneling experiments are done in the same samples in which the thermodynamic DOS measurements of chapter 3 are made, integrating into one experiment measures of both the single-particle and thermodynamic DOS.

The tunneling experiments of chapter 4 have led to some striking results. The most dramatic feature that we have seen is a strong (up to a factor of 10) temperature dependent suppression of the tunneling conductance when a magnetic field is applied perpendicular to the plane of the 2d electron gas. These data are fit well by a model which presumes the formation of an energy gap at the Fermi energy, induced by the magnetic field, in the single-particle spectrum of electrons in 2d electron gas of width equal to about 5% of the cyclotron energy.

## 1.2 Quantum Dot Systems

In recent years, the subject of quantum confinement to dimensions fewer than the two dimensions discussed above has become a popular topic in the literature. The simplest structures, “quantum wires” and “quantum dots”, have

produced captivating results. Although single mode quantum wires appear only now on the threshold of being produced,<sup>11</sup> results have appeared from multi-mode wires ( $\approx 10$  modes), and these have produced peculiar and unexpected results, particularly in Hall effect measurements.<sup>12</sup> Experiments have been carried out on both the photoresponse and transport properties of quantum dot systems. Some evidence now exists for resolution of lateral states in a quantum dot system.<sup>13</sup> In this thesis, we present measurements on arrays of quantum dots. We pursue not only resolution of lateral states but electrostatic “energy levels” having to do with the very small size of electron packets.

The main difficulties in quantum dot experiments have been in finding appropriate techniques for lateral confinement (confinement other than the initial 2d confinement built into the heterostructure devices) of electrons. In chapter 5, we present the fabrication process that we have used to produce lateral confinement of electrons. The size and number of electrons in these dots is varied by means of a gate voltage. Chapter 5 also presents a measure of the size of these electron packets.

### *Important Energy Scales in Quantum Dots*

As alluded to above, there are two energy scales that are important in quantum dot systems. One is the mean quantum level spacing of the one electron energy states  $\delta_{mean}$  (the inverse of the density of states in the dot) and the other is the energy  $\Delta$  of charging a dot associated with the addition of a single electron. The latter can be described in terms of the capacitance of the dot to its surroundings  $C$  and is given by  $\Delta = e^2/C$ . In the configuration of our experiments,  $\Delta$  is of order 10 times larger than  $\delta_{mean}$ . Hence the effects of the charging energy on an experiment in which the population of electrons in

the dot is changed should be more pronounced than those of the quantum level spacing.

Effects of the single electron charging energy have been explored in capacitance experiments before, the earliest being the “tunnel capacitor” work of Lambe and Jacklevic.<sup>14</sup> Later work by Cavicchi and Silsbee<sup>15</sup> in our lab demonstrated the consequences of the charging energy in features in the tunneling conductance of electrons between small metal particles and an electrode. Both of these experiments were done in oxide capacitors with the packets of electrons being contained in a large number of nonuniformly sized small metal particles close enough to one electrode so that tunneling of electrons between the particles and the electrode could occur. The electron occupancy of the small metal particles is controlled by varying the voltage between the capacitor electrodes. More recent experiments by Fulton and Dolan<sup>16</sup> have demonstrated one electron charging effects in tunneling in a single metal particle coupled to electrodes by two tunnel junctions.

In the oxide capacitors of Cavicchi and Silsbee, for a single small metal particle, one expects a transfer, periodic in voltage applied across the capacitor, of single electrons between the small particle and the nearby electrode. This periodic spectrum of electron additions to the particle arises from the Coulomb blockade which demands that the electrostatic potential at the particle be changed by an amount  $\Delta$  between electron additions (or subtractions) to the particle. For a particular small metal particle, there are well defined voltages at which electron transfer between the particle and the electrode is allowed. At these voltages, there is a peak in the device capacitance,  $dQ/dV$ , as a small change in bias voltage leads to a sudden change in the charge configuration of the device.

At first glance, one expects a capacitor containing an ensemble of particles all with the same charging energy,  $\Delta$ , to have sharp periodic peaks in its capacitance as the voltage across the capacitor is varied. The problem with this idea is that even assuming that all particles have the same periodicity of electron additions, inhomogeneities in real devices will offset these individual particle spectra from one another by fixed device voltages. For instance, particles may allow electronic additions to occur at every 5 mV change in gate bias; some particles will add electrons at 0,5,10,... mV device bias while others will add them at 2,7,12,... mV. There is a distribution in these offset voltages for the spectra of different particles. Typically, it is so wide as to indicate a nearly uniform distribution of offset voltages over a device bias range for one electron addition to a particle. One might then think that capacitance peaks due to individual electron additions would be hopelessly smeared out. The distribution though does contain fluctuations from uniformity, and they will be reflected as features in the device capacitance repeating with the periodicity in device voltage of the single electron additions to the particles.

There have been attempts in our lab,<sup>17</sup> in tunnel capacitors similar to those used by Cavicchi and Silsbee, to observe capacitance fluctuations from single electron additions to small metal particles. These however were largely thwarted by conduction between the small metal particles in the sample configuration used and polarization effects in the oxide of the type described by Lambe and Jaklevic.<sup>14</sup> Further, the nonuniformity of the sizes of the small metal particles and their capacitance to the surroundings may cause difficulties in the interpretation of data revealing capacitance fluctuations. The oxide capacitors are expected to have a wide distribution of charging energies among the small metal particles. The polarization effects are not expected to occur in

GaAs/AlGaAs heterostructures, and packets of electrons can be constructed with much greater uniformity of charging energy than is the case in oxide capacitors. The other feature of the GaAs system is the small effective mass which enhances the contribution of the quantum level spacing to the capacitance spectrum and increases the likelihood that quantum size effects can be observed.

In chapter 6 we describe both computer simulations and observations of capacitance fluctuations in quantum dot arrays in GaAs associated with the addition of single electrons to small packets of electrons. Using the area of the quantum dots as a function of gate bias obtained from capacitance measurements in chapter 5, we determine a spectrum of single electron additions to the quantum dots as a function of gate bias. These are only “quasi-periodic” electron additions. For one thing the charging energy decreases as the size of the dots grows leading to an increase in the number of allowed electron additions to a dot per unit gate voltage as the dot size grows. Further, the fact that  $\delta$ , the average energy spacing between quantum levels not including the zero energy spacing of degenerate levels (different from  $\delta_{mean}$  which is the average splitting including the zero energy spacings), is equal to about a third of the charging energy also adds irregularity to the spectra.

Again, spectra for different dots are expected to be offset in gate bias from one another due to device inhomogeneities. The width of the distribution of these offsets can be estimated from device capacitance features. This distribution contains deviations from a smooth shape due to statistical fluctuations. We have carried out computer simulations incorporating these statistical fluctuations which indicate that, despite the deviations from perfect regularity of the electron addition spectra, peaks of order a few femto-Farads occur in the capacitance

spectrum of the quantum dot array, and these peaks occur with the same frequency in gate bias as the underlying electron additions to the quantum dots.

In Chapter 6, we explore the capacitance of quantum dot arrays to a resolution of 0.1 fF, and have seen peaks in the capacitance spectrum. These peaks occur quasi-periodically, in a fashion similar to those predicted by our model, and are also of the same amplitude as indicated by the model. In essence, comparison to computer simulation indicates that through capacitance measurements, we have observed, albeit with less than perfect resolution, the spectrum of single electron additions to quantum dots.

Hansen et. al.<sup>18</sup> have made capacitance measurements to much lower resolution on quantum dot arrays very similar to ours. They observed fluctuations in the device capacitance as the gate bias on their device was varied. They considered these fluctuations to be a reflection of the underlying quantum level structure in a quantum dot. We believe that this interpretation neglects charging effects in the dot. In chapter 7, we present a computer simulation indicating that, if the charging energy is taken into account, these capacitance features can be the result of statistical fluctuation in the spectrum of capacitance peaks due to one electron addition to the the quantum dots and not clearly associated with quantum levels.

First, we start with chapter 2, which describes the apparatus used to take the data presented in this thesis. It is a bridge which measures the capacitance and loss tangent of samples as a function of frequency over the entire audio range. Its special facilities for the use of small measuring signals, for making precision measurements, and most importantly for highly automated data taking, have allowed us to acquire the data necessary for the DOS, tunneling, and fluctuation spectra results discussed above.

## References

1. K. von Klitzing, G. Dorda, and M. Pepper, Phys. Rev. Lett. **45**, 494 (1980)
2. A.B. Fowler, F.F. Fang, W.E. Howard, and P.J. Stiles, Phys. Rev. Lett. **16**, 901 (1966)
3. R.B. Laughlin, Phys. Rev. B **23**, 5632 (1981)
4. B.I. Halperin, Phys. Rev. B **25**, 2185 (1982)
5. M. Kaplit and J.N. Zemel, Phys. Rev. Lett. **21**, 212 (1968)
6. E. Abrahams, P.W. Anderson, D.C. Licciardello, and T.V. Ramakrishnan, Phys. Rev. Lett. **42**, 673 (1979)
7. A.M.M. Pruisken, Phys. Rev. Lett. **61**, 1297 (1988)
8. P.A. Lee, Phys. Rev. B **26**, 5882 (1982)
9. M. Büttiker and R. Landauer, Phys. Rev. Lett. **49**, 1739 (1982)
10. B.L. Altshuler, A.G. Aronov, and P.A. Lee, Phys. Rev. Lett. **44**, 1288 (1980)
11. H.L. Störmer, private communication
12. M.L. Roukes, A. Scherer, S.J. Allen, Jr., H.G. Craighead, R.M. Ruthen, E.D. Beebe, and J.P. Harbison, Phys. Rev. Lett. **59**, 3011 (1987)
13. M.A. Reed, J.N. Randall, R.J. Aggarwal, R.J. Matyi, T.M. Moore, and A.E. Wetsel, Phys. Rev. Lett. **60**, 535 (1988)
14. John Lambe and R.C. Jaklevic, Phys. Rev. Lett. **22**, 1371 (1969)
15. R.E. Cavicchi and R.H. Silsbee, Phys. Rev. B **37**, 706 (1988)
16. T.A. Fulton and G.J. Dolan, Phys. Rev. Lett. **59**, 109 (1987)
17. N. Ramsey, Master's thesis, Cornell University (1986)
18. W. Hansen, T.P. Smith, III, K.Y. Lee, J.A. Brum, C.M. Knoedler, J.M. Hong, and D.P. Kern, Phys. Rev. Lett. **62**, 2168 (1989)

## Chapter II

### Computerized Capacitance Bridge

#### 2.1 Introduction

All of the data presented in this thesis was derived from capacitance-loss tangent measurements on our samples. We have experimented with many samples and taken enormous number of capacitance measurements. Initially, these measurements were all taken by hand balancing a capacitance bridge. This is an extraordinarily tedious process that requires at least 20 sec for each capacitance measurement. Further, for A.C. signal levels less than a few mV, noise would make the determination of balance subjective at best. Often we have needed to take measurements at very low signal levels,<sup>1-3</sup> a feat which would have been impossible in measurements taken by hand. We needed an automated system capable of signal averaging over very long periods to take these measurements.

This chapter describes an automated capacitance-loss tangent bridge that we have developed which has made measurements of samples of capacitance to below 10 pF over the range of frequencies from 2 Hz to 30 kHz. This is done with signal levels as low as 30  $\mu$ V rms. The bridge can accurately measure loss tangents as low as  $10^{-4}$ . Depending on the background noise, measuring signal level, and signal averaging time, the bridge can measure absolute capacitance



to a precision of .01% and make relative capacitance measurements good to 1 part in  $10^6$ . Typically with a 1 mV rms measuring signal at 1 kHz, samples of capacitance of around 50 pF can be measured to 0.1% precision in 15 sec. The bridge has taken over 1,000,000 capacitance measurements including all of the data presented in this thesis.

The bridge is in some ways similar to the earlier generation bridge of Cavicchi and Silsbee<sup>4</sup>. Analogously to that bridge, it adjusts voltages on the arms of the bridge instead of adjusting the value of circuit elements. However unlike the Cavicchi bridge, it uses a computerized algorithm to find balance instead of an analog feedback network. The operation of the bridge described here is continuously monitored by a computer whose software has built-in solutions for most problems that might cause the bridge to “hang up” on a measurement. This allows the bridge to run unsupervised for days at a time. The other main difference between the bridge described here and the Cavicchi bridge is the elimination of a resistance standard in the balancing arm of the bridge. In the new bridge, only a capacitance standard is used, with the resistive part of the impedance of samples balance by adjusting the phase on the voltage applied to this standard. This eliminates the Johnson noise produced by a resistance standard.

## 2.2 Rough Schematic

Fig. 2.1 displays the essential elements of the balancing circuit. An A.C. voltage  $V_d$  (drive voltage), whose amplitude remains fixed in the bridge balancing, is applied to one side of the sample of unknown impedance,  $Z_{samp}$ . Two voltages, each of variable amplitude, are summed and applied to a precision air dielectric standard capacitor whose impedance is  $Z_{stand}$ . One of

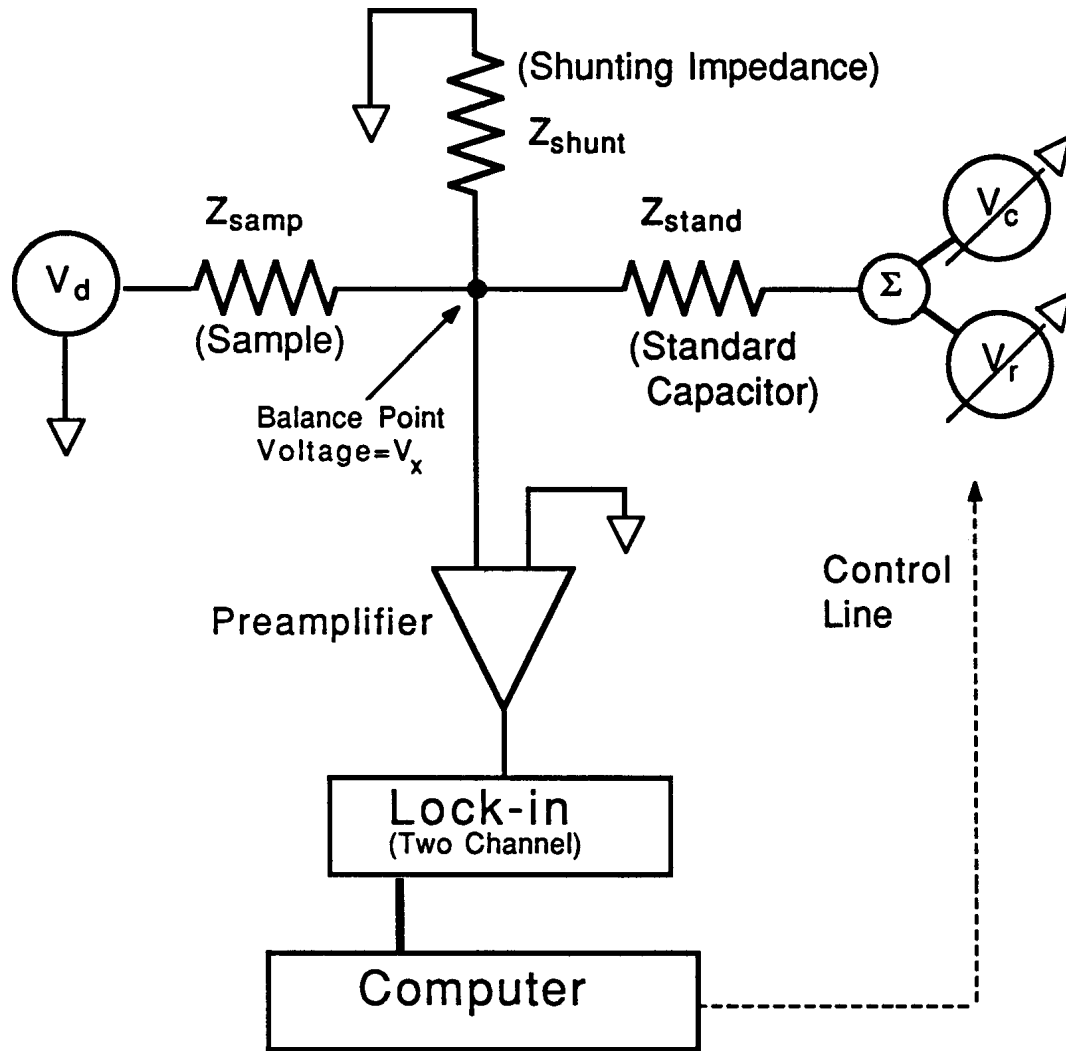


**Fig. 2.1** The figure displays a basic schematic of the automated bridge. The voltages  $V_c$  and  $V_r$  summed and applied to the standard capacitor (of capacitance  $C_{\text{stand}}$  and impedance  $Z_{\text{stand}}$ ) have phases  $180^\circ$  and  $+90^\circ$  respectively compared with the drive voltage applied to the sample,  $V_d$ . The basic idea behind the bridge is to null the voltage  $V_x$  at the balance point so that the sample impedance is given by Eqs. 2.5 & 2.6.

the voltages,  $V_c$   $180^\circ$  out of phase with the drive, and the other  $V_r$ , leading the drive voltage by approximately  $90^\circ$  are applied to the standard capacitor whose impedance is  $Z_{stand}$ . The basic idea behind the bridge is to null the voltage,  $V_x$  at the “balance point” where the standard capacitor and the sample meet. In the simplest configuration (as shown in Fig. 2.1), knowledge of the values of  $|V_c|/|V_d|$  and  $|V_r|/|V_d|$  needed to achieve balance, the phase relations of  $V_r$ ,  $V_c$ , and  $V_d$ , and  $Z_{stand}$  is sufficient to determine  $Z_{samp}$ . Because measurement is made when the voltage  $V_x$  is nulled, no current flows across the impedance (mostly from shunt capacitance) shunting the balance point to ground,  $Z_{shunt}$ , at balance, and the value of  $Z_{shunt}$  does not enter into the determination of  $Z_{samp}$ .

A preamplifier feeds the voltage signal at the balance point into a lock-in amplifier. A computer (IBM, PC-AT) reads the signals  $L_1$  and  $L_2$  from the two channels of the lock-in. These measure the in phase and out of phase signals of the voltage  $V_x$  with respect to the reference signal entering the lock-in. The phase of the lock-in with respect to  $V_d$  is irrelevant to the balancing procedure and to the determination of the sample impedance and need not be considered in this discussion. The computer controls the amplitudes  $|V_r|$  and  $|V_c|$  and uses the procedure described in the next section to adjust these to null the voltage  $V_x$ .

## 2.3 Theory of Operation

### *Determination of Balancing Voltages*

This section describes mathematically how the balance condition is determined by the computer. Because most of our samples are, to an excellent approx-

imation for the measuring voltage used here, linear devices, we can immediately write two linear equations describing the signals at the lock-in output. The multi-step balancing procedure described here can still achieve an accurate balance even with samples which contain some nonlinearity in their current-voltage relation.  $L_1$  and  $L_2$  can be written in terms of the voltage amplitudes  $|V_r|$  and  $|V_c|$  by:

$$\begin{aligned} L_1 &= K_{r,1}|V_r| + K_{c,1}|V_c| + M_1 \\ L_2 &= K_{r,2}|V_r| + K_{c,2}|V_c| + M_2. \end{aligned} \tag{2.1}$$

The variables  $K$  are independent of the voltage amplitudes, and  $M_1$  and  $M_2$  are the lock-in output voltages which are measured on channels 1 and 2 when the voltages  $V_c$  and  $V_r$  are set to zero. The phases of  $V_r$  and  $V_c$  are constant with respect to the phase of  $V_d$  throughout the balancing procedure.

First, consider the constants,  $K$ , as known variables. Their values depend on the values of  $Z_{shunt}$ ,  $Z_{stand}$ , and  $Z_{samp}$ . We describe later the algorithm which determines them. With the  $K$ 's known, reading the lock-in output with the voltage amplitudes  $|V_r|$  and  $|V_c|$  set to arbitrary values  $|V_r^\alpha|$  and  $|V_c^\alpha|$  determines the values of  $M_1$  and  $M_2$  and thus specifies the values to which  $|V_r|$  and  $|V_c|$  should be set to null the lock-in outputs  $L_1$  and  $L_2$ . Denoting the lock-in output values as  $L_1^\alpha$  and  $L_2^\alpha$  when  $|V_r|$  and  $|V_c|$  are set to  $|V_r^\alpha|$  and  $|V_c^\alpha|$ , it is easy to show that these values,  $|V_r^0|$  and  $|V_c^0|$ , are given by:

$$|V_r^0| = |V_r^\alpha| + \frac{P}{K_{r,1}} \left( -L_1^\alpha + \frac{K_{c,1}}{K_{c,2}} L_2^\alpha \right), \tag{2.2}$$

and

$$|V_c^0| = |V_c^\alpha| + \frac{P}{K_{c,2}} \left( -L_2^\alpha + \frac{K_{r,2}}{K_{r,1}} L_1^\alpha \right), \tag{2.3}$$

where

$$P = \left( 1 - \frac{K_{c,1}K_{r,2}}{K_{r,1}K_{c,2}} \right)^{-1}.$$

Equations 2.2 & 2.3 make it clear how balance is found once the values of the variables  $K$  are known. Determination of the values of these variables follows very simply by monitoring changes in the lock-in output values  $L_1$  and  $L_2$  as the voltage amplitudes  $|V_r|$  and  $|V_c|$  are varied. This can be done in three successive stages: **1)** With  $|V_r|$  and  $|V_c|$  at fixed starting values,  $L_1^1$  and  $L_2^1$  are measured; **2)** Only  $|V_r|$  is changed to a value  $|V_r| + \Delta|V_r|$  and  $|V_c|$  kept fixed at the same value as in step (1).  $L_1^2$  and  $L_2^2$  are measured; **3)**  $|V_c|$  is changed to a value  $|V_c| + \Delta|V_c|$  and  $|V_r|$  is changed back to its starting value in step (1). Finally,  $L_1^3$  and  $L_2^3$  are measured. It is then trivial to show that:

$$\begin{aligned} K_{r,1} &= \frac{L_1^2 - L_1^1}{\Delta|V_r|}, & K_{r,2} &= \frac{L_2^2 - L_2^1}{\Delta|V_r|}, \\ K_{c,1} &= \frac{L_1^3 - L_1^1}{\Delta|V_c|}, & K_{c,2} &= \frac{L_2^3 - L_2^1}{\Delta|V_c|}. \end{aligned} \quad (2.4)$$

Quite obviously, for fixed noise errors  $\delta L_1$  and  $\delta L_2$ , the greatest precision in the values of the various  $K$  variables is obtained when  $\Delta|V_r|$  and  $\Delta|V_c|$  are made as large as possible.

### *Two Cycles to Achieve Balance*

The bridge thus operates in two cycles. During the first cycle, the procedure of the last paragraph is carried out and each of the  $K$  variables is determined using Eqs. 2.4. During the second cycle, balance is achieved by adjusting the amplitudes  $|V_r|$  and  $|V_c|$  according to Eqs. 2.2 & 2.3.

A certain amount of (digital) signal averaging takes place during each measurement of  $L_1$  and  $L_2$  during each part of both cycles. An attempt is made to adjust the time spent in each part of both cycles to minimize the errors  $\delta V_r^0$  and  $\delta V_c^0$  in the final “balancing” values of  $|V_r|$  and  $|V_c|$  for the given total amount of time desired to be spent on signal averaging. Further, we find that

these errors are smaller if the balancing (second) cycle proceeds in two steps rather than one step. The first step achieves approximate balance, setting the amplitudes  $|V_r|$  and  $|V_c|$  to the values indicated by Eqs. 2.2 & 2.3, starting with amplitudes  $|V_r|$  and  $|V_c|$  arbitrarily far away from their balancing values,  $|V_r^0|$  and  $|V_c^0|$ . The second step in the balancing cycle starts from this approximate balance. Because the signal is near balance, digitization error of the lock-in output values  $L_1$  and  $L_2$  can become significant. For this reason, during this step the gain on the preamplifier feeding into the lock-in is increased by a factor of 10. Then the second balancing step using Eqs. 2.2 & 2.3 is undertaken to achieve better experimental values of  $|V_r^0|$  and  $|V_c^0|$ .

## 2.4 Evaluation of Sample Impedance

We point out that the treatment of the operation of the bridge has up to this point made no use of the phase relation between the voltages  $V_r$  and  $V_c$ , applied to the standard capacitor, with each other or with the drive voltage,  $V_d$ . However, knowledge of these phase relations is needed to determine the value of  $Z_{samp}$ . Consider  $V_r$  to lead  $V_d$  by exactly  $90^\circ$  and  $V_c$  to be  $180^\circ$  out of phase with  $V_d$ . In the bridge that we constructed,  $V_r$  is actually a known phase shift (between  $0$  and  $0.3^\circ$  of phase lag) away from being exactly  $90^\circ$  ahead of  $V_d$ . This complicates the  $Z_{samp}$  determination only slightly; but for simplicity here, we consider  $V_r$  as leading  $V_d$  by exactly  $90^\circ$ .

We consider  $Z_{samp}$  to consist of a parallel combination of a capacitance,  $C_{samp}$ , and a conductance,  $G_{samp}$ . In this case one finds, summing all of the currents into the balance point when the voltage at the balance point is nulled,

the following relations:

$$G_{smp} = \omega C_{stand} \frac{|V_r^0|}{|V_d|}, \quad (2.5)$$

and

$$C_{smp} = C_{stand} \frac{|V_c^0|}{|V_d|}. \quad (2.6)$$

The solution for arbitrary phase of  $V_r$  is of course obtained simply by splitting  $V_r$  into components in and out of phase with the drive voltage, adding the in phase part to  $|V_c|$  in Eq. 2.6 and replacing  $|V_r|$  in Eq. 2.5 with the out of phase part.

## 2.5 Implementation of Bridge

The hardware in the bridge was purposely kept very simple, leaving the control of almost all functions to the computer. Fig. 2.2 displays a more detailed view of the function of the bridge. The voltages  $V_c$ ,  $V_r$ , and  $V_d$  are all derived from the same signal generator. This signal, aside from going directly to the sample (actually by means of a voltage divider and a circuit which applies a bias voltage), goes to the inputs of two 12 bit multiplying D/A converters (MDACs). These MDACs control the voltage amplitudes  $|V_c|$  and  $|V_r|$ .

The output of the MDAC (MDAC#1) in Fig. 2.2 which controls  $|V_r|$  is fed into an op-amp integrator<sup>5</sup> which is used to produce the  $+90^\circ$  phase shift in the voltage  $V_r$ . A feedback resistor (40 k $\Omega$ ) shunts the capacitor in integrator to keep it from charging to a large D.C. voltage. Because we need the bridge to operate over a wide range of frequencies, and because the gain of the integrator is inversely proportional to the applied frequency and the integrating capacitance, relays are used to switch to different integrating capacitances (from 5000 pF to 5  $\mu F$  in powers of 10) depending on the frequency and considerations described

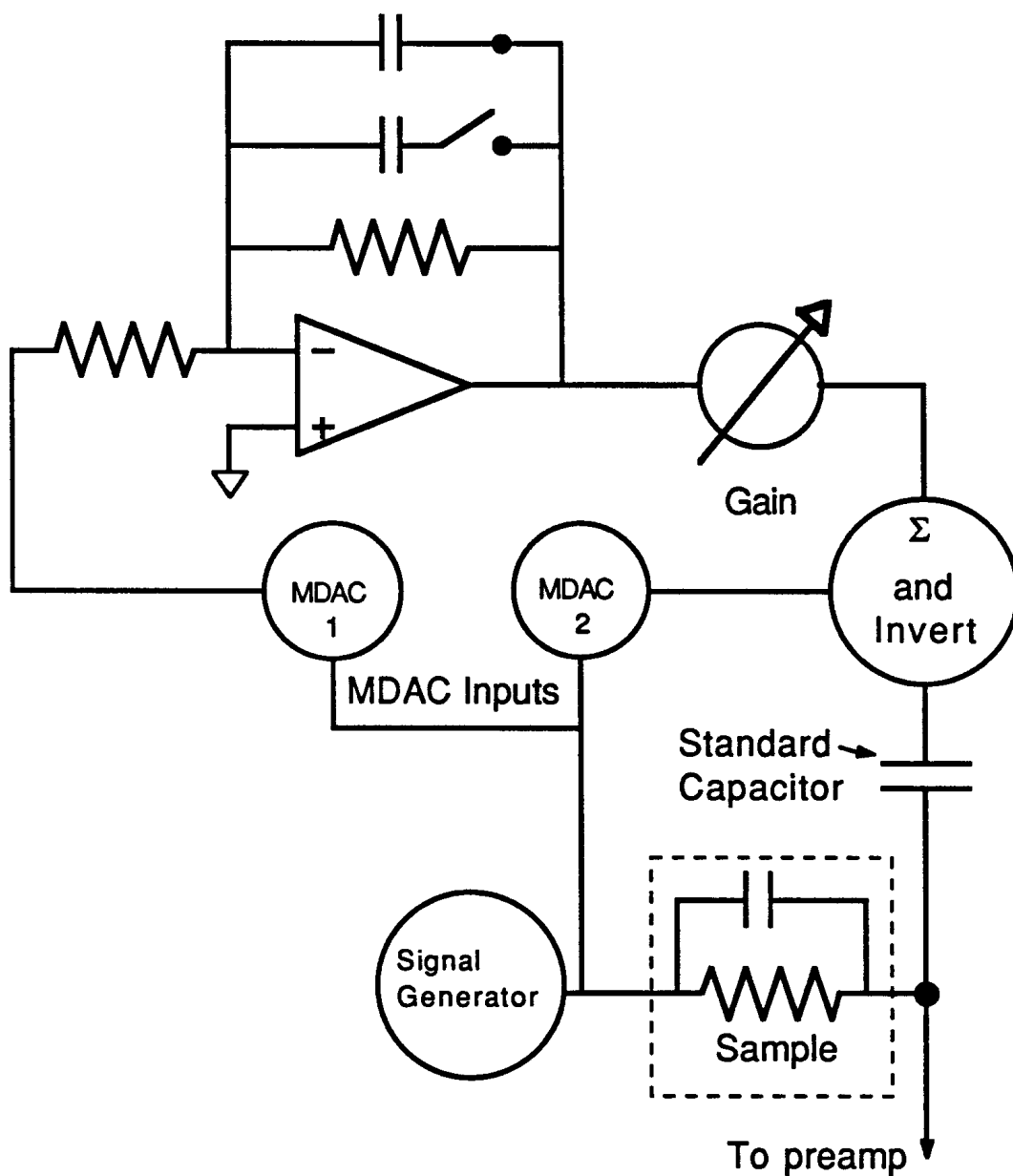


**Fig. 2.2** The figure shows the basic inner workings of the bridge circuitry. Signal levels are varied using two computer controlled multiplying D/A converters (MDACs). The digital inputs to these MDACs are typically cycled through the algorithm of section 2.3. The output of one MDAC is fed into an op-amp integrator which provides a  $90^\circ$  phase shift to balance resistive components of the sample impedance. The signals from this integrator circuit and the other MDAC are summed and inverted and applied to the arm of the bridge containing the standard capacitor.



below. We note that the feedback resistance causes the final signal phase to lag slightly from a  $90^\circ$  degree phase advance relative to the signal from the signal generator.

Although this is not a problem because we know the value of this phase lag, we prefer to keep it small. The reason for this is that the elements used are off the shelf capacitors and resistors whose value may drift with time. Typically we need for our experiments greater accuracy in capacitance measurements than for loss measurements; hence we would like any signal coming through the integrator circuit that deviates from  $90^\circ$  to be small so that the errors due to imprecise knowledge of component values in the integrator circuit are small in the capacitance measurement. For this reason, we keep the integrating capacitance as large as possible without making it so large that the output of the integrator stage is so small as to give poor signal to noise in the input of the next stage. The next stage is a variable gain amplifier (gain variable discretely in powers of 10) which adjusts the strength of the signal leaving the integrator before it is summed with the signal leaving the MDAC which controls  $|V_c|$  (MDAC#2 in Fig. 2.2). The summed signal is then inverted and divided by a factor of 1000 using a resistive voltage divider (not shown in Fig. 2.2) before it is applied to the sample. The large voltage dividers allow us to process signals at large signal levels inside the bridge to improve signal to noise while permitting sample measurement at low signal levels and at low output impedance ( $5\Omega$ ) from the bridge signal sources.

The bridge is typically run through the algorithm described in section 2.3. The idea is to adjust MDAC#1 and MDAC#2 so that the signal at the balance point is nulled. The bridge software adjusts the gain on the stage after the integrator so that if MDAC#1 and MDAC#2 are the same “distance” (in MDAC

input bit counts) off balance, similar sized off balance signals appear in the lock-in in both channels. This ensures that resolution is not lost in either the capacitance or the loss tangent measurement due to the signals from one MDAC being much larger than from the other.

The lock-in, preamplifier, and signal generator are also under computer control. The bridge software adjusts the lock-in and the preamplifier gain to be appropriate for the signal levels used in the measurement. The bridge also contains circuitry to apply a bias voltage on samples. This bias voltage, the amplitude of signals used to measure samples, and the frequency of these signals, are all under the control of the bridge software.

We mention briefly a few features used in the bridge to minimize 60 Hz and other noise. Most of the bridge circuitry is run by batteries to eliminate potential ground loops in power lines. All computer lines to the bridge circuitry and the preamplifier are optically isolated. Also, the reference signal from the bridge circuits to the lock-in is optically isolated as well. The preamplifier, which is also run off of batteries, has its output coupled into the lock-in via an audio frequency transformer. This allows the bridge circuits, which are grounded to the signal generator, to attach to power line ground at only one point, eliminating ground loops. All of the bridge circuitry (which is in shielding metal boxes) and batteries are kept in a cage surrounded by copper screening.

## 2.6 Special Features

We mention briefly a few features implemented on the bridge which have facilitated data taking and data analysis. One important feature is the calculation of errors in the final values obtained for the real and imaginary parts of the sample impedance. All data received from the lock-in is digitally signal

averaged, and the standard deviation in each set of averaged values is calculated. These errors on each measurement are propagated as indicated by the algorithm of section 2.3 to determine error bars on the sample impedance measurement. Knowledge of these errors is helpful because in curve fitting to our measurements (described in later chapters) it is important to know how much “weight” to give to various measurements.

In some of our work<sup>2</sup> it has been very important to ensure that stray high frequency signals did not appear across samples. For this reason, we have occasionally added low pass filters (cutoff  $\approx 30$  kHz) on both sample leads. Provisions are built into the bridge software to compensate sample impedance results for these filters. Another correction that the bridge software makes in obtained values for the sample impedance is needed because phase shifts result in signals passing through the MDACs due to the fact that the MDACs contain some small output capacitance ( $\approx 30$  pF) and the signals from the MDACs are fed into op-amps with finite open loop gain.<sup>6</sup> These phase shifts grow larger with frequency. Because these phase shifts depend somewhat on the settings of the MDACs it becomes difficult to correct bridge measurements for them at high frequencies. These phase shifts are responsible for the high frequency limit of operation of the bridge at 30 kHz.

Finally for very high resolution measurements, the bridge is run using a different procedure than that described in section 2.3. The MDACs contain a gain error of about 1 part in  $10^4$ . For higher precision than this in impedance measurements, the MDACs must be kept at a fixed value (their gain appears to be stable to better than 1 part in  $10^6$  over one hour), and the amount to which signals at the balance point are different from zero are interpreted to determine the sample impedance. The bridge software has built in it the ability to measure

shunt impedance and then interpret an off balance signal in terms of capacitance and loss tangent of the sample. Typically, we wish to measure how much the sample capacitance and loss tangent change as the applied bias across the sample is varied. The protocol now becomes as follows. At a particular applied gate bias, the bridge is balanced. The gate bias is now varied and measurements are made with the MDAC digital inputs fixed at these values. This high resolution mode is especially important in the work of Ch.6, where we measure samples of capacitance 35 pF to a resolution of .1 fF.

## References

1. R.C. Ashoori, J.A. Lebens, N.P. Bigelow, and R.H. Silsbee, Phys. Rev. Lett. **64**, 681 (1990)
2. *See Chapter 4*
3. *See Chapter 6*
4. R.E. Cavicchi and R.H. Silsbee, Rev. Sci. Instrum. **59**, 176, (1988)
5. Paul Horowitz and Winfield Hill, *The Art of Electronics* (Cambridge University Press, 1989)
6. D. Sheingold, J. Wilson, and G. Whitmore, Application Guide to CMOS Multiplying D/A Converters, Analog Devices, Norwood, MA, 1978

## Chapter III

# Quantitative Measurement of the Two-Dimensional Thermodynamic Density of States

### 3.1 Introduction

The shape and size of Landau level density of states (DOS) peaks in a two dimensional (2d) electron gas in the presence of a magnetic field applied perpendicular to the plane of the electron gas has generated considerable interest over the past two decades.<sup>1</sup> The thermodynamic DOS is an equilibrium property of the 2d electron gas. It makes no distinction between localized or extended states. However, ideas involving the processes resulting in localization of states<sup>2</sup> can be investigated through observation of the shape density of states peaks associated with Landau levels. The notion of a nonzero DOS between Landau levels has been crucial in formulating ideas of the Quantum Hall Effect.

A variety of experiments, including specific heat,<sup>3,4</sup> magnetization,<sup>5</sup> and capacitance<sup>6-8</sup> studies have sought to probe the 2D DOS. In most cases, measurements have determined the DOS of a system with a fixed electron density in the 2D layer, with variation of parameters such as applied field and temperature. Typically, models of the 2d electron gas refer instead to the density of states at the Fermi energy as the Fermi energy is varied. Information from such a model (as for example in Ref. 3) must be transformed in an

appropriate form in order to compare with the data. This procedure may introduce ambiguity as to the shape of the original DOS peak as a function of energy. Many of these experiments have, in fact, given only qualitative results on the DOS shape, and not a quantitative description of the DOS.

### **3.1.1** *Extraction of the DOS from capacitance measurements*

The technique presented in this chapter uses capacitance measurements to determine the 2d DOS. Previous experiments have suffered from large errors in the 2d DOS determined through capacitance measurements<sup>9</sup> due to imprecise knowledge of sample parameters (barrier thicknesses, dielectric constants, positions of electronic charges, etc.). In the experiments described here, two normalization conditions, derived from the known parameters of Landau level degeneracy and Landau level energy spacing, remove uncertainties normally present in other techniques and provide us a means for accurate measurement of the DOS at the Fermi energy versus energy.

Unlike many experiments, ours are carried out at a constant magnetic field strength; we instead vary the electronic density in a quantum well by means of a gate bias. The technique used here relates this gate bias to the Fermi energy in the quantum well and yields the DOS from the capacitance data, which can then be plotted as a function of Fermi energy.

Results from Goodall, Higgins, and Harrang<sup>6</sup> have revealed some of the difficulties involved in the DOS determinations using capacitance spectroscopy due to the large conductivity variations in the plane of the 2d electron gas as the Landau index is varied. Attempts at circumventing these problems have been made by restricting the experiments to low measuring frequencies<sup>7,8</sup> and low magnetic fields ( $< 2\text{T}$ ).<sup>7</sup> Our experiments are done on samples where

the 2d electron gas is coupled by tunneling to a conducting substrate. This allows charge to be transferred to all regions of the 2d electron gas even when the “in-plane conductance” is very low, allowing us to make capacitance measurements which are largely insensitive to the magnetoresistance of the 2d layer. Similarly designed samples have been used previously to qualitatively determine the DOS at the Fermi energy as a function of magnetic field up to very large field strengths.<sup>9</sup>

### 3.1.2 *Essential DOS Results*

A detailed outline of this new technique is presented here, as well as DOS results obtained using this technique on samples from three different wafers grown using molecular beam epitaxy (MBE). The bulk of the chapter focuses on the DOS in magnetic fields 4.0 T and below, with some results from higher fields (8.5 T) presented near the end of the chapter. In low magnetic fields ( $<4\text{T}$ ), where the effect of the spin splitting is too small to be observed in the level shape, we observe a striking difference between lineshapes determined from our experiment, displayed here as a function of Fermi energy, and lineshapes inferred by others from data taken at constant electron density in the 2d gas. The lines are well fit by Lorentzian lineshapes in contrast with most existing literature in which Gaussian shapes with perhaps the addition of a constant background DOS<sup>3,10</sup> are used. Lorentzians give good fits to DOS results from all three samples even though the three samples are very different in terms of the positioning of dopants in an AlGaAs barrier near the quantum well which contains the 2d electron gas. Also remarkable in our data is the fact that the widths of DOS peaks observed in our experiment, while dependent on the Landau level index, show almost no dependence on magnetic field strength.



In essence, the picture of the Landau level DOS developed here is a significant departure from that of previous work.

We also obtain the DOS in the high field region (up to 8.5 T), where there is strong exchange enhancement of the Zeeman energy of electrons in the 2d gas. We use the exchange model of Ando and Uemura<sup>11</sup> using both Gaussian and Lorentzian fits for determination of the spin exchange energy,  $E_{exch}$ , to provide comparison with other recent determinations of this parameter.<sup>12,13</sup>

### **3.1.3** *Measurements probing the localization length of states*

Another important question in the physics of the 2d electron gas asks: As the Landau level filling factor,  $\nu$ , in the 2d electron gas is varied how does the localization length of states vary? A great deal of theoretical work,<sup>14,15</sup> and more recently experimental work,<sup>16</sup> has been devoted to understanding the behavior of the localization length. Much of this work has been concerned with the region around a Landau DOS maximum, where it is thought that the localization length diverges. Effort has been focused on the nature of the divergence; much less work has been done on the absolute length scales of the localized levels or their behavior well away from the divergence.

In a later section of this chapter, we introduce a new technique for the determination of the localization length as a function of Fermi energy. This technique is particularly sensitive to the localization length when the Fermi energy is between Landau levels, a region where the localization length is not easily probed by transport experiments. We present qualitative results from this technique.

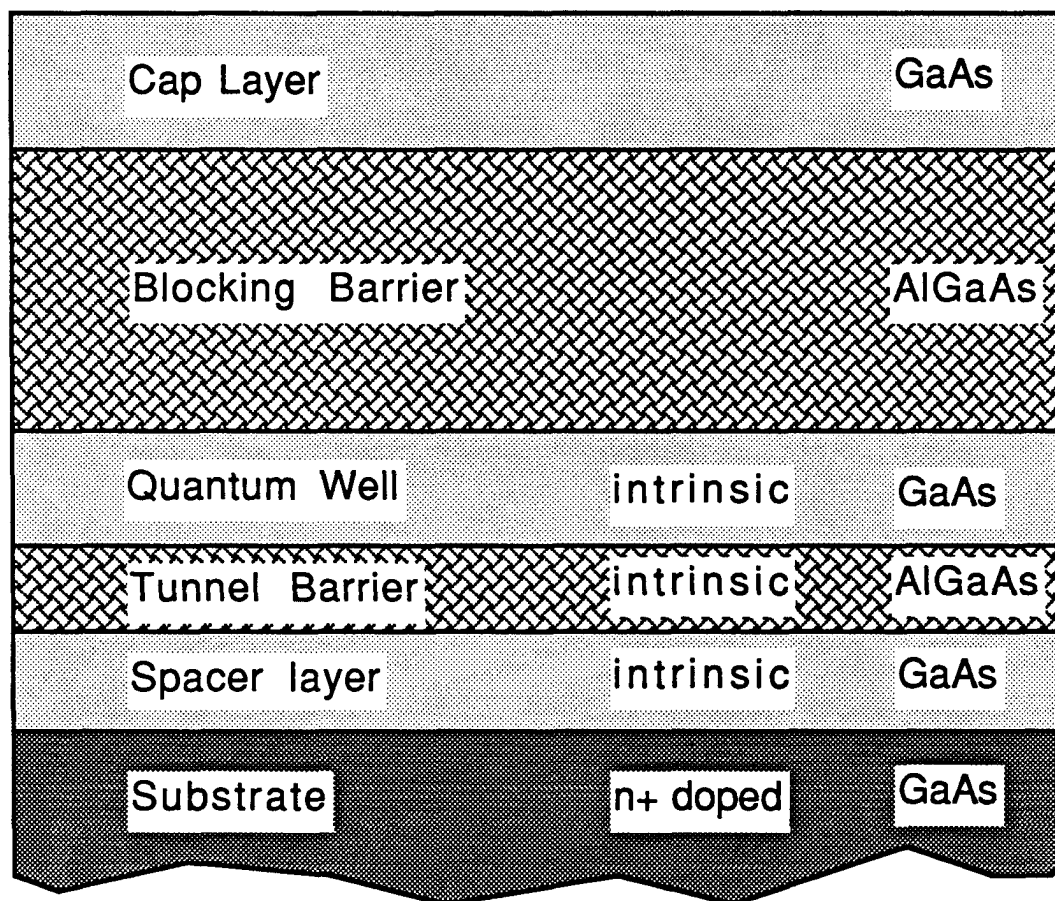


**Fig. 3.1** The essential layer structure of the samples. In samples **A** and **C** the blocking barrier contains Si doping commencing at distances of 100 Å and 150 Å respectively away from the edge of the quantum well.

### 3.2 Sample Design

We will refer to the three different samples used in this study as **A**, **B**, and **C**. Figure 3.1 displays the essential layer by layer construction of our MBE grown wafers, and Fig. 3.2a shows the conduction band edge structure in sample **B** which is very similar to that in the other samples. All wafers are grown on  $n^+$  GaAs substrates which remain conducting at 4 K and lower temperatures. On top of the substrate, an AlGaAs tunnel barrier is grown, and then a GaAs quantum well. Beyond this, there is an AlGaAs “blocking barrier” which allows no electrical conduction over the range of gate biases applied in the measurements described here. Samples **A** and **C** each have a dopant layer in the blocking barrier; sample **B** has no dopants in the blocking barrier. A GaAs cap layer is grown above the blocking barrier in all of the samples. In samples **A** and **B**, this layer is heavily doped, and ohmic contact is made to this layer, which then serves as a “gate” for our device. In sample **C**, the cap layer is undoped; a Cr Schottky contact is made to the surface and the Cr metal acts as the gate.

Sample **A** has been described extensively.<sup>17,18</sup> The wafer used to produce this sample consists of a degenerately n (Si- $1 \times 10^{17}\text{cm}^{-3}$ ) doped substrate in GaAs, a 30 Å GaAs undoped spacer layer, an AlGaAs tunnel barrier (160 Å wide), a GaAs quantum well (150 Å wide), a thick AlGaAs blocking barrier (1550 Å wide), and a degenerately n doped GaAs surface contact region. A doped region ( $5 \times 10^{17}\text{cm}^{-3}$ ) exists from 100Å to 200Å away from the edge of the quantum well in the blocking barrier. These donors are fully ionized for the range of electron filling of the quantum well from  $0 - 5 \times 10^{11}\text{cm}^{-2}$ . All AlGaAs in sample **A** has an Al concentration of 30%.

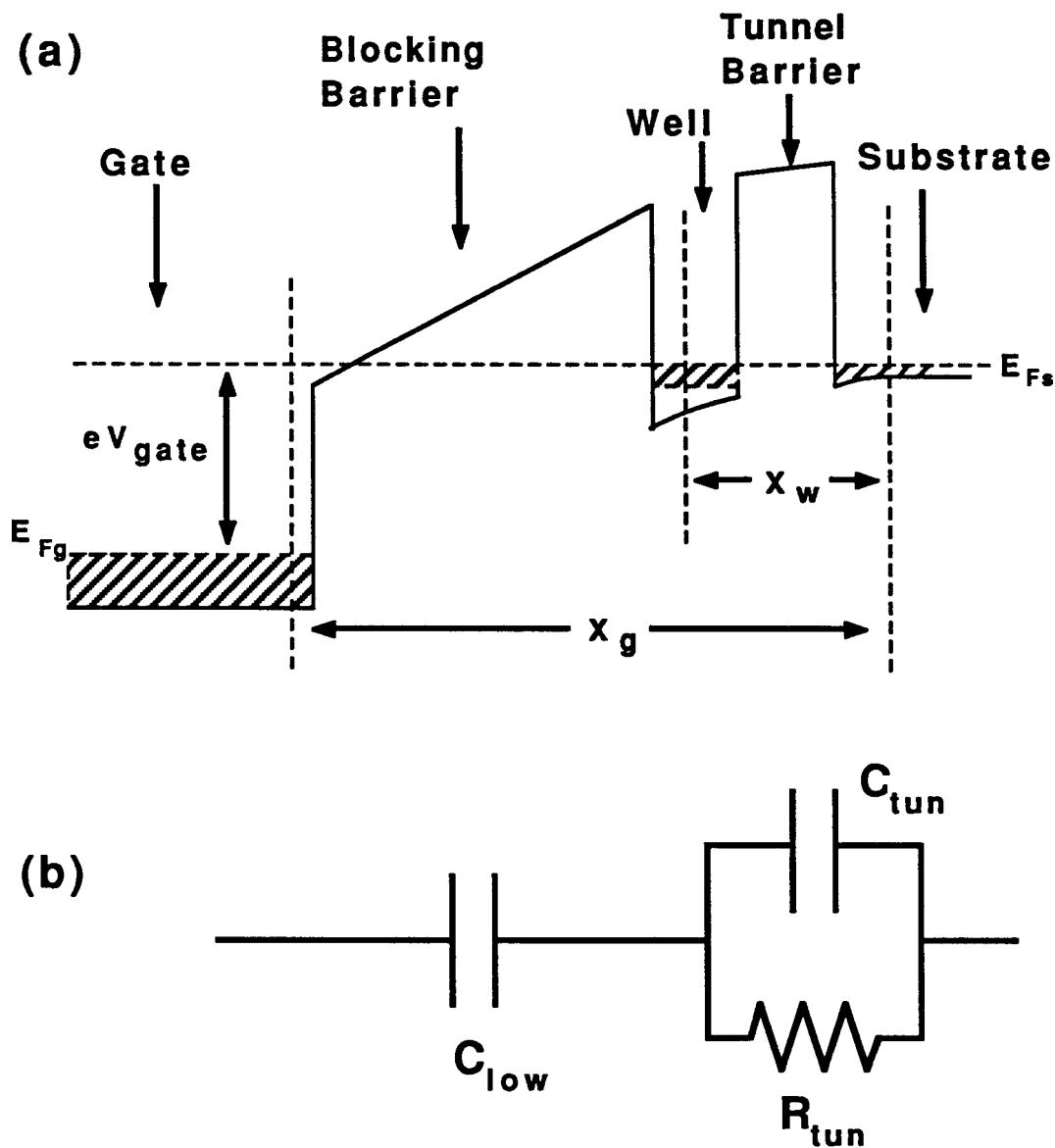


**Fig. 3.2** (a) shows the essential structure of the samples. Electron transfer through the tunnel barrier brings the electron gases in the substrate and the quantum well into equilibrium. The density of electrons in the quantum well may be varied through the application of a gate bias ( $V_{gate}$  in the figure). Capacitive coupling to the well allows us to measure both the thermodynamic density of states (DOS) in the well and tunneling from the well to the substrate. (b) displays the model of the sample which is used in curve fitting to extract low and high frequency capacitances used to determine density of states in the quantum well.

Sample **B** has a GaAs substrate doped at  $\text{Si-}4 \times 10^{17} \text{cm}^{-3}$ , a 30 Å undoped GaAs spacer layer, an AlGaAs tunnel barrier (133 Å wide), a GaAs quantum well (150 Å wide), an AlGaAs blocking barrier (800 Å wide), and a degenerately n ( $3 \times 10^{18} \text{cm}^{-3}$ ) doped GaAs surface contact region. To help achieve high mobility, this sample contains no dopants in the blocking barrier. Moreover, the sample temperature was lowered during the growth of the GaAs spacer layer to reduce Si donor impurity migration and the tunnel barrier was grown with periodic growth interruptions (every 23 Å and with one monolayer of GaAs grown at each interruption) to increase interface smoothness. These techniques are thought to enhance the mobility of systems with AlGaAs grown below the 2d layer.<sup>19</sup> All AlGaAs in sample **B** has an aluminum concentration of 41%.

Sample **C** has a degenerately n ( $\text{Si-}4 \times 10^{17} \text{cm}^{-3}$ ) doped substrate in GaAs, a 150 Å GaAs undoped spacer layer, an AlGaAs tunnel barrier (150 Å wide), a GaAs quantum well (150 Å wide), an AlGaAs blocking barrier (500 Å wide) and an undoped 300 Å wide GaAs cap layer. The cap layer never contains electrons over the range of gate biases applied to the sample for the measurements in this chapter. The 300 Å cap layer can thus be considered as part of the blocking barrier. Cr Schottky contact is made to the surface of the sample. A heavily doped ( $6 \times 10^{17} \text{cm}^{-3}$ ) region exists in the AlGaAs from 150 Å to 500 Å away from the edge of the quantum well and the AlGaAs blocking barrier. These donors are fully ionized for the range of measurements presented here. All AlGaAs in sample **C** has an aluminum concentration of 30%.

Metallic discs (AuGe ohmic contacts for samples **A** and **B** and Cr for **C**) ranging in size from 200  $\mu\text{m}$  to 400  $\mu\text{m}$  in diameter act as gate contacts and also served as etch masks for a mesa etch defining devices upon which capacitance measurements are made. In each of the samples, the electron concentration in

the quantum well can be varied by application of a gate bias. The 2d density in **A** can be varied from  $0 - 6 \times 10^{11} \text{cm}^{-2}$  before there is any measurable current through the blocking barrier. Samples **B** and **C** each have a range of  $0 - 4 \times 10^{11} \text{cm}^{-2}$ .

### 3.3 Measurements

Our DOS determination derives from measurement of two capacitances of our devices, one measured at low and the other at high frequencies. The samples have been designed so that the frequency,

$$f_{peak} \approx \frac{1}{2\pi R_{tun} C_{tun}},$$

lies within the range audio frequencies at which we make capacitance measurements. Here  $R_{tun}$  and  $C_{tun}$  are the resistance and capacitance of the tunnel barrier respectively, and  $f_{peak}$  is the frequency at which the loss tangent for the device reaches a maximum. A frequency dependence of the sample capacitance arises near the frequency  $f_{peak}$ . This can be intuitively understood by considering that at low frequencies, where the measured capacitance is  $C_{low}$ , there is enough time during one half cycle of the measuring frequency for charge to move into the quantum well from the substrate and bring the two into equilibrium. At high frequencies, during one half cycle of the measuring frequency little charge can be transferred between the substrate and the well, and the measured capacitance  $C_{high}$  is lower, of value appropriate to the distance from the gate contact region to the substrate charge. An essential issue our DOS determination is that  $C_{low}$  depends on the DOS in the 2d electron gas. If the quantum well had an infinite DOS, then it would fully shield the substrate from the gate field, and  $C_{low}$  would be the capacitance simply deduced from the distance from the gate

to the 2d gas. For a finite DOS, however, this shielding is not complete, and our analysis provides a means to deduce the DOS from the measured capacitances.

In practice, at each value of temperature, magnetic field, and gate bias for which we wish to measure the DOS, we measure the capacitance as a function of frequency over the range from 15 Hz to 30 kHz and obtain  $C_{low}$  and  $C_{high}$  from fits to this data. Figure 3.3 displays the measured capacitance and loss tangent from a 200  $\mu\text{m}$  diameter mesa from sample **B**. The capacitance remains constant, of value  $C_{low}$ , at the lowest frequencies, decreases over a range of about a decade in frequency, at frequencies around  $f_{peak}$ , then levels off to  $C_{high}$  at the highest frequencies. The loss tangent moves through a peak at the same frequencies where the measured capacitance is decreasing most sharply with frequency.

The capacitance  $C_{low}$  is the capacitance of the nonshunted capacitor in Fig. 3.2b.  $C_{tun}$  is the capacitance of the capacitor shunted by the tunneling resistance  $R_{tun}$  in the model, and  $C_{high}$  is the series combination of  $C_{low}$  and  $C_{tun}$ . We fit the data to forms indicated by the simple circuit model given in Fig. 3.2b and extract the parameters  $C_{low}$ ,  $C_{high}$ , and  $f_{peak}$  (and hence  $C_{tun}$  and  $R_{tun}$ ). The form for the capacitance fit as a function of frequency is:

$$C(f) = \frac{C_{high}C_{low}[1 + (f/f_{peak})^2]}{C_{high} + C_{low}(f/f_{peak})^2}. \quad (3.1)$$

In other work,<sup>17,20–22</sup> we have focused on results for the tunneling conductance. The model of Fig. 3.2b is only appropriate for extracting the tunneling conductance in the limit of infinite DOS in the 2d electron gas; for finite DOS, the interpretation of the tunneling conductance in terms of  $f_{peak}$  and the other fitting parameters must be modified. However, the functional forms indicated by the model for the loss tangent and the capacitance vs. frequency are valid for all values of the DOS.<sup>22</sup> For the present work only the values of  $C_{low}$  and  $C_{high}$ ,

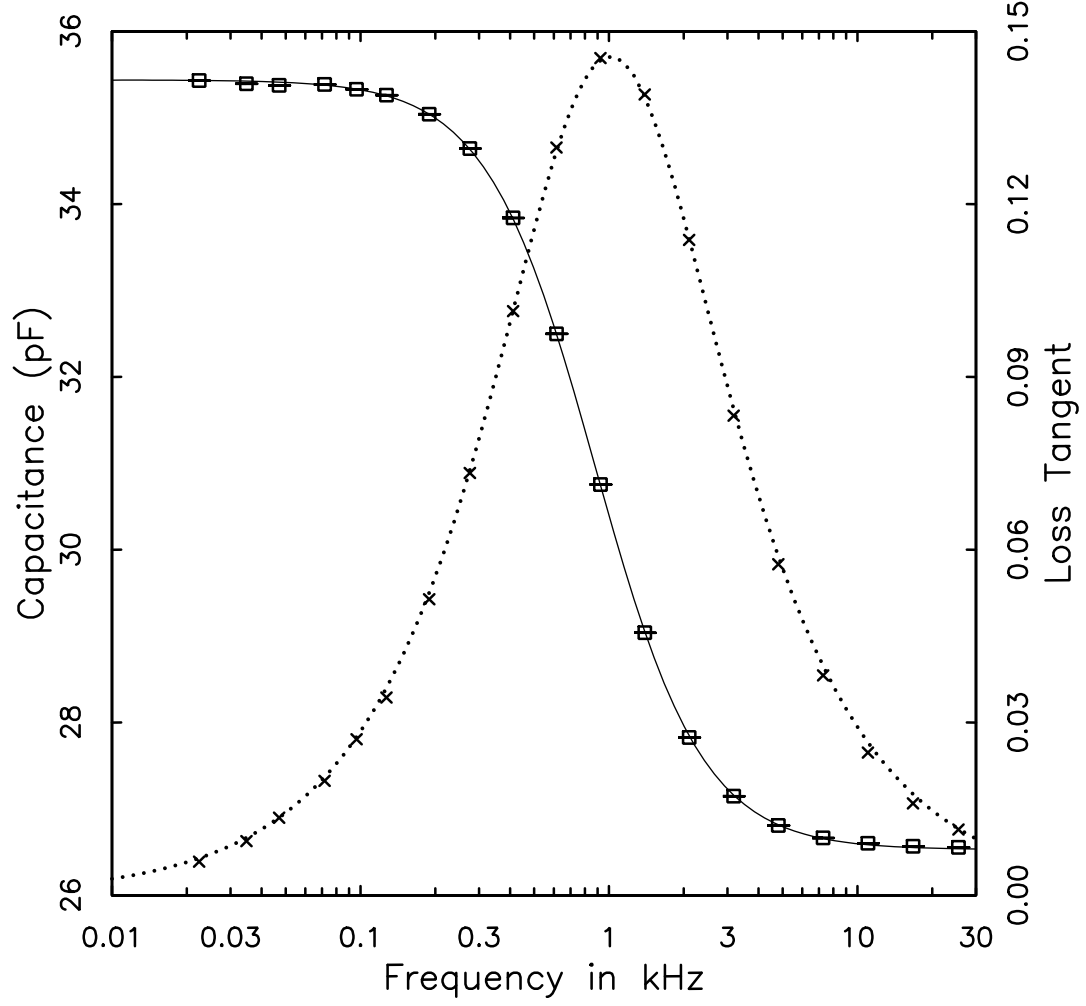


**Fig. 3.3** Capacitance and loss tangent of a  $200\ \mu\text{m}$  mesa etched on sample **B**. The solid and dotted curves are fits from the circuit model presented in Fig. 3.2b. At low frequencies, electron transfer from the substrate to the well can take place, and the capacitance  $C_{low}$  is measured. At frequencies high compared to the RC time of the tunnel barrier, no electron transfer to the well takes place, and the measured capacitance,  $C_{high}$  drops to a value consistent with the distance from the top gate to the substrate layer.

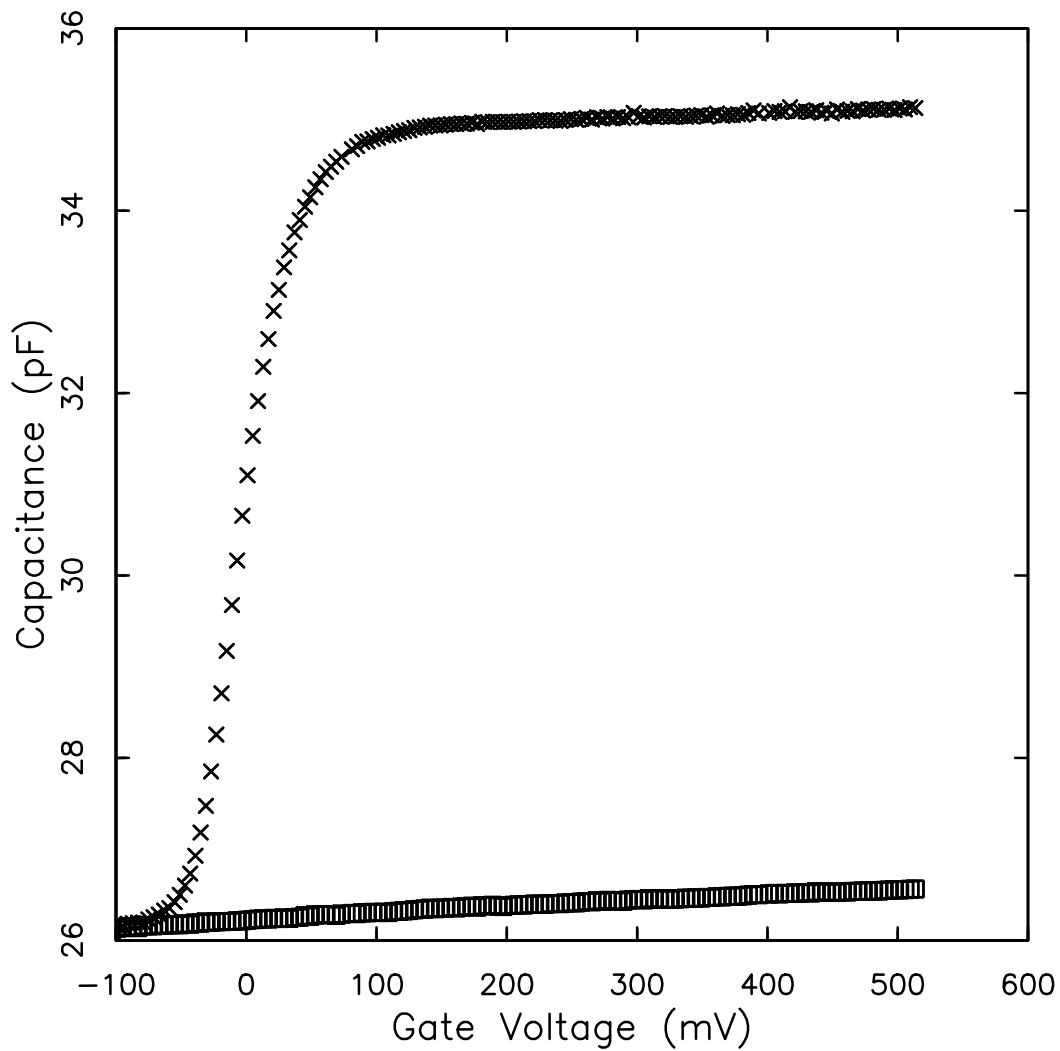


extracted correctly from fitting data using Eq. 3.1, are important in determining the DOS.

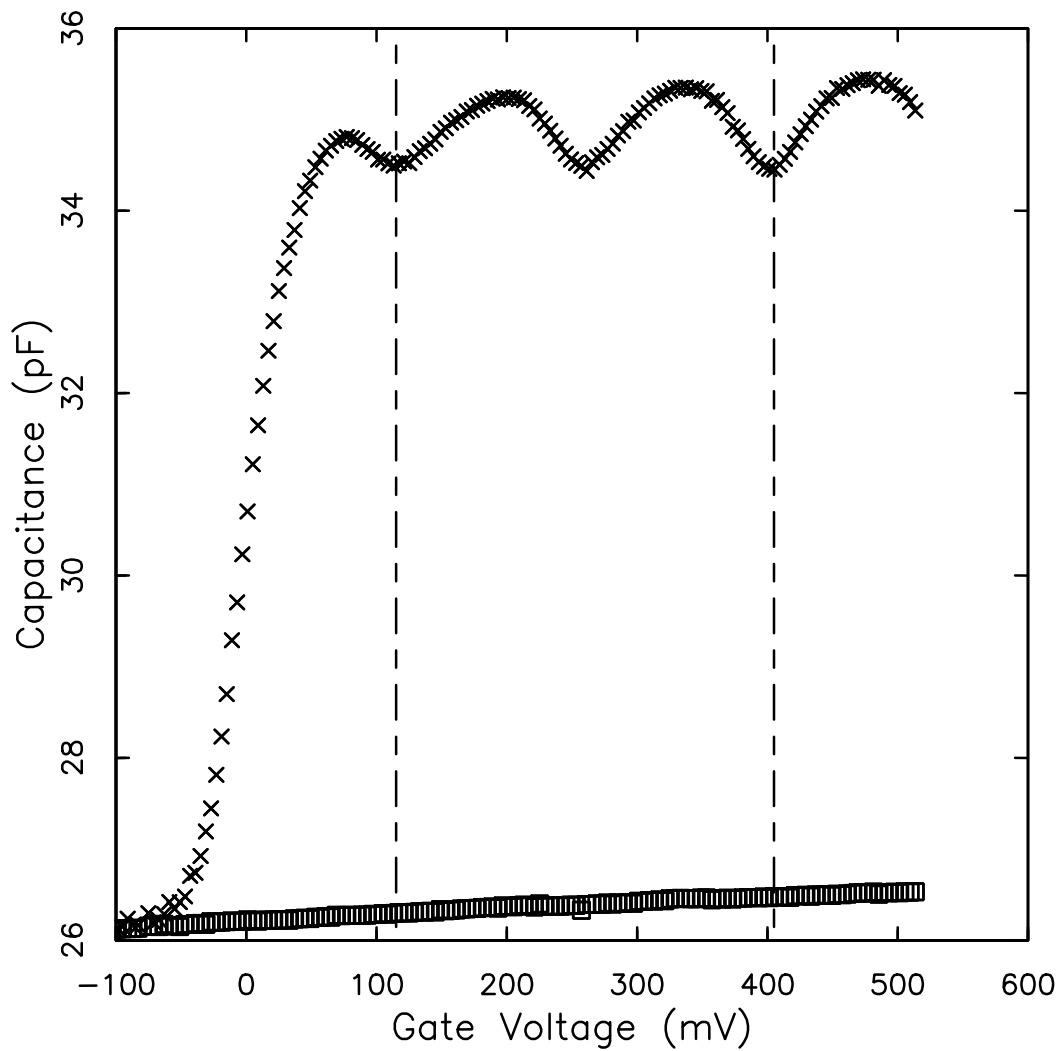
Figure 3.4 displays  $C_{low}$  and  $C_{high}$  obtained from fits as a function of gate bias for sample **B** at 4.2 K and with no applied magnetic field. At the lowest gate biases (below -80 mV) the quantum well is completely devoid of electrons. At these gate biases, the capacitance of the sample measured as a function of frequency is a constant. As the gate bias is increased, electrons enter the well, and there is a sharp rise in the low frequency capacitance. At this step, the bound state energy in the well is dropping below the Fermi energy in the substrate. Beyond this step, the low frequency capacitance is almost constant aside from a slight slope due to the shift of the mean position of charges in the well and the substrate with gate bias. This constancy reflects the fact the 2d DOS in the absence of magnetic field is a constant in energy. The high frequency capacitance continues to measure the capacitance with no charge transfer to the well and no significant change is observed in this capacitance as the well fills. The slight slope in  $C_{high}$  seen in Fig. 3.4 is due to a variation with gate biases in the position of charges in the substrate.

Figure 3.5 shows  $C_{low}$  and  $C_{high}$ , again for sample **B**, at 2.0 T and 2.1 K.  $C_{low}$  develops some obvious oscillations in the presence of magnetic field in regions of gate bias where the well contains electrons. These are due to the Landau level DOS now reflecting the variations of the 2d DOS in the well in the presence of magnetic field. Again,  $C_{high}$  does not probe the DOS in the well, and consequently does not undergo oscillations as the gate bias is varied.

In previous capacitance DOS determinations from samples with the same essential structure as ours, where charge can be transferred from a 2d gas to a conducting substrate, only capacitances analogous to  $C_{low}$  have been measured.<sup>9</sup>



**Fig. 3.4** Capacitances  $C_{low}$  and  $C_{high}$  (described in the text) determined from fits to capacitance vs. frequency data on sample **B**. The sharp increase in  $C_{low}$  occurs as the well begins to fill with electrons. Here, there is no magnetic field applied and the temperature is 4.2 K.



**Fig. 3.5** Capacitances  $C_{low}$  and  $C_{high}$  for sample **B** at 2.0 T and 2.1 K. Note the oscillations in the low frequency capacitance. These arise from the Landau level DOS in the well. The high frequency capacitance is insensitive to the DOS in the well and does not display any such oscillations. The two dashed vertical lines are limits of integration described in section 3.4.3 of the text.

The next section of this chapter will show that in measuring both  $C_{low}$  and  $C_{high}$  a much more complete determination of the DOS can be made with no sample parameters other than sample area entering the calculation.

### 3.4 Analysis Procedure

We present an analysis procedure which allows us to extract the density of states in the quantum well. The desired result is to extract the DOS  $g$  from the measurements of  $C_{low}$  and  $C_{high}$ , and to plot this DOS as a function of Fermi energy in the well, measured with respect to the bound state energy in the well. It should be understood that references to the DOS or  $g$  in this section describe the thermodynamic DOS,  $\partial n / \partial \mu$ . (In a single particle picture it may be thought of as the zero temperature DOS  $g_0$  convolved with the derivative of the Fermi distribution function.) This section describes how the DOS is extracted from the data and how a conversion is made from gate bias to energy in the well.

We start with a model which places all of the electronic charge in the well at a plane in the well and treats charges in the substrate and contact as planar charges near, but not necessarily at, the physical interfaces between insulating and metallic regions. Later, we make a correction for the sheet charge approximation of the distribution of charge in the well. As we will discuss, the shape of the electron charge distribution in the  $x$  (vertical) direction in the well is important. There is no change of the DOS determination in going to a more precise model which considers charges in the substrate and contact regions to be distributed in the  $x$  dimension. For simplicity, we neglect the effect of the doping spike here. This has no effect on the DOS determination. Also, we will neglect the effects of the nonzero polarizability of electrons in the well. The contribution of this polarizability to the measured capacitance is less than 1%

of the sample capacitance, and a simple correction can be made for its effects on the DOS results.

Referring to the sample geometry outlined in Fig. 3.2, Poisson's equation determines the following set of equations:

$$U_g = \frac{e^2}{\epsilon}[\sigma_g x_g + \sigma_w x_w] \quad (3.2)$$

$$U_w = -\frac{e^2}{\epsilon}\sigma_s x_w \quad (3.3)$$

$$eV_{gate} = U_g + E_{Fg} - E_{Fs}. \quad (3.4)$$

All definitions given in this paragraph are understood to be in the sheet charge model.  $x_w$  and  $x_g$  are the distances between the mean position of the excess charge density in the substrate and the mean position of the electronic charge distribution in the well and gate (top contact) respectively.  $U_w$  is the potential energy at the conduction band edge, again compared to the band edge in the substrate, in the well at position  $x_w$ .  $U_g$  is the energy of electrons at the band edge in the gate region compared to the band edge in the substrate.  $V_{gate}$  is the gate voltage applied from gate to substrate, and the electronic charge is taken as positive in this discussion in order to make comparison with to figures.  $E_{Fg}$  is the Fermi energy in the contact region (gate) measured with respect to the conduction band edge in the contact region, and  $E_{Fs}$  is the Fermi energy in the substrate measured with respect to the conduction band edge in the substrate.  $e$  is the magnitude of the electronic charge, and  $\epsilon$  is the dielectric constant of the medium (differences in dielectric constant between GaAs and AlGaAs do not influence our DOS determination).  $\sigma_g$ ,  $\sigma_w$ , and  $\sigma_s$  are the number densities of excess electrons in the gate region, the well, and the substrate region respectively.

Electron transfer through the tunnel barrier brings the electron gases in the substrate and in the well into equilibrium. If the density of states in the well is

constant, the number density of electrons in the well is given by,

$$\sigma_w = \int_{U_{bound}}^{E_{Fs}} g(E) dE = g[E_{Fs} - U_{bound}]. \quad (3.5)$$

$U_{bound}$  is the energy of the ground state in the well, which is the only well electronic state ever occupied in our measurements, again measured with respect to the band edge in the substrate. If, in the sheet charge model, the bound state energy is considered to be at a fixed energy  $E_0$  with respect to the potential energy in the well at position  $x_w$  (the position of the sheet), then we could write

$$U_{bound} = U_w + E_0. \quad (3.6)$$

The more realistic model of charge distributed in the well and a bound state energy which depends on the potential at positions other than  $x_w$  gives

$$U_{bound} = U_w + E_0 - \eta\sigma_w. \quad (3.7)$$

The additional term, linear in the well charge density, corrects the bound state energy for the nonzero width of the electronic charge distribution in the well. The bound state energy difference between the sheet and distributed charge models,  $\eta\sigma_w$ , serves as a correction in the sheet charge model for both the band edge energy difference given by the models at position  $x_w$  and the quantum mechanical variation in the bound state energy in the well with respect to  $U_w$  due to changes in the shape of the potential along the well bottom as the well is filled. Modeling the electrons as being in a plane at the center of the well overestimates the electrostatic energy at position  $x_w$ . Also, the quantum mechanical energy of the bound state compared to the conduction band edge at position  $x_w$  decreases due to increased curvature of the well bottom as electronic charge is added to the well. These facts indicate that  $\eta > 0$ . A detailed discussion of the term,  $\eta$ , is given in Appendix A.

Replacing  $U_{bound}$  in Eq. 3.5 with the expression from Eq. 3.7, we obtain

$$\sigma_w = \frac{g}{1 - g\eta} [(E_{Fs}) - (U_w + E_o)]. \quad (3.8)$$

Our analysis requires the differential form

$$\delta\sigma_w = \frac{-g}{1 - g\eta} \delta U_w, \quad (3.9)$$

since our interest is in a nonconstant DOS function  $g$ . Finally, charge neutrality dictates that

$$\sigma_g + \sigma_w + \sigma_s = 0. \quad (3.10)$$

Solving differential forms of Eqs. 3.2, 3.3, 3.4, & 3.10 and Eq. 3.9 we obtain the following differential changes in charge density per change in the voltage applied to the gate:

$$\delta\sigma_w = \frac{-\epsilon g x_w}{e^2 g (x_g - x_w) x_w + \epsilon (1 - g\eta) x_g} \delta(eV_{gate}),$$

and

$$\delta\sigma_s = \frac{\epsilon(1 - g\eta)}{e^2 g x_w} \delta\sigma_w.$$

Further, we know by definition that  $d\sigma_w/dU_{bound} = g$ . Thus the “lever-arm”, or change in energy of the bound state per change in gate energy, is

$$\frac{dU_{bound}}{d(eV_{gate})} = \frac{x_w \epsilon}{e^2 g (x_g - x_w) x_w + \epsilon (1 - g\eta) x_g}. \quad (3.11)$$

In the case  $g = 0$  this expression reduces to the simple “geometric lever-arm” or  $dU_{bound}/d(eV_{gate}) = x_w/x_g$ . Knowledge of the lever-arm will allow us to convert the DOS known as a function of gate bias into DOS as a function of  $E_{Fs} - U_{bound}$ .

The capacitance  $C_{low}$ , measured at frequencies small compared with  $1/2\pi RC$ , where  $RC$  is the characteristic relaxation time of the tunnel barrier, is then

$$C_{low} = -Ae \frac{\delta\sigma_w + \delta\sigma_s}{\delta V_{gate}} = A\epsilon \frac{e^2 g x_w + \epsilon(1 - g\eta)}{e^2 g (x_g - x_w) x_w + \epsilon(1 - g\eta) x_g}, \quad (3.12)$$

where  $A$  is the area of the sample. Pausing briefly to examine this equation, we see that the value of  $C_{low}$  can vary between  $C_{low} = Ae/(x_g - x_w)$  for infinite DOS to  $C_{low} = Ae/x_g$  for zero DOS in the well. Physically, this can be explained as follows. In an infinite DOS capacitor model, electrons added to the well completely screens the region between the well and the substrate where there can thus be no electric field. However, in the finite  $g$  model, the energy of the bound state,  $U_{bound}$  must decrease at a rate inversely proportional to  $g$ , thus leaving an electric field in the region between the well and the substrate. A change in the gate voltage induces charge in the substrate along with the quantum well; the applied voltage is dropped over a longer distance, and the capacitance is less than  $Ae/(x_g - x_w)$ .

The other measured quantity in our experiment is the high frequency capacitance,  $C_{high}$ , measured at frequencies large compared to  $1/2\pi RC$ , such that no charge transfer can occur between substrate and well. In our model, the value of  $C_{high}$  is

$$C_{high} = \frac{A\epsilon}{x_g}. \quad (3.13)$$

It is clear that for zero DOS,  $C_{low} = C_{high}$ , and for  $g > 0$ ,  $C_{low} > C_{high}$ . These ideas can be compared to the data shown in Fig. 3.5. At gate biases below  $-50$  mV, the bound state in the well is at a higher energy than the Fermi energy in the substrate. In this case, the DOS in the well can be considered to be zero. For this range of voltages, the figure shows that  $C_{low} = C_{high}$  as indicated by the ideas given here. At higher gate voltages, the bound state in the well begins to fill, and  $C_{low}$  increases to a value larger than  $C_{high}$ . The value of  $C_{low}$  however, varies due to the variation in the DOS at the Fermi energy as the gate bias is varied. The maxima and minima in  $C_{low}$  correspond to maxima and minima in the Landau level DOS respectively.



### 3.4.1 Lever-Arm and DOS Determined from Measured Quantities

Now we consider the lever-arm once again. We introduce the quantity

$$C_{geom} = \frac{A\epsilon}{x_w},$$

the “geometric capacitance” between the well and the substrate. In terms of this quantity and  $C_{low}$ , the lever-arm becomes

$$\frac{dU_{bound}}{d(eV_{gate})} = \frac{C_{low}}{Ae^2g + C_{geom}(1 - g\eta)}. \quad (3.14)$$

Eqs. 3.12, 3.13, & 3.14 may be solved to give

$$\frac{dU_{bound}}{d(eV_{gate})} = \frac{C_{low}}{C_{geom}} - \left(\frac{C_{low}}{C_{high}} - 1\right)\left(1 - \frac{\eta C_{geom}}{Ae^2}\right), \quad (3.15)$$

and

$$Ae^2g = C_{geom}\left(\frac{C_{low}}{C_{high}} - 1\right)\frac{d(eV_{gate})}{dU_{bound}}. \quad (3.16)$$

Equations 3.15 & 3.16 are the core of our analysis. Both the lever-arm and the DOS are obtained through them. Equation 3.16, can be stated another way. The differential change in charge density in the well for a differential change in gate voltage is

$$gdU_{bound} = d\sigma_w = \frac{C_{geom}}{Ae}\left(\frac{C_{low}}{C_{high}} - 1\right)dV_{gate}.$$

For infinite  $g$ ,  $C_{high}$  becomes the series combination of  $C_{low}$  and  $C_{geom}$ , and this equation reduces to

$$d\sigma_w = \frac{C_{low}}{Ae}dV_{gate},$$

with  $C_{low}$  given in this case by  $A\epsilon/(x_g - x_w)$ . This is exactly what would be expected for an infinite DOS capacitor.

If confident of a model for  $\eta$ , and knowing the geometry of the sample to obtain  $C_{geom}$ , Eqs. 3.15 & 3.16 give the desired quantities; but modeling of the sample typically will *not* give sufficient accuracy in determination of unmeasured parameters to allow for confidence in the DOS results.

Our method requires no such sample modeling. Two normalization conditions are available to determine  $C_{geom}$  and  $\eta$  through knowledge of the experimentally measured quantities,  $C_{low}$  and  $C_{high}$ . For the time being, we treat the parameters  $C_{geom}$  and  $\eta$  as constants over the range of gate bias applied to the sample; their values are expected to change by less than a few percent over the range of our measurements.

The degeneracy of a Landau level, when the sample is placed in magnetic field perpendicular to the electron gas in the quantum well is the number of flux quanta threading the sample per unit area times the spin degeneracy of two, or  $2Be/h$ . Assuming a fixed value of  $C_{geom}$  (for nonconstant  $C_{geom}$  this procedure yields an averaged value of  $C_{geom}$  over the range of gate biases that comprises one Landau level) as the density in the quantum well changes, we obtain

$$\frac{2Be}{h} = \frac{C_{geom}}{Ae} \int_{L.level} \left( \frac{C_{low}}{C_{high}} - 1 \right) dV_{gate}. \quad (3.17)$$

This equation determines  $C_{geom}$ . The minima in the DOS between Landau levels are easily identified; they correspond to minima in the measured quantity,  $C_{low}/C_{high}$ .

It is also known that the lever-arm, when integrated in  $V_{gate}$  over a Landau level, must give  $\hbar\omega_c/e$ , where  $\omega_c$  is the cyclotron frequency.  $\eta$ , is determined through satisfying the equation

$$\hbar\omega_c/e = \int_{L.level} \frac{C_{low}}{C_{geom}} - \left( \frac{C_{low}}{C_{high}} - 1 \right) \left( 1 - \frac{\eta C_{geom}}{Ae^2} \right) dV_{gate}. \quad (3.18)$$

With  $C_{geom}$  and  $\eta$  determined by these conditions, Eq. 3.16 gives the DOS directly from the data and knowledge of the sample area. Further, through Eq. 3.15 this technique yields the DOS as a function of Fermi energy in the well, in contrast with existing work.

### 3.4.2 Further Contributions to the Analysis Procedure

There are several other additions to the analysis procedure used in this chapter that are not explicitly included in the equations derived above. One of these is the motion of the mean positions of the charge densities in the gate, well, and substrate as the gate bias is varied. Of chief concern is the variation in the spacing between the mean positions of the charge densities in the well and in the substrate. Variation of this spacing as the well is filled will cause  $C_{geom}$  to vary also. Lebens<sup>18</sup> estimates a shift of the mean position of the substrate charge of 10 Å over the range of gate biases used in sample **A** using the Thomas-Fermi approach of Baraff and Appelbaum.<sup>23</sup> The same calculations carried out on samples **B** and **C** give similar results. A perturbation theory calculation on the electronic wavefunction in the well and self consistent computer calculations<sup>24</sup> indicate that the mean position of electrons in the quantum well also changes by only about 10 Å as the well density is varied through its range in each of our samples. Moreover, these two charge densities move somewhat in tandem, both the charge in the substrate and the well move closer to the top gate as the gate bias is made more positive. A 10 Å change in the well charge to substrate charge separation over the range of gate biases used would indicate a 3% change in  $C_{geom}$  over the same range. The parameter  $\eta$  is also subject to small variations as the gate bias is varied. The assumption that  $\eta$  is a constant is equivalent to the statement that there is little change in the shape of the ground

state wave function of the well as the well is filled with different densities of electrons. Perturbation theory arguments, calculating the change in the shape of the charge density as the gate bias induces a change in the shape of the bottom of the well, give an expected variation in  $\eta$  of about 3%.

Simulations of our data have shown that the addition of a small term, linear in gate bias, to  $C_{geom}$  can successfully take these small variations into account in calculating the DOS. This linear addition to  $C_{geom}$  is adjusted so that the analysis procedure results in a DOS which is constant in the absence of magnetic field. This technique is described in detail in appendix B.

There is also the question of the effects of the shift with gate voltage of the mean positions of charges in the substrate, well, and gate contact regions, and the contribution of these shifts to the device capacitance. Motion of these charges makes a contribution to the measured device capacitance. Consider a parallel plate capacitor with plate separation  $x$ . If the plate separation changes with a rate  $dx/dV$  then added to the simple geometric device capacitance is

$$C_{motion} = \frac{dQ}{dx} \frac{dx}{dV} = CV \left( \frac{-1}{x} \right) \frac{dx}{dV}. \quad (3.19)$$

It is immediately clear that this capacitance due to the motion of the charge plates grows linearly with the charge on the capacitor plates. Using the numbers given above for the distances between charged regions in our samples and for the motion of the well charge as the gate bias is varied, we arrive at a rough estimate for this effect in our samples.  $C_{motion}$ , due to the motion of charges in the well, increases from zero to at most 1% of the device capacitance when the well density is  $6 \times 10^{11} \text{ cm}^{-2}$ . This adds to both the low and the high frequency capacitances measured. The high frequency capacitance is also effected by motion of the charge in the substrate. These are small effects whose changes to the DOS

determination can be nulled by appropriate choice of  $C_{geom}$  using the technique described above.

### 3.4.3 Application of Analysis to Capacitance Data

Before describing our DOS results in detail, we give another brief description, this time considering the data of Fig. 3.5, of the procedure which gives the DOS results from the capacitance data. Referring to Fig. 3.5, it is clear from Eq. 3.12 for the low frequency capacitance that minima in  $C_{low}$  correspond to minima in  $\partial n/\partial\mu$  in the well. We integrate the ratio  $C_{low}/C_{high}$  over gate bias between these minima, as indicated by Eq. 3.17, in order to determine  $C_{geom}$ . The two vertical lines shown in Fig. 3.5 demarcate the limits of integration. Integration is carried out here over two Landau levels in order to minimize error due to uncertainty in the position of the minima. We estimate errors in determining the exact positions of these minima, which limit the accuracy of our measurement of  $C_{geom}$ , to be about 3%. Errors in  $\partial n/\partial\mu$  due to error in the value  $C_{geom}$  used in the DOS calculation are of nearly the same value. The value  $C_{geom}$  obtained this way (corresponding to a well charge to substrate charge distance of about 325 Å in sample **B**) is in good agreement with simple ideas about where charge is positioned in the quantum well and substrate. In appendix B, we present a method for obtaining the value of  $C_{geom}$  to even greater accuracy.

Using this value of  $C_{geom}$  and starting with a value of  $\eta$  determined from perturbation theory,<sup>18</sup> we determine the lever-arm from Eq. 3.15 and  $\partial n/\partial\mu$  from Eq. 3.16 as functions of gate bias. Integrating the lever-arm, we plot the DOS as a function of well energy. The value of  $\eta$  is then adjusted so that the peaks lie  $\hbar\omega_c$  (using  $m^* = .067m_0$ ) apart in energy as in Fig. 3.6. We thus

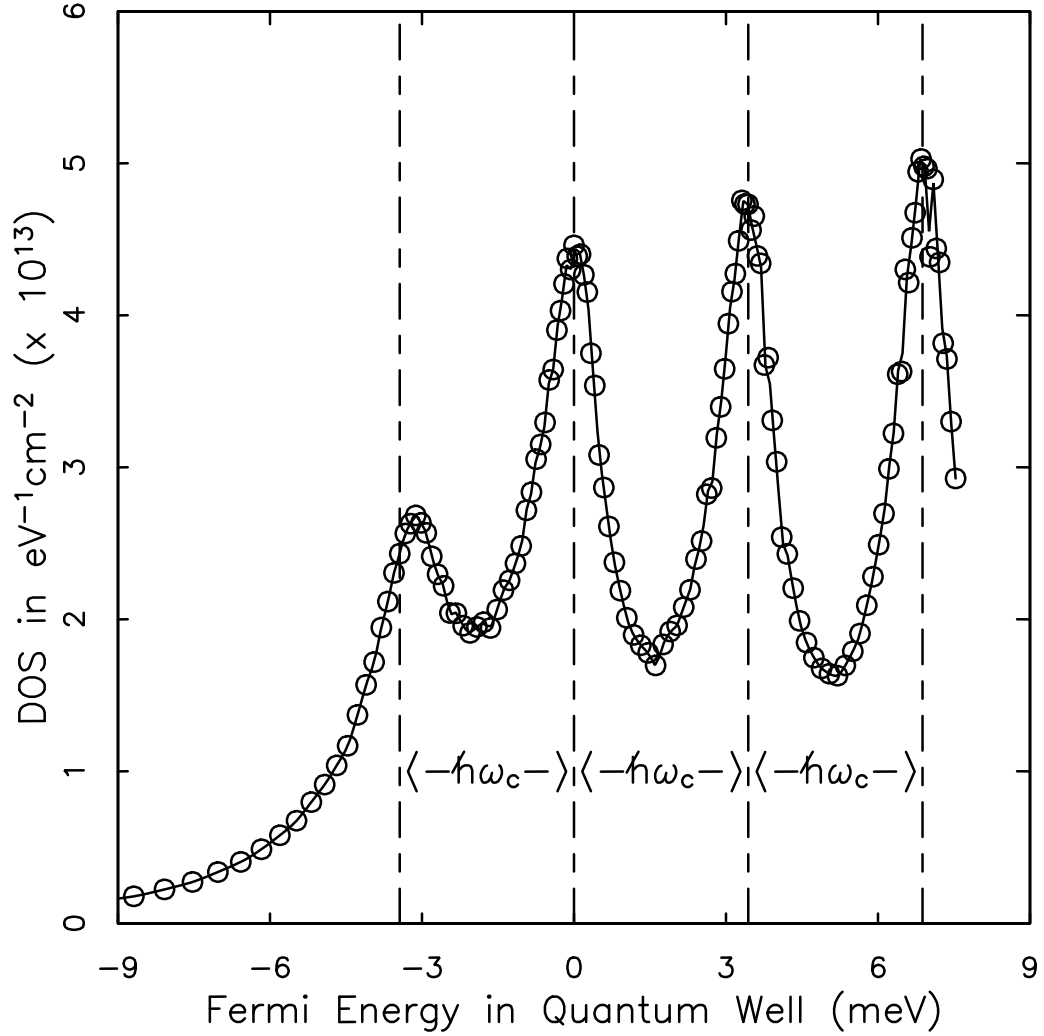


**Fig. 3.6** Density of states ( $\partial n / \partial \mu$ ) vs. Fermi energy in sample **B** at 2.0 T and 2.1 K, extracted using the analysis procedure described in the paper, from the data presented the data of Fig. 3.5. The vertical lines drawn are  $\hbar\omega_c$  apart in energy. The deviation of the spacing between the first and second peaks arises from inhomogeneous “puddling” of electrons in the well as the well is emptied. The first peak is thus outside of the region of validity of our model.

determine the only two unknowns in the DOS determination. The only sample parameter relied upon for this calculation is the area of the mesa on which the measurements were taken. This is known to better than 1%. Using two different values of the area in the analysis procedure, differing from one another by 1%, yields indistinguishable results on the scale of the graphs presented in this chapter.

The analysis procedure discussed above assumes  $C_{geom}$  and  $\eta$  to be independent of gate voltage. The data of Fig. 3.4 display a slight slope to both  $C_{low}$  and  $C_{high}$  in the region of gate biases where the well contains electrons. This slope arises largely from the fact that charges in the well and in the substrate move closer to the gate as the gate bias is increased (made more positive). These smaller distances of charges to the gate at higher gate biases result in larger capacitances. Also changing may be the spacing between charges in the well and in the substrate. Empirically, we find that we need to supplement the analysis described above by including a small variation in  $C_{geom}$ , linear in gate voltage, amounting to 3% of  $C_{geom}$  over the full range of gate voltage. This term was included in the analysis leading to the results of Fig. 3.6. The magnitude of the linear correction is chosen to assure that the density of states deduced at zero magnetic field is independent of filling. This term also serves to correct the DOS results for the small variation in  $\eta$  as the well is filled; the DOS calculation is much less sensitive to this variation than the  $C_{geom}$  variation. It also corrects for the very slight effects of the contribution of the motion of charge planes to the capacitance. This linear variation in  $C_{geom}$  is the *only* variation in a parameter with gate bias in our analysis. Data simulated by computer and analyzed using our procedure demonstrates the validity of correcting for these other variations by adjusting the linear term in  $C_{geom}$ . In essence, there

are three first order variations which are corrected by the linear term in  $C_{geom}$ , chosen empirically to give a constant DOS in zero magnetic field.

Note that the zero on the abscissa in Fig. 3.6 is chosen arbitrarily. The first oscillation in the graph is the lowest Landau level in the well, at an energy of  $0.5\hbar\omega_c$  above the energy of the ground state of the well. We set the second and third peaks seen in the figure  $\hbar\omega_c$  apart by adjusting the parameter  $\eta$ . As is clear in the figure, the third and fourth peaks also fall  $\hbar\omega_c$  apart. This serves as one of several checks of the validity of our method. Notice also that the spacing between the first and second peaks is not  $\hbar\omega_c$  as it should be. We believe that this incorrect spacing occurs because of the breakdown of the assumption, implicit in our model, of uniform filling in the well in this region of well energy. As the gate bias is lowered into this region, the well becomes depleted of electrons in a nonuniform fashion,<sup>25</sup> and this “puddling” makes interpretation of the data more difficult in this region of energy. One can no longer think of electric field lines between the well and the substrate all pointing perpendicular to the plane of the 2d electron gas. Further, portions of the 2d electron gas are depleted of electrons; it is difficult to determine whether a decrease in the low frequency capacitance may be due to an increase in depleted area or a decrease in the 2d DOS.

The integrated lever-arm used to convert the DOS results from data of Fig. 3.5 from gate bias to well energy is shown in Fig. 3.7. Most interesting here are the oscillations superimposed on a linearly increasing background. These can be thought of qualitatively in a very simple way. When the DOS is large, electrons can be added to the well with little change in Fermi energy. This explains the regions of the figure that are more “flat” in gate bias. The steeper



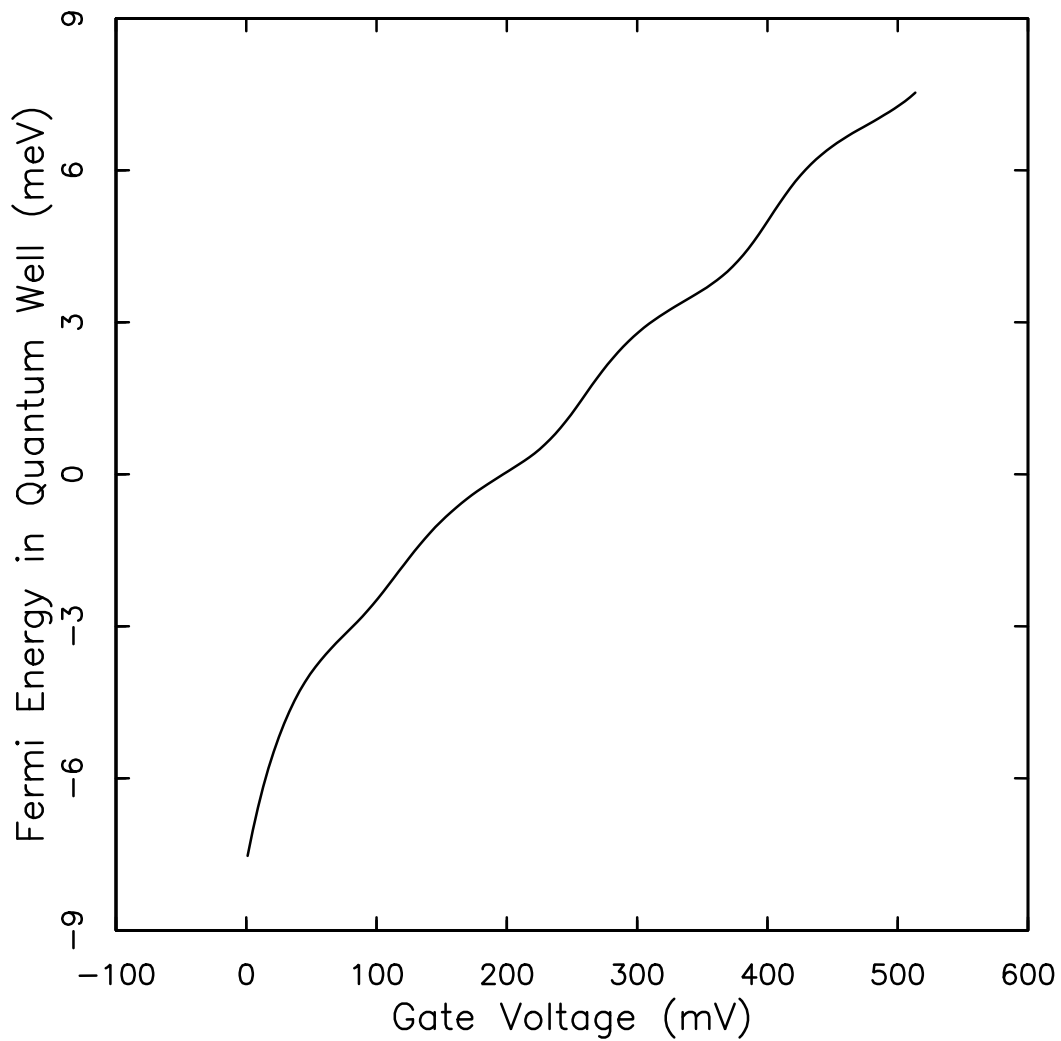


**Fig. 3.7** The integrated “lever-arm” used to convert DOS results from gate bias to Fermi energy in the well. The lever-arm along with the DOS is determined directly from the data. The flatter regions of the curve occur where the DOS in the well is high, and addition of electrons to the well changes the Fermi energy little. The steeper regions occur where the DOS is low.

regions occur where the DOS is low, and there is a larger change in the Fermi energy in the well for each electron added to the well.

Figure 3.8 displays  $\partial n/\partial\mu$  in zero field determined using the same values for the parameters  $C_{geom}$  and  $\eta$  used in the determination of the 2 Tesla DOS above. The horizontal line drawn in the figure is the expected value of the 2d DOS,  $2.8 \times 10^{13} eV^{-1} cm^{-2}$ . As stated earlier a term linear in gate bias is added to  $C_{geom}$  to make the DOS constant over a wide range of well energy. Without this linear term, the curve obtained for  $\partial n/\partial\mu$  appears to have a slight slope. Our model for this system works well in the range of energy where  $\partial n/\partial\mu$  shown here is flat.

The zero on the horizontal scales in Figs. 3.6 & 3.8 have been adjusted to correspond to the same Fermi energy with respect to the bound state in the well. Our method for determining that they are the same is explained in appendix C. Our analysis procedure should be valid over the region where the curve in Fig. 3.8 is flat (at energies above  $-2$  meV). Hence, it is believed that the DOS presented in Fig. 3.6 is also valid at energies above  $-2$  meV in that figure.

#### 3.4.4 Effects of Thermal Broadening

Recall again that our method results in determination of  $\partial n/\partial\mu$ , the thermally broadened DOS. Before attempting to describe systematically the lineshapes we observe experimentally, it is important to understand the effects of temperature on the lineshapes. This section describes the observed effects of nonzero temperature on the DOS results in magnetic fields weak enough so that effects of the exchange enhanced spin splitting are not observed.

The bulk of the  $\partial n/\partial\mu$  results to be shown in this chapter are for temperatures around 2.0 K or  $k_B T$  of approximately 0.2 meV. This is much

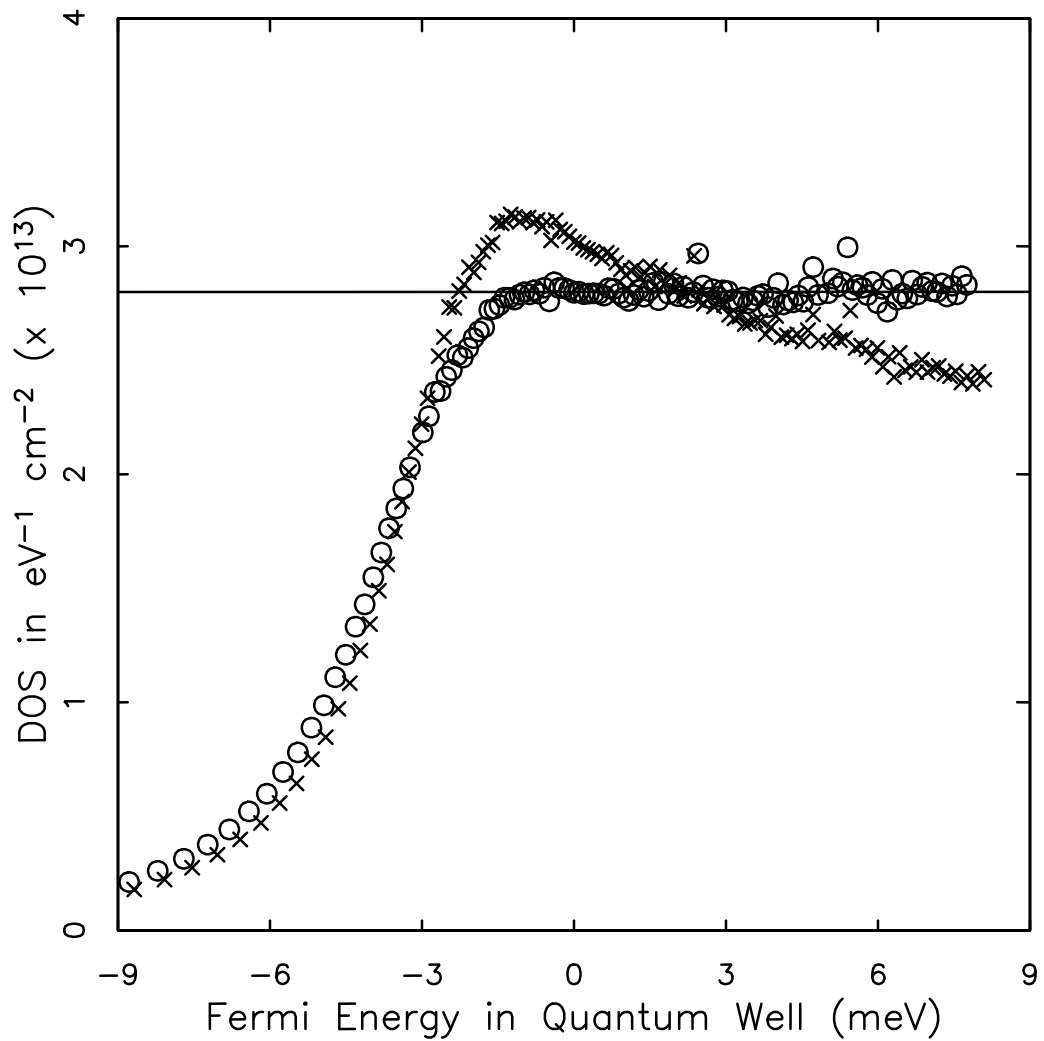


**Fig. 3.8** Zero field DOS results from sample **B** with and without correction to  $C_{geom}$  described in the text. Note the long flat region of the corrected curve (circles) at which the DOS is set equal to the expected  $2.8 \times 10^{13} \text{eV}^{-1} \text{cm}^{-2}$  by the appropriate choice of  $C_{geom}$  and  $\eta$  (see Appendix B).

smaller than the linewidths (full width half maximum) of about 2 meV of the Landau levels shown so far. The scattering effects which cause the broadening of the DOS from ideal delta functions are not expected to be temperature dependent in this temperature range; any broadening due to increased temperature here is likely to be simple thermal broadening. In order to see just how much change should be expected in the lineshapes, we have experimented, on the computer, with adding thermal broadening to various presumed underlying shapes for the DOS. The thermally broadened DOS is given by:

$$\frac{\partial n}{\partial \mu} = \int_0^{\infty} g_0(E) \frac{\partial f(E - \mu)}{\partial \mu} dE. \quad (3.20)$$

Here  $g_0(E)$  is the zero temperature DOS.

We have looked at Lorentzian lineshapes of width 0.9 meV. These, when convolved with the derivative of the Fermi function as in Eq. 3.20, show a 5% reduction in peak height with very little change in the rest of the curve. Moreover, the qualitative shape of the curve does not change with this small amount of thermal broadening. Thermally broadened Gaussian lineshapes show even less change owing to their more rounded maxima. We conclude that for the widths of our lineshapes observed at 2 K, the lineshapes are a reasonable approximation to the zero temperature DOS and can be used for the purpose of determining lineshapes. A deconvolution of the exact zero temperature DOS from our data has so far proved to be too sensitive to error to be useful. We have taken data at much lower temperatures (down to 90 mK) on sample **A**<sup>21</sup>; though these data are significantly noisier than those presented here, the peaks sharpen only slightly at lower temperatures.

We now present a method for checking the applicability of the DOS determination techniques described so far. The systematic effects of inhomogeneity

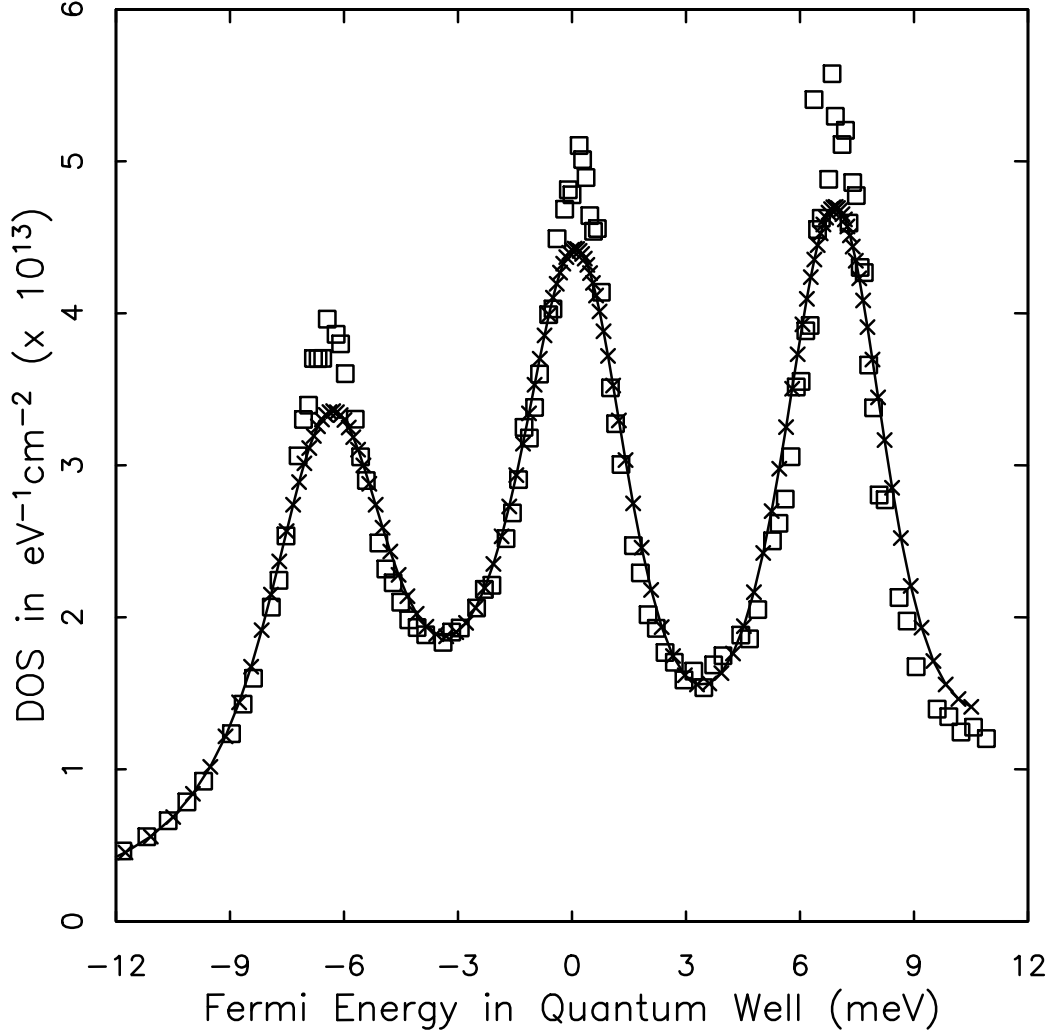


**Fig. 3.9**  $\partial n/\partial\mu$  from the data of Fig. 3.10 (for our purposes here, assumed to be the same as the zero temperature DOS) convolved with the derivative of the Fermi Distribution function at 7.0 K (crosses), compared to  $\partial n/\partial\mu$  determined from the data at 7.0 K (squares). The excellent agreement between the 7.0 K and the results of the convolution serves as another consistency check of the model. The slight deviation of the peaks is believed to arise largely from the fact that the data used in the convolution is not the zero temperature DOS but instead at 1.9 K. Note that the horizontal (energy) scale is different from that plotted in Fig. 3.6 to allow the full density range of sample **A** to be plotted.

in the well which could cause error in the DOS obtained using our technique can be ruled out, and the general validity of our analysis procedure confirmed, if the temperature dependence of  $\partial n/\partial\mu$  is in accord with the thermal broadening given in Eq. 3.20. Fig. 3.9 shows the results of treating the 4 T data of sample **A** at 1.9 K as though it is the zero temperature DOS, and using Eq. 3.20 to simulate a thermally broadened DOS at 7.0 K. The simulation is compared with data actually taken at 7.0 K. The two curves are in generally very good agreement. At half maximum, the 7.0 K data is slightly narrower than the convolved 1.9 K data. This is, at least in part, due to the convolution having been done on 1.9 K and not zero temperature results. Simulations of 0.9 meV wide Lorentzian levels broadened first to 1.9 K and then convolved again to 7.0 K show similar results when compared with 0.9 meV wide Lorentzians broadened directly to 7.0 K. This effect is also partially responsible for some of the difference in peak heights seen in Fig. 3.9. Also, the 7.0 K data is much noisier than the 1.9 K data, and the DOS results at the peaks tend to be biased towards larger DOS by noise. In all, the deviations between the two results are slight, and serves as a confirmation of the sample model. Both the quantitative values of the DOS measured and the qualitative “shape” of the Landau peaks observed are meaningful for comparison to models.

### 3.5 Low Field Landau Level Fitting

The “shape” of Landau level peaks in the 2D electron gas as a function of Fermi energy has been of great interest in the last several years. Several experiments done with a fixed 2d electron gas density<sup>3–5</sup> or Fermi energy,<sup>8</sup> often cited as giving weight to a particular shape of the DOS, determine the DOS at fixed density or fixed Fermi energy as a function of magnetic field,  $\text{DOS}(B)$ .

These groups have assumed a form for the DOS as a function of energy,  $\text{DOS}(E)$ , and determined what the  $\text{DOS}(B)$  at constant density *would* look like given the assumed form. This deduced  $\text{DOS}(B)$  is then compared to the data. The novelty of the experiment presented here lies in the direct observation of the DOS as a function of Fermi energy. We can now test ideas for the DOS directly on our results.

In this section, we examine several key issues involving the Landau level DOS. In particular, we test to see if the DOS peaks are fit better by Lorentzian or Gaussian lineshapes. Also investigated are the widths of the Landau level DOS peaks and the dependence of this width on both the electronic density of the 2d electron gas and the strength of the magnetic field. Finally, we carry out this survey on samples **A**, **B**, and **C** to gain information on the sample dependence of our results.

Many different ideas exist for what the shapes of the levels should be. We concentrate here on the DOS in magnetic fields low enough that the exchange enhanced spin splitting does not make an important contribution to the width of the observed Landau level, saving the high field results for a later section. The short range scattering model of Ando and Uemura<sup>1,26</sup> predicts elliptical lineshapes for the Landau level peaks. In this model, the width of density of states peaks can be determined directly from scattering times obtained from the zero field sample mobility. Others<sup>3</sup> have shown that these fit density of states data rather poorly. A more complete theory including self consistently screened long range Coulomb scattering and inter-Landau level coupling effects has been developed by Das Sarma and Xie<sup>27</sup>. For heterostructure samples with doping in AlGaAs farther than a few 10's of angstroms from the 2D electron gas the Das Sarma and Xie theory predicts significantly broader Landau level

peaks than indicated by scattering times obtained from the sample mobility. The qualitative shape of the Landau level peaks is predicted to depend greatly on sample parameters other than the zero field mobility. This more complete theory requires substantial computer calculation and will not be a source of comparison here.

Several authors<sup>3,5,7,12</sup> have used a Gaussian broadened density of states as a function of energy to fit data of density of states as a function of field. Gornik et. al.<sup>3</sup> find for their specific heat results from their semiconductor superlattices at magnetic fields up to 8 T that a Gaussian density of states with an added field independent background gives a superior fit to a Lorentzian density of states. Recent theoretical work<sup>10</sup> has attempted to explain the necessity for this background which was initially used for fitting data in an ad hoc fashion.<sup>3</sup> We fit the DOS results to the following Gaussian function including a background,

$$D(E) = \beta + \left(\frac{2Be}{h} - \beta\hbar\omega_c\right) \sum_{i=1}^6 \frac{1}{\sqrt{2\pi}\Gamma_i} \exp\left[-\frac{1}{2} \frac{(E - (i + 1/2)\hbar\omega_c)^2}{\Gamma_i^2}\right]. \quad (3.21)$$

Where  $\beta$  is the background density of states, and  $1.18\Gamma_i$  is the half width at half maximum (HWHM) for a particular level. The factor  $2Be/h$  in front of the summation arises because we consider these peaks to be spin-degenerate Landau maxima.

For our fits, we first turn to the DOS results in sample **A** at 4 T and 1.9 K.  $\partial n/\partial\mu$  results are shown as the circles in Fig. 3.10. Note again that the lower half of the lowest level is believed to be out of the range of validity of our model, as discussed above. The larger field here has increased the degeneracy of the levels (the area underneath the peaks), the cyclotron energy, and the peak to valley ratio of the DOS peaks compared to the data of Fig. 3.6, making it easier to discriminate between the DOS from one peak and that from another. Note also the change of scale on the abscissa in Fig. 3.10 compared to Fig. 3.6, needed



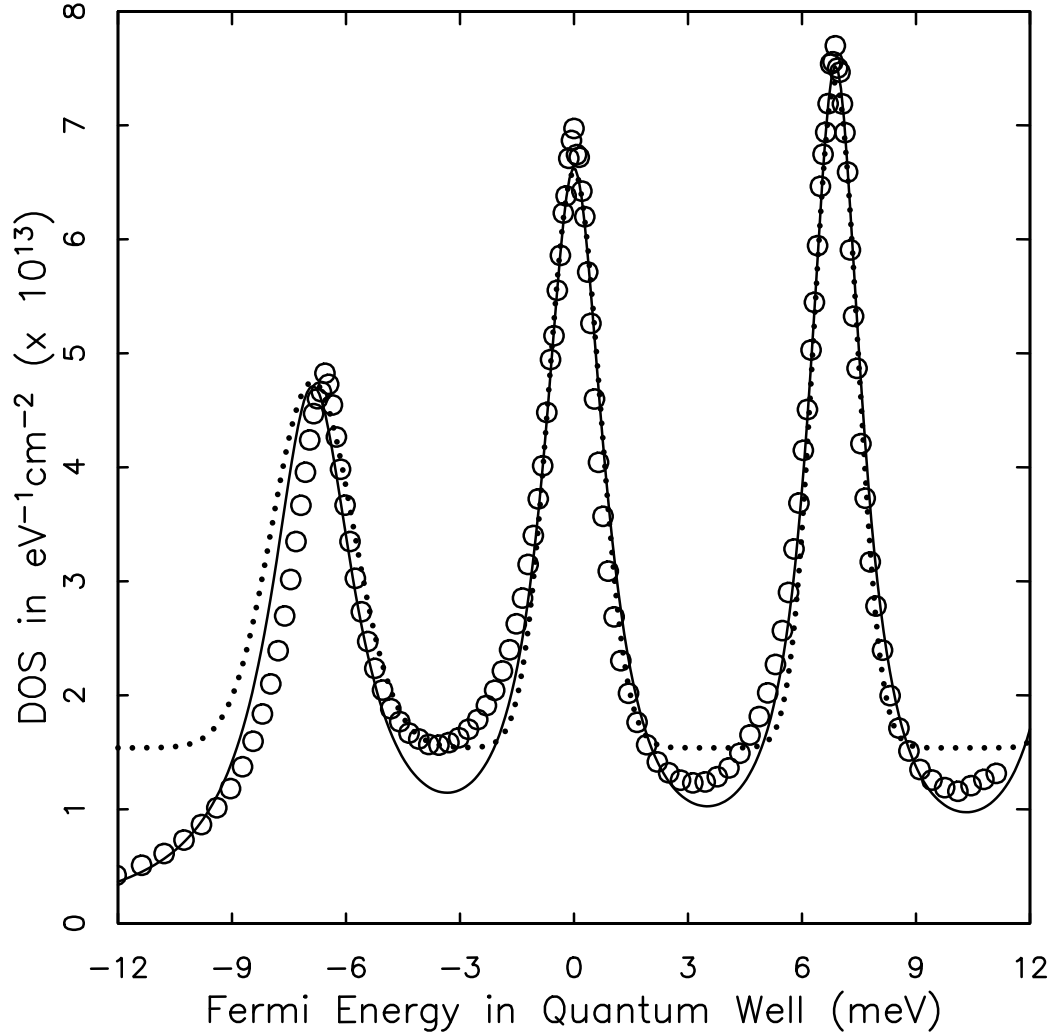


**Fig. 3.10**  $\partial n / \partial \mu$  of sample **A** at 4.0 T and 1.9 K. Circles are data. The solid curve is a fit to Lorentzian lineshapes, and the dotted curve is a fit to Gaussian shapes plus an added energy independent background of  $\beta = 1.52 \times 10^{13} \text{ eV}^{-1} \text{ cm}^{-2}$ . The other fitting parameters from Gaussian plots give:  $\Gamma_1 = 1.08 \text{ meV}$ ,  $\Gamma_2 = .689 \text{ meV}$ , and  $\Gamma_3 = .597 \text{ meV}$ . Note that the large background causes the fitted widths to be much narrower than fits that do not include a background. The fitting parameters for the Lorentzian fits are  $\Gamma_1 = 1.34 \text{ meV}$ ,  $\Gamma_2 = .969 \text{ meV}$ , and  $\Gamma_3 = .847 \text{ meV}$ .

to display the wider range of densities available to sample **A**.  $\beta, \Gamma_1, \Gamma_2, \Gamma_3$  are the four fitting parameters used in the Gaussian fit of Fig. 3.10. The widths of higher index Landau levels,  $\Gamma_4, \Gamma_5$ , and  $\Gamma_6$ , were constrained to be equal to  $\Gamma_3$ . The results of this fit give  $\beta = 1.52 \times 10^{13} \text{eV}^{-1} \text{cm}^{-2}$ ,  $\Gamma_1 = 1.08 \text{ meV}$ ,  $\Gamma_2 = .689 \text{ meV}$ , and  $\Gamma_3 = .597 \text{ meV}$ . We note that the background required for this fit is more than half of the zero field DOS.

In Fig. 3.10 we also fit the same data to a set of Lorentzians. The form for this fit is

$$D(E) = \frac{2Be}{h} \sum_{i=1}^6 \frac{1}{\pi} \frac{\Gamma_i}{(E - (i + 1/2)\hbar\omega_c)^2 + \Gamma_i^2}, \quad (3.22)$$

with *no* free background parameter. In this case, there are three free fitting parameters,  $\Gamma_1, \Gamma_2, \Gamma_3$ . Again,  $\Gamma_4, \Gamma_5$ , and  $\Gamma_6$  were set equal to  $\Gamma_3$  in the fits. In this case the  $\Gamma_i$  are the HWHM of the levels. The results of this fit give  $\Gamma_1 = 1.34 \text{ meV}$ ,  $\Gamma_2 = .969 \text{ meV}$ , and  $\Gamma_3 = .847 \text{ meV}$ .

Both the Gaussians with the large added background and the Lorentzians give reasonable characterizations of the data. The remarkable feature of the Lorentzians here is that they fit the data of Fig. 3.10 so well with only three free parameters. Also, the Gaussians tend to bow out more than the Lorentzians near the maximum of the DOS peak and broaden less than the Lorentzians at the base of the Landau levels. Both the narrowness of the DOS results near the peak and the breadth of the DOS peaks near the base of a level favor the Lorentzian shape over a Gaussian shape even after the ad hoc background is added to the Gaussians. With no background, the Gaussians do much less well at fitting (fit not shown) to the data of Fig. 3.10. The main difficulty with no background is that they cannot fit to the large interlevel DOS. This contrasts with Lorentzian shapes, which more naturally fit the interlevel DOS as a consequence of their

slower fall off compared to Gaussian shapes at energies well away from the peak DOS.

We continue fitting to results from sample **A**. Figure 3.11 shows the 3 T results from sample **A**, now displayed with both Gaussian with background and Lorentzian fits. For the Gaussians, there are now five free parameters, the widths of the first four levels (again higher index levels are constrained to have the same width as level 4) and the background. In this case, the nonlinear least squares fitting routine that we used to fit the data chooses a negligibly small background. It does this because the interlevel DOS between different levels is a strong function of filling, and a constant background does not improve the fitting in this region. The Gaussian widths from fits are made larger than necessary to fit the main part of the peaks in an attempt (by the nonlinear least squares fit) to fit the interlevel DOS. The Gaussian widths are a compromise between fitting the Landau level peaks and the between level DOS. There is no such conflict for the Lorentzian fits where no distortion of the peak width occurs. The data are fit in the range from -7 meV to 10 meV where the DOS results are believed to be valid. The four free parameters in the Lorentzians fits are the widths of the first four levels. The Lorentzian shapes in Fig. 3.11 again seem to capture the essential shape of the levels better than the Gaussians. Only in the low density regime is there significant deviation of the Lorentzian fits from the data. Aside from a very slight deviation between Landau levels, the fits are almost identical to the data at higher densities. The fitting parameters obtained are listed in the figure caption.

We now fit to the data of sample **B** which shows much higher DOS contrast at low fields than sample **A**. in Fig. 3.12 we fit the 2.0 T 2.1 K data of sample **B**. This time, only Lorentzian fits are plotted as they very obviously fit the DOS

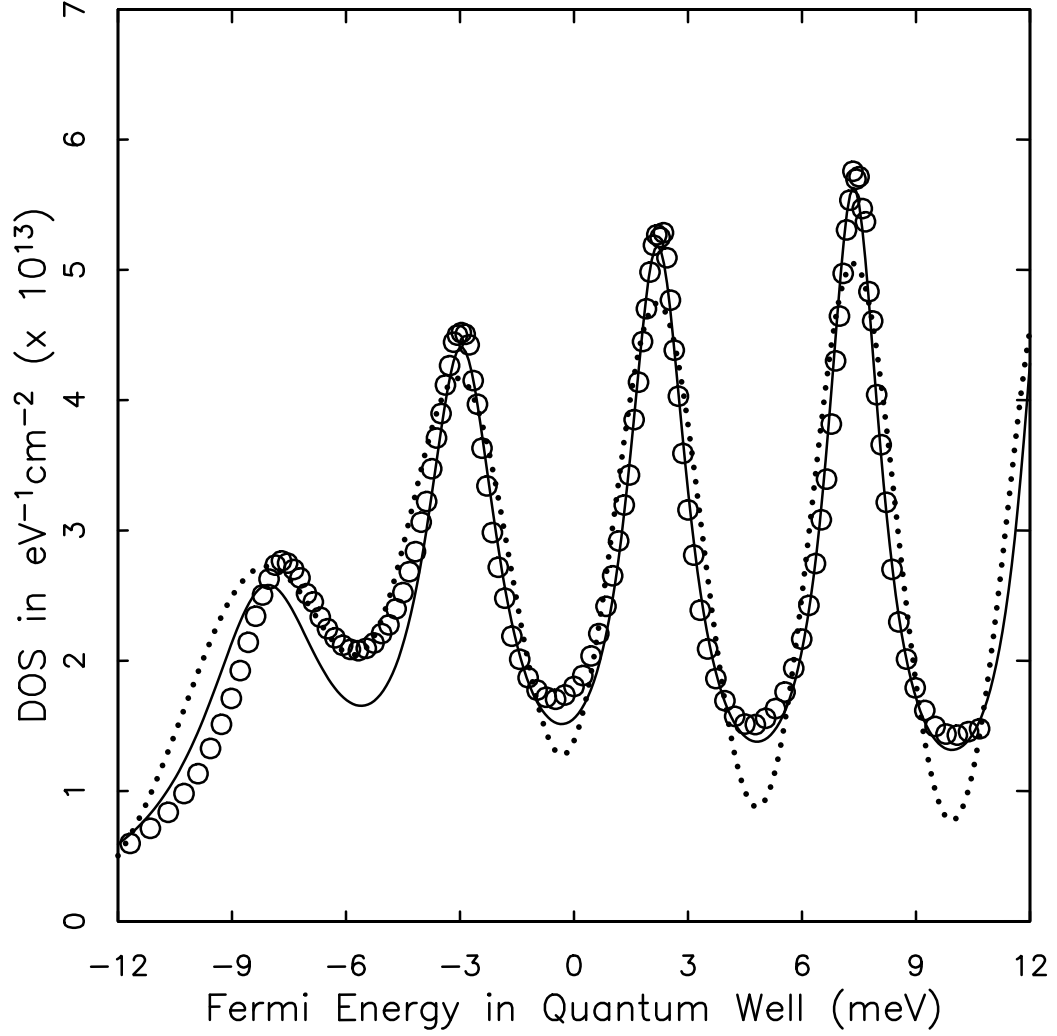


**Fig. 3.11**  $\partial n / \partial \mu$  of sample **A** at 3.0 T and 1.9 K. Circles are data. The solid curve is a fit to Lorentzian lineshapes, and the dotted curve is a fit to Gaussian shapes. The fitting parameters for the Lorentzians are:  $\Gamma_1 = 1.98$  meV,  $\Gamma_2 = 1.18$  meV,  $\Gamma_3 = .976$  meV, and  $\Gamma_4 = .885$  meV. The fitting parameters for the Gaussian fits are:  $\beta = 1.0 \times 10^9$  eV $^{-1}$ cm $^{-2}$  (negligible background),  $\Gamma_1 = 2.11$  meV,  $\Gamma_2 = 1.43$  meV,  $\Gamma_3 = 1.21$  meV, and  $\Gamma_4 = 1.14$  meV.

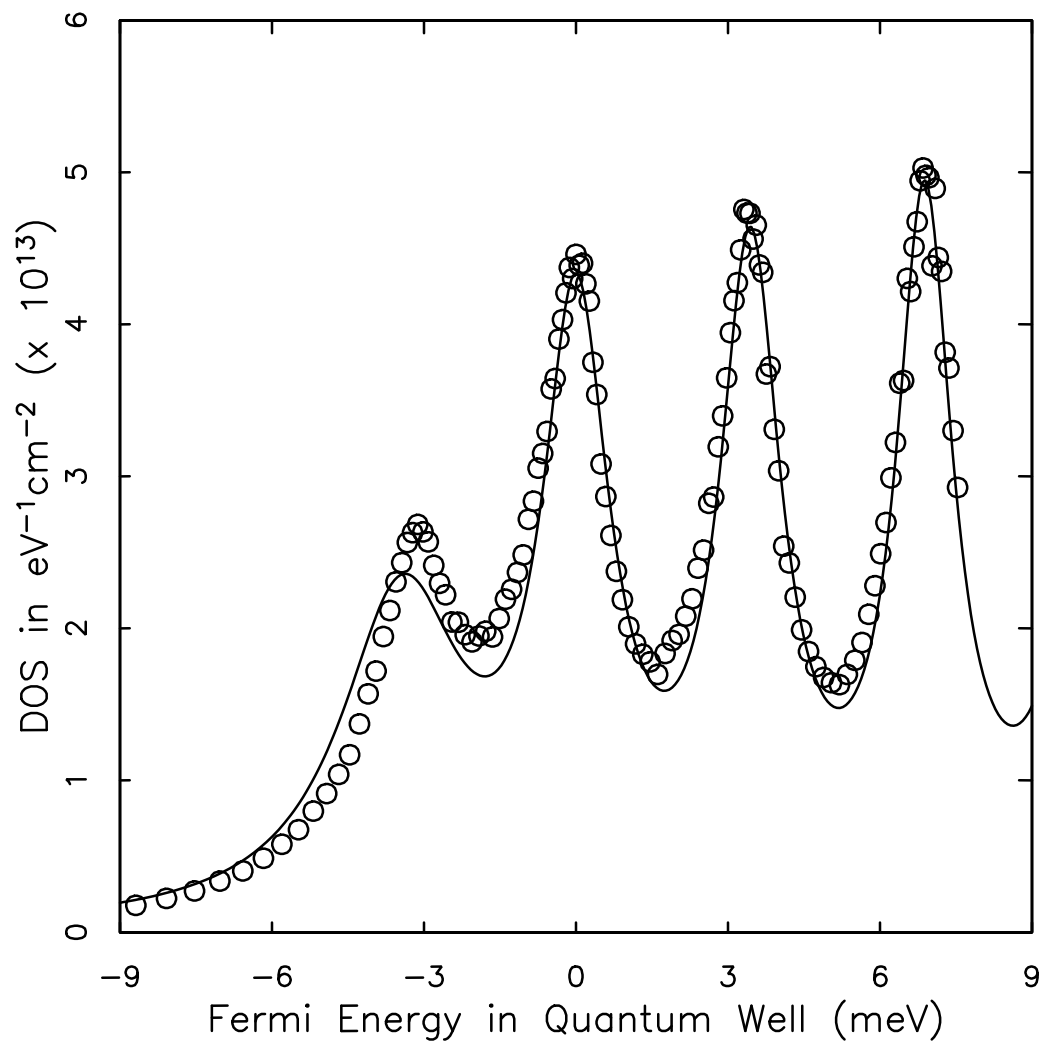


**Fig. 3.12**  $\partial n / \partial \mu$  of sample **B** at 2.0 T and 2.1 K. Circles are data. The solid curve is a fit to Lorentzian lineshapes. The fitting parameters are:  $\Gamma_1 = 1.47$  meV,  $\Gamma_2 = .810$  meV,  $\Gamma_3 = .737$  meV, and  $\Gamma_4 = .678$  meV

results better. The widths of the Lorentzians are again described in the figure caption. The quality of fit in this case is excellent. At the second level and beyond, there is almost no deviation of the fits from the data anywhere along the curves, even between Landau levels. 3 T results from the same sample give similar agreement. At 4 T, the exchange enhanced spin becomes so large in this sample as to cause great difficulty in determining the underlying lineshape.

For purposes of comparison, we move back to sample **A**. Fig. 3.13 displays  $\partial n / \partial \mu$  in this sample at 2.0 T and 1.9 K. There are actually six levels plotted here. Five are visible as large DOS oscillations, and the other is a very broad level in the low density regime. In comparison with Fig. 3.12 for sample **B**, there are several features here that are particularly noticeable. One is that the amplitude of the oscillations in sample **A** is much smaller than those of sample **B**. Depending on the Landau level index, the amplitude of the oscillation is between 30% to 50% smaller. This, we attribute to lower mobility in sample **A** probably mostly due to the presence of a doped layer in the AlGaAs blocking barrier. Note also that there is a larger dependence of the amplitude of oscillation on Landau index in sample **A** than for sample **B**. Finally, and most significantly, notice that despite these differences Lorentzians fit both data sets well.

Finally, Fig. 3.15 displays  $\partial n / \partial \mu$  in the well in sample **C** at 4.2 K and 4.0 T. Although the temperature is 4 K, the thermal contribution to the width is small compared to the observed full width of around 2.5 meV of these levels. Notice here that the amplitude of oscillation is much smaller than in either samples **A** or **B**, and the levels are about 20-30% broader than those in sample **A** at the same field. We think that this breadth arises from the very high doping density in the AlGaAs blocking barrier in sample **C**. The solid line in this figure is a fit to a Lorentzian lineshape. The fit is again quite good with only a small discrepancy

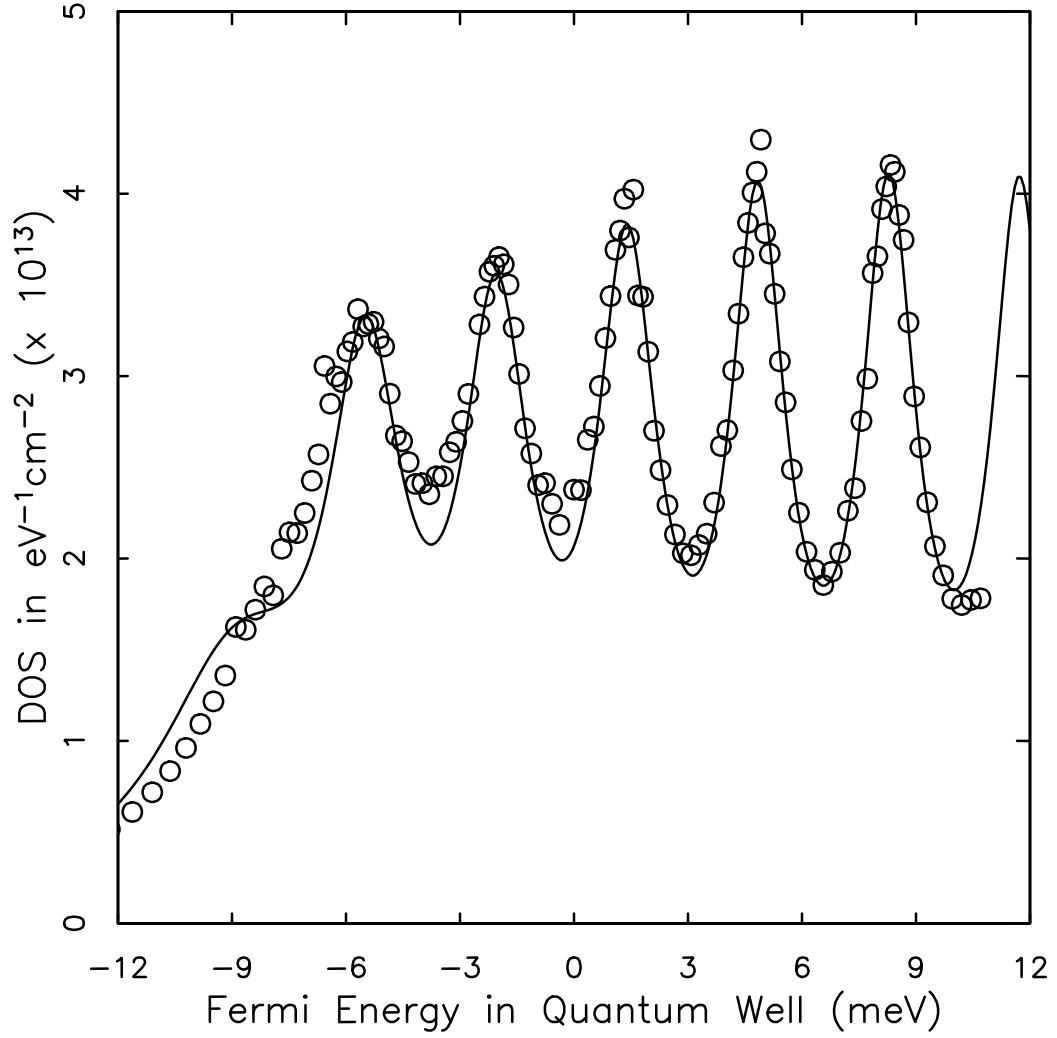


**Fig. 3.13**  $\partial n/\partial \mu$  of sample **A** at 2.0 T and 1.9 K. The solid curve is a fit to Lorentzian lineshapes with fitting parameters given by:  $\Gamma_1 = 2.52$  meV,  $\Gamma_2 = 1.21$  meV,  $\Gamma_3 = 1.10$  meV,  $\Gamma_4 = .987$  meV,  $\Gamma_5 = .909$  meV, and  $\Gamma_6 = .892$  meV

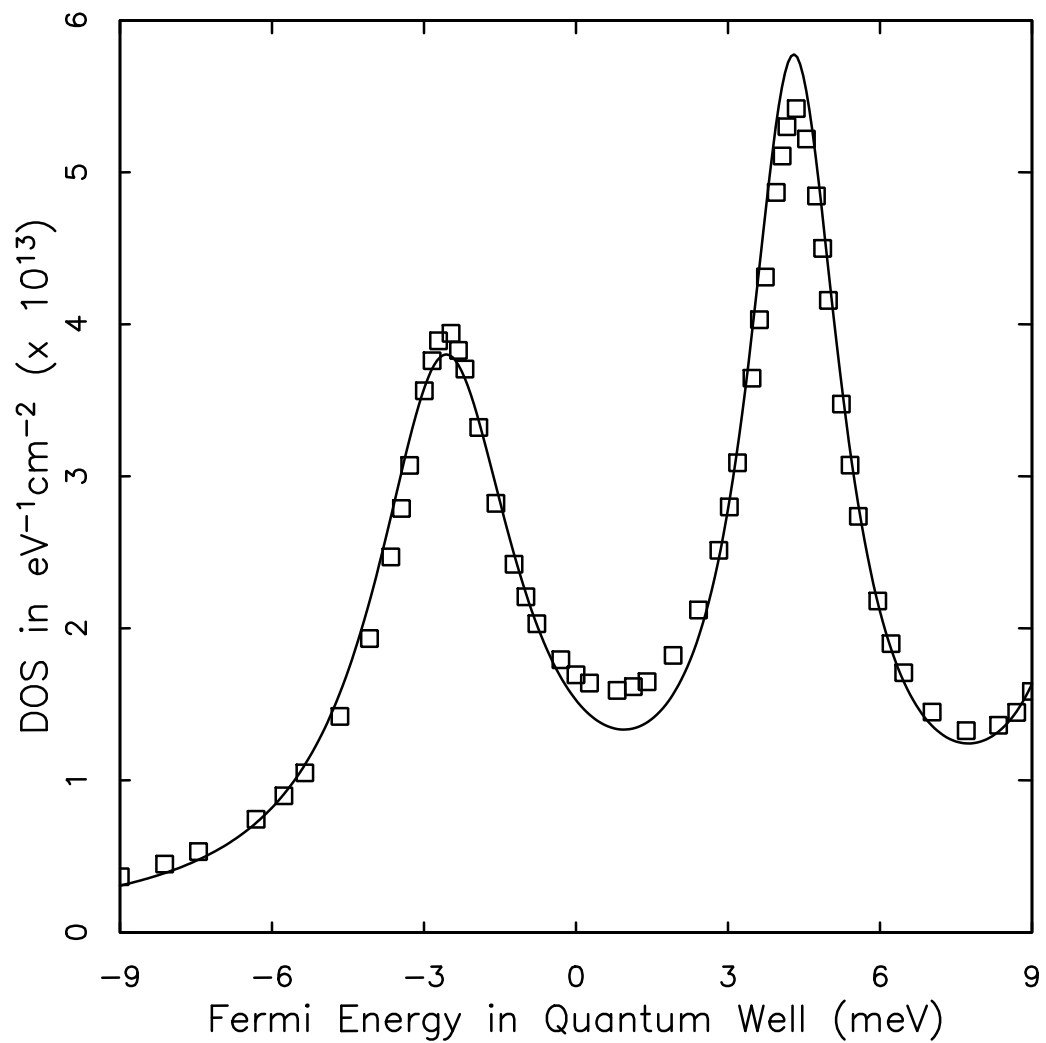


**Fig. 3.14**  $\partial n / \partial \mu$  of sample **C** at 4.0 T and 4.2 K. The solid curve is a fit to Lorentzian lineshapes with parameter values of:  $\Gamma_4 = 1.70$  meV, and  $\Gamma_2 = 1.14$  meV.



between the fit and the data between levels. The levels here are much broader, with  $\Gamma_1=1.70$  meV and  $\Gamma_2=1.14$  meV. For the purposes of fitting, higher index Landau levels were forced to have the same width as the second level.

### 3.5.1 *Picture Implied By Fits*

The DOS shape fitting implies a picture which is surprisingly different from that obtained by other experimentalists and many theorists to this date. The results indicate that for fields below 4 T, regardless of the doping configuration in the sample, Landau levels are essentially Lorentzian in lineshape. All three samples exhibit qualitatively similar lineshapes despite level widths that differ by more than 50% between sample **B** and sample **C**.

Another striking feature of the data is the magnetic field independence of widths of the Landau levels. It is clear in the DOS results given above that the width of the levels is dependent on the Landau level index. The level width always narrows monotonically as the index increases. One notion is that the level width is independent of field and depends only on the electronic density in the quantum well. In order to test this idea we plot, in Fig. 3.16, the half width  $\Gamma$  from Lorentzian fits on sample **A** vs. the 2d density at which the Landau level peaks occur. The results strongly support the idea of an underlying universal curve for widths vs. density with level width independent of magnetic field strength. Data from sample **B** from 2 and 3 Tesla support the same conclusion. We have not taken sufficient data on sample **C** to verify this result in that sample.

The solid curve in Fig. 3.16 is a power law fit using the form,

$$y = Cx^\gamma.$$

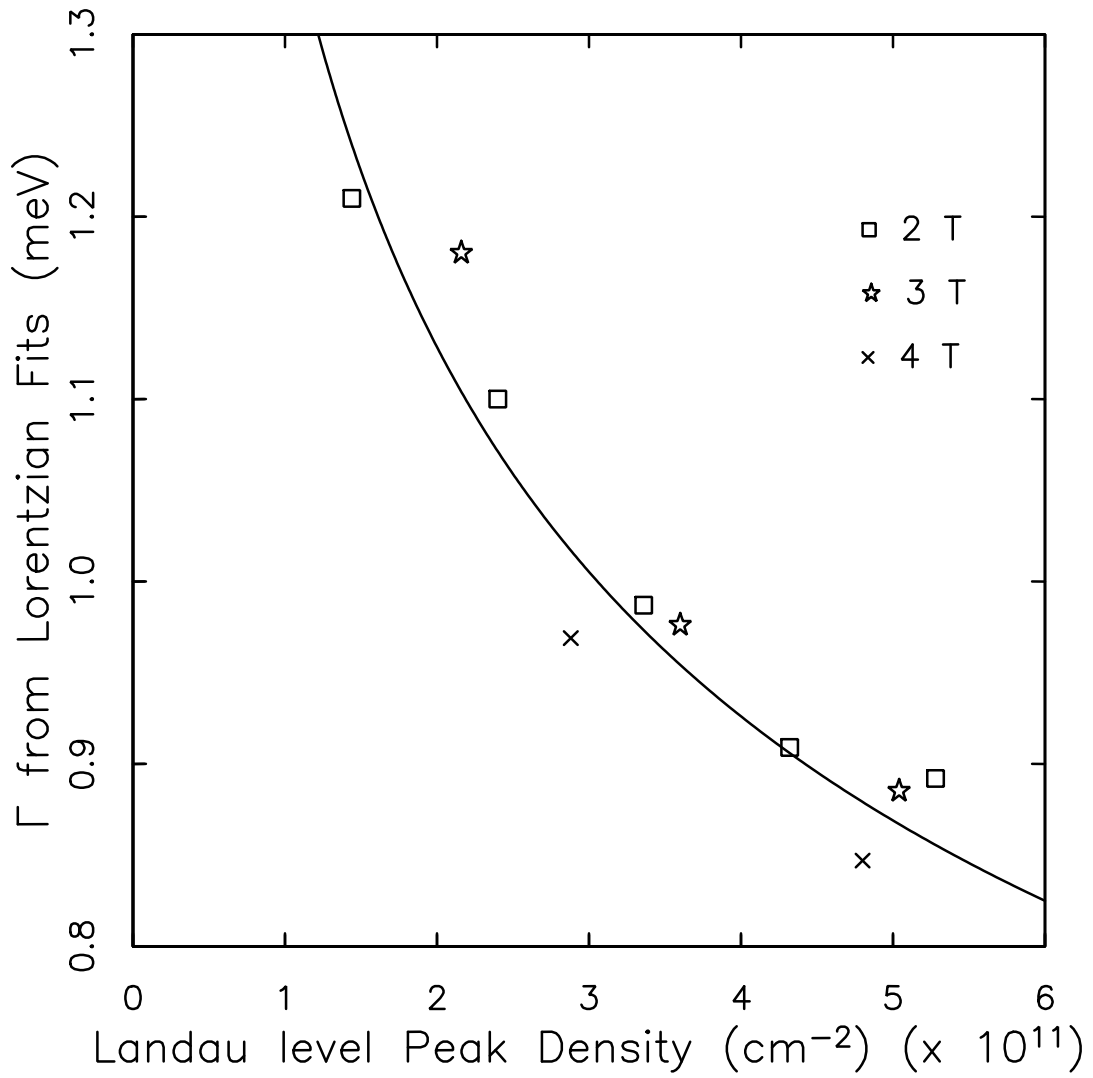


**Fig. 3.16** Widths of Landau levels plotted as a function of the density at which the Landau level peak occurs for magnetic fields of 2, 3 and 4 T. The solid curve is a power law fit described in the text. The figure suggests that the Landau level widths are independent of magnetic field strength.

Here  $C$  is a constant and  $\gamma$  is a constant exponent. The exponent used in the plot is  $\gamma = -0.28$ . The power law gives a reasonable characterization of the data with only two free parameters. Experimental work by Hirakawa and Sakaki<sup>28</sup> has demonstrated a power law dependence of the low temperature mobility of 2d electron gas systems on the density in GaAs/AlGaAs heterostructures. They obtain exponents of between 1.1 and 1.7 on plots of mobility vs. carrier concentration. The value of the exponent in their experiment depends most strongly on the distance from the 2d gas to the ionized impurities in the AlGaAs layer adjacent to the well. If we consider the elastic scattering time in our samples to be inversely proportional to the width of the DOS peaks, and considering the mobility to be proportional to this scattering time, then our results imply an exponent of 0.28 on a mobility vs. carrier concentration plot. There is an obvious discrepancy between these results and those of Hirakawa and Sakaki.

It has long been thought that the scattering times associated with the widths of Landau level DOS peaks and the scattering times derived from mobility determinations are not the same. Das Sarma and Stern<sup>29</sup> point out the differences, arising from sensitivity of the conductivity to the angle of deflection of an electrons in scattering events, between the single particle scattering time and the scattering time that appears in the Drude formula for the conductivity. These two scattering times may differ considerably. The position of ionized impurities which cause elastic scattering in the sample is thought to be important in determining the relation between these two times. Assuming that the widths of Landau levels in our samples are more closely related to the single particle scattering time may explain the difference between ours and the Hirakawa results. We cannot measure the mobility of our samples directly; however, if

we assume, as in the Hirakawa experiment, that we would obtain an exponent of between 1.1 and 1.7 from a mobility vs. carrier concentration plot, then our experiment indicates that the ratio between these two times varies as the carrier concentration is varied.

The thrust of our results can be summarized in three simple statements. **1)** Landau levels are characterized very well by Lorentzian lineshapes for field 4 T and below. **2)** The shape of the DOS peaks is *not* influenced by the details of the doping configuration in our samples. Only the width varies. **3)** The width of Landau levels is independent of magnetic field and varies only weakly with electron concentration.

### 3.5.2 Comparison Between These and Previous Results

We first review published widths of Landau level peaks. Gornik et. al.<sup>3</sup> determine widths (HWHM= $1.18\Gamma_{Gaussian}$ ) of around 0.9 and 1.5 meV, independent of  $B$ , for two samples with mobilities of 80,000 cm<sup>2</sup>/V·s and 40,000 cm<sup>2</sup>/V·s respectively. Fits in that paper considered the width to be independent of field. Eisenstein et. al.<sup>5</sup> obtain a half width of  $1.2 \text{ meV}/T^{1/2}\sqrt{B}$ , giving 2.5 meV at 5 T. The capacitance measurements, at fields up to 2 T of Smith et. al.<sup>7</sup> give half widths of around 1.1 meV. Finally, Wang et. al.<sup>4</sup>, obtain a half width of around 3 meV at 4.8 T. The range of half widths from these groups runs from 0.9 to 3 meV. Our half widths fall toward the lower end of this range. At densities between  $3 \times 10^{11} \text{ cm}^{-2}$  and  $4 \times 10^{11} \text{ cm}^{-2}$ , we obtain widths ranging from 0.76 meV for sample **B** to around 1.3 meV for sample **C**.

A clear distinction between our results and those given previously is the shape of the DOS fits. Three of the above groups<sup>3,5,7</sup> use Gaussian fits for comparison to their results. In fact, Gornik et. al.<sup>3</sup> determine that a Gaussian

with a constant background gives a fit to their data which is superior to that given by Lorentzians. Wang et. al.<sup>4</sup>, in specific heat measurements, use a Gaussian with a level width which both is a function of magnetic field and oscillates with Landau index. This form, for constant field and varying filling fraction, produces, as a function of Fermi energy, peaks which have more the appearance of Lorentzians than Gaussians but bases which are more like Gaussians. This is in somewhat better agreement with our results. However, Wang's results indicate level widths which are more than twice those measured here. It is important to note that these DOS measurements as well as several others<sup>3,5</sup> were done on multiple layer heterostructures. This raises the possibility that layer to layer inhomogeneity in samples in these experiments could account for the discrepancy in the observed lineshapes with those in our experiment.

Our results indicating a field independence for the Landau level width are in sharp contrast with the magnetization results of Eisenstein et. al.<sup>5</sup> who suggest a  $\sqrt{B}$  dependence of the width of levels on magnetic field. The level width of Wang et. al. is also field dependent. Below 4 T though, they obtain a field dependence of the width which is much smaller than that of Eisenstein. There are also others who either do not remark on a field dependence of the level width<sup>3</sup> or suggest that it is masked by inhomogeneity in the 2d gas.<sup>7</sup>

### 3.6 High Fields

The shape of the DOS peaks in fields above around 4 T in our samples differs considerably from that in lower fields. This difference arises from the exchange enhancement of the electronic  $g$  factor in the 2d electron gas in GaAs which causes a large splitting between the spin subbands of a Landau level at high fields.

This exchange enhancement can be understood in a simple heuristic fashion. If a Landau level is half full, then the energy savings to the system in placing one electron in the lower energy spin subband instead of the higher energy subband is larger than that indicated by the Zeeman energy,  $g_L\mu_B B$ . Here  $g_L$  is the Landé  $g$  value for GaAs which has a value of around -0.44 due to spin-orbit interactions.<sup>30</sup> The increased spin splitting arises from the electron-electron repulsion. In order to reduce the electron-electron Coulomb energy, electrons should be spaced as far apart as possible. If all of the electrons are in the same spin subband, then by the Pauli principle the spatial wavefunction must be antisymmetric. The antisymmetric spatial wavefunction here automatically places electrons farther apart than does a symmetric one. Energy can be saved by the system by placing all of the electrons in the same spin subband. This increases the energy splitting of the spin subbands. The augmented splitting can be characterized by an enhanced  $g$  value,  $g^*$ .

Ando and Uemura<sup>11</sup> first determined that the enhanced  $g$  factor should be an oscillatory function of filling as the Fermi energy passes through Landau levels. Recent measurements of this exchange enhanced  $g$  value in GaAs have been made using level-coincidence (developed by Fang and Stiles<sup>31</sup>) of Shubnikov-de Haas oscillations in a tilted magnetic field and by measuring low temperature activation of  $\sigma_{xx}$  when the Fermi energy is in the middle of a spin split Landau level.<sup>13</sup> Goldberg, Heimann, and Pinczuk used a laser absorption probe to measure thermal occupation of the spin subbands of the lowest Landau level in order to determine  $g^*$ . In this section, we use capacitance measurements to obtain the DOS at large magnetic fields to which we fit the model of Ando and Uemura and determine an effective  $g$  and make comparisons to previous measurements.

### 3.6.1 DOS analysis in high fields

We have made measurements only on sample **A** at fields above 4 T. Because they show the spin splitting effects best, we concentrate here only on the results from 8.5 T, the highest magnetic field strength used. The DOS determination proceeds the same way as the low field DOS determination but with one complication. The mean position of the excess charge density in the substrate may be different at high magnetic fields than at low magnetic fields. This can arise because  $k_{Fermi}$  in the substrate, in the direction perpendicular to the plane of the 2d electron gas, decreases when the magnetic field is increased due to the large degeneracy of states in the direction perpendicular to the magnetic field. This means that  $C_{geom}$  must be determined separately for high fields. Eq. 3.17 is difficult to apply in this case because there is only one full Landau level observed, and the low density tail of this level falls into the region of the device operation where the 2d gas empties in a nonuniform fashion. This region is outside of the validity of our analysis, so we instead use the normalization condition, Eq. 3.18, to determine  $C_{geom}$ , using the same value of  $\eta$  as obtained in low fields. The difficulty is that at 8.5 T the Landau level degeneracy is so large that the second Landau level, comprised of the  $\nu = 3$  and  $\nu = 4$  spin split levels, is at the high filling edge of our device. Fig. 3.17 illustrates this situation. This figure shows the DOS at 8.5 T and 1.85 K in sample **A**. The two vertical lines drawn are  $\hbar\omega_c$  apart in energy. It is difficult to say exactly where the right hand vertical line should be placed due to incomplete observation of the second Landau level. We estimate that this situation introduces an error of about 5% in the observed spacing between the peaks of the lowest Landau level and the same error in the effective  $g$  value observed. This is still relatively high precision for a measurement of the enhanced  $g$  value.

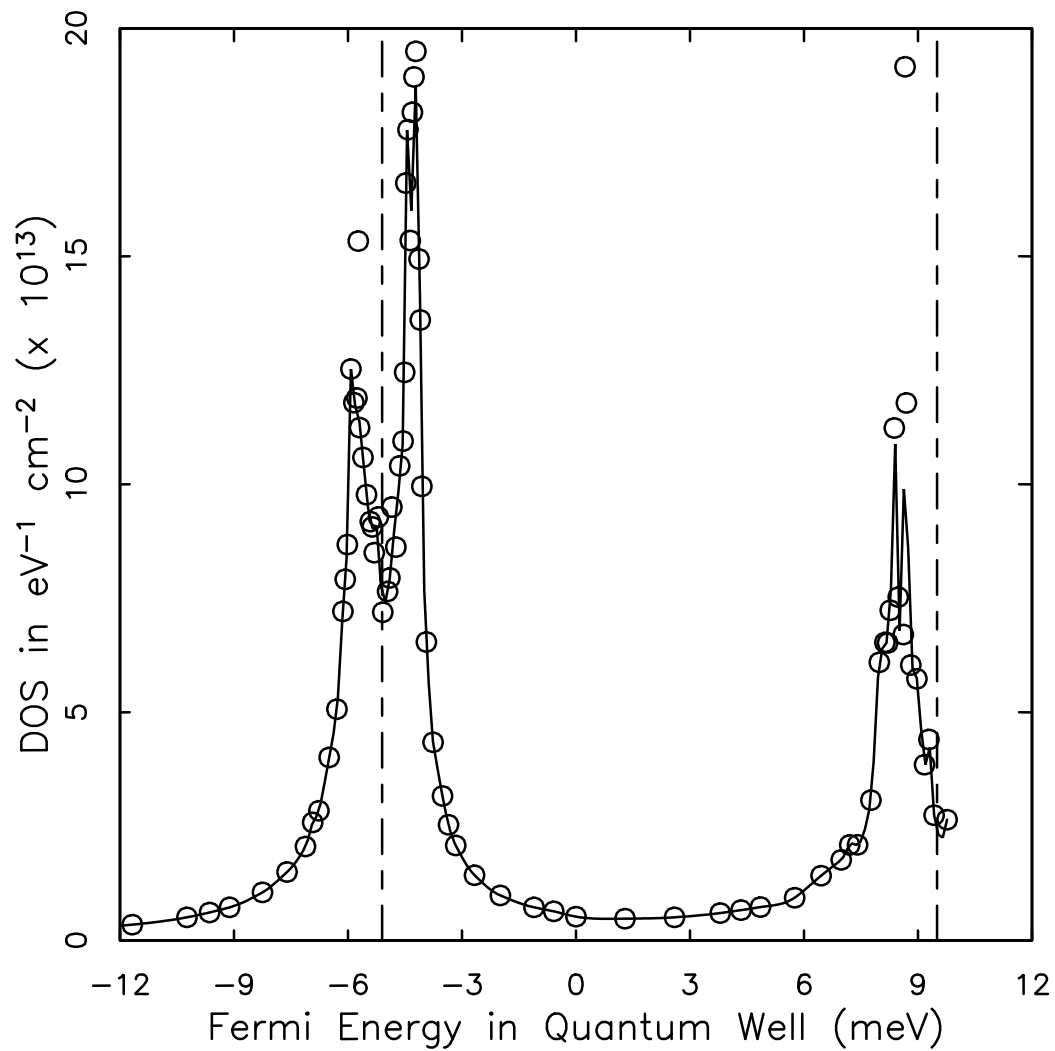


**Fig. 3.17** Plotted is  $\partial n / \partial \mu$  at 8.5 T and 1.85 K. This figure illustrates the main difficulty in the DOS determination at high fields. Because the second level is at the high density limit of operation of the device, it is difficult to do a precise adjustment of the parameters of the DOS determination ( $C_{geom}$  and  $\eta$ ).



### 3.6.2 Curve fitting to the spin split level

With this caveat, we proceed with a detailed analysis of the lowest Landau level. Figs. 3.18 & 3.19 zoom in on the lowest level from Fig. 3.17. We now attempt to fit to the detailed shape of this curve as well as the spin splitting.

The theory of Ando and Uemura<sup>11</sup> indicates that the spin splitting in a Landau level in the case of only one level occupied (or for negligible overlap of different Landau level DOS peaks with several filled levels) should be given by the following formula:

$$g^* \mu_B B = g_L \mu_B B + E_{ex}(n_+ - n_-). \quad (3.23)$$

Here,  $E_{ex}$  is known as the exchange energy and  $n_+$  and  $n_-$  are the fractional fillings of each of the spin split Landau levels. Let the energy (mean energy) of the two spin subbands of a Landau level with the Zeeman and exchange interactions turned off be called  $E_\alpha$ . Turning these interactions back on, the energies of the two subbands are given by

$$E_\pm = E_\alpha \pm \frac{1}{2}[g_L \mu_B B + E_{ex}(n_+ - n_-)]. \quad (3.24)$$

For a given Fermi energy, the fractional occupations of  $n_+$  and  $n_-$  are given by

$$n_\pm = \frac{h}{eB} \int_{-\infty}^{E_F} f(E - E_F; T) g_\pm(E + \frac{1}{2}[g_L \mu_B B + E_{ex}(n_+ - n_-)]) dE. \quad (3.25)$$

The term in front of the integral is the inverse of the Landau level degeneracy which serves to normalize the integration,  $f(E - E_F; T)$  is the Fermi distribution function, and  $g_+(E)$  and  $g_-(E)$  are the subband DOS for each spin direction. (The reader is cautioned not to confuse the DOS,  $g_\pm$ , with the Landé and enhanced  $g$  values.)

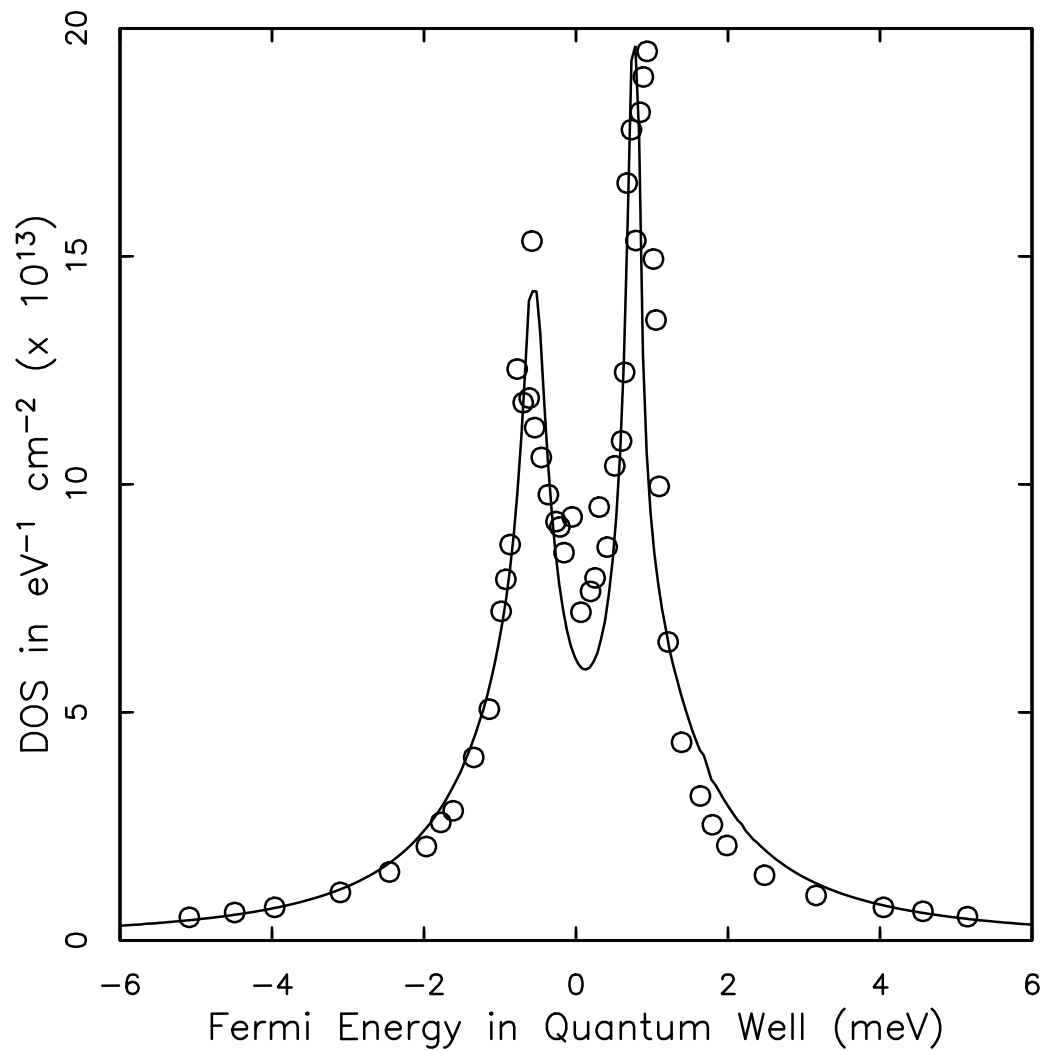


**Fig. 3.18** Plotted is  $\partial n / \partial \mu$  of the lowest Landau level at 8.5 T and 1.85 K. The solid curve is a fit using the theory of Ando and Uemura and assuming underlying Lorentzian lineshapes. The exchange energy in the fit is 3.8 meV. The initial parameters describing the Lorentzians (see Eq. 3.22) for the up and down spin bands are  $\Gamma_+ = 1.0$  meV and  $\Gamma_- = 0.9$  meV.

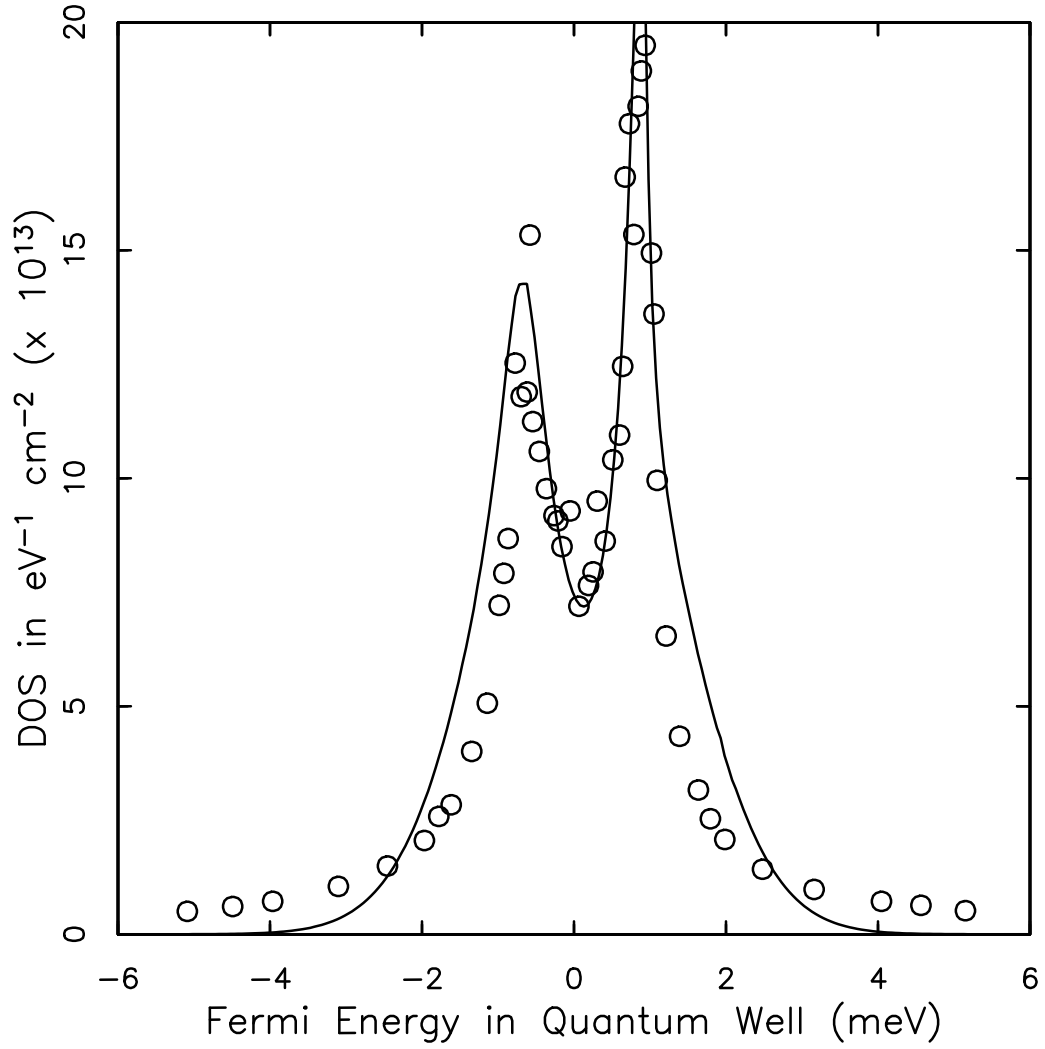


**Fig. 3.19** Plotted is  $\partial n / \partial \mu$  of the lowest Landau level at 8.5 T and 1.85 K. The solid curve is a fit using Gaussian lineshapes and the theory of Ando and Uemura. The exchange energy from the fit is 3.3 meV. The parameters describing the Gaussians are  $\Gamma_+ = 1.2$  meV and  $\Gamma_- = 1.05$  meV.

To make fits to our data, we start with two DOS peaks,  $g_+(E)$  and  $g_-(E)$  (of either Lorentzian or Gaussian shape), each initially centered at energy  $E_\alpha$ . The two peaks typically have different linewidths because of the variation in scattering times with electron concentration in our samples. Equation 3.25 suggests an iterative solution. We explain first the most obvious method to obtain a DOS fit and then describe a more computationally efficient technique that we use. For a particular value of  $E_F$ ,  $n_+$  and  $n_-$  can be calculated from Eq. 3.25 starting from the assumption that  $n_+ = n_-$ . The Zeeman term makes the values of  $n_+$  and  $n_-$  slightly different from each other. Then these values for  $n_+$  and  $n_-$  are placed on the right hand side Eq. 3.25 once more and new values for  $n_+$  and  $n_-$  are calculated. These steps can be continued until  $n_+$  and  $n_-$  cease to change between cycles. This process determines  $n_+$  and  $n_-$  for a particular value of  $E_F$ .

The actual procedure used in computation is slightly different but leads to the same results. Starting with no spin splitting, we calculate the functions  $n_+^0(E_F)$  and  $n_-^0(E_F)$  using the equation

$$n_\pm^0(E_F) = \frac{h}{eB} \int_{-\infty}^{E_F} f(E - E_F; T) g_\pm(E) dE.$$

We then iterate the following equation, starting with values  $n_\pm^0(E_F)$  on the right hand side:

$$n_\pm = n_\pm^0(E_F \pm \frac{1}{2}[g_L \mu_B B \pm E_{ex}(n_+ - n_-)]).$$

We do this as a function of  $E_F$  to obtain  $n_+(E_F)$  and  $n_-(E_F)$ . Finally, to obtain the total density of states, we use the following equation:

$$\frac{\partial n}{\partial \mu} = \frac{eB}{h} \frac{d}{dE_F} [n_+(E_F) + n_-(E_F)].$$

This result is compared to the data.

Band nonparabolicity, even though it has only a very small effect on the effective mass at these energies may influence the Landé  $g$  nonnegligibly.<sup>30</sup> We use a value of  $g_L = -0.40$  as do Nicholas et. al.<sup>13</sup> determined from photoconductivity<sup>32</sup> measurements on their sample. We recognize that  $g_L$  in our samples may actually vary somewhat as the electronic density is varied, but we do not attempt to correct for this in fitting.

In Fig. 3.18 and Fig. 3.19 we fit the 8.5 T data to Lorentzian and Gaussian spin split levels respectively. Because the process described above for generating the fits is rather complicated, we tune each of the various parameters by hand, observe the results, and retune. The fits shown in Figs. 3.18 and 3.19 are subjectively the best fits for the two different forms. For both the Lorentzians and the Gaussians, there are 3 fitting parameters. These are  $\Gamma_+$  and  $\Gamma_-$  the widths of each of the spin split levels and the exchange energy,  $E_{ex}$ . The widths used are stated in the figure caption. The exchange energy determined clearly depends on the underlying lineshape used. For Lorentzians and Gaussians, we determine exchange energies of 3.8 meV and 3.3 meV respectively.

Although the model curves in Figs. 3.18 and 3.19 can be made to fit the experimental peaks of the spin split DOS reasonably well, it is clear that neither fit matches the data with nearly the same precision as did the Lorentzian fits in low fields. With the Lorentzians one problem is that the fits require a large  $E_{ex}$ ; but when  $E_{ex}$  is increased to fit the peaks well,  $\partial n / \partial \mu$  drops too low in the density of states trough between the two levels. Both the Lorentzians and the Gaussians have difficulty fitting to the very steep sidewalls of the observed Landau level DOS. The Gaussians do less well at fitting these sidewalls, and the Gaussian fit drops to zero DOS between Landau levels where the data show substantial interlevel DOS. As with the fits made to data at lower magnetic

field values, the Gaussian gives an inadequate DOS in the tails of the peak. To compensate for this, the model calculation has a larger width than otherwise necessary to fit the central portion of the DOS peak.

The value for  $E_{ex}$  obtained here, 3.3 meV (from Gaussian fits), is the same as that determined by Nicholas et. al;<sup>13</sup> Goldberg, Heiman, and Pinczuk obtain 2.8 meV. Both of these groups use Gaussian lineshapes to fit their data. We point out that it is important to consider the effect of the assumed lineshape on the determination of  $E_{ex}$ . Our experience indicates that the value of  $E_{ex}$  can vary by 20% or more depending on the lineshape used.

One can easily determine the maximum value of  $g^*$  from our fits by equating the maximum value of  $E_+ - E_-$ , obtained with the Fermi energy at the Landau level center, to  $g^* \mu_B B$ . In doing this, we obtain a value of  $g^*$  of 4.6 for Lorentzian fits (maximum splitting of 2.3 mV) and 5.4 for Gaussian fits (maximum splitting of 2.7 mV) for 8.5 T and 1.85 K. We have taken data at temperatures down to 90 mK for our tunneling experiments<sup>21</sup> which seem to indicate an increased value of  $g^*$  at lower temperatures. This is consistent with Eq. 3.23 given that the lowering of the temperature effectively narrows the width of the spin states. However these data are not of sufficient quality for detailed fits to be meaningful.

To conclude this section, we note that the difficulty in fitting to the data in Figs. 3.18 and 3.19 calls into question either the underlying Gaussian or Lorentzian lineshapes used or the validity of Eq. 3.23. The sidewalls of the Landau level DOS observed are so steep that no Gaussian or Lorentzian lineshape, when entered into our fitting protocol, can fit them and the rest of the DOS curve at the same time. Using the better fitting Lorentzian lineshapes, we determine a value for the exchange energy of  $3.8 \pm .2$  meV.

### 3.7 Observations Regarding the Spatial Extent of States

Since just after the discovery of the quantum Hall effect, the notion has been widely discussed that two kinds of electronic states, with very different character, exist in the 2d electron gas in the presence of a magnetic field. These are localized states, thought to exist between Landau levels, and extended states found at the “core” of a Landau level. Most simply, Hall plateaus occur when the Fermi energy is in a region of localized states which do not contribute to the Hall voltage. Only when the Fermi level passes through the core of extended states in a Landau level does the Hall voltage make a transition from one plateau to the next. Very low temperature experiments<sup>33</sup> demonstrating sharp transitions between hall plateaus indicate a very narrow range of extended states. One often sees<sup>2</sup> sketches of the 2d magnetic field DOS drawn with lines separating regions of localized and extended states. In analogy to the metal-insulator transition, this line is referred to as the mobility edge. In gauge arguments for the existence of the quantum Hall effect,<sup>34,35</sup> the presence of mobility gaps and a mobility edge, separating in energy localized and extended states, is used to account for the Hall plateaus.

The transition region between localized and delocalized states has been of great interest in recent years. The localization length  $\xi$  and its dependence on the position of the Fermi level in the Landau level have been at the center of interest. Specific attention has been placed on the region in energy near the core of a Landau level. Here,  $\xi$  is thought to diverge. The self consistent theory of Ono<sup>14</sup> and scaling theory<sup>15</sup> each make different predictions on the form of the  $\xi$  in the vicinity of the divergence. The region of the divergence has been probed experimentally in transport experiments.<sup>16</sup> The transition from delocalized to localized states, the effective mobility edge, is thought to

occur where the Fermi energy traverses a position in the Landau level structure at which  $\xi$  decreases below a characteristic length, typically taken to be an inelastic scattering length. Effectively, the behavior of the localization length near the divergence can be probed in a Hall experiment through measurements of  $d\rho_{xy}/dB$  and  $d\rho_{xx}/dB$  as a function of temperature.<sup>16</sup> However, it is difficult using these means to achieve an absolute measure of the size of localized states. As we will show, our measurements are instead more sensitive to the region between Landau levels where the states are well localized, probing a different regime than previous experiments. Further the method used here, with appropriately designed samples, may offer a way of measuring the absolute extent of localized states.

### **3.7.1** *Sensitivity in our experiment to the localization length*

Our low and high frequency capacitance measurements determine the 2d DOS, an equilibrium property of the system not dependent on the localized or extended character of the electronic states. We show below that if tunneling rates vary for different regions of the 2d electron gas, then the frequency dependence of the capacitance in our experiment is sensitive to the in-plane conductivity of the 2d electron gas. Specifically, when the in-plane conductivity of the sample is very low, the 2d gas can be thought of as made of isolated domains (each with slightly different tunneling conductivities) which do not transfer appreciable charge to one another during an RC time of the tunnel barrier. The simple circuit model of Fig. 3.2b breaks down. Although we cannot make direct contact to the 2d gas to measure the transport, we exploit this sensitivity to the in-plane conductivity to explore the nature of the states in the region of the Fermi level. Further, our probe is sensitive to the bulk of the 2d



gas and not particularly to the edges of the sample. The theory of edge states in the quantum Hall effect<sup>36</sup> indicates that in transport experiments when the Fermi energy is in the region of localized states between Landau levels currents used to probe the sample pass mainly the edges of the sample and not the bulk. Our experiment, microwave experiments<sup>37</sup>, cyclotron resonance experiments<sup>38</sup>, and surface acoustic-wave attenuation experiments<sup>39</sup> are instead sensitive to the bulk regardless of the Fermi level position within the Landau level structure.

### 3.7.2 Sample Model

At low temperatures and when the Fermi energy is between Landau levels in the 2d electron gas the longitudinal conductance,  $\sigma_{xx}$ , drops to very low values. Physically, the only states in the bulk at the Fermi level are highly localized states which do not conduct. From the temperature dependence of the longitudinal resistance in Hall samples,<sup>40</sup> it is thought that variable range hopping between localized states forms the main conduction mechanism in the bulk in high magnetic field at temperatures below 4 K. At higher temperatures, thermal excitation of carriers to bands of extended states<sup>41</sup> causes increased conductance as the temperature is raised.

In cases where the in-plane conductance “freezes-out” in our samples, the circuit model of Fig. 3.2b can no longer be used, and it should be replaced with a more sophisticated model such as the one in Fig. 3.20. This model is similar to those used to describe the frequency dependence of the capacitance and loss tangent of Si MOSFETs with electronic traps in the oxide layer with different tunneling times from the different traps to the electronic inversion layer of the MOSFET.<sup>42</sup> In the model of Fig. 3.20 for our device, the 2d gas is considered to be made up of many different domains, linked by resistors

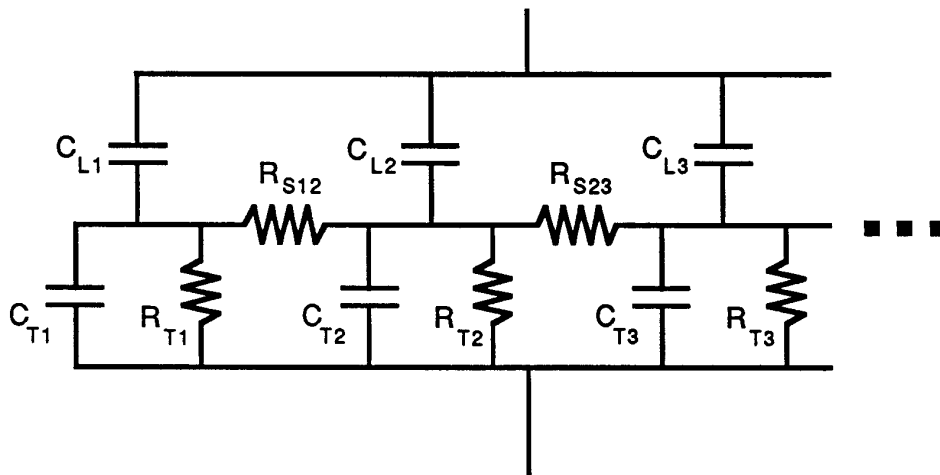


**Fig. 3.20** The figure shows a more realistic model of the sample than that of Fig. 3.2 when the in-plane conductance of the 2d gas vanishes. The sample can be thought of as broken up into separate domains connected by the resistances  $R_S$ . At zero temperature, these resistances diverge.

$R_S$ . Due to inhomogeneity (in the tunnel barrier thickness or in other factors influencing tunneling) the  $RC$  times describing charge flow between the domains and the substrate may vary among isolated domains. The capacitance from the top gate to each domain is modeled through the capacitors  $C_L$ . The capacitance and tunneling resistance from each domain to the substrate of the sample are modeled by capacitors  $C_T$  and resistors  $R_T$ . When the in-plane conductivity of the sample has frozen out the variation in  $RC$  times for the different domains (now electrically isolated from one another) produces loss tangent and capacitance vs. frequency curves for our sample which are broadened as shown in Fig. 3.21. This is in contrast with the curves of Fig. 3.3 which correspond to a single  $RC$  time for the whole system. Figure 3.21 plots the loss tangent and capacitance as a function of frequency for sample **A** with a gate bias applied so that the Fermi level is between Landau levels at a magnetic field of 8.5 T and at a temperature of 875 mK. The solid and dotted lines are fits which will be described below.

We now describe the limiting cases of the circuit model of Fig. 3.20. In the case where the resistors  $R_S$  have zero resistance (i.e. when the 2d gas is perfectly conducting), then all of the resistors  $R_T$  can be seen as being in parallel, and the sets of capacitors  $C_L$  and  $C_T$  can also be seen as adding in parallel. In this case, we simply recover the circuit model of Fig. 3.2b with a Debye loss tangent shape. In the other limit, the resistors  $R_S$  have infinite resistance. Then the sample can be seen essentially as being made up of many small samples, each encompassing one domain, all in parallel. These domains may each have different  $RC$  times for the tunnel capacitor-resistor combination. This means that the different domains each have different frequencies  $f_{peak}$  at which the loss tangent moves through a peak (or equivalently, the domains have different frequencies at

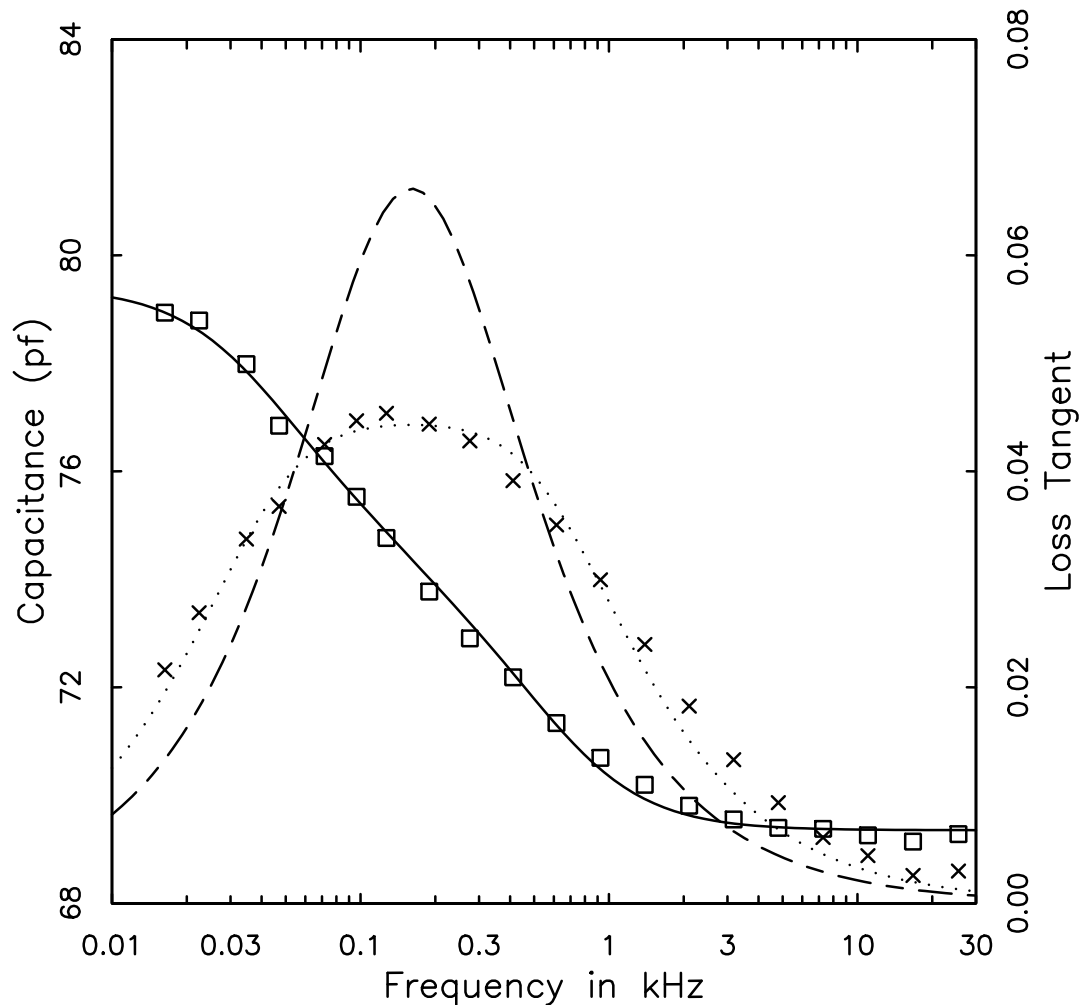


**Fig. 3.21** Plotted are capacitance and loss tangent curves at a particular gate bias for sample **A** at 8.5 T and 875 mK. Notice that the curves are broader in frequency than those of Fig. 3.3. In this case, the broadening parameter (described in the text),  $\chi$ , has a value of 3.46. The dashed line is a theoretical loss tangent curve with the same value of  $f_{peak}$  but no broadening ( $\chi = 1$ ).

which the capacitance decreases from  $C_{low}$  to  $C_{high}$ ). These “mini-devices” are all effectively in parallel. Assuming that the capacitances per unit area from the gate and substrate to the 2d gas remain the same, both the capacitance at very low frequencies (compared to  $1/2\pi RC$  for the slowest domains) and at high frequencies (compared to  $1/2\pi RC$  for the fastest domains) are unaffected by the breakup of the 2d gas into electrically isolated domains. The differences in  $RC$  times for the tunnel barrier in the different domains only affect the frequency dependence of the loss tangent and the capacitance between low and high frequencies.

There obviously exists a crossover regime with the resistances  $R_S$  between the limits of zero and infinity described above. Very roughly, loss tangent and capacitance curves begin to show broadening when the characteristic time for one domain to transfer charge to another becomes on order of the  $RC$  time for a domain to transfer charge to the substrate. This occurs when the resistances  $R_S$  in Fig. 3.20 approach the tunneling resistances  $R_T$ . The exact details of the crossover are complicated, depending on typical domain size, variation in domain sizes, the number of closely neighboring domains, and variation in the resistances  $R_S$  shunting the domains.

In the presence of the broadening, we no longer fit the capacitance vs. frequency curves with Eq. 3.1. We instead use the following form:

$$C(f) = .2C(f; f_{peak}) + .4C(f; \chi f_{peak}) + .4C(f; f_{peak}/\chi). \quad (3.26)$$

This equation can be read as regarding 20% of the area of the sample contributing to the capacitance with a peak frequency of  $f_{peak}$ , 40% contributing with a peak frequency of  $\chi f_{peak}$ , and 40% contributing with a peak peak frequency of  $f_{peak}/\chi$ .  $f_{peak}$  is taken to be a “mean peak frequency” for the domains, here taken to have individual peak frequencies distributed symmetrically about this

mean. We have introduced the parameter  $\chi$  which we call the “broadening parameter”. The parameter  $\chi$  determined from fits is a measure in the variation of peak frequencies from the different domains. The weighting, 20%, 40%, 40%, chosen in Eq. 3.26 is somewhat arbitrary. Experimentally, we find that this weighting tends to give a good fit to data, such as that presented in Fig. 3.21 regardless of the level of broadening. Other weightings, for example 30%, 35%, 35%, do nearly as well. Using this weighting increases the deduced value for  $\chi$  by up to around 20% from that obtained with the 20%, 40%, 40% weighting. With a particular weighting scheme chosen,  $\chi$  is useful as a measure of *relative* variations in the breadth of capacitance vs. frequency curves as the sample temperature, gate bias, and magnetic field are varied. It is also a rough measure of the absolute variation in peak frequencies,  $f_{peak}$ , throughout the different domains. With more data points and very high precision it may be reasonable to obtain a distribution function of the peak frequencies from the capacitance.

We now briefly explore the effects of temperature on the broadening parameter,  $\chi$ , obtained from fits. Fig. 3.22 displays the broadening parameter as a function of temperature in sample **A** at a magnetic field of 8.5 T, with the gate bias adjusted at each temperature so that the the Fermi level is at the same position between the first and second Landau levels ( $\nu = 2$ ; i.e. 2 spin subbands filled) at each temperature plotted. Above 4 K, the value of  $\chi$  parameter is one. This means that the fits detect no broadening of the capacitance vs. frequency curves. The sample behaves as though it is in the limit where the resistors  $R_S$  of Fig. 3.20 perfectly shunt the domains. There is no broadening, and the model of Fig. 3.2b is appropriate. Below 4 K, the  $\chi$  begins to increase as the temperature decreases. A crossover region exists between 0.5 K and 4 K, and below this  $\chi$  levels off to a saturated value  $\chi_{sat}$ . Curves such as that plotted

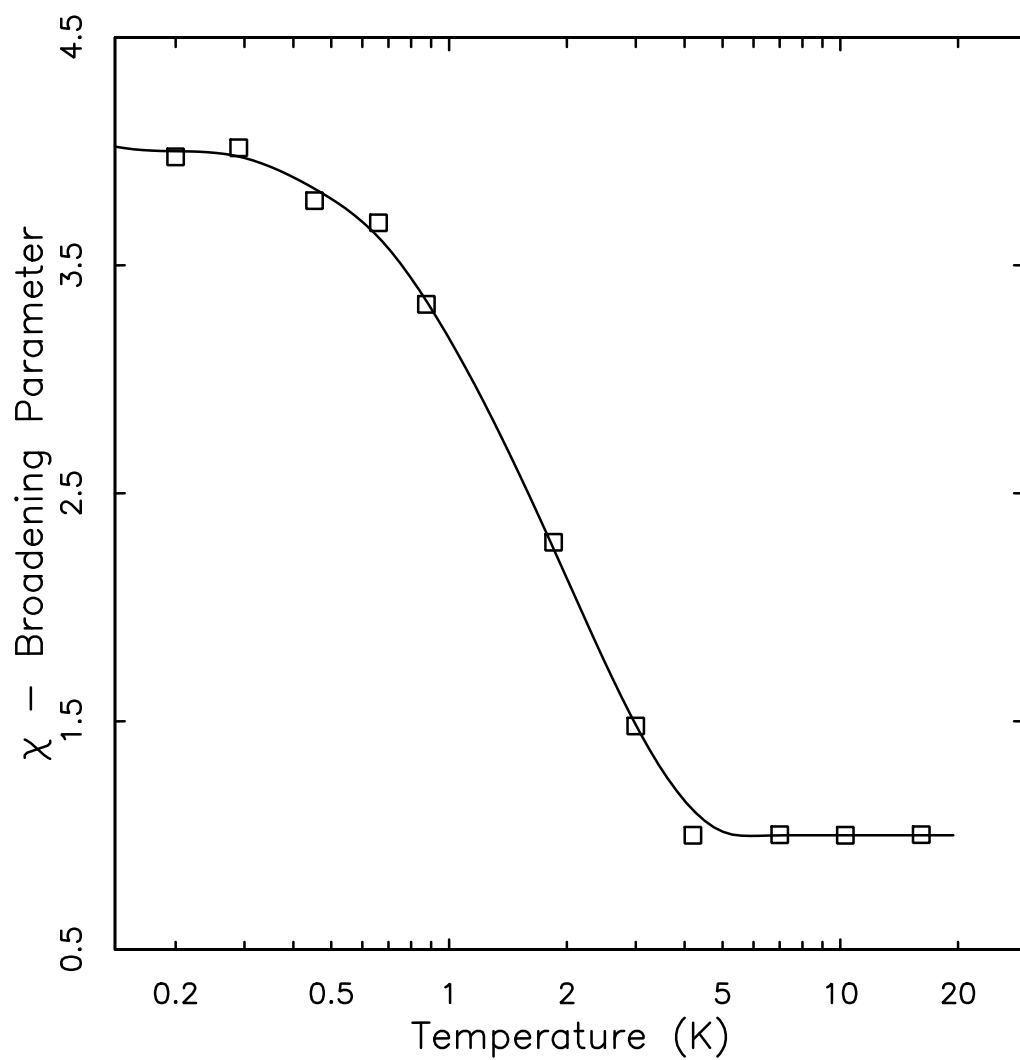


**Fig. 3.22** The figure plots the broadening parameter,  $\chi$ , as a function of temperature at a fixed Fermi energy. The Fermi energy is fixed at a value of 4 meV on Fig. 3.23. Note the saturation of  $\chi$  below about 0.5 K. The solid curve is a guide to the eye.

in Fig. 3.22 depend both on the magnetic field strength and the position of the Fermi level with respect to the Landau level structure. Experimentally we find that the temperature range for the crossover displays very little dependence on the position of the Fermi energy within the Landau level structure, but this temperature range does depend on the magnetic field strength.

### 3.7.3 Saturation of the Broadening Parameter at Low Temperatures

We briefly concentrate on the “saturated” value of the broadening parameter at low temperatures. The value of  $\chi_{sat}$  depends on both the Fermi energy and the magnetic field strength. In general, the value of  $\chi_{sat}$  is the largest when the Fermi level is nearly midway between two Landau levels. We find in sample **A** (the only sample for which we have data below 1 K), that at the lowest temperatures measured, we observe complete saturation of the broadening parameter only at the highest fields measured, 8.5 T and 6.5 T. At 8.5 T with the Fermi energy midway between Landau levels the onset of broadening typically occurs at 4 K and saturation occurs by 0.5 K. From plots of  $\chi$  vs. temperature it appears that  $\chi$  is close to saturation at 90 mK for a field of 4 T. For both fields of 8.5 T and 6.5 T, the largest saturated values of  $\chi$  are 4.5 and 3.5 respectively. At 4 T,  $\chi$  never exceeds 2.5, and no broadening ( $\chi = 1$  for all positions of the Fermi energy) is apparent for any gate bias in fields of 2 T and 1 T in temperatures down to 90 mK.

What is the physical significance of  $\chi_{sat}$ ? The following arguments suggest an interpretation of saturated broadening parameter as measure of the roughness of the tunnel barrier. Recognizing that for domain sizes much larger than  $350\text{\AA}$ , the separation between the 2d gas and the substrate charge, the capacitance per unit area of the domain to substrate capacitance is independent of domain



size, we expect the variation in peak frequencies to reflect mostly the variation in tunneling conductances from the different domains to the substrate. We identify the localization length  $\xi$  as the size scale of the domains here. The magnetic length acts as a lower bound on the localization length. At fields of 8.5 T and below, it is thus certain that domains are larger than  $\approx 100\text{\AA}$ . Depending on the magnetic field strength and the position of the Fermi level within the Landau level structure, the localization length varies. As the magnetic field increases and as the Fermi level is moved towards the middle of the band of localized states, this length decreases and so does the typical domain size. Smaller domains probe smaller regions of the tunnel barrier and hence result in larger variation in tunneling time from domain to domain. If the tunnel barrier roughness were known as a function of lateral distance along the tunnel barrier, the broadening of capacitance and loss tangent curves vs. frequency could be translated into information on the distribution of localization lengths for a particular value of the Fermi energy.

Fig. 3.23 illustrates some of the ideas presented above. Plotted along with  $\partial n/\partial\mu$  results taken at 8.5 T for 1.85 K is the broadening parameter vs. Fermi energy for temperatures ranging from 200 mK to 3 K. In the high DOS regions, the broadening parameter  $\chi$  is identically 1, regardless of temperature. Between Landau levels  $\chi$  increases with decreasing temperature and, for most regions of Fermi energy,  $\chi$  follows a curve of saturated values below 500 mK. The only exception is between the two spin subbands of the lowest Landau level. Here  $\chi$  is still increasing as the temperature is lowered to 200 mK. This continued temperature dependence of  $\chi$  arises because the exchange interaction splits the spin subbands still farther apart and diminishes the DOS between them as the temperature is lowered, decreasing both the in-plane conductivity and

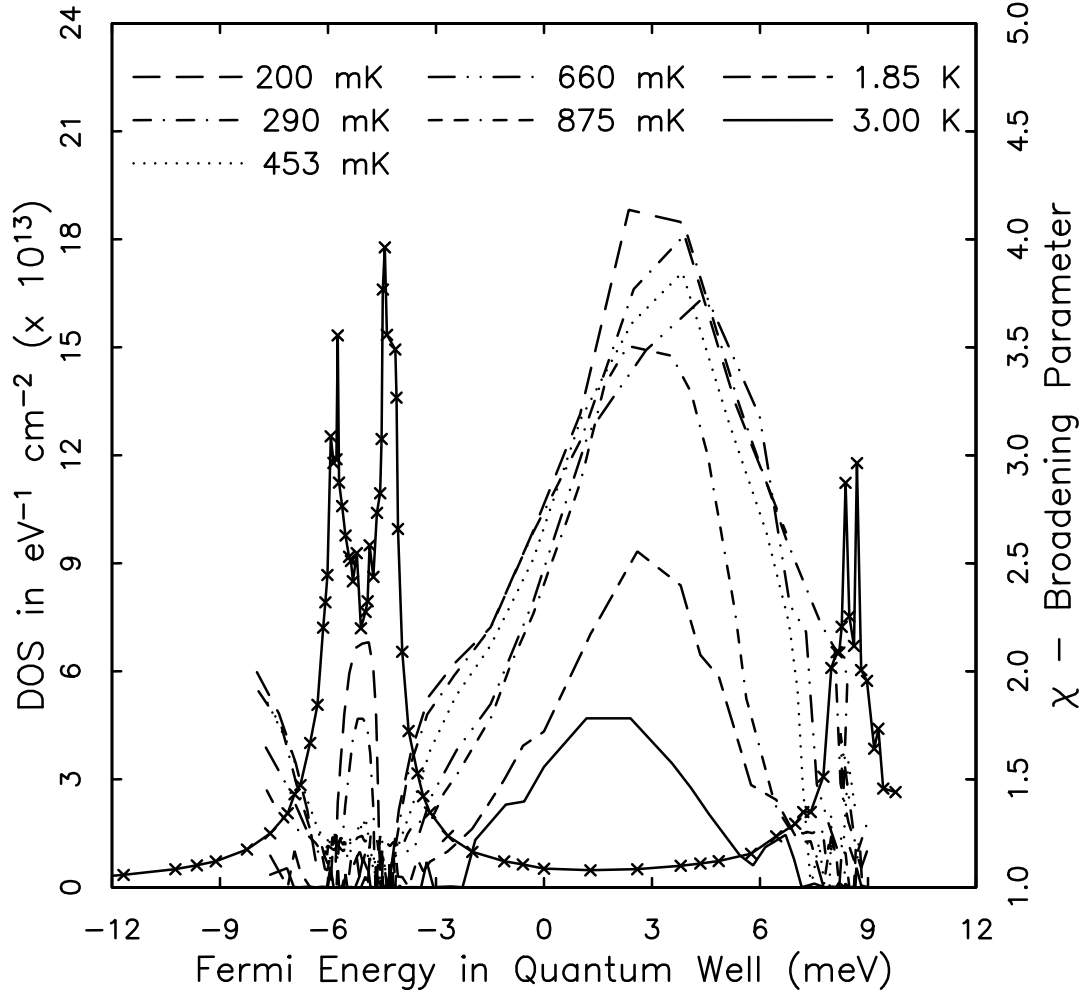


**Fig. 3.23** Plotted is  $\chi$  as a function of Fermi energy in sample **A** at 8.5 T for temperatures ranging from 0.2 K to 3 K along with  $\partial n / \partial \mu$  at 8.5 T and 1.85 K. Note that the temperature dependence of  $\chi$  is roughly independent of Fermi energy;  $\chi$  saturates everywhere along the curve at about 0.5 K. The fact that the region between the spin split Landau levels shows a different temperature dependence does not reflect the physics of the broadening; instead it arises because the exchange enhancement of the spin splitting continues to increase as the temperature is lowered.

the localization length of states between the subbands. The behavior of  $\chi$  as a function of temperature for these energies is complicated because it reflects both the increasing spin splitting and the freezeout of the in-plane conductance as the temperature is lowered. Concentrating instead on the region between Landau levels, we see an interesting universal behavior. The temperature range over which the  $\chi$  increases from 1 to  $\chi_{sat}$  is independent of the position of the Fermi energy between Landau levels. We will return to this interesting phenomena below.

The curve of  $\chi_{sat}$  in Fig. 3.23 has a very interesting detailed structure. A peak exists about midway between Landau levels. Moving down on either side of this peak, there are plateaus and then inflections and a sharp drop to  $\chi = 1$ . The origin of this structure, according to our model, may arise from either a “non-white” distribution function for the tunnel barrier roughness or, in the case of a white noise distribution function for the roughness, an interesting behavior of the localization length.

Fig. 3.24 plots  $\chi$  obtained from capacitance data taken at 4 T and 140 mK on sample **A**. Also plotted is  $\partial n / \partial \mu$  at 4 T and 1.9 K. This is plotted in place of the noisier 140 mK DOS results. Again, the value of  $\chi$  here appears, from  $\chi$  vs.  $T$  plots, to be close to full saturation, and we will refer to the results as reflecting  $\chi_{sat}$ . Upon comparison with the 8.5 T data, we see an interesting difference. The peak value of  $\chi_{sat}$  at 4 T is much smaller than that obtained at 8.5 T. In fact, the peak value of  $\chi_{sat}$  at 4 T is about the same as  $\chi_{sat}$  at 8.5 T midway from the Landau level peak DOS position and the position of the peak in  $\chi_{sat}$ . Considering the same value of  $\chi_{sat}$  as indicating the same typical localization length allows a comparison of localization lengths in different fields.

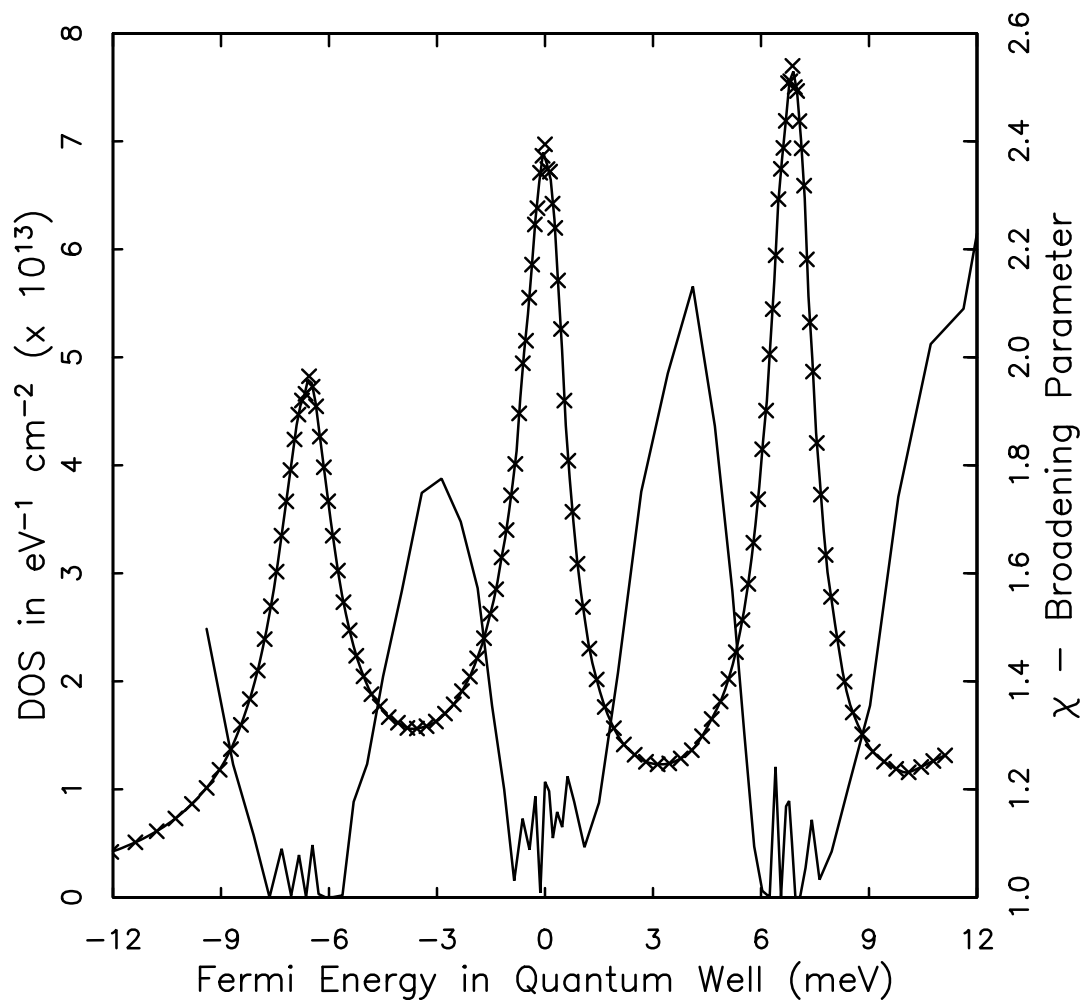


**Fig. 3.24** The figure plots  $\chi$  as a function of Fermi energy at 4 T and 140 mK in sample **A**. Also plotted is  $\partial n / \partial \mu$  at 4 T and 1.9 K.

Although we cannot measure the Hall resistance, we believe the position in Figs. 3.23 and 3.24 at which  $\chi$  begins to deviate from  $\chi = 1$  is different from the position at which the Hall resistance enters a plateau. Indeed, this position shows little temperature dependence; whereas the breadth of Hall plateaus<sup>33,43</sup> show much temperature dependence.  $\chi$  begins to deviate from 1 when  $\xi$  becomes shorter than some temperature independent length fixed by the tunnel barrier roughness; whereas a Hall plateau commences when  $\xi$  becomes shorter than an inelastic mean free path or some other temperature dependent length.

One rough interpretation of the maximum value 4 for the  $\chi_{sat}$  is that it indicates a factor of about 4 variation in tunneling conductance to the substrate from the different domains. This is a reasonable amount of variation given that monolayer ( $5.6\text{\AA}$ ) thickness fluctuations on both sides of the tunnel barrier, for the height in energy of our tunnel barrier, would be expected to give rise to nearly the same size of tunneling conductance fluctuation. This comparison assumes that the value of the maximum value of  $\chi_{sat}$  would not increase much more if the magnetic field strength were increased beyond 8.5 T.

If a method could be devised to controllably place lateral inhomogeneity in the tunnel barrier, broadening parameter information in such a system might yield a quantitative measurement of the localization length. If a grid composed of thinner and thicker regions of the tunnel barrier could be produced, large changes in the broadening parameter would occur as the localization length ranges through sizes smaller and larger than the period of the grid.

Although we have not made such a sample, we have in our lab produced arrays of “quantum dots”,<sup>44</sup> laterally confining electrons in the 2d gas into small pockets less than 100 nm wide, and observed broadening in the loss tangent and capacitance vs. frequency curves. This dot sample was produced from the same

MBE grown wafer from which sample **C** was processed. At first thought, one would think that the broadening in such a sample, where the size scale of the domains is known, should be useful for comparison to results for the 2d gas in magnetic field. Unfortunately, tunneling from small dots is complicated by single electron charging effects<sup>45</sup> which also cause broadening, making comparison to the broadening caused in a magnetic field by loss of in-plane conductivity in the 2d electron gas difficult.

Additionally, we speculate that RHEED oscillations monitored during MBE growth of the sample<sup>46</sup> can give information on the nature of the nonuniformity of the tunnel barrier. Such knowledge be useful in interpreting  $\chi_{sat}$  data to find typical localization lengths of states.

#### **3.7.4** *Connection to Magnetic Field Tunneling Suppression*

We have previously described<sup>21,22</sup> a novel temperature dependent suppression of the tunneling rate of electrons from the 2d gas to the substrate in our samples that occurs only in the presence of a magnetic field perpendicular to the plane of the 2d gas. This suppression has been observed in samples **A**, **B**, and **C**. A key feature of this tunneling suppression is that it occurs uniformly, independent of the position of the Fermi energy within the Landau level structure. The mechanism for this suppression is unknown, although we have been able to fit the tunneling data to a model which places an energy gap at the Fermi energy in the 2d electron gas. The size of this energy gap varies nearly linearly with magnetic field strength. The tunneling suppression is seen to commence at a particular temperature as the temperature is lowered and saturate at low temperatures.

A particularly intriguing behavior of the broadening parameter is that the temperature range for  $\chi$  to move from a value of 1 to a value of  $\chi_{sat}$  is independent of the position of the Fermi energy within the Landau level structure. Also, the temperature over which  $\chi$  moves from 1 to  $\chi_{sat}$  is roughly *the same* as the temperature range over which the tunneling suppression commences and saturates. As with the tunneling suppression, the temperatures over which  $\chi$  moves from 1 to  $\chi_{sat}$  decrease as the magnetic field strength decreases.

The model presented earlier in this section predicts that  $\chi$  approaches  $\chi_{sat}$  as the resistances between the domains become much larger than the tunneling resistances of the domains to the substrate. The temperature dependence of  $\chi$  arises from the temperature dependence of the in-plane conductivity. Since the tunneling suppression and  $\chi$  have the same temperature dependence this suggests that there is a connection between the processes which causes freezeout of the in-plane conductivity and the tunneling suppression. Strangely, the tunneling suppression occurs uniformly throughout the Landau level structure, whereas the in-plane conductivity depends heavily on the position of the Fermi energy within the Landau level structure.

### 3.8 Summary

In conclusion, we have developed a new technique which has allowed us to make a systematic quantitative study of 2d Landau level DOS as a function of Fermi energy in the 2d electron gas. This study was made on three different samples with different doping configurations. Analysis of the results in magnetic fields small enough so that the exchange enhanced spin splitting small compared to the Landau level width has lead to three principle conclusions. Landau levels are described well by Lorentzian lineshapes; this lineshape is independent

of the doping profile in the sample; and, the widths of Landau levels, while dependent on sample doping profile and 2d electron gas density, are independent of magnetic field strength. In high fields, the exchange enhanced spin splitting is observed, and fits are made to the lineshapes using the model of Ando and Uemura.<sup>11</sup> These fits determine a value for the exchange energy that is in good agreement with past determinations in 2d systems in GaAs.<sup>12,13</sup> Lastly, we have shown that the frequency dependence of the capacitance and loss tangent in systems such as our own can be used as a gauge of the localization length,  $\xi$ , in the 2d electron gas.

## Appendix A - Explanation of $\eta$ term

Here we give a brief explanation of the term  $\eta$  which is a correction for the nonzero extent of charge in the vertical ( $x$ ) dimension in the well. Recall that  $\eta\sigma_w$  given in Eq. 3.7 serves to correct the energy of the bound state in the well as given by the sheet charge model ( $U_w + E_0$  from Eq. 3.6) for the nonzero width of distribution of charge in the well.  $\eta\sigma$  is an energy which is subtracted from the energy of the bound state determined by the sheet charge model and which grows linearly with charge density. This appendix describes the two contributions to  $\eta$  as well as giving some justification for why the sheet charge model with the correction  $\eta$  can be used in place of a distributed charge model for the well.

It should be noted that the capacitance,  $C_{geom}$ , deduced from the data through Eq. 3.17 specifies a position  $x_w$  for the charge in the well. The significance of this position is described pictorially in Fig. 3.25. For the distributed charge model, it can be shown that the linear extrapolations of  $V(x)$  (the electrostatic potential due to the charge densities  $\sigma_g, \sigma_w$ , and  $\sigma_s$ )



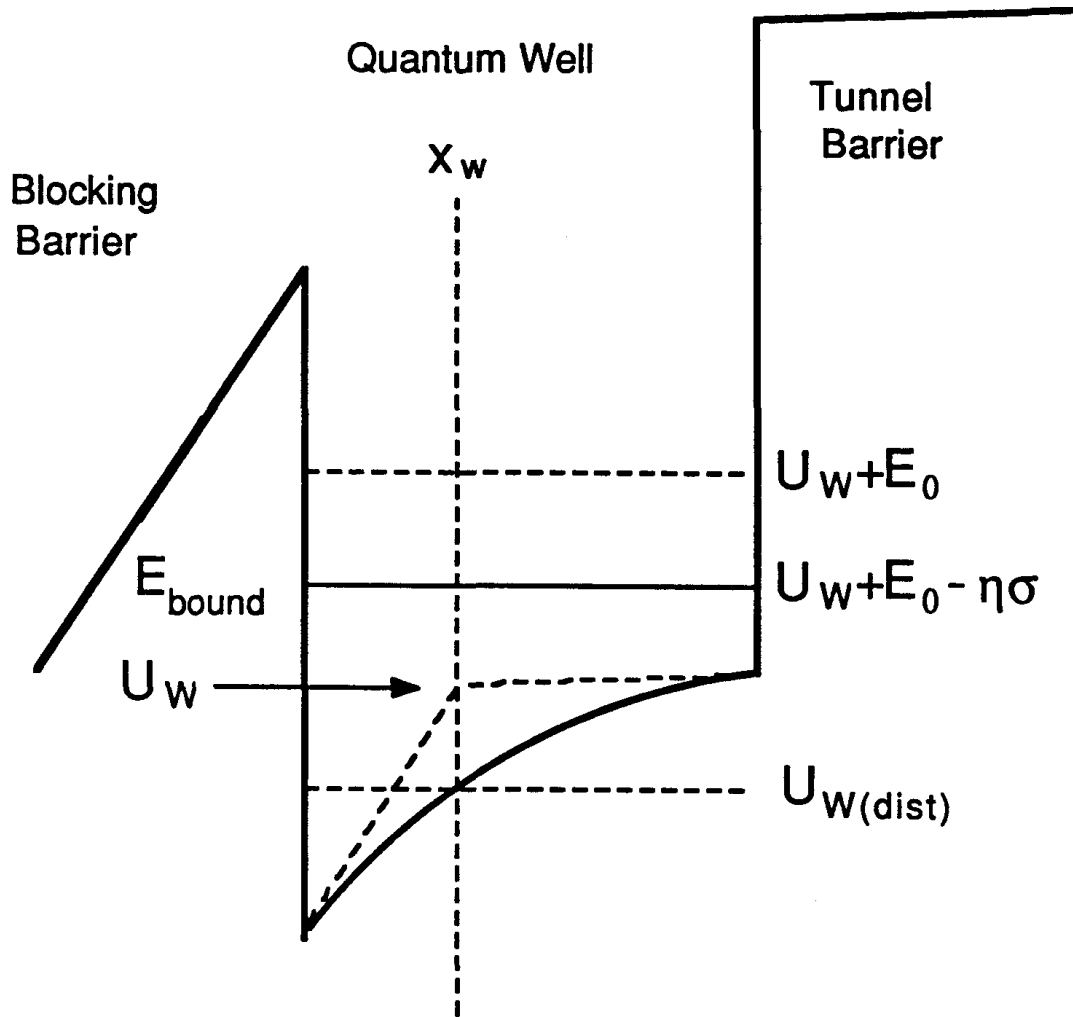


**Fig. 3.25** This figure pictorially describes the origin of the term  $\eta$  in our DOS calculation. In the sheet charge model,  $U_w$  is the energy of the band edge at the position of electrons and  $U_w + E_0$  is the energy of the bound state. A distributed charge model spreads out the electrons, and the energy of the band edge at the mean position of electrons is reduced to  $U_{w(dist)}$ . This, and the fact that electrons sense the potential energy at positions other than  $x_w$  reduces the bound state energy to  $U_w + E_0 - \eta\sigma_w$ .

from charge free barriers into the quantum well intersect at the position:

$$x_w = \int x \rho(x) dx.$$

Here  $\rho(x)$  is the charge density distribution (normalized to unity) in the well in the  $x$  (vertical) dimension. Eq. 3.2, though derived in the sheet charge model, is still correct in the distributed charge model provided that the position  $x_w$  is taken as the mean position of the charge in the well. In the series of equations that are solved in the sheet charge model to obtain expressions for the capacitances, and hence the expressions for the DOS using measured capacitances, only the expressions for  $U_w$  (Eq. 3.3) and  $U_{bound}$  (Eq. 3.6) are different in the distributed charge model.

First, we concentrate on Eq. 3.3. Figure 3.25 depicts the potential energy at the band edge at position  $x_w$ ,  $U_w$  in the sheet charge model being greater than that given by the distributed charge model. Eq. 3.3, modified in order to take into account the nonzero  $x$  extent of the charge in the well, becomes

$$U_{w(dist)} = -\frac{e^2}{\epsilon} \sigma_s x_w - \Delta U_w,$$

where  $\Delta U_w$  is given by,

$$\Delta U_w = \frac{e^2 \sigma_w}{\epsilon} \int_0^{x_w} \rho(x) (x_w - x) dx. \quad (3.27)$$

Thus when the charge in the well is spread out, the potential energy of electrons at the band edge at position  $x_w$  is reduced. If the charge distribution function  $\rho(x)$  retains the same shape and as the well is filled, the reduction term  $\Delta U_w$  will increase by an amount proportional to  $\sigma_w$ .

Our sheet charge model considers the energy of the bound state to be given by  $U_{bound} = U_w + E_0$  (Eq. 3.6). The energy of the bound state is thus taken to

be a fixed energy  $E_0$  above the energy of electrons at the band edge at position  $x_w$ . We define  $E_0$  as being the energy added to  $U_w$  to give the actual bound state energy when the gate bias is moved to the point where the first electron enters the well (i.e. before there is any curvature to the well bottom). In a naïve model, the energy of the bound state is  $U_{w(dist)} + E_0$ . However, as the well fills, the curvature of the band edge potential energy at the well bottom increases, and the quantum mechanical bound state energy decreases with respect to the potential energy at  $x_w$ . This happens because electrons in the well sense the potential at positions other than  $x_w$ , and the particular shape of the potential in our samples, leads to a decrease in the bound state energy as the well is filled. In first order perturbation theory, the energy difference between the bound state energy and  $U_{w(dist)}$  decreases linearly with increasing charge density.

With the assumptions that the shape of the charge distribution does not change and that first order perturbation theory is correct in calculating the shift of the bound state energy as the well fills, the difference between the actual bound state energy in the well and that indicated by the sheet charge model grows linearly. This linearity allows us to approximate the behavior in the distributed case by inclusion the term  $\eta\sigma_w$  in Eq. 3.7 in our analysis.

## Appendix B - Details of the DOS Calculation

We have outlined a protocol earlier in this chapter that can be used to determine the values of  $C_{geom}$  and  $\eta$  from the low and high frequency capacitance data. This appendix addresses some of the subtleties of the DOS determination not immediately apparent in the model.

*Limits to our knowledge of the values of  $C_{geom}$  and  $\eta$*

We start first with the limitations of our knowledge of the parameters  $C_{geom}$  and  $\eta$  and the effects of this uncertainty. Some basic questions are: 1) How large is the error in the determination of the parameters  $C_{geom}$  and  $\eta$ ? 2) How do the parameters  $C_{geom}$  and  $\eta$  vary as the gate bias is varied? and 3) How do these effects influence the DOS determination?

We estimate the error in determining  $C_{geom}$  from Eq. 3.17 to be near two or three percent. These errors arise from several factors. There is a breadth to the Landau minima in the capacitance which prevents precise determination of the limits of integration in Eq. 3.17. Moreover, there may be some overlap of the DOS from different levels, which for the case of adjacent levels with different shapes, can change the expected value of the left hand side of Eq. 3.17 from  $2Be/h$  by a few percent. Given a value for  $C_{geom}$ , determination of  $\eta$  can be made with better precision. Tips of the Landau level DOS peaks plotted as a function of well energy are well defined; the breadths of the Landau levels are typically a meV or less with sharp tips. Also, the peak spacing or cyclotron energy  $\hbar\omega_c$  is well known from the GaAs effective mass of  $0.067m_0$ .

What is the effect of the error in the value of  $C_{geom}$  used on the DOS determination? Increasing the value of  $C_{geom}$  used in the DOS determination (for typical values of parameters for the samples measured here) decreases the gate to well energy lever-arm,  $dU_{bound}/d(eV_{gate})$ , and hence tends to bring closer together peaks of Landau levels plotted as a function of Fermi energy in the well. Also, as can be seen in Eq. 3.15, decreasing the value of  $\eta$  used in the DOS determination again decreases the lever-arm and brings the positions of the observed Landau level peaks closer together. If the error in  $C_{geom}$  leads the value of  $C_{geom}$  used in the DOS determination to be larger than the actual value,

then the value of  $\eta$  which positions the Landau level peaks  $\hbar\omega_c$  apart will be larger than its actual value. In a plot, sketched in Fig. 3.26, of  $C_{geom}$  vs.  $\eta$  there is a curve of values for these two quantities upon which the DOS determination will give the correct Landau level spacing. The important question is then: For the range of values given by the error in the  $C_{geom}$  determination, what is the variation in the shape of observed Landau levels for levels that are spaced  $\hbar\omega_c$  apart? Upon trying different values ( $\pm 3\%$ ) of  $C_{geom}$  in the DOS calculation and using the corresponding values of  $\eta$  from Eq. 3.18, we observe no visible change in the shapes of levels. Using a value for  $C_{geom}$  that is 3% less than the actual value will, by Eq. 3.17, lead to a 3% error in the normalization of the total degeneracy of a Landau peak. On the scale of the resolution of the plots shown in this chapter, this error is invisible.

*Method for more precise determination of  $C_{geom}$  and  $\eta$*

Is it possible then, using our measurements, to “pin down” the values of  $C_{geom}$  and  $\eta$  even though, with the constraint that Landau level peaks have the correct separation, these values have no observable effect on the shapes of the DOS peaks? We have developed a method to do this. The zero field DOS is given by  $g_0 = m^*/\pi\hbar^2$  or  $2.8 \times 10^{13} \text{ cm}^{-2}\text{eV}^{-1}$ . Referring back to Fig. 3.26, there is only one set of values of  $C_{geom}$  and  $\eta$  which, in the absence of magnetic field, yield  $g_0$  in the DOS determination.

The protocol then becomes slightly more complicated. We start with capacitance data and using Eq. 3.17 make the first rough determination of  $C_{geom}$ . Then  $\eta$  is determined by making certain that Landau peaks have the correct spacing. This determines one point on the imaginary curve. The zero field DOS is then deduced using these parameter values. Depending on the value of the

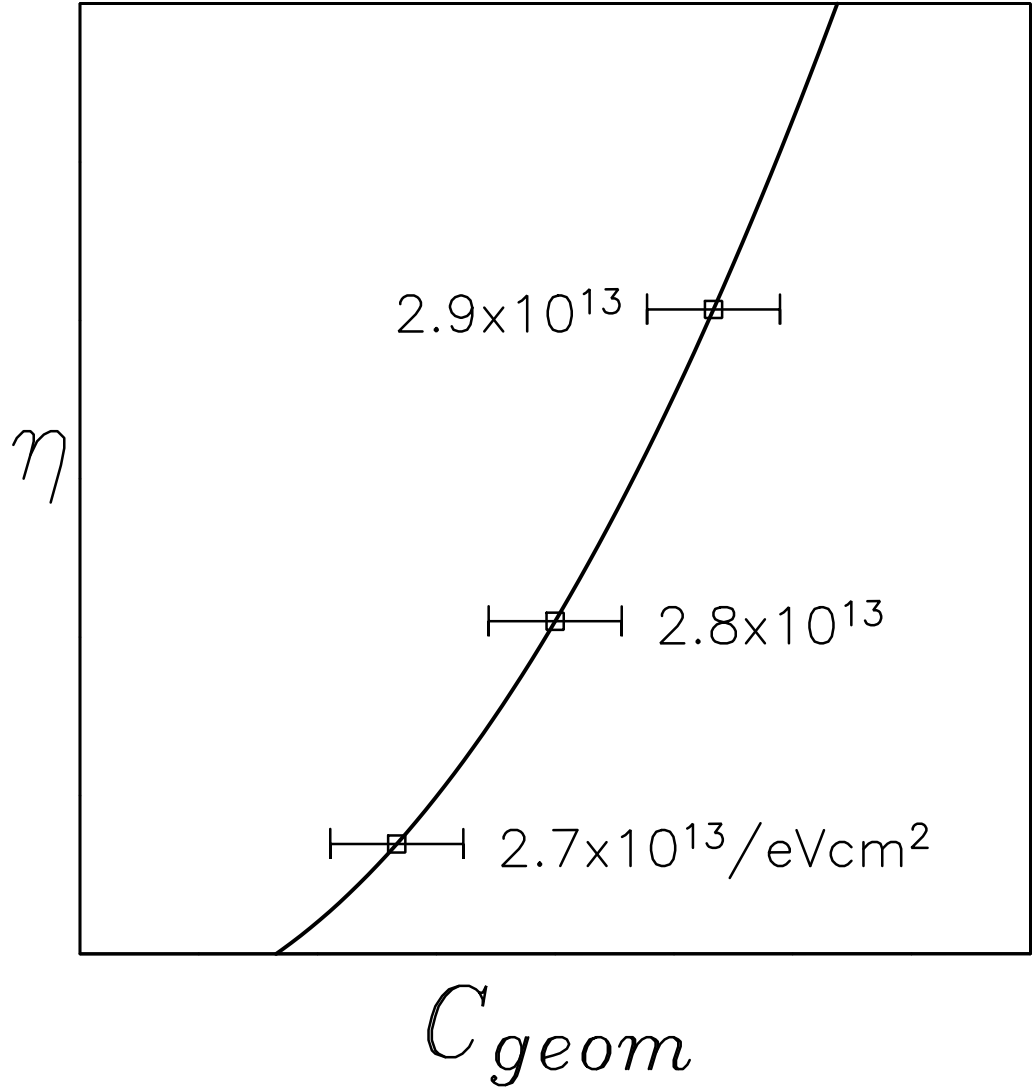


**Fig. 3.26** The curve plotted is the locus of points in parameter space for which the Landau level DOS, deduced using the analysis of this chapter, contains peaks spaced  $\hbar\omega_c$  apart. Different points on the curve correspond give different values of the zero field DOS; labels next to the box symbols give the zero field DOS obtained using these values of  $C_{geom}$  and  $\eta$ . The error bars on the points illustrate the error in  $C_{geom}$  after using the techniques involving the zero field DOS discuss in the text. Because of the steepness of the slope of the curve, the error in  $C_{geom}$  is translated into a much larger uncertainty in the value of  $\eta$ .

zero field DOS obtained, we increase the value of  $C_{geom}$  (increases observed zero field DOS) or decrease it (decreases observed zero field DOS) and redetermine  $\eta$  by looking again at the data with field. We then redetermine the zero field data using this new value of  $\eta$ . The correct value of  $C_{geom}$  can be interpolated from a graph of  $g_0$  vs.  $C_{geom}$  (where for each value of  $C_{geom}$ ,  $\eta$  has been adjusted to satisfy Eq. 3.18) to give the correct value of  $g_0$ .

The values for  $C_{geom}$  and  $\eta$  obtained this way are in accord with simple estimates. For example, in sample **B**,  $C_{geom}$  is about 102.5 pF (which translates into a distance  $325\text{\AA}$  for  $x_w$  using a dielectric of 12 for the medium) and  $\eta = 3.2 \times 10^{-14} \text{eVcm}^2$ . These numbers are very plausible. In sample **B**, charge in the substrate is expected to be about a Thomas-Fermi screening length of  $100\text{\AA}$  away from the substrate-tunnel barrier interface.<sup>18,23</sup> Note, there is an undoped GaAs spacer layer at the substrate, and the potential configuration here is quite complicated. The tunnel barrier is  $133\text{\AA}$  thick, and the mean position of the charge in the well is about  $85\text{\AA}$  from the well-tunnel barrier interface.<sup>24</sup> The sum of these numbers,  $318\text{\AA}$ , is close to the experimentally determined value for  $x_w$ . Considering the electronic wavefunction in the well to be given by a sine wave and use of first order perturbation theory<sup>18</sup> gives  $\eta = 2.7 \times 10^{-14} \text{eVcm}^2$ , again in close agreement with the result determined using our protocol. However, the error in the experimentally determined value of  $\eta$  is still very large. The steepness of the slope of the curve in Fig. 3.26 is meant to illustrate this; a small error in  $C_{geom}$  will lead to a large error in  $\eta$ . Our fit to  $g_0$ , due to statistical error in the data, uncertainty in the value of the effective mass in the quantum well, and small drifts in capacitance shunting the sample (typically 0.1 pF) between runs can only be trusted to about  $\pm 2\%$ . This leads to a  $\pm 2\%$  uncertainty in the value for  $C_{geom}$ . In this range of probable

values for  $C_{geom}$  indicated by this uncertainty, the value of  $\eta$  needed to keep Landau levels spaced by  $\hbar\omega_c$  is about 50% smaller for  $C_{geom}$  at 100.5 pF than that for  $C_{geom}$  set at 104.5 pF.

It is clear then, that to obtain a meaningful measure of  $\eta$  for comparison to models, one needs greater precision in the experiment than we have in the data presented here. For the purposes of the DOS determination however, the precise value of  $\eta$  appears to be irrelevant.

#### *Variation of $C_{geom}$ and $\eta$ as the well fills*

Another complication in our DOS determination is the variation of  $C_{geom}$  and  $\eta$  as the gate bias is varied. Both the mean positions of the charge densities in the well and the substrate are expected to move as the gate bias is varied. They tend to move in the same direction (as the gate bias is made more positive, these charge densities shift towards the gate) but not necessarily at the same rate. This causes a change in  $x_w$  and thus in  $C_{geom}$ . Also, the shape of the conduction band edge energy in the well and the charge distribution in the well change as well filling is varied. Thus  $\eta$  will also have some gate bias dependence. We now refer back to Fig. 3.8. This figure shows the results for the DOS in zero magnetic field both with no corrections to either  $C_{geom}$  or  $\eta$  for variation with gate bias and with the correction described below. In the curve which includes the correction,  $C_{geom}$  varies linearly with gate bias. For sample **B** the formula for  $C_{geom}$  that we use is

$$C_{geom} = 101.0\text{pF} + (0.0060\text{pF/mV})V_{gate},$$

where the gate voltage is measured in mV. The factor 0.0060 pF/mV was determined empirically as the number which causes the observed zero magnetic



field DOS to be constant. This represents a 3% variation in the value of  $C_{geom}$ , or an approximately  $10\text{\AA}$  variation in  $x_w$ , over the range of gate biases used in sample **B**. The value of 102.5 pF given for  $C_{geom}$  above is an average value.

Suppose the variation which causes the DOS in the uncorrected curve of Fig. 3.8 to vary with gate bias were actually a variation of  $\eta$  with gate bias and not a variation of  $C_{geom}$ . We have also succeeded in making the observed zero magnetic field DOS flat by adding a term linear in gate voltage to  $\eta$  and keeping  $C_{geom}$  constant. Whichever method was used to make the observed zero field DOS flat, the DOS results with field were identical. This is not surprising given our remarks above about the insensitivity of the DOS results on the precise values of  $C_{geom}$  and  $\eta$  as long as these parameters are adjusted so that the observed Landau level peaks lie  $\hbar\omega_c$  apart.

One concern is that the correction made, through observation of the zero field DOS results, for variation in the parameters  $C_{geom}$  and  $\eta$  using a term in  $C_{geom}$  linear in gate bias might not be appropriate when the magnetic field is applied. For a given sample, the position of the excess charge in the substrate is solely a function of the electric field at the tunnel barrier. That is to say, for a given electric field at the tunnel barrier the self-consistent problem of the position of charges in the substrate can be solved independently of variations in the positions of charges in other parts of the sample. For a constant separation between the excess charge in the substrate and the mean position of the charge in the well, this electric field is proportional (neglecting small nonlinearity arising from distributed charge in the well) to the bound state energy in the well as measured with respect to the Fermi energy in the substrate. One might expect then that lowest order variation in  $C_{geom}$  should be taken as a linear term in well energy and not gate bias.

We have experimented with translating, using a lever-arm, the variation in  $C_{geom}$  from gate bias to well energy. In zero magnetic field, the lever arm is nearly constant (about 1:42 for Sample **B**), and this translation is trivial. Instead of 0.0060 pF/mV gate voltage variation, the variation is 0.254 pF/meV at the well. We use this same value in the well in the case with field and translate back to gate voltage using the lever-arm determined by using the zero field variation of  $C_{geom}$  in gate bias. We then use the variation in  $C_{geom}$  obtained this way in the DOS and lever-arm determination. Now an improved lever-arm is obtained and it can be used again to determine the variation of  $C_{geom}$  with gate bias. This procedure can then be iterated until there is no further change in  $C_{geom}$  as a function of gate bias.

We find that the size of the variation in  $C_{geom}$  is too small to cause any observable change in the the Landau level DOS that we obtain. In fact, in the iterative procedure outlined above we see only a minute change (much too small to be observed in the DOS results) to the lever-arm with field after the first determination of  $C_{geom}$  as a function of gate bias. Further iteration yields no more change. In short, characterizing the effect, which causes the deduced zero field DOS to have a slight slope in Fig. 3.8, in terms of either gate bias or well energy yields the same Landau level DOS.

### *Robustness of the DOS calculation*

The procedure used to obtain the Landau level DOS given in this chapter is very robust. Experimentation with the protocol shows that the effects of adding a constant capacitance shift as large as 2% of the measured value to  $C_{low}$ , provided that parameters  $C_{geom}$  and  $\eta$  are adjusted to insure that the observe Landau levels are  $\hbar\omega_c$  apart, are almost unobservable in the DOS results.

Similarly, a capacitance shift of several percent can be added to both  $C_{low}$  and  $C_{high}$  with no change in the DOS results. This indicates that even if there were a small unobserved capacitance of several picofarads shunting our device (we believe that any shunt capacitance is less than 0.5 pF), the effects of this on the final DOS determination would be inconsequential.

### *Computer Simulations*

We have used computer simulations of data to understand better the observed robustness of the DOS results and their insensitivity to the means used to correct them for the variation in  $C_{geom}$  and  $\eta$ . It is a simple matter, starting with assumed values for  $C_{geom}$ ,  $\eta$ , and  $g$  (the DOS) to obtain the  $C_{low}$  and  $C_{high}$  as a function of gate bias by reversing Eqs. 3.15 & 3.16. We can then run the capacitance values obtained through the analysis procedure.

Typically, we start with Lorentzian or Gaussian lineshapes, convert these into capacitance values after adding some deviation to the simple model (such as a variation in  $\eta$  with gate bias) and convert the resulting values of  $C_{low}$  and  $C_{high}$  through the analysis procedure. We can in this way isolate the effects of the variability of  $C_{geom}$  and  $\eta$  as well as the effects of shunt capacitance and its drift in the capacitance measurements. Our correction of the variation of  $C_{geom}$  using a term linear in gate bias, even though it may be more appropriate to consider the variation in  $C_{geom}$  as linear in well Fermi energy, is justified by the computer model, as well as is our method for correcting any variation in  $\eta$  by adjusting the correction term in  $C_{geom}$ . Also, these simulations justify the correction of the effects of  $C_{motion}$  (which increases linearly in charge density; see Eq. 3.19) described in section 4.3 by adjustment of the linear term in  $C_{geom}$ . In each case, for the expected values for variation of these parameters, the computer

simulations show, on the scale of the graphs in this chapter, errors incurred by using a linear variation in gate voltage of  $C_{geom}$  to correct all of the variations are at or below the threshold of being visible. The robustness of the method to shunt capacitance as large as several pF is also verified by these calculations.

## Appendix C - Comparison of Abscissas on DOS Plots

In section 3.4.3 we stated that the abscissas on Figs. 3.6 and 3.8 corresponded to the same Fermi energies in the well with respect to the well bound state. To explain how we know this to be true, we start by examining Eq. 3.11. For constant parameter values of  $x_w$ ,  $x_s$ , and  $\eta$ , it is easy to show that

$$\Delta V_{gate} = A\Delta U_{bound} + B\Delta\sigma_w,$$

where  $A$  and  $B$  are constants. Because the DOS, averaged over a Landau level is the same, independent of magnetic field, this equation indicates that the lever-arm, averaged over a Landau level, is also independent of field. As stated earlier, our analysis procedure breaks down for low electronic densities in the well. If it were valid in this regime, we could state that the gate bias which places the Fermi energy in a Landau minimum (in the case of Landau levels symmetric in energy, the Landau maxima also) would give the same Fermi energy with respect to the bound state energy in the well in the absence of field. The collapse of our analysis in the low density regime prohibits us from making this statement directly based on our model. We observe experimentally however, that the gate voltage which places the Fermi energy at Landau minima at 4 T also corresponds to the same Fermi energy at 2 T.

We take this to mean that the Fermi energy with respect to the bound state energy in the well is the indeed the same in the absence of magnetic field for the

same gate bias which places the Fermi energy in a Landau minimum (or Landau maximum in the case of symmetric levels) in the presence of field. In Figs. 3.6 and 3.8 we have chosen the zero of energy on the abscissa to correspond to the same gate voltage, a gate voltage which places the Fermi energy at a Landau maxima of a nearly symmetric Landau level in Fig. 3.6. We thus believe that the horizontal scales in the two figures correspond to the same Fermi energies above the bound state in the well.

## References

1. T. Ando, A.B. Fowler, and F. Stern, Rev. Mod. Phys. **54**, 437 (1982) and references therein
2. R.E. Prange and S.M. Girvin, *The Quantum Hall Effect* (Springer-Verlag, New York, 1987)
3. E. Gornik, R. Lassnig, G. Strasser, H.L. Störmer, A.C. Gossard, and W. Wiegmann, Phys. Rev. Lett. **54**, 1820 (1985)
4. J.K. Wang, J.H. Campbell, D.C. Tsui, and A.Y. Cho, Phys. Rev. B **38**, 6174 (1988)
5. J.P. Eisenstein, H.L. Störmer, V. Narayanmurti, A.Y. Cho, A.C. Gossard, and C.W. Tu, Phys. Rev. Lett. **55**, 875 (1985)
6. R.K. Goodall, R.J. Higgins, and J.P. Harrang, Phys. Rev. B **31**, 6597 (1985)
7. T.P. Smith, B.B. Goldberg, P.J. Stiles, and M. Heiblum, Phys. Rev. B **32**, 2696 (1985)
8. V. Mosser, D. Weiss, K. von Klitzing, K. Ploog, and G. Weimann, Solid State Comm. **58**, 5 (1986)
9. T.P. Smith III, W.I. Wang, and P.J. Stiles, Phys. Rev. B **34**, 2995 (1986)
10. Vidar Gudmundsson and Rolf R. Gerhardt, Phys. Rev. B **35**, 8005 (1987)
11. T. Ando and Y. Uemura, J. Phys. Soc. Jpn. **37**, 1044 (1974)
12. B.B. Goldberg, D. Heiman, and A. Pinczuk, Phys. Rev. Lett. **63**, 1102 (1989)
13. R.J. Nicholas, R.J. Haug, K.v. Klitzing, and G. Weimann Phys. Rev. B **37**, 1294 (1988)
14. Y. Ono, J. Phys. Soc. Jpn. **51**, 2055 (1982)
15. Hideo Aoki and Tsuneya Ando, Phys. Rev. Lett. **54**, 831 (1985)
16. H.P. Wei, D.C. Tsui, M.A. Paalanen, and A.M.M. Pruisken, Phys. Rev. Lett. **61**, 1294 (1988)
17. J.A. Lebens, R.H. Silsbee, and S.L. Wright, Appl. Phys. Lett. **51**, 840 (1987)
18. J.A. Lebens, Ph.D. thesis, Cornell University (1988)
19. U. Meirav, M. Heiblum, and Frank Stern, Appl. Phys. Lett. **52**, 1268 (1988)

- 20. J.A. Lebens, R.H. Silsbee, and S.L. Wright, Phys. Rev. B **37**, 10308 (1988)
- 21. R.C. Ashoori, J.A. Lebens, N.P. Bigelow, and R.H. Silsbee, Phys. Rev. Lett. **64**, 681 (1990)
- 22. *See Chapter 4*
- 23. G.A. Baraff and Joel A. Appelbaum, Phys. Rev. B **5**, 475 (1972)
- 24. F. Stern and S.E. Laux, private communication
- 25. John A. Nixon and John H. Davies, Phys. Rev. B **41**, 7929 (1990)
- 26. T. Ando and Y. Uemura, J. Phys. Soc. Jpn. **36**, 959 (1974)
- 27. S. Das Sarma and X.C. Xie, Phys. Rev. Lett. **61**, 738 (1988)
- 28. Kazuhiko Hirakawa and Hiroyuki Sakaki, Phys. Rev. B **33**, 8291 (1986)
- 29. S. Das Sarma and Frank Stern, Phys. Rev. B **32**, 8442 (1985)
- 30. Claudine Hermann and Claude Weisbuch, Phys. Rev. B **15**, 823 (1977)
- 31. F.F. Fang and P.J. Stiles, Phys. Rev. **174**, 823 (1968)
- 32. D. Stein, K. v. Klitzing, and G. Weimann, Phys. Rev. Lett. **51**, 130 (1983)
- 33. M.A. Paalanen, D.C. Tsui, and A.C. Gossard, Phys. Rev. B **25**, 5566 (1982)
- 34. R.B. Laughlin, Phys. Rev. B **23**, 5632 (1981)
- 35. B.I. Halperin, Phys. Rev. B **25**, 2185 (1982)
- 36. *see for example* P. Streda, J. Kucera, and A. H. MacDonald, Phys. Rev. Lett. **59**, 1973 (1987)
- 37. F. Kuchar, R. Meisels, G. Weimann, and W. Schlapp, Phys. Rev. B **33**, 2965 (1986)
- 38. D.Heitmann, M. Ziesmann, and L.L. Chang, Phys. Rev. B **34**, 7463 (1986)
- 39. A. Wixforth, J.P. Kotthaus, and G. Weinmann, Phys. Rev. Lett. **56**, 2104 (1986)
- 40. D.C. Tsui, H.L. Störmer, and A.C. Gossard Phys. Rev. B **25**, 1405 (1982)
- 41. H.P. Wei, A.M. Chang, D.C. Tsui, and M. Razeghi, Phys. Rev. B **32**, 7016 (1985)

- 42. E.H. Nicollian and A. Goetzberger, Appl. Phys. Lett. **10**, 60 (1967)
- 43. A. Briggs, Y. Guldner, J.P. Vieren, M. Voos, J.P. Hirtz, and M. Razeghi, Phys. Rev. B **27**, 6549 (1983)
- 44. *See Chapter 5*
- 45. *See Chapter 6*
- 46. J.M. Van Hove, C.S. Lent, P.R. Pukite, and P.I. Cohen, J. Vac. Sci. Technol. B **1**, 741 (1983)



## Chapter IV

# Equilibrium Tunneling from the Two Dimensional Electron Gas

### 4.1 Introduction

Study of the two-dimensional (2d) electron gas formed at the interface of a semiconductor and an insulator has revealed much important physics, the most dramatic being the quantized Hall effects. The work presented in this chapter grew from a study intended to probe the modification of the density of states (DOS) in the 2d electron gas produced by a magnetic field perpendicular to the plane of the gas, a measurement of “the Landau-level DOS at the Fermi level.” The technique used provided two independent measures of the DOS, one a thermodynamic DOS explored in chapter 3, the other a tunneling or single-particle DOS described here. The experiment extends earlier capacitance spectroscopy of the Landau level DOS<sup>1</sup> to lower temperatures and, most importantly, also measures the tunneling conductance between the 2d gas and an  $n^+$  substrate.

It differs as well from other tunneling measurements<sup>2,3</sup> which determine an  $I$ - $V$  characteristic. In our experiment, the Fermi energy in a quantum well is varied in a controlled fashion by application of a gate voltage, and the Fermi energies on both sides of the tunnel barrier are kept within  $k_B T$  of one another.

We measure the equilibrium tunneling conductance as a function of the Fermi energy in the well, not the more usual differential conductance as a function of the difference in Fermi energies across the barrier.

The experiment shows, in addition to the structure expected from the development of Landau levels, an unexpected suppression of the electron tunneling which is greater than an order of magnitude at a field of 8 T and a temperature of 100 mK. We interpret these data as evidence for the development of a new magnetic field induced energy gap forming at the Fermi energy of the 2d gas.

This chapter is divided into two parts. First we explore the temperature dependence of tunneling data taken in the presence of magnetic field perpendicular to the plane of the 2d electron gas. We then turn to data taken in the absence of magnetic field. Unlike the data taken in the presence of magnetic field, these data show no temperature dependence except at low electronic densities in the well ( $< 1 \times 10^{11} \text{ cm}^{-2}$ ), where the data again reveal a tunneling suppression as the temperature is lowered. Strangely, the two different tunneling suppression effects have similar temperature dependences. This similarity may indicate that the same physical mechanism is responsible for the tunneling suppression in both cases. At the end of the chapter, we offer a possible explanation for the suppression effects seen at low density as well as speculations regarding the suppression effects induced by a magnetic field.

## 4.2 Samples and Method

Mesas etched from three wafers grown using molecular beam epitaxy have been studied. The essential structure of the wafers is shown in Fig. 4.1a. The three wafers, **A**, **B**, and **C**, have been described in detail in chapter 3.

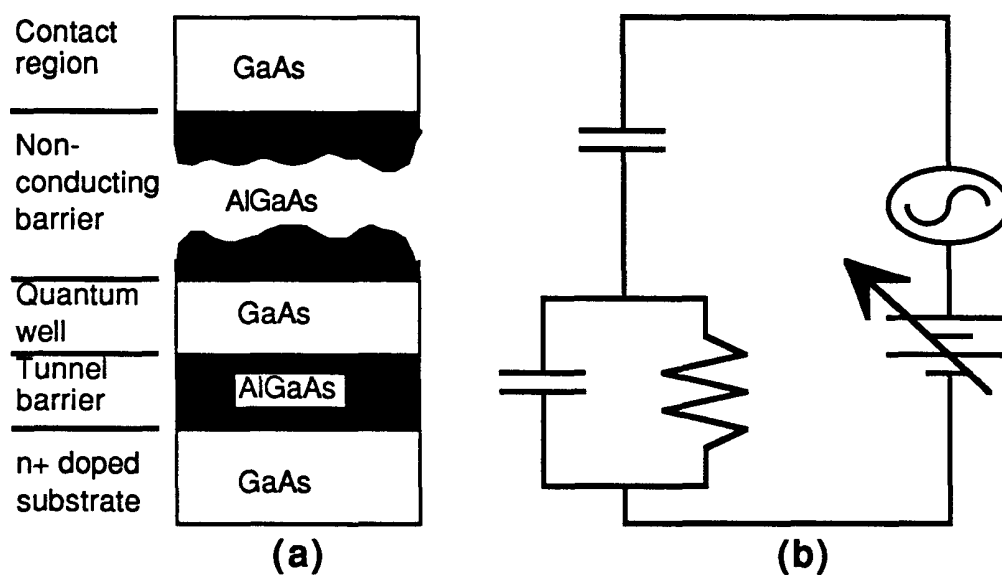


**Fig. 4.1** (a) shows the essential structure of the samples. Tunneling from the GaAs quantum well to the substrate across the AlGaAs tunnel barrier is observed by means of capacitive coupling through the thick nonconducting barrier. (b) displays a simplified model of the sample.

Also, tunneling measurements on sample **A** have been described in previous publications.<sup>4-7</sup> Each wafer consists of a degenerately  $n$  doped substrate in GaAs, an AlGaAs tunnel barrier, a GaAs quantum well, a thick nonconducting AlGaAs barrier, and a degenerately doped GaAs surface contact region. In all wafers, only the lowest electronic subband of the well is occupied. The electron density in the quantum well can be varied by the application of a gate bias across the sample.

Tunnel barriers in our samples can be regarded as capacitors shunted by a tunneling conductance. These were designed to have  $RC$  times which lie within the range of our measurements. The capacitance and the loss tangent of patterned mesas were measured at 20 frequencies between 15 Hz and 30 kHz. Low-pass filtering<sup>8</sup> was employed on sample leads to reduce any noise that might cause spurious voltage excitation across the tunnel barrier. The loss tangent displays a Debye lineshape which peaks, and concurrently the measured capacitance decreases, as the measuring frequency is swept through  $1/2\pi RC$ .

Fig. 4.1b shows the model which we use to characterize our capacitance and loss tangent vs. frequency data set. The data can be fit with suitable choices for the three circuit elements shown. If the thermodynamic DOS in the well were infinite, the value of the conductance (resistor shown in the figure) obtained by these fits would be the tunneling conductance. With a finite DOS, this correspondence no longer holds. The analysis of chapter 3, however, allows deduction of the thermodynamic DOS from the data set, and a simple extension of that analysis, given below, gives the tunneling conductance as well. In actuality, the capacitances shown in the model depend both on sample dimensions and the thermodynamic DOS<sup>9</sup> in the quantum well.<sup>10</sup> Discussed here are the results of a series of experiments in which the the tunneling

conductance is measured as a function of the electron density in the quantum well, the temperature of the sample, and the magnetic field strength (applied perpendicular to the plane of the 2d electron gas).

### 4.3 Extraction of Tunneling Conductance from Capacitance Data

#### *Equilibration of 2d and 3d Charge Densities*

In this section we describe how fits of capacitance vs. frequency and loss tangent vs. frequency curves are used to determine the tunneling conductance between the 2d electron gas and the substrate. To understand this problem, we first need to describe how the electron densities in the well and the substrate, starting slightly out of equilibrium, transfer electrons between one another through tunneling to bring the two charge densities into equilibrium. Once the time constants for approaching equilibrium are known, it is a simple matter to determine how the overall device impedance behaves as a function of frequency. The device operation is more complicated than is suggested by the circuit model of Fig 4.1b due to the finite density of states in the quantum well. In fact, both the single particle (tunneling) DOS,  $g_s$ , and the thermodynamic DOS,  $g_d$ , must be taken into account to correctly deduce the tunneling conductance from the capacitance data. We note that in chapter 3 we considered only the problem of the thermodynamic DOS.

Figure 4.2 shows the situation when the “quasi-Fermi level” in the quantum well  $E_{Fw}$  is greater than the Fermi level in the substrate,  $E_{Fs}$ . We are interested in the quantity  $E_{Fw} - E_{Fs}$ , as it describes the degree to which the electron gases are out of equilibrium.  $E_{Fw}$  is determined by the sum of two components. One is the energy of the bound state in the well with respect to the conduction

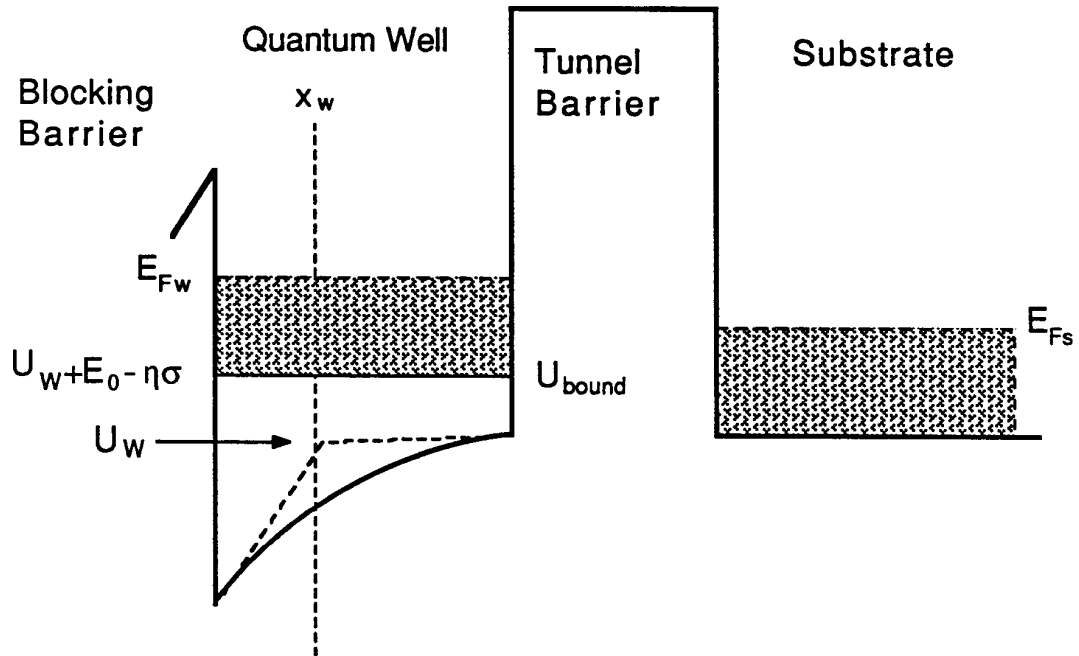


**Fig. 4.2** The figure shows the band diagram of the quantum well, tunnel barrier, and the substrate with the electronic density in the well slightly out of equilibrium with the electronic density in the substrate. The “quasi-Fermi level” in the well  $E_{Fw}$  in time relaxes so that it becomes equal to the Fermi energy in the substrate,  $E_{Fs}$ ; as it changes,  $U_{bound}$  also changes.

band edge deep within the substrate. The other is the width of the band of filled 2d electronic states within the well which arises from the noninfinite thermodynamic DOS in the well. As the electronic charge in the well changes both of these energies change. The Fermi energy in the substrate (all energies here are measured with respect to the band edge deep within the substrate) does not vary as charge in the well is changed. Using the terminology of chapter 3, we can write

$$\frac{d(E_{Fw} - E_{Fs})}{dt} = \frac{dU_{bound}}{dt} + \frac{1}{g_d} \frac{d\sigma_w}{dt}, \quad (4.1)$$

where, as in chapter 3,  $U_{bound}$  is the bound state energy,  $\sigma_w$  is the number density of electronic charge in the well, and it is understood that  $g_d$  corresponds to the thermodynamic DOS at the Fermi energy. The inverse of the *thermodynamic* DOS multiplies  $d\sigma_w/dt$  in Eq. 4.1 because the equilibration of Fermi energies in the quantum well and the substrate occurs on long time scales (audio frequencies).

In chapter 3, we described the term,  $\eta$ , which is a correction to the energy of the bound state in the well determined using a sheet charge model, given by  $U_w + E_0$  where  $E_0$  is a constant energy, for the nonzero width of the wavefunction in the well. The bound state energy including the  $\eta$  correction term is given by

$$U_{bound} = U_w + E_0 - \eta\sigma_w.$$

Here, the last term accounts for two effects. One is the difference in the electrostatic energy of the bound state associated with charge being distributed in the well rather than in a sheet. The other is the quantum mechanical change in the bound state energy due to the change of the shape of the well bottom in the presence of charge. We can then write

$$\frac{dU_{bound}}{dt} = \frac{dU_w}{dt} - \eta \frac{d\sigma_w}{dt}. \quad (4.2)$$

The tunneling current may be expressed in terms of a single particle DOS in the well  $g_s$ , at the Fermi energy, and a mean tunneling rate per electron of  $1/\tau_{tun}$ .<sup>11</sup>

$$I_{tun} = Ae(E_{Fw} - E_{Fs})\frac{g_s}{\tau_{tun}}, \quad (4.3)$$

where  $e$  is the magnitude of the electronic charge and  $A$  is the sample area. Note that this expression is correct only for temperatures and applied biases small enough so that only electrons in a narrow range over which  $g_s$  is constant can tunnel. As will be discussed in a later section, at higher temperatures,  $g_s$  must be replaced with its thermal average. In the “equilibrium tunneling” measurements presented here,  $|E_{Fw} - E_{Fs}|$  is always kept less than  $k_B T$  by suitable choice of measuring voltage. Given the tunneling current, it is simple to determine  $d\sigma_w/dt$  and  $dU_w/dt$ . These are given by

$$\frac{d\sigma_w}{dt} = \frac{-I_{tun}}{Ae} = -(E_{Fw} - E_{Fs})\frac{g_s}{\tau_{tun}} \quad (4.4)$$

and

$$\frac{dU_w}{dt} = \frac{-I_{tun}}{C_w} = \frac{-Ae}{C_w}(E_{Fw} - E_{Fs})\frac{g_s}{\tau_{tun}}. \quad (4.5)$$

Here,  $C_w$  is the capacitance in the sheet charge model, of the quantum well to the surroundings (substrate and top gate). It is given by

$$C_w = C_{geom} \frac{x_g}{x_g - x_w}, \quad (4.6)$$

where, as in chapter 3,  $x_w$  and  $x_g$  are the distances from the substrate charge to the charge in the quantum well and top gate respectively, and  $C_{geom}$  is the “geometric capacitance”,  $Ae/x_w$ , of the quantum well sheet charge to the substrate. See chapter 3 for a careful discussion of these terms.

Rewriting Eq. 4.1 again using Eqs. 4.2–5 and 4.6 gives

$$\frac{d(E_{Fw} - E_{Fs})}{dt} = -\frac{(E_{Fw} - E_{Fs})}{\tau_{tun}} \left[ \frac{Ae^2 g_s}{C_{geom}} \left(1 - \frac{x_w}{x_g}\right) - \eta g_s + \frac{g_s}{g_d} \right].$$



The solution of this first order differential equation is of course given by an exponential decrease of  $E_{Fw} - E_{Fs}$  with time. The relaxation rate is

$$\frac{1}{\tau_r} = \frac{1}{\tau_{tun}} \left[ \frac{Ae^2 g_s}{C_{geom}} \left( 1 - \frac{x_w}{x_g} \right) - \eta g_s + \frac{g_s}{g_d} \right]. \quad (4.7)$$

In our samples, the sum of the first two terms in the brackets is, in zero magnetic field, of order 10, whereas the third is unity or less. This means that the relaxation rates in our samples are typically faster than the tunneling rates.

This difference between the relaxation rate and the tunneling rate can be explained heuristically as follows. Consider one electron tunneling from or to the quantum well. This single electron, because of the electrostatic energy it carries with it, brings the electron gases in the well and substrate much closer to equilibrium than would an “uncharged electron” equilibrating the two regions simply by changing chemical potentials. This “speeds up” the equilibration of the two electron gases. At zero magnetic field in our samples, the average quantum level spacing in the 2d electron gas,  $1/Ae^2 g_s$ , is about 10% of the electrostatic energy for adding one charge to the well,  $e^2/C_w$ . However, if the single particle density of states becomes small enough, the relaxation rate simplifies to:

$$\frac{1}{\tau_r} = \frac{1}{\tau_{tun}} \left[ \frac{g_s}{g_d} \right].$$

In the case where the thermodynamic and single particle densities of states are equivalent, the relaxation time and the tunneling time are the same in this low DOS limit.

### *Fitting to Capacitance and Loss Tangent Curves*

Using the expressions above we can calculate the capacitance and the loss tangent for the device as a function of frequency. We start by calculating the

current through the device after (at time  $t = 0$ ) a voltage  $\delta V$  is suddenly applied across between the top gate and the substrate. Only the fraction of  $(x_w/x_g)\delta V$  of the applied voltage appears between the charge density in the well and substrate. Further, only the fraction  $(x_w/x_g)I_{tun}$  of the current which moves between the quantum well and the substrate should be counted in the device current because the current only traverses part-way through the device. The total device current is then

$$I_{dev}(t) = (\delta V)Ae^2 \frac{g_s}{\tau_{tun}} \left( \frac{x_w}{x_g} \right)^2 e^{-t/\tau_r} + (\delta V) \frac{C_{high}}{\tau_{fast}} e^{-t/\tau_{fast}}. \quad (4.8)$$

We define  $C_{high}$  (high frequency capacitance) as the capacitance of the device with no current traversing the tunnel barrier. In terms of device parameters, its value is  $A\epsilon/x_g$ .  $\tau_{fast}$  is the charging time of the capacitance  $C_{high}$  due to any resistance in series with our device. We consider  $\tau_{fast}$  to be much shorter than the period of the measuring signals in our experiment.

The A.C. admittance of the device is given by  $j\omega$  times the Fourier transform of this “step response”. In the limit where  $\tau_{fast}$  goes to zero, the A.C. current through the sample is

$$I = Ae^2 \frac{g_s}{\tau_{tun}} \left( \frac{x_w}{x_g} \right)^2 \frac{\omega^2 \tau_r^2 + j\omega \tau_r}{1 + \omega^2 \tau_r^2} V + j\omega C_{high} V, \quad (4.9)$$

where  $V$  is the amplitude of the measuring voltage  $Ve^{j\omega t}$ . The tunneling conductance is given by

$$G_{tun} = Ae^2 \frac{g_s}{\tau_{tun}}. \quad (4.10)$$

Rewriting Eq. 4.9 again, dividing by the voltage, we find that the device admittance is

$$Y(\omega) = G_{tun} \left( \frac{x_w}{x_g} \right)^2 \frac{\omega^2 \tau_r^2}{1 + \omega^2 \tau_r^2} + j\omega \left[ G_{tun} \left( \frac{x_w}{x_g} \right)^2 \frac{\tau_r}{1 + \omega^2 \tau_r^2} + C_{high} \right]. \quad (4.11)$$

The term in the brackets of this equation can immediately be identified as the device capacitance. At low frequencies, the device capacitance from Eq. 4.11 here reduces to the same form as given in chapter 3 (using  $g_d$  for  $g$  in the expression for  $C_{low}$ ). The loss tangent for the sample is given by the real part of the admittance divided by the imaginary part.

We can now write down the device capacitance and loss tangent as functions of frequency. From Eq. 4.11 for the sample admittance above and using the expression for  $C_{low}$  from chapter 3, we have for the capacitance

$$C(f) = \frac{C_{high}C_{low}[1 + (f/f_{peak})^2]}{C_{high} + C_{low}(f/f_{peak})^2}, \quad (4.12)$$

and for the loss tangent

$$D(f) = 2D_{peak} \frac{f/f_{peak}}{1 + (f/f_{peak})^2}. \quad (4.13)$$

Here, the loss tangent peak height  $D_{peak}$  is given by

$$D_{peak} = \sqrt{\frac{C_{high}}{C_{low}}} \left( \frac{C_{low}}{C_{high}} - 1 \right), \quad (4.14)$$

and the frequency at which the loss tangent goes through a peak  $f_{peak}$  is related to the tunneling conductance in the following fashion:

$$G_{tun} = 2\pi f_{peak} C_{geom} \frac{C_{geom}}{\sqrt{C_{low}C_{high}}} \left( \frac{C_{low}}{C_{high}} - 1 \right). \quad (4.15)$$

Note that to arrive at Eq. 4.15 we have made substantial use of the formulas relating  $g_d$  and  $\eta$  to  $C_{low}$ ,  $C_{high}$ , and  $C_{geom}$  developed in chapter 3. The value of  $C_{geom}$  used here is known to within 2% using the methods of the previous chapter. (Note, as discussed in detail the previous chapter, in the presence of low in-plane conductivity of the 2d electron gas, Eqs. 4.12 and 4.13 must be modified somewhat in order to properly fit the data.) The fits given by Eqs. 4.12

and 4.13 are identical to the functional forms for the capacitance and the loss tangent indicated by the circuit model of Fig. 4.1b, but the interpretation of the fitting parameters is different.

The present chapter concerns itself with the value of  $G_{tun}$  as determined from fits to the capacitance and loss tangent.  $G_{tun}$  is proportional to the single particle DOS  $g_s$ , whereas the focus of the previous chapter was on the thermodynamic DOS.

#### 4.4 Sample Characterization

The widths of thermodynamic DOS peaks attributed to Landau levels in each of the samples studied here were discussed in chapter 3. Elastic scattering times in the well can be estimated in the three wafers from the widths of the DOS peaks of Landau levels in a magnetic field.<sup>12</sup> According to the theory of Ando and Uemura<sup>13</sup> the half-widths of Landau level DOS peaks are related to the elastic scattering time by the relation

$$\Gamma = \hbar \left( \frac{2}{\pi} \frac{\omega_c}{\tau_s} \right)^{1/2}.$$

Here  $\omega_c$  is the cyclotron frequency and  $\tau_s$  is the elastic scattering time. In chapter 3, we showed that widths of Landau level DOS peaks were nearly independent of magnetic field, in disagreement with this relation. Because the Landau levels in chapter 3 fit well to Lorentzian lineshapes, we can estimate elastic scattering times, and hence sample mobilities from the relation for Lorentzian lineshapes,

$$\tau_s = \frac{\hbar}{\Gamma}.$$

$\Gamma$  is the half-width of the Lorentzian lineshape. Using this formula, wafer **A** would have a nominal 2.0 K mobility in the well of approximately

21,000  $\text{cm}^2\text{V}^{-1}\text{sec}^{-1}$  as defined by this single-particle scattering time; wafer **B** would have a mobility of 25,000  $\text{cm}^2\text{V}^{-1}\text{sec}^{-1}$ ; and sample **C** would have a mobility of 15,000  $\text{cm}^2\text{V}^{-1}\text{sec}^{-1}$ . Actual transport mobilities are expected to be substantially higher.<sup>14</sup> The magnetic field suppression effect discussed here has been observed in all three samples. More data have been taken on wafer **A**, both with and without magnetic field, than on either samples **B** or **C**. We will concentrate mostly on the results from sample **A**; over 200,000 capacitance measurements were taken on one  $400\mu\text{m}$  diameter mesa produced on this wafer.

#### 4.5 Tunneling in the Presence of Magnetic Field

Figure 4.3 displays the logarithm of the tunneling conductance of sample **A** at 4 T for different temperatures. The highest temperature curves oscillate about the zero field curve,<sup>4</sup> indicating the development of Landau level structure in the DOS in the 2d gas. At lower temperatures, the tunneling conductance is strongly suppressed. In contrast with this behavior in magnetic field, the zero field tunneling conductance shows no substantial variation with temperature over the range 90 mK to 10 K except for electron densities near full depletion ( $< 1 \times 10^{11} \text{ cm}^{-2}$ ). The temperature dependent suppression occurs only in the presence of the magnetic field applied perpendicular to the plane of the 2d electron gas; a magnetic field applied parallel to the plane<sup>5</sup> does not induce a temperature dependent suppression. We note that the doping levels in the substrate are high enough ( $10^{17} \text{ cm}^{-3}$ ) to discount magnetic freezeout<sup>15</sup> as the cause of the effect. Finally, the thermodynamic DOS in the well,<sup>10</sup> as determined from the capacitance values distinct from conductance results, shows no unexpected behavior reflecting the tunneling suppression.

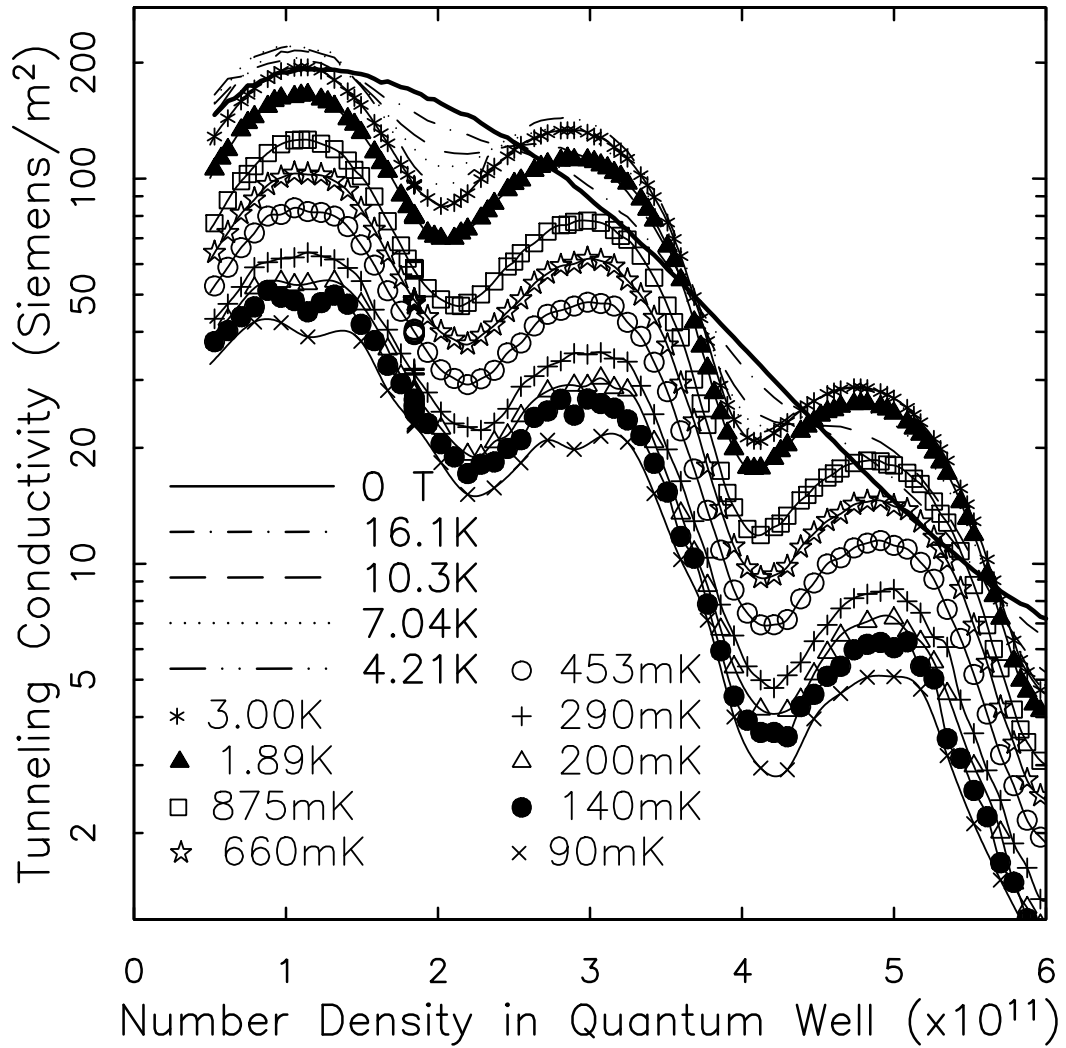


**Fig. 4.3** Tunneling conductivity in sample **A** (log scale) vs. electron number density in the quantum well for zero field (bold solid curve) and for a variety of temperatures with 4.0 T magnetic field applied perpendicular to the plane of the electron gas in the quantum well. The smooth curves joining the points are guides to the eye.

The temperature dependence suggests that the suppression is due to a tunneling anomaly restricted to energies near the Fermi energy. To explore this idea, a high frequency signal (period shorter than the  $RC$  relaxation time of the tunnel barrier) was injected across the sample during capacitance measurements. This signal provides an oscillating Fermi level offset between the 2d gas and the substrate allowing tunneling to occur from a band of states of width given by double the amplitude of the injected signal. We find that as the excitation voltage that appears across the barrier due to the injected signal is made larger than  $k_B T/e$ , the suppression effects induced by the low temperature of the sample recede. At very low temperatures, where the suppression appears to be saturated, the effect of excitation, of rms amplitude  $V_e$ , on conductance is roughly the same as increasing the temperature in absence of excitation to a value  $eV_e/k_B$ . This implies that the suppression would be observed in a conventional  $I$ - $V$  characteristic as a zero bias anomaly, not as a general bias independent suppression.

The data shown in Fig. 4.3 are striking in that the suppression is nearly independent of the Landau level filling number in the well. Also, at low temperatures, where the contrast associated with the Landau levels has developed, the suppression has roughly the same strength when the Fermi level is between Landau levels as when it is at a Landau maximum.

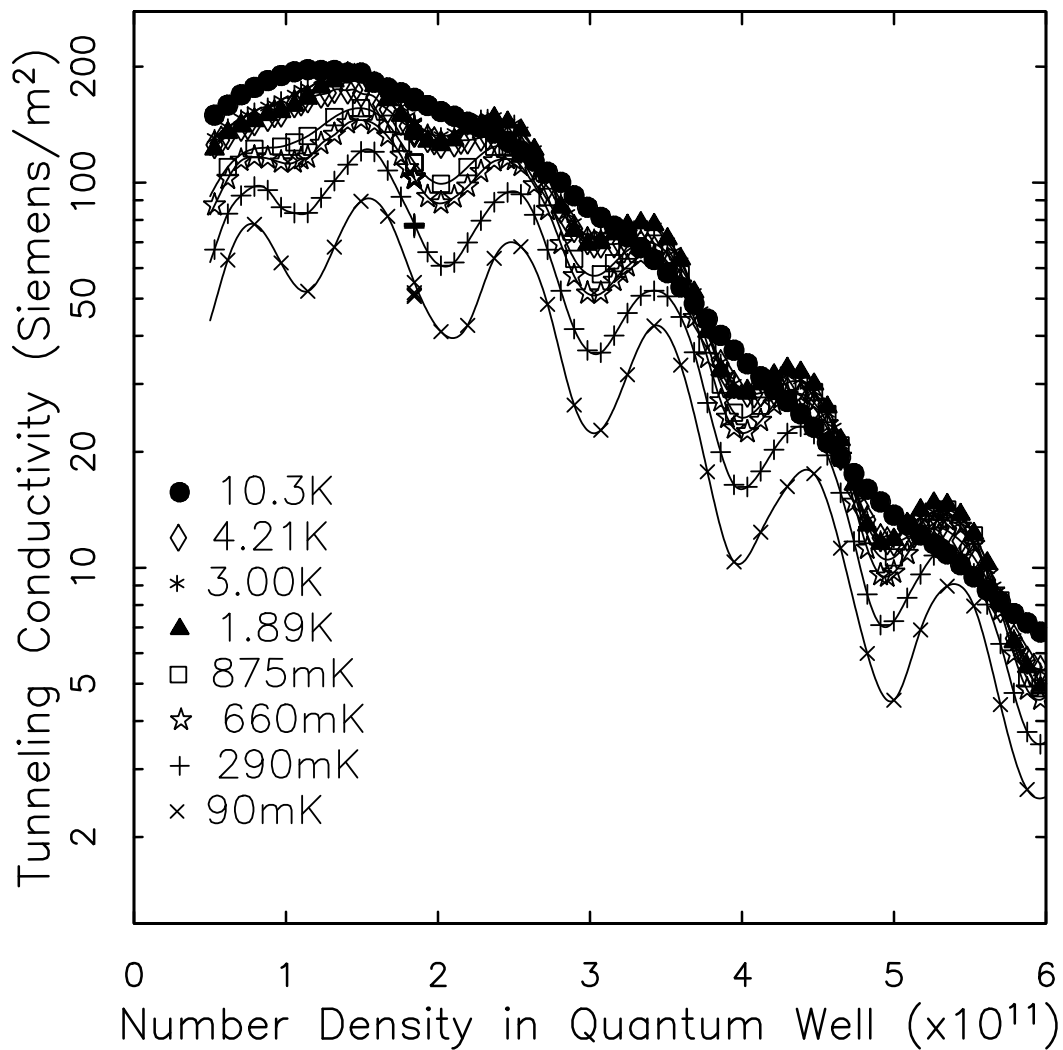
In Fig. 4.3, tunneling at densities higher than  $3.9 \times 10^{11} \text{ cm}^{-2}$  should be forbidden in the absence of scattering. At these densities, the Fermi level is in the third Landau level in the well, whereas in the substrate the third Landau level lies outside of the Fermi surface. Indeed, the tunneling conductance is markedly lower in this range of density. Interestingly, the strength of suppression due to the magnetic field is approximately the same in the forbidden region as it is in

the range of densities for which tunneling is allowed. This observation suggests that the suppression is not some consequence of the change in spatial character of the one electron wave functions associated with the development of Landau states.

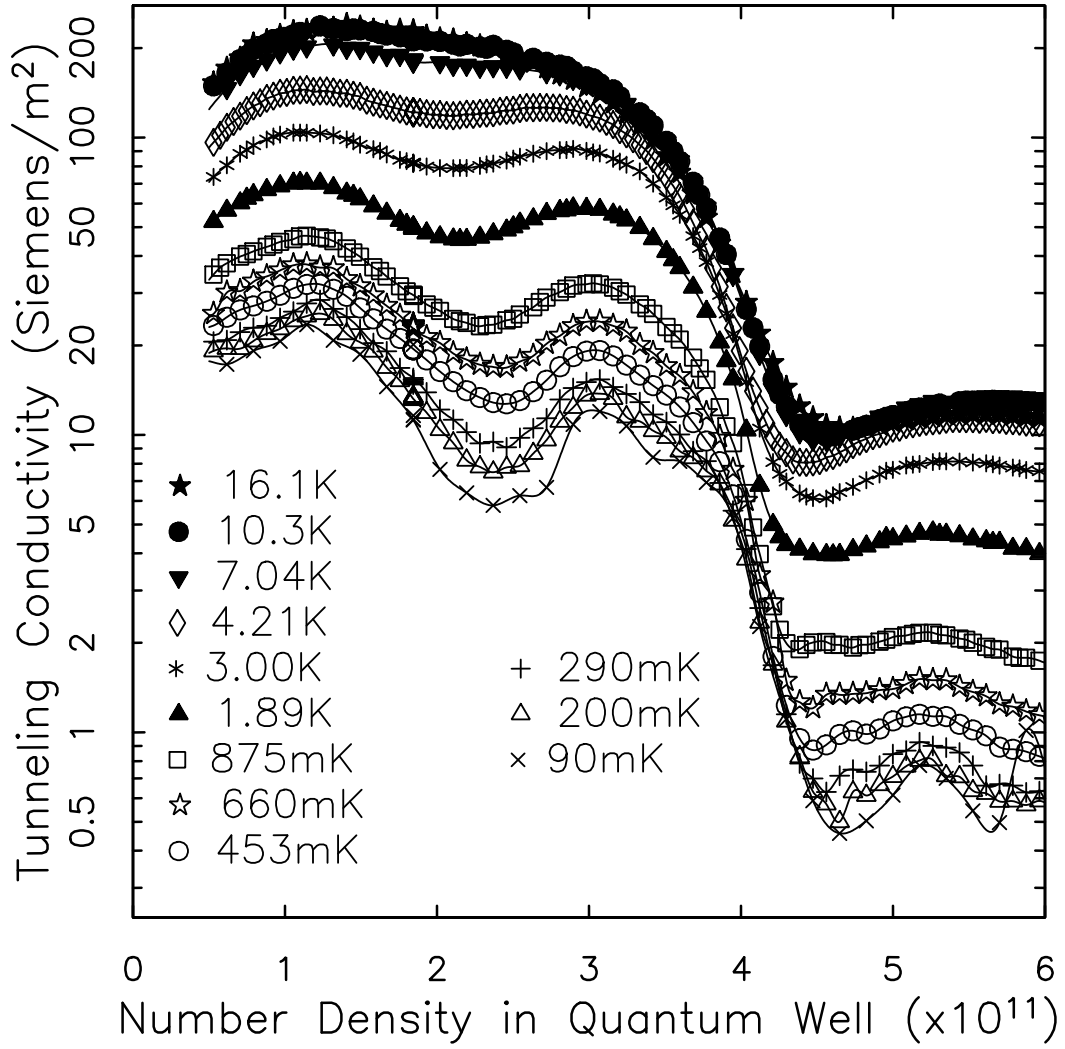
For completeness here, we show tunneling conductivity vs. number density curves in the same sample for different magnetic field strengths. Figure 4.4 displays the tunneling conductivity at various temperatures for a 2.0 T applied magnetic field. The tunneling suppression here appears to be weaker and sets in at lower temperatures than for the data in Fig. 4.3. Just the opposite is true of the data taken at 8.5 T shown in Fig. 4.5. Strong suppression commences at higher temperatures than for the data of Fig. 4.3. In Fig. 4.5, the first two peaks that appear in the tunneling conductivity correspond to the spin split bands of the lowest Landau level. At 8.5 T, the second Landau level in the substrate is outside of the Fermi surface, and tunneling at electron densities above  $4.1 \times 10^{11} \text{ cm}^{-2}$  should be forbidden. Once again, despite the sharp decrease in the tunneling conductance as the electron density is increased into this forbidden region, the temperature dependent tunneling suppression still persists in this region.

Figure 4.6 displays the tunneling conductivity of sample **B** at 4 T and at 1.9 and 4.2 K. The same suppression effect occurs in this sample as in sample **A**. Notice that while there is, as with sample **A** at these temperatures, some increased definition of the Landau level as the temperature is decreased, the suppression strength is again roughly independent of the 2d electron gas density. As with the data of sample **A**, on average the 1.9 K conductance data is again about 20-30% less than the conductance at 4.2 K. We have data in sample **C** only at temperatures of 4 K and near 6 K. The suppression effect is observed in this





**Fig. 4.4** Tunneling conductivity in sample **A** vs. electron number density in the quantum well at 2 T magnetic field applied perpendicular to the plane of the electron gas in the quantum well. The oscillations here correspond to Landau levels, the first peak shown being the lowest level. Note that the oscillations here continue to develop increased contrast as the temperature is lowered below 1 K, even though the thermodynamic DOS is nearly fully developed at 1 K.



**Fig. 4.5** Tunneling conductivity in sample **A** vs. electron number density in the quantum well at 8.5 T magnetic field applied perpendicular to the plane of the electron gas in the quantum well. The first two peaks shown as the density is increased are the spin split levels of the lowest Landau level. Note that the vertical scale is different here than in Figs. 4.3 and 4.4.

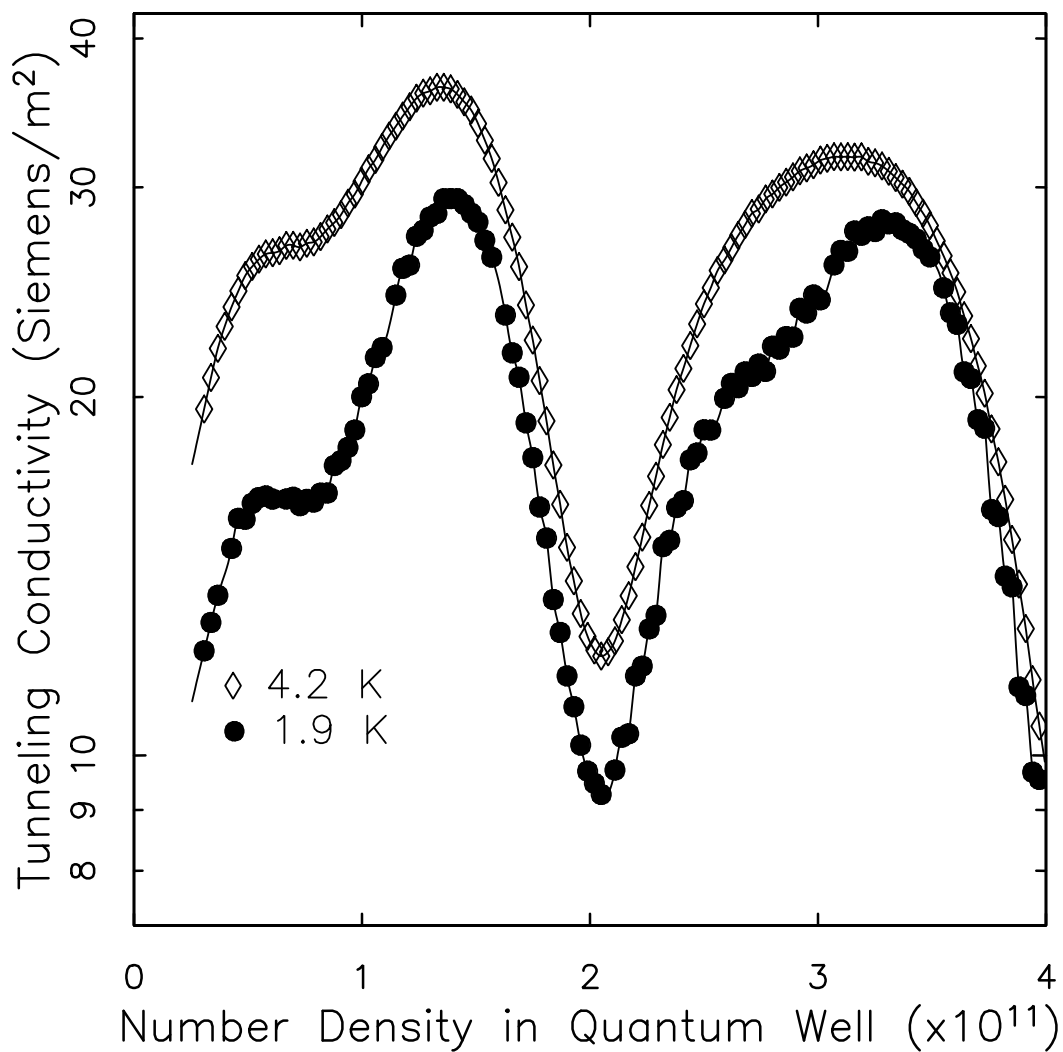


**Fig. 4.6** Tunneling conductivity vs. number density in sample **B** at a magnetic field of 4.0 T. The suppression effect is clearly visible in this sample. Also apparent is the spin splitting of the Landau levels which becomes increasingly prominent as the temperature is reduced.

sample as well although it is somewhat less transparent because, as with sample **A** in this temperature range at this magnetic field strength, the strength of the suppression is small and there is at the same time considerable temperature dependence of the Landau level widths.

#### 4.6 Average Conductance

In this section, to summarize the data from sample **A** for different fields, we perform an average of the conductance data over a range of well fillings (over a half integral or integral number of Landau levels) for each value of the magnetic field and for each temperature measured. The averaging is needed to isolate changes in the tunneling conductance arising from the tunneling suppression from changes in the conductance due to varying detail in the Landau level structure, such as the increased contrast of levels as the temperature is reduced or spin splittings which are resolved only at low temperature. We then relate this average conductance to the single particle DOS in the well.

There is a subtlety involved in determining the average value of the tunneling conductance. When  $k_B T$  is of order the Landau level width, the Landau level structure changes markedly. The average of the conductance must be taken with respect to the Fermi energy in the well, not with respect to well density, to assure that changes in contrast of the Landau level structure do not contribute to an apparent but unreal change in the average value of the tunneling conductance. The following paragraphs formalize these statements.

Considering the tunneling rate  $1/\tau_{tun}$  to be a constant over an energy of order  $k_B T$ , basic tunneling theory<sup>11</sup> implies that  $g_s$  in Eq. 4.10 should be replaced by a thermal average so that the tunneling conductivity,  $G(T; B; E_F)$ ,

becomes

$$G(T; B; E_F) = -\frac{e^2}{\tau_{tun}(E_F)} \int_0^\infty g_s(E; B) \frac{\partial f(E; T)}{\partial E} dE, \quad (4.16)$$

where  $f(E; T)$  is the Fermi distribution function,  $E$  is the kinetic energy of electrons in the 2d electron gas, and  $E_F$  is the Fermi energy in the well measured with respect to the bound state energy in the well,  $U_{bound}$ .

We describe here why in Eq. 4.16  $\tau_{tun}$  is taken to be a function only of the Fermi energy in the well and not of the magnetic field strength. First we discuss the situation in zero field.  $\tau_{tun}$  depends on the tunneling matrix element coupling states in the well to those in the substrate as well as the density of states in the substrate. These two elements depend on the “longitudinal momentum”  $\hbar k_z$ , the momentum of electrons in the substrate perpendicular to the plane of electrons in the quantum well, but not on the “transverse momentum”. Because transverse momentum conservation specifies the transverse wavenumbers,  $k_x, k_y$ , of an electron in the substrate which has tunneled from the quantum well, the appropriate substrate DOS to use in the tunneling calculation is the one dimensional DOS<sup>4</sup> which depends only on the value of  $k_z$ . Recalling again that  $U_{bound}$  is the energy of the bound state in the well with respect to the conduction band edge deep within the substrate, transverse momentum conservation, along with the approximation of equal effective masses in the 2d and 3d electron gases, dictates that

$$k_z = \sqrt{\frac{2m^*U_{bound}}{\hbar^2}}, \quad (4.17)$$

where  $m^*$  is the electron effective mass. Because the Fermi energy in the well is fixed, equal to that in the substrate, specifying  $E_F$ , the energy difference between the Fermi energy and  $U_{bound}$ , also specifies  $U_{bound}$ . For these reasons, we can write  $\tau_{tun}(k_z) = \tau_{tun}(k_z(E_F))$ .

In the case of magnetic field applied perpendicular to the plane of the 2d electron gas, the magnetic field is pointed along the direction tunneling and hence is not expected to alter matrix elements for tunneling in this direction. Also, the Schrödinger equation is still separable into terms involving  $k_z$  and quantum numbers involving degrees of freedom perpendicular to the field direction. These quantum numbers are again conserved and Eq. 4.17 still holds.  $\tau_{tun}(E_F)$  is thus independent of magnetic field strength.

In the absence of a magnetic field,  $g_s(E)$  is constant in energy, and Eq. 4.16 takes the form:

$$G_{B=0}(T; E_F) = \frac{e^2}{\tau_{tun}(E_F)} g_0$$

where  $g_0$  is the (single-particle) zero field DOS. In this model, the ratio of the tunneling conductance in magnetic field to the tunneling conductance in the absence of field, for the same values of the Fermi energy in the well, is equal to the ratio of the thermally averaged DOS in magnetic field to  $g_0$ .

In a picture where the electrons are noninteracting free particles, the ratio of these densities of states, averaged over a Landau level is, of course, equal to one. The fact that in some of our low temperature measurements the tunneling conductance falls everywhere below the zero field conductance (such as for the lowest temperature data plotted in Figs. 4.3, 4.4 and 4.5) suggests that the single particle DOS is lower, at energies near the Fermi energy, in magnetic field than in the absence of magnetic field. As discussed below, the temperature dependence of the tunneling suppression suggests that the single particle DOS is only decreased for energies near the Fermi energy.

The capacitance data provide sufficient information to allow a conversion from filling to energy, yielding the conductance as a function of Fermi energy in the well.<sup>10</sup> For all but the 8.5 T data, the average of the conductance divided by

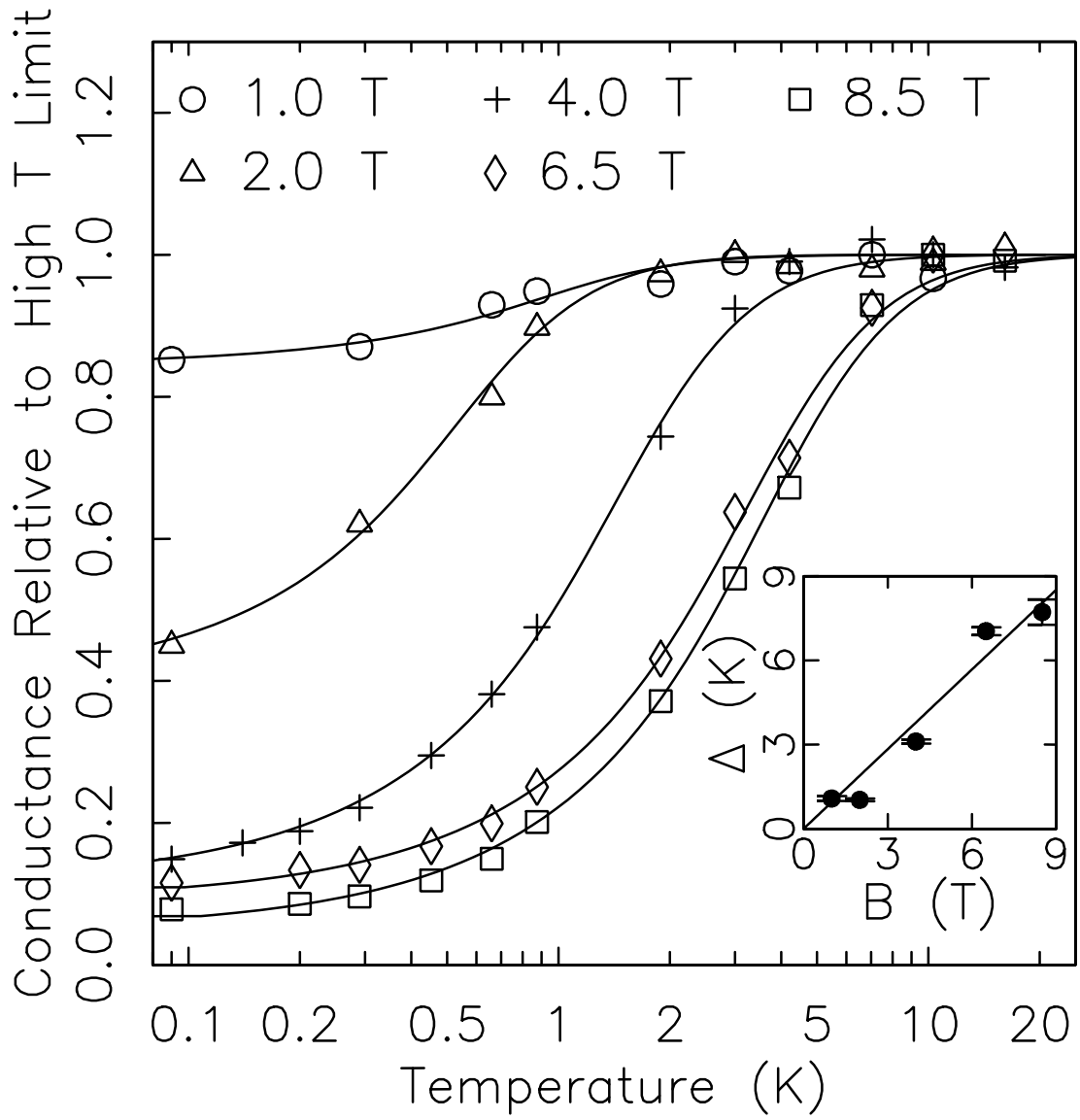


**Fig. 4.7** Plotted as symbols are the averaged conductances relative to the high temperature limit of the conductance plotted against temperature (log scale). The smooth curves are fits described the text. Shown in the inset is  $\Delta$  in Kelvins plotted against the applied magnetic field. The line is given by  $\Delta = 0.047\hbar\omega_c/k_B$ .

the zero field conductance at the same value of the Fermi energy (and hence the same value of  $U_{bound}$ ),  $\Lambda(T; B)$ , at high temperatures approaches a value of one which is taken to be the high temperature limit. In Fig. 4.7 the ratio  $\Lambda(T; B)$  compared to its high temperature limiting value is plotted as a function of temperature. Ambiguities of interpretation of the 8.5 T data at high temperature imply a 10% uncertainty in the normalization of the 8.5 T data.

We hypothesize that the tunneling suppression is a consequence of a gap in the single particle DOS  $g_s(E)$ , centered at  $E_F$ . In this case, the appropriate form for  $\Lambda(T; B)$  would be

$$\Lambda(T; B) = - \int_0^{\infty} \frac{g_s(E; B)}{g_0} \frac{\partial f(E; T)}{\partial E} dE. \quad (4.18)$$

For reasons described below, we fit with the following gap:

$$\begin{aligned} g_s(E) &= Sg_0 + \frac{(1-S)g_0|E - E_f|}{\Delta} & (E \leq 2\Delta) \\ g_s(E) &= g_0 & (E > 2\Delta). \end{aligned} \quad (4.19)$$

The fits shown in Fig. 4.7 are the result using this “linear” gap.

We call attention to a few principal features of the summary data in Fig. 4.7 and of the fits. (a) For low fields, 1 T and 2 T, the width parameter  $\Delta$  depends little on B, but the depth of the gap  $(1 - S)$  increases with increasing field. (b) For high fields, 6.5 T and 8.5 T, the gap is nearly fully developed in depth and the width is increasing with field, with some indication of saturation at high fields. (c) The data consistently show more temperature dependence in the low temperature limit than do models in which the gap is nonsingular at the Fermi energy, e.g. square or smooth bottomed gap functions. The linear singularity is not unique in giving good fits to the data; a variety (e.g. a gap where  $g \propto \sqrt{|E - E_F|}$ ) of other singular behaviors will do as well. (d) At fields 2 T and higher, the gap width  $\Delta$  has a value of about 5% of the cyclotron energy,



$\hbar\omega_c$ . (e) The errors generated in the averaging procedure at high temperatures (where the Landau level structure washes out) by the Landau level shape changes leave the results ambiguous as to whether or not there is temperature dependence of the gap in this temperature regime.

We interpret the results in terms of a gap, rather than of an influence of the field on the single particle tunneling dynamics, because the temperature and excitation dependences indicate that the tunneling is suppressed only for states near the Fermi energy. Before discussing possible candidates for such a gap, or other proposals, we turn first to another tunneling suppression that we have observed.

#### **4.7 Low Density Tunneling Suppression in the Absence of Magnetic Field**

As noted above, in the case of zero magnetic field or magnetic field parallel to the plane of the 2d electron gas, no temperature dependent tunneling suppression is observed for most of the range of densities of the 2d electron gas. Temperature dependence, other than that associated with thermal broadening, is, however, observed at densities below  $\approx 1 \times 10^{11} \text{ cm}^{-2}$ . Fig. 4.8 displays the tunneling conductance (obtained in a model described in the next section) in sample **A** as a function of device gate bias for sample temperatures ranging from 95 mK to 16 K. The shape of this curve at densities above  $1.2 \times 10^{11} \text{ cm}^{-2}$  has been explained previously in terms of momentum conservation rules in tunneling.<sup>4,7</sup> For gate voltages above about -800 mV (about  $1 \times 10^{11} \text{ cm}^{-2}$  mean well density as determined from magnetic field measurements), low frequency capacitance measurements indicate that the quantum well area is fully occupied. At voltages below -800 mV a significant temperature dependence of

the conductance appears. As in the case of perpendicular applied magnetic field, the tunneling conductance is suppressed as the temperature is decreased. A suppression at low densities has been observed as well in samples **B** and **C**. The technique used to plot the tunneling conductance here differs at low densities from that used in previous figures. The next few paragraphs describe the differences as well as why a different method is needed in the low density limit.

### *Capacitance vs. Frequency Curve Fitting in the Low Density Regime*

Equation 4.15 above yielded the tunneling conductance of samples in terms of the loss peak frequency and the low and high frequency capacitances of the device. This relation, as well as the framework used in developing it, breaks down at low electron densities in the well if there are portions of the well unoccupied by electrons. Experimentally, a decrease in the low frequency capacitance of the device is observed as the gate bias is lowered in the low density region. We explore here reasons for this decrease and develop interpretations of the capacitance and loss data in the low density regime.

We proceed to model the sample with low densities in the well using the the assumption that occupied and unoccupied regions of the sample are larger than a few hundred angstroms in size so that fringing fields can be neglected. Because there are unoccupied regions of the well, a capacitance shunting the top gate to the substrate must be added to the circuit model of Fig. 4.1a. The shunting capacitance in the model has a value of  $C_{high}(1 - \alpha)$  where  $\alpha$  is the fractional area of the 2d electron gas which is occupied by electrons. This sample model is shown in Fig. 4.9. The division the device this way into two regions,

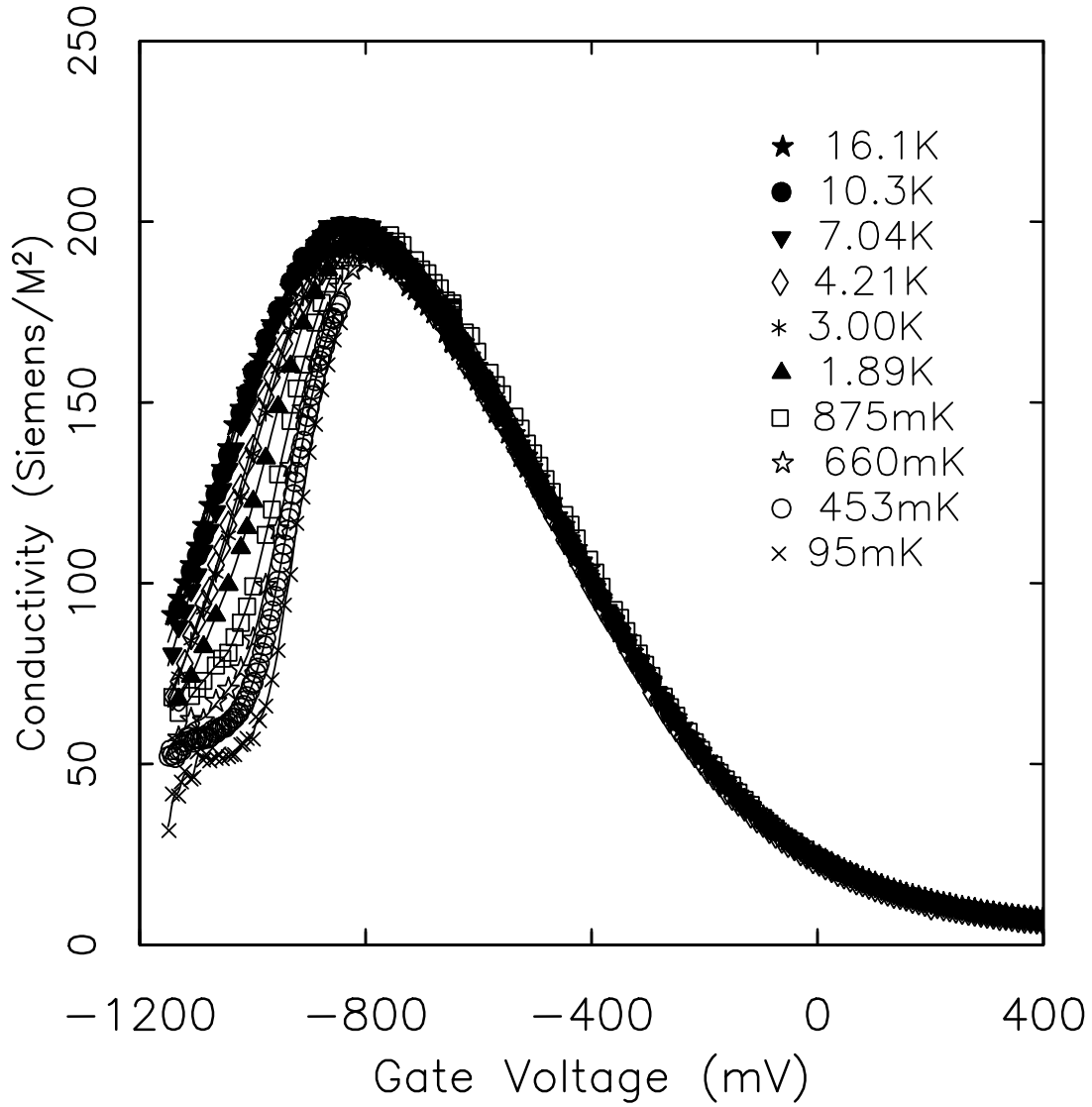


**Fig. 4.8** Tunneling conductivities (linear scale) in zero magnetic field vs. gate voltage in sample **A** at temperatures ranging from 95 mK to 16.1 K. Note that at a gate voltage of -800 mV, the electron density is about  $1 \times 10^{11} \text{ cm}^{-2}$  and rises linearly with gate voltage to a value of around  $6 \times 10^{11} \text{ cm}^{-2}$  at a gate bias of 400 mV. Below -800 mV gate bias, the quantum well begins to depopulate nonuniformly, leaving unoccupied regions of the well. In this region, the electron density is no longer linear in gate bias, and the rate of electron density change with gate bias is decreased. The conductance is obtained from the capacitance data using the “puddling” model described in the text.

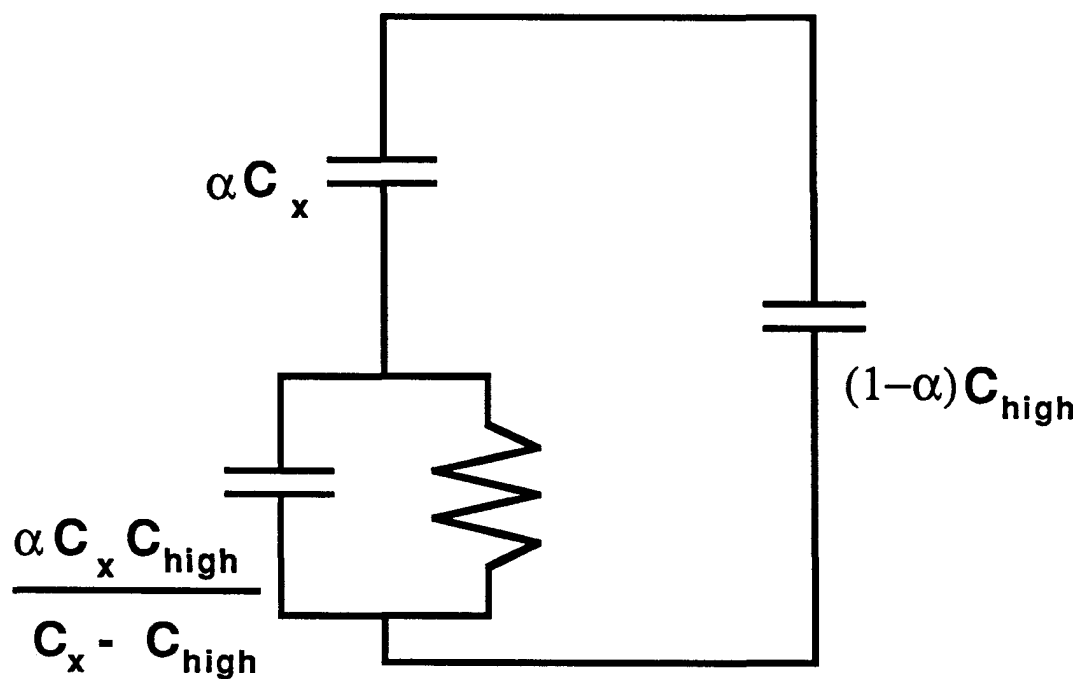


**Fig. 4.9** This figure displays the circuit model used to fit capacitance vs. frequency curves taken in the low density region of the device operation. The capacitance on the right,  $(1 - \alpha)C_{high}$  is the capacitance measured from unoccupied regions of the quantum well. The two capacitor model on the left corresponds to the regions in the quantum well which are occupied by electrons.

one depleted and the other filled with electrons, gives the form

$$C(f) = \frac{\alpha C_{high} C_x [1 + (f/f_{peak})^2]}{C_{high} + C_x (f/f_{peak})^2} + (1 - \alpha) C_{high} \quad (4.20)$$

for fits to capacitance vs. frequency curves. The parameter  $C_x$  is the capacitance that *would* be measured at low frequencies if the well had no unoccupied regions. The measured low frequency capacitance,  $C_{low}$ , is given by

$$C_{low} = \alpha C_x + (1 - \alpha) C_{high}.$$

At this point, fits can be made to the capacitance data using  $C_{low}$ ,  $C_{high}$ ,  $\alpha$ , and  $f_{peak}$  as fitting parameters.

We have made such fits and found that there is a large error in the deduced values of  $\alpha$  and  $C_x$  (obtained from  $\alpha$  and other fitting parameters). This occurs because, in the fitting,  $\alpha$  is sensitive to subtle changes in the shape of the capacitance vs. frequency curves, such as broadening of the of the type discussed in chapter 3, and to small random errors.

In order to obtain reasonable fits, we use Eq. 4.20 and fix the value of  $C_x$ . Equation 4.20 can be written in terms of the ratio  $C_x/C_{high}$ ,  $C_{high}$ ,  $f_{peak}$ , and  $\alpha$ . We get results which fit the capacitance data well by setting the ratio  $C_x/C_{high}$  to the value of  $C_{low}/C_{high}$  when the well is fully occupied and using  $C_{high}$ ,  $f_{peak}$ , and  $\alpha$  as the fitting parameters. The value of  $C_{low}/C_{high}$ , in the case where the density in the well is high enough so that it is undoubtedly occupied everywhere (where  $C_{low}$  ceases to be a strong function of gate bias in zero magnetic field), depends, except for slight changes due to variation in  $\eta$  and  $C_{geom}$  with gate bias discussed in chapter 3, only on the thermodynamic density of states in the well.<sup>10</sup> Setting  $C_x/C_{high}$  equal to the value of  $C_{low}/C_{high}$  when the well is full and letting  $\alpha$  vary in the fits defines a model which we call the “puddling model”.

In the puddling model, there are filled and unfilled regions of the well; in the filled regions, the thermodynamic DOS is equal the constant 2d DOS given by  $m^*/\pi\hbar^2$ . This contrasts with the “filled well” model, which considers electrons to inhabit every portion of the well and accounts for the decrease observed in the low frequency capacitance at low gate biases through a gradual decrease in the thermodynamic DOS as electrons are removed from the well. We proceed with the puddling model discussing our reasons for using it instead of the filled well model below. Models similar to this puddling model are used in chapters 5 and 6 to understand quantum dots.

The tunneling conductance is easily evaluated in the puddling model. Its value is given by:

$$G_{tun} = 2\pi f_{peak} \alpha C_{geom} \frac{C_{geom}}{\sqrt{C_x C_{high}}} \left( \frac{C_x}{C_{high}} - 1 \right). \quad (4.21)$$

Of course, what is interesting physically is not the total conductance, but the conductivity per unit filled area, which is this formula divided by the quantity  $\alpha A$ , where  $A$  again is the area of the mesa.

We note that the puddling model considers all of the decrease in  $C_{low}$ , as the electron density is lowered, to arise from depleted area. It neglects DOS anomalies that can arise from a nonuniform potential in the well; i.e. the potential in the well is not a constant everywhere which can lead to the DOS being something other than a constant as it is in 2d. The results shown in Fig. 4.8 were determined using the puddling model; the “filled well” model also displays a temperature dependent tunneling conductivity. Using the filled well model (forcing  $\alpha$  to be equal to one and allowing  $C_x$  to vary, in which case  $C_x \equiv C_{low}$  and the model becomes identical to that used at high densities) leads to different conductance vs. gate bias curves in which the tunneling conductivity falls off very rapidly at low densities, much faster (for all temperatures) than

does the device capacitance at low densities. This is implausible in a framework where the tunneling conductivity depends only on the DOS in the well but, as interaction effects may influence the tunneling, this does not necessarily rule out the filled well model as applicable to the device. The results from attempts at fitting capacitance vs. frequency curves with both  $\alpha$  and  $C_{low}$  as free parameters, while ambiguous, favor the puddling model interpretation. Finally, theoretical models<sup>16</sup> typically describe the 2d electron gas in heterostructures at densities near full depletion in terms of filled and unfilled regions.

The low frequency capacitance may decrease at low gate biases due both to regions of the well becoming unoccupied and the occupied regions having a decreased DOS; the puddling model and the filled well model are two limiting interpretations. The rest of this section and later sections use the puddling model to describe the sample with the caveat that the real behavior of the system lies between the two limits.

Finally, one salient feature of the puddling model is the simplicity in determining the tunneling conductivity. Because  $C_{high}$  and  $C_{geom}$  change very little over the range of gate biases for the device, and  $C_x/C_{high}$  is fixed to its value at high densities, Eq. 4.21 gives that the tunneling conductance is simply proportional to the loss peak frequency.

#### *Detailed Observation of Low Density Tunneling Conductance*

We use the puddling model framework to plot in Fig. 4.10,  $\alpha$ , the fraction of the area of the quantum well which is occupied as a function of gate bias. The curve was obtained from data taken in zero magnetic field and at at 1.85 K. We have fitted curves of capacitance vs. frequency from a variety of temperatures from 95 mK to 16 K and see little change in this curve. Within the resolution

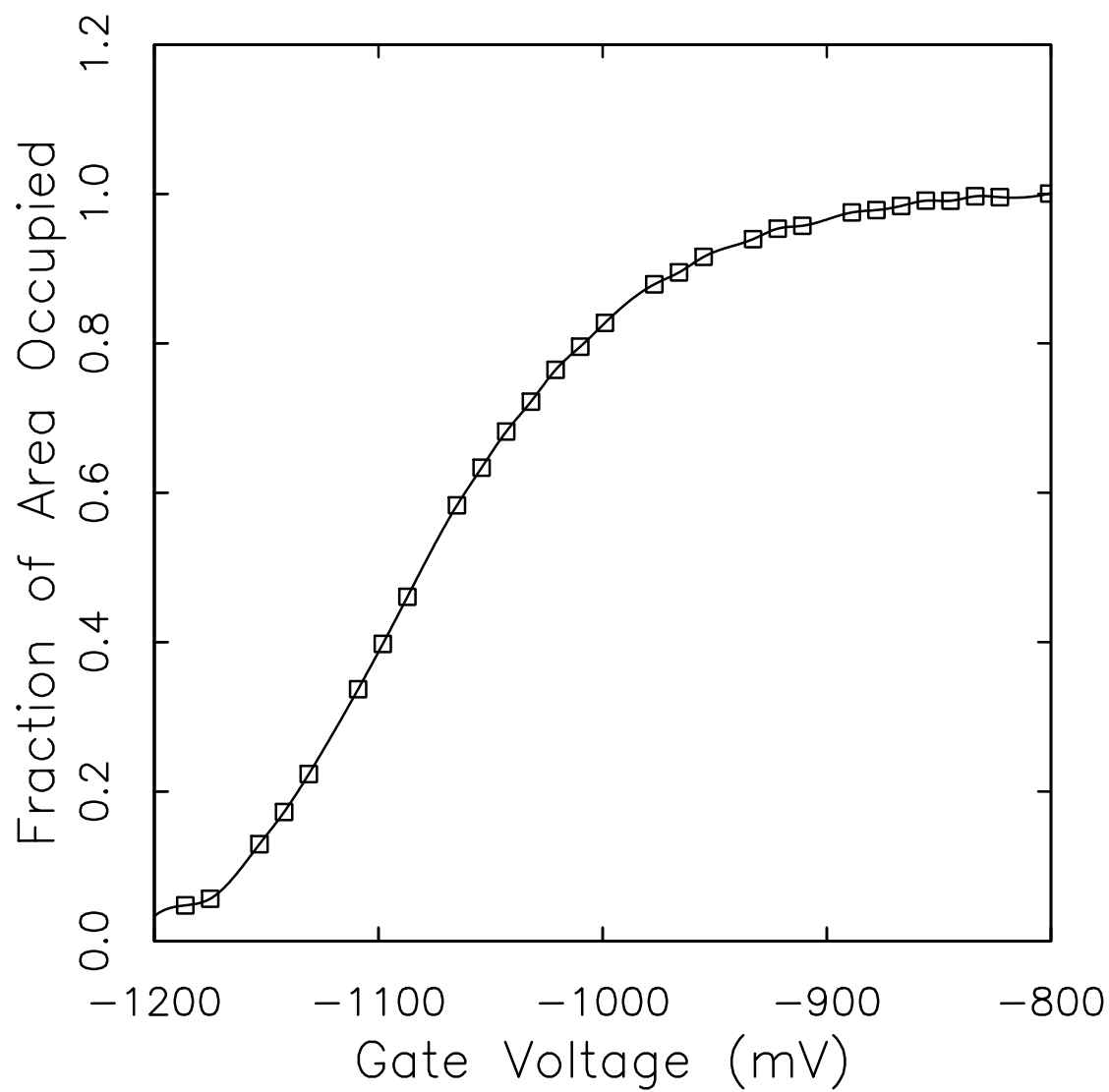


**Fig. 4.10** Displayed is the fractional areal occupation of the quantum well,  $\alpha$ , as determined from capacitance vs. frequency curves fitted by Eq. 4.20 and the model of Fig. 4.9. The solid curve is a guide to the eye.



of these results, we observe no thermal smearing of this curve occurs up to the highest temperatures. In the following discussion we treat the occupied area and electron density as fixed at a particular gate bias, independent of sample temperature.

Figure 4.11 “zooms in” on the tunneling conductivity, determined in the puddling model, in low density region of sample **A** as a function of gate bias for temperatures from 95 mK to 16 K. The temperature dependence is immediately striking. For the whole region of gate biases plotted, above around 7 K the conductivity saturates to a high temperature limiting value; below about 500 mK the tunneling conductance saturates to a low temperature value. For the entire curve, most of the shift of the conductance with temperature happens between 1 K and 3 K. The other surprising feature in Fig. 4.11 is the plateau which develops in the conductivity at low temperatures. This reason for this plateau, as well as the rest of the shape of the tunneling conductivity plot as a function gate bias, is not understood presently.

#### *Low Density Conductivity as a Function of Temperature*

At this point, we note the striking similarity of the temperature dependence of the tunneling conductivity at low densities to the tunneling suppression induced by a magnetic field illustrated in Fig. 4.7. In the case of the low density data, we simply take the conductivity at a particular value of gate bias and plot it as a function of temperature. Figure 4.12 displays the conductivity relative to its high temperature value plotted as a function of temperature for a gate bias fixed at -1050 mV. The resemblance the shape of this curve to the curves of Fig. 4.7 is readily apparent. The solid line is a fit to the data obtained using Eq. 4.18 and Eq. 4.19, the *same* gap used to fit the magnetic field data. In

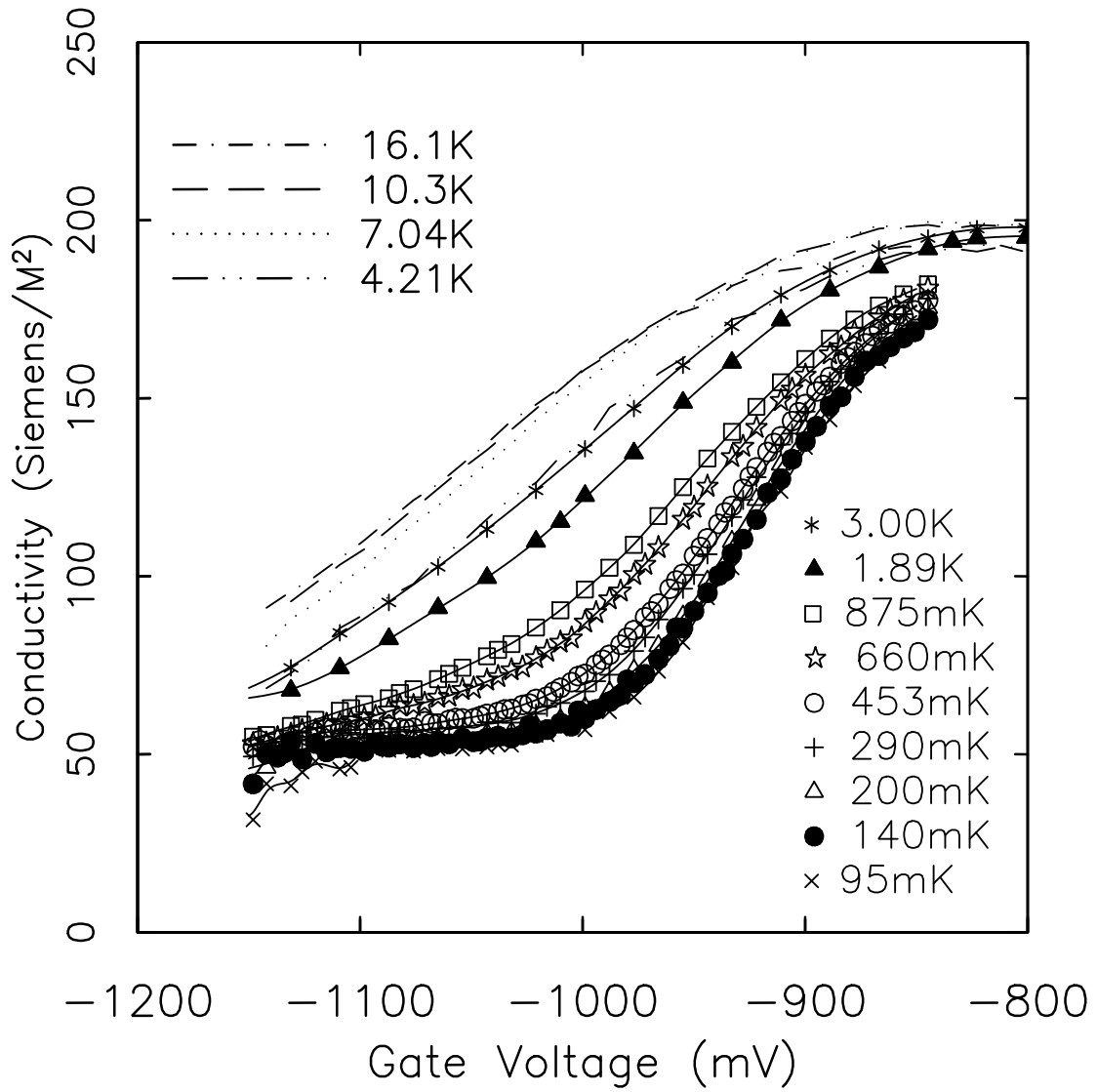


**Fig. 4.11** The figure displays in detail the tunneling conductivity (conductance per unit occupied area) determined using Eqs. 4.20 and 4.21 for a variety of temperatures between 95 mK and 16.1 K. Two features of the plot stand out. Firstly, there appear to be low and high temperature limiting values to the conductivity. The transition between these two values always occurs at between 0.5 and 3 K, independent of gate bias. Secondly, an unexplained plateau develops at low temperatures in the conductivity at biases below -1050 mV.

Fig. 4.12,  $\Delta$  has a value of about 4.7 K, and the gap depth parameter  $S$  has a value of 0.4. By adjusting the values of  $\Delta$  (which undergoes only slight variations with gate bias in the low density regime) and  $S$  the gap model of Eq. 4.19 can be made to fit the data well for any gate bias in the low density region. We will return below to this similarity in the temperature dependences of the two suppression effects.

#### 4.8 Low Density Region with Magnetic Field Applied

Now that we have examined in detail both the suppression of tunneling by magnetic field at high densities and the suppression at low densities in zero magnetic field, it is interesting to ask: what happens at low density in the presence of a magnetic field? We again use the puddling model of the last section to fit the capacitance data and extract the tunneling conductivity.

Before proceeding, we note that at high fields ( $>6.5$  T) curves of the occupied area obtained using the puddling model in the well vs. gate bias are slightly shifted towards positive values of gate bias compared to the results from zero field shown in Fig. 4.10 above. This is largely due to effects of the zero point energy in the well. At lower fields (4 T and below), these effects are not visible on the scale of Fig. 4.10, and it is reasonable to consider, for these low field data, that equivalent gate voltages for the sample for different magnetic field strengths correspond to the same area fraction of the well filled.

Figure 4.13 displays the conductivity of sample **A** at a temperature of 290 mK at magnetic fields ranging from 0 to 8.5 T. At the highest fields, the magnetic field conductivity suppression is still very strong at these low electron gas densities, and the 6.5 T and 8.5 T curves remain well below the 0 T curve over the full range of gate biases shown. The data from lower fields show an

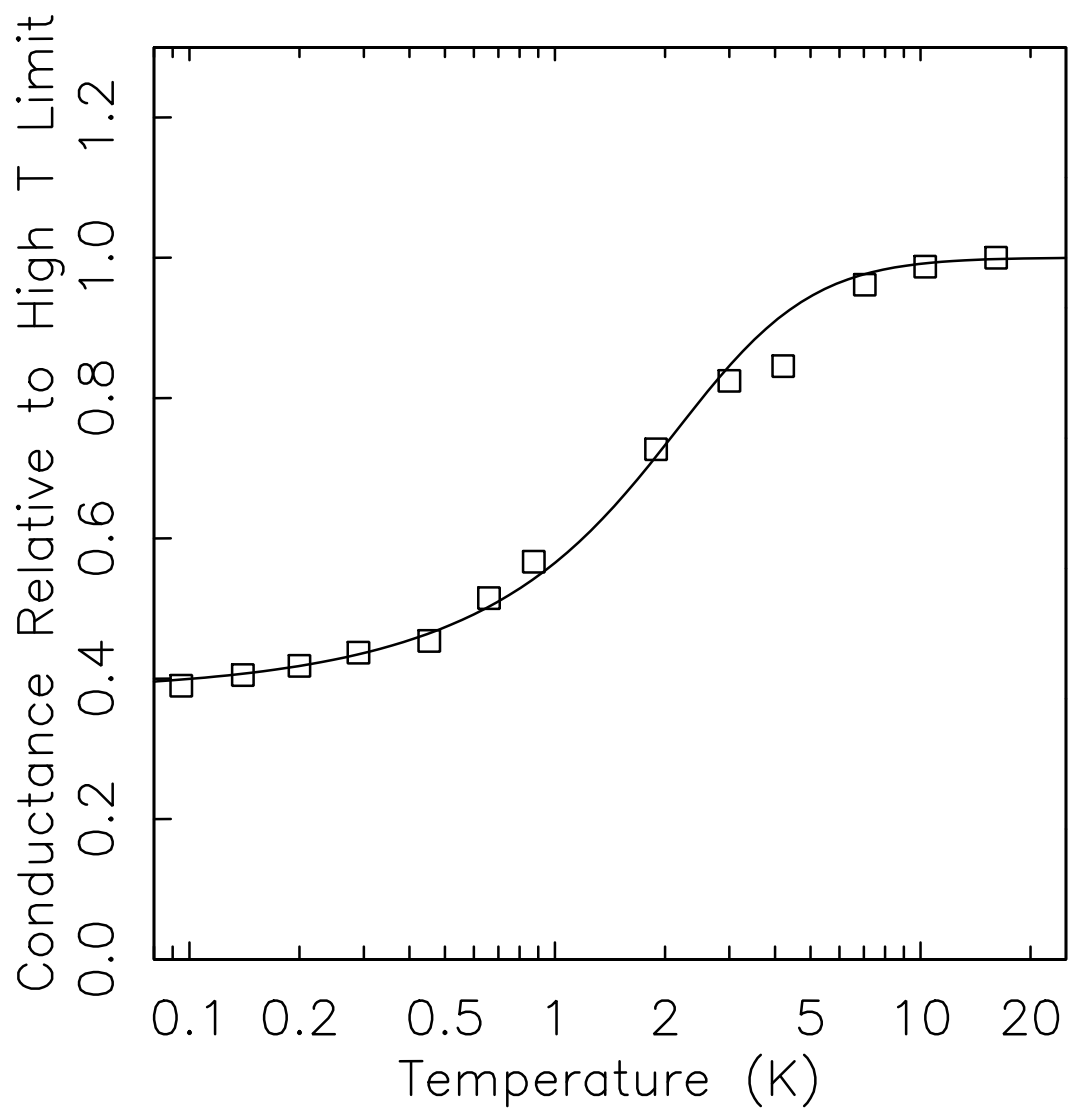


**Fig. 4.12** Plotted as boxes is the conductivity from Fig. 4.11 at -1050 mV plotted as a function of temperature (log scale). The solid curve is a fit using Eq. 4.18 and the same “linear gap” of Eq. 4.19 that was used to fit the magnetic field induced suppression. The fit has  $\Delta$  adjusted to a value of 4.7 K.

intriguing behavior. At higher gate bias values in Fig. 4.13, the 1 and 2 T curves fall below the zero field curve due to the magnetic field suppression. As the gate bias (and thus the average electronic density) is reduced, the low field curves merge at a certain gate bias with the zero field curve and then follow along the zero field curve as the gate bias is reduced further. This same behavior persists at a variety of different temperatures. Further, the curve at 2 T always merges with the zero field curve at gate biases between -950 mV and -975 mV, independently of the temperature.

In effect, the magnetic field conductivity suppression at low densities has an electronic density dependence, unlike the suppression effect at higher densities. This density dependence provides a strong indication that the source of the field induced conductivity suppression lies in the 2d electron gas and not in the substrate. Further, the merging behavior of the curves in Fig. 4.13 is suggestive that three regimes exist, a high density regime where the magnetic field suppression dominates, a low density regime where the low density suppression dominates, and a crossover regime which is where the curves merge together. Strangely, the magnetic field does not enhance the suppression in the low density regime.

#### **4.9 Speculations Regarding Possible Causes for the Suppression Effects**

We briefly review the main characteristics of suppression effects in the tunneling conductivity described above. A magnetic field, only when perpendicular to the plane of the 2d electron gas, produces a tunneling suppression that can be characterized by an energy gap at the Fermi energy in the 2d electron gas. We focus on the 2d electron gas as the source of the suppression for two reasons.

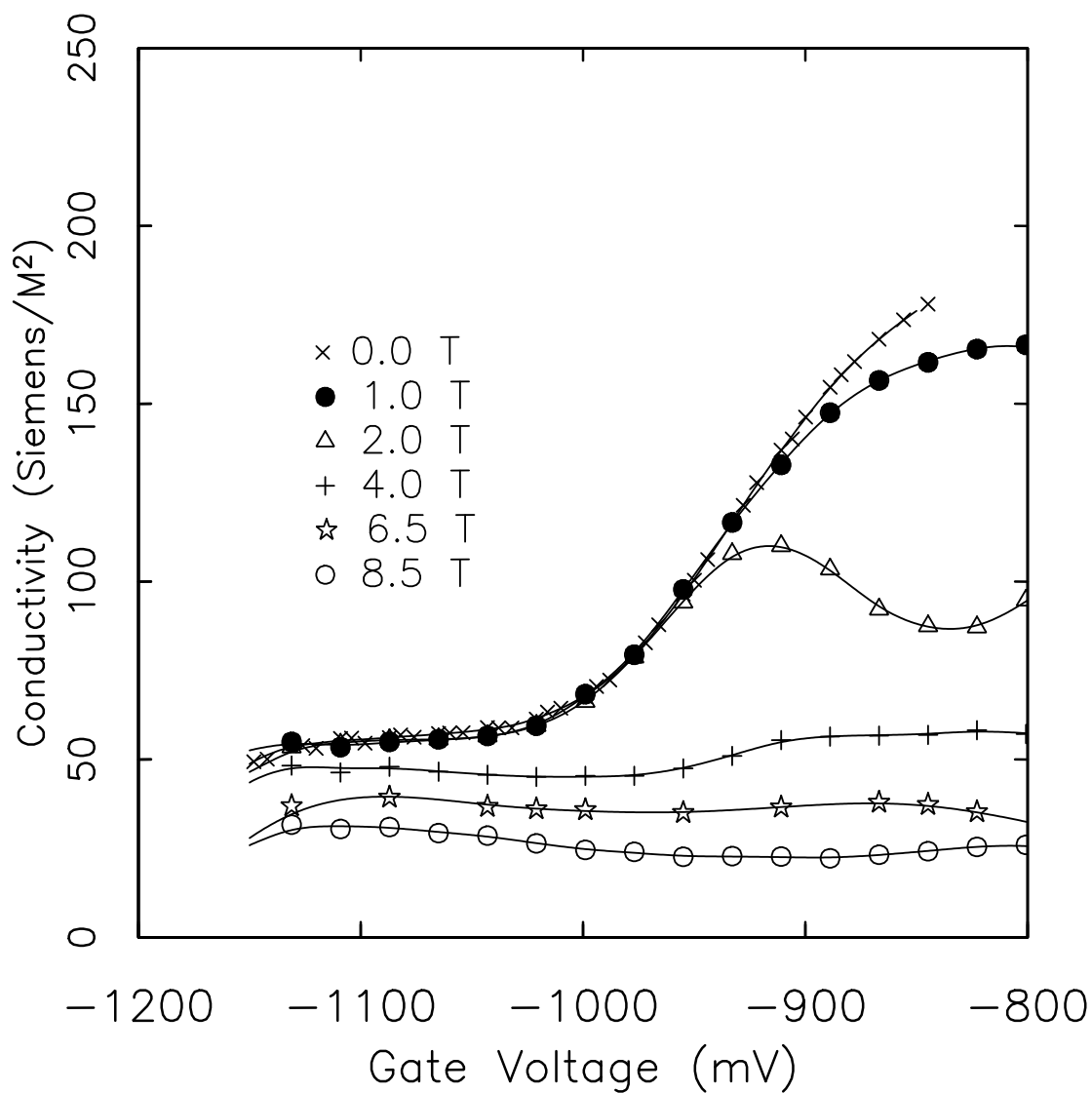


**Fig. 4.13** Tunneling conductivity as a function of gate bias for different magnetic field values at 290 mK. Notice that the curves taken at higher magnetic fields are significantly suppressed below the curve at zero field. Curves taken at 1 and 2 T display an interesting merging with the curve taken in absence of field as the gate bias is reduced.

First, anomalies in the 3d gas should be present for arbitrary orientation of the magnetic field, but the suppression is observed only with the field perpendicular to the 2d gas. Second, density dependence of the suppression is observed near depletion of the 2d gas, as described in the previous section, suggesting the properties of the 2d gas as the source of the suppression effect. In the case of zero applied magnetic field, tunneling suppression is again observed at low densities of the 2d electron gas and can be characterized by the same “linear gap” that fit the data well in the case of the magnetic field conductivity suppression.

### *Tunneling Conductivity Suppression at Low Densities*

We first focus on the low density zero field suppression because this low density region of the 2d electron gas has shown a number of interesting properties previously, some of which are understood theoretically. Far infrared absorption experiments<sup>17</sup> on the 2d electron gas in silicon MOSFETs at low densities ( $< 4 \times 10^{11} \text{ cm}^{-2}$ ) have shown a frequency dependence of the electronic conductivity at photon energies below  $\approx 0.5 \text{ mV}$ . These have been explained by arguments invoking localization in a disordered system.<sup>18</sup> Also, in low density inversion layers in silicon MOSFETs, Bishop, Dynes, and Tsui<sup>19</sup> have observed a logarithmic temperature dependence in the low temperature in plane conductivity of the 2d electron gas which they interpret in terms of localization models.

Altshuler, Aronov, and Lee<sup>20</sup> have suggested that localization effects should cause an energy gap to form at the Fermi energy in the single particle (tunneling) DOS in disordered systems. In the simplest heuristic model, this gap arises for the following reasons. In a disordered material with a background random potential, electrons eventually find a configuration in which they minimize both

their energy with respect to the random potential and also the energy associated with the electron-electron repulsion. Suddenly adding or subtracting another electron forces the system to rearrange and requires it overcome energy hurdles to find a new stable state. In two dimensions, Altshuler et. al. predict that near the Fermi energy, this gap should have the form

$$\frac{\delta g(E)}{g(E)} = -\frac{\hbar}{2\pi E_F \tau_s} \ln\left(\frac{(E - E_F)\tau_s}{\hbar}\right). \quad (4.22)$$

Tunneling experiments have been done in both thin indium oxide films<sup>21</sup> and in thin tin films<sup>22</sup>. In both of these experiments, the thicknesses of the films were varied to test certain aspects of the theory. These measurements, in cases where the films were thin enough to be considered two dimensional, have shown the logarithmic behavior in the tunneling conductance as a function of the voltage across the tunneling barrier (at voltages <20 mV) expected from the Altshuler theory.

Due to difficulties in creating structures to observe tunneling with small applied biases from the 2d electron gas, the capacitive technique that we use has allowed the only detailed tunneling study of the 2d electron gas in semiconductors samples at low voltages across the tunnel barrier. Novel structures<sup>23</sup> may allow study with more conventional I-V measurements.

We note that the gap used in Fig. 4.12 is, like the Altshuler gap, singular (the derivative diverges) at the origin. Indeed, this singularity was necessary to account for the low temperature behavior of the tunneling conductance. Again, there is not sufficient sensitivity in these fits to discern the precise shape of an energy gap. Given the results of previous work done in tunneling from disordered systems, it seems reasonable to conclude that the Altshuler gap is the source of the tunneling suppression at low densities in our samples. One intriguing feature of the data of Fig. 4.11 is the independence of the temperature range



over which the tunneling conductance undergoes large variation. This is always in the range of 1 and 3 K. With the “linear gap” used to fit the data, this yields a gap parameter  $\Delta$  which is independent of gate voltage. This is odd given that Eq. 4.22 predicts that the gap should deepen and widen as the Fermi energy is decreased. Lastly, we note that as the gate bias is reduced, the system may at some bias move to the insulating side of the metal-insulator transition. In this case, electrons are fully localized, and it is more appropriate to speak of a Coulomb gap.<sup>24</sup>

### *Tunneling Conductivity Suppression by a Magnetic Field*

At present, we have no clear understanding of the mechanism which produces the apparent energy gap in the single particle DOS in a magnetic field. The similarities between the temperature dependence of the low density suppression results in Fig. 4.12 and the magnetic field results in Fig. 4.7 lead us to speculate that these two effects might be different incarnations of the same underlying physics. The main problem with interpreting the magnetic field results this way, however, is that one would expect the strength of the gap to depend upon the thermodynamic DOS which varies by more than a factor of 10 (at the highest fields used here) as the Fermi energy moves from the center of a Landau level to between Landau levels. Our magnetic field results instead indicate that the strength of the gap is independent of the position of the Fermi energy within the Landau level structure.

Aside from an energy gap, another proposal for the cause of the tunneling suppression in magnetic fields is the enhancement, by some mechanism involving the magnetic field, of the coupling of the tunneling transition to other excitations of the system, e.g. phonons or plasmons. The limiting value of the suppression

at low temperatures would, as observed, decrease with increasing field as more tunneling oscillator strength is transferred from the elastic to the inelastic channels. There is no obvious candidate for the coupled excitation which would need to have a characteristic energy of order 0.5 meV in order to explain, even crudely, the temperature dependence of the suppression.

Finally we mention two characteristics in the magnetic field data that may relate to the cause of the tunneling suppression in magnetic field. These involve the shape of the capacitance vs. frequency curves for the device and the contrast in the tunneling conductance at the DOS maxima compared to that at the DOS minima.

As noted in chapter 3, when the Fermi energy is positioned between Landau levels at low temperatures, loss tangent and capacitance vs. frequency deviate from the simple curves given by the circuit model of Fig. 4.1a due to freezeout of the in-plane conductance of the 2d electron gas. Intriguingly, this freezeout has a similar temperature dependence to the magnetic field tunneling suppression.<sup>10</sup>

Another interesting feature of the data, described previously,<sup>7</sup> is that the amplitude of the oscillations due to the Landau level structure are much smaller in the tunneling conductance than in the thermodynamic DOS. This is true for all three samples. At present, we have no explanation for this effect. Qualitatively, it appears that the curves taken at lower magnetic field values (such as at 2 T), at the lowest temperatures (well below 1 K), do achieve nearly the same 2:1 peak to valley ratios that are seen in the thermodynamic DOS measurement. Strangely, tunneling conductance results from 2 T develop this contrast only at temperatures well below 1 K even though the thermodynamic DOS Landau level peaks are nearly fully developed at 1 K. At higher magnetic field strengths the 2:1 peak to valley ratio is not surpassed in the tunneling

conductance even though the thermodynamic DOS results have much larger ( $\approx 10:1$ ) peak to valley ratios.

We find it intriguing that thermodynamic DOS results of chapter 3 and tunneling results show the same amount of contrast at high temperatures where the Landau level structure is nearly washed out due to thermal broadening. As the temperature is decreased both the thermodynamic DOS and the tunneling conductance results develop contrast equally. However, at some temperature (at around 7 K for the data at 4 T shown in Fig. 4.3), the tunneling data ceases to develop contrast (or develops it only slowly) while the thermodynamic DOS continues to show more contrast as the temperature is reduced. Interestingly, this bifurcation takes place at temperature around  $2\Delta/k_B$ , where  $\Delta$  is the gap parameter. We speculate that the development of the gap may wash out features in the single particle DOS of energy width on order of the gap energy.

#### 4.10 Summary

In summary, we observe two novel tunneling suppression effects in the tunneling of electrons between a 2d electron gas and a 3d substrate. We have completed a detailed study of the temperature dependence of these effects. One of these, a tunneling suppression that occurs only for low densities of the 2d electron gas, may be related to the energy gap seen previously in tunneling from thin metal film systems and thought to arise from electron-electron interaction effects in the presence of disorder. The other tunneling suppression effect occurs over a wide range of densities of the 2d electron gas in the presence of a magnetic field perpendicular to the plane of the 2d electron gas. This suppression can be characterized by a field induced gap in the single particle DOS tied to the Fermi energy of width roughly 5% of  $\hbar\omega_c$ .

## References

1. T.P. Smith, B.B. Goldberg, P.J. Stiles, and M. Heiblum, Phys. Rev. B **32**, 2696 (1985)
2. E. Böckenhoff, K. v. Klitzing, and K. Ploog, Phys. Rev. B **38**, 10120 (1988)
3. B.R. Snell, K.S. Chan, F.W. Sheard, L. Eaves, G.A. Toombs, D.K. Maude, J.C. Portal, S.J. Bass, P. Claxton, G. Hill, and M.A. Pate, Phys. Rev. Lett. **59**, 2806 (1987)
4. J.A. Lebens, R.H. Silsbee, and S.L. Wright, Appl. Phys. Lett. **51**, 840 (1987)
5. J.A. Lebens, R.H. Silsbee, and S.L. Wright, Phys. Rev. B **37**, 10308 (1988)
6. R.C. Ashoori, J.A. Lebens, N.P. Bigelow, and R.H. Silsbee, Phys. Rev. Lett. **64**, 681 (1990)
7. J.A. Lebens, Ph.D. thesis, Cornell University (1988)
8. *See Chapter 2*
9. P.A. Lee, Phys. Rev. B **26**, 5882 (1982)
10. *See Chapter 3*
11. E.L. Wolf, *Principles of Electron Tunneling Spectroscopy*, Chap. 2 (Oxford Univ. Press, 1985)
12. J.P. Eisenstein, H.L. Störmer, V. Narayanmurti, A.Y. Cho, A.C. Gossard, and C.W. Tu, Phys. Rev. Lett. **55**, 875 (1985)
13. T. Ando and Y. Uemura, J. Phys. Soc. Jpn. **36**, 959 (1974)
14. S. Das Sarma and Frank Stern, Phys. Rev. B **32**, 8442 (1985)
15. T.W. Hickmott, Phys. Rev. Lett. **57**, 751 (1986)
16. John A. Nixon and John H. Davies, Phys. Rev. B **41**, 7929 (1990)
17. S.J. Allen, Jr., D.C. Tsui, and F. DeRosa, Phys. Rev. Lett. **35**, 1359 (1975)
18. A. Gold, S.J. Allen, B.A. Wilson, and D.C. Tsui, Phys. Rev. B **25**, 3519 (1982)
20. B.L. Altshuler, A.G. Aronov, and P.A. Lee, Phys. Rev. Lett. **44**, 1288 (1980)

21. Yoseph Imry and Zvi Ovadyahu, Phys. Rev. Lett. **49**, 841 (1982)
22. Alice E. White, R.C. Dynes, and J.P. Garno, Phys. Rev. B **31**, 1174 (1985)
23. J. Smoliner, W. Demmerle, G. Berthold, E. Gornik, G. Weimann, and W. Schlapp, Phys. Rev. Lett. **63**, 2116 (1989)

## Chapter V

### Creation of Quantum Dots

#### 5.1 Introduction

Additional confinement of an initially two-dimensional system has been a very popular subject of research in recent years. In this chapter, we discuss a fabrication technique which allows us to move from studying electrons free in two dimensions (2d) in a quantum well to electrons trapped in all dimensions. The confinement technique described here produces “quantum dots”, packets of from one to several hundred electrons. The number of electrons in these packets can be varied by means of a gate bias. Because ours is a capacitance experiment, we need on the order of  $10^5$  dots each having a capacitance of around 0.1 fF, to obtain sufficient signal for our measurements. For the average of capacitance signals from the individual dots to be meaningful, our experiment requires that there be high uniformity of the size and shape of the many electron packets. Hence there must also be uniformity in the potential which produces the confinement from dot to dot. Lastly and most importantly, we seek to minimize the number of process steps required to produce the dots in order to enhance the chances for successful processing.

Before describing the confinement technique that we use, we briefly motivate it by reviewing some different confinement schemes that we have experimented with in our lab. The most obvious way to achieve this kind of lateral confinement has been to etch wires or pillars out of the 2d electron gas. This technique of a “fabrication induced confining potential” has been used successfully in photoluminescence and resonant tunneling experiments. Photoluminescence experiments<sup>1</sup> done on arrays of small pillars show that even though there is a large surface state density in GaAs, the surfaces produced by etching do not serve as efficient nonradiative recombination sites. However, in tunneling experiments using this type of confinement surface states are a major consideration. Because surface states pin the Fermi energy at the surface to a position of  $\approx 0.9$  V beneath the conduction band edge in n doped GaAs,<sup>2,3</sup> in  $n^+$  pillar there results a carrier depletion layer at the edges of the sample. Obviously, in order to do a tunneling experiment the pillar must not be fully depleted of electrons. Reed et. al.<sup>4</sup> have made measurements on single pillars made on a resonant tunnel structure. From observation of the current in a pillar in comparison to that of broad area samples patterned on the same wafer, they conclude that the width of the conducting channel in a 1000 Å diameter pillar is only 130 Å. A previous attempt in our lab<sup>5</sup> to produce dots for capacitance measurements by simply etching through pillars resulted in fully depleted dots. It was decided to explore a different confinement technique.

Gating techniques have been used to produce small wires. Thornton et. al.<sup>6</sup> first used gating techniques to produce wires small enough so that effects of the quantum level structure on the wires<sup>7</sup> could be observed. Topological considerations make such a technique to produce dots considerably more difficult than for producing wires. In our lab, Lebens<sup>5</sup> developed a dual gate technique

to produce quantum dots. This technique, had it been successfully realized, would have given some degree of independent control of both the number of electrons in a dot and the size of a dot. The procedure for producing these dots entailed a large number of process steps, a few of them being rather tricky. Two samples were realized; however, both of these had leakage problems either between the dual gates or between one of the gates and the substrate. Because of the complexity involved, we decided to forsake this confinement scheme and to develop another with fewer process steps. Only very recently, Alsmeyer, Batke, and Kotthaus<sup>8</sup> have achieved confinement of electrons into dots using a very similar dual gate technique. Their dots are produced on Si, which allows them to use SiO<sub>2</sub> barriers that avoid the leakage problems. Another feature of their fabrication method is that it requires no metal-semiconductor ohmic contacts unlike our dual gate method.

Our next design (when I took over the fabrication), was a single gate technique to reduce the number of process steps. In this sample, we attempted to make good ohmic contact to short  $n^+$  GaAs pillars produced on the surface of the sample etched down a few hundred angstroms to an AlGaAs insulating barrier. This exposed edge of the AlGaAs barrier was still about 800 Å away from the quantum well (on the other side of the AlGaAs barrier) containing the 2d electron gas. After producing these pillars we evaporated Al metal to form a Schottky barrier everywhere else. The basic idea behind this confinement scheme was to use the electrostatic potential produced by the Schottky barrier in the region surrounding a pillar and the lack of a Schottky barrier potential under the  $n^+$  pillar to produce an electrostatic potential at the well which would confine electrons. Two samples were made; one produced on the same M.B.E. material that was used by Lebens and the other from the M.B.E. material from which



sample **B** of chapter 3 was fabricated. Capacitance measurements revealed no obvious results indicative of confinement of electrons in small packets. At the time these samples were produced, we were uncertain of how reasonable it was to expect that GeAu ohmic contact could be made to each of the pillars diffusing enough Ge into the GaAs to counter the effects of surface depletion. We gave up on this technique, deciding that one possible cause for the lack of a small packet signature in the capacitance was that ohmic contact was not being made to all, or even a large fraction, of the dots. Recent work by Blanc et. al.<sup>9</sup> has shown that the average distance between conducting grains in a GeNiAu contact similar to the type that we used is about 4100 Å, which is larger than the 2500 Å diameter of the pillars that we used.

Each of the three confinement techniques used up to this point had required ohmic contact be made to the tops of small pillars. We then sought out a technique to make quantum dots without having to make these ohmic contacts. At about the same time, Smith's group at IBM was also working on making quantum wires<sup>10</sup> and quantum dots<sup>11</sup> for capacitance measurements. They developed a technique<sup>12</sup> which requires no ohmic contact and requires only a single gate to produce confinement on samples grown on conducting substrates. Although there are differences between our experiment and theirs (we measure tunneling to and from the dots as well as the capacitance and use a quantum well to create the initially 2d electron gas, whereas they rely on a self consistent potential well forming at a GaAs/AlGaAs interface), we decided to adapt the some features of their technique to our experiment. The rest of this chapter discusses the confinement technique and its implementation on our samples.

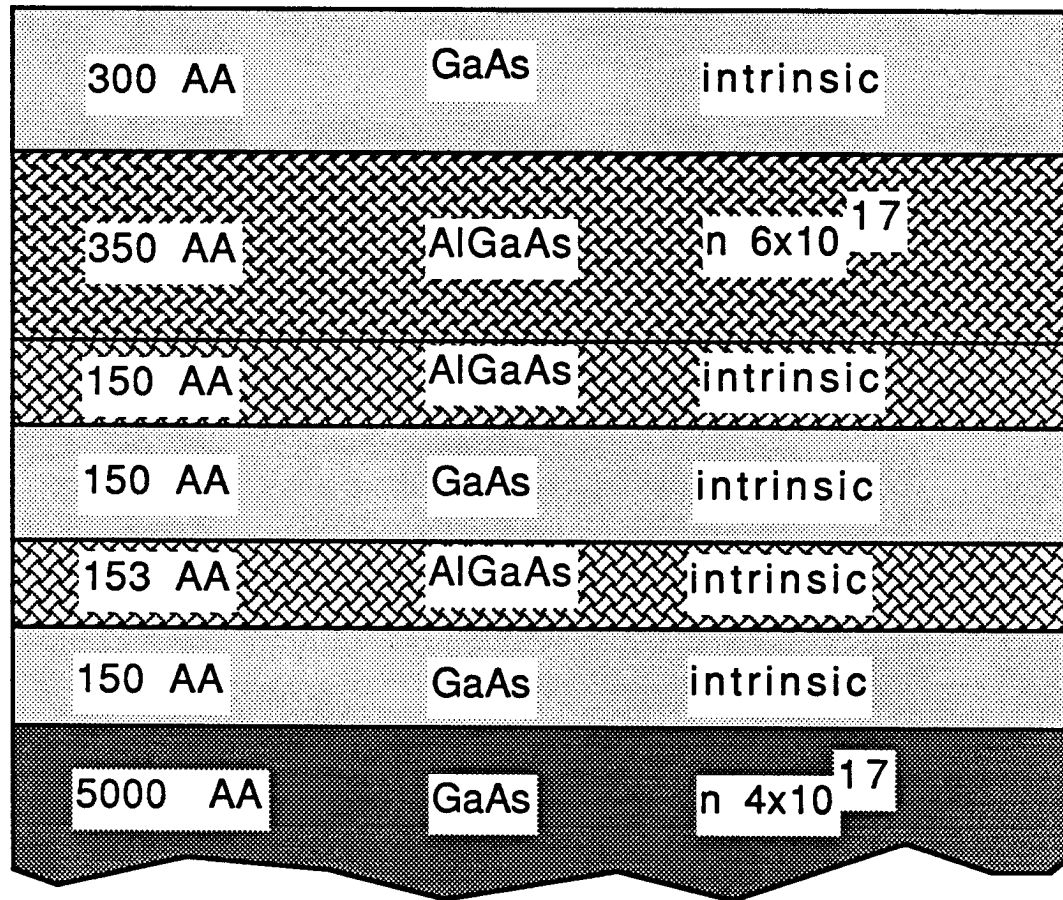
## 5.2 Physics of the Confinement Technique

The confinement technique used here requires only a 300 Å corrugation of the surface of the sample to confine electrons in the quantum well which is about 600 Å below the surface of the sample. This section describes how this surface corrugation produces the confinement.

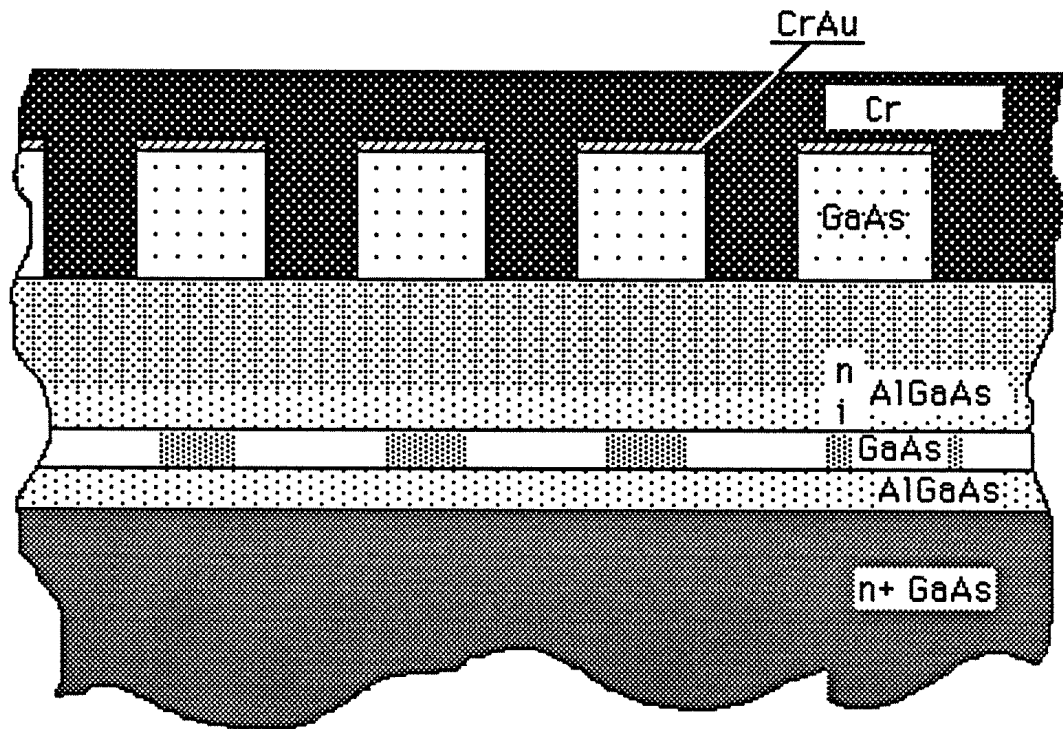
Fig. 5.1 outlines the layer structure of the wafer that we use. The wafer was grown using M.B.E. by L. Pfeiffer and K. West at AT&T Bell Laboratories. On top of a conducting substrate are grown: A 5000 Å GaAs  $n^+$  layer, a 1500 Å  $n^+$  ( $4 \times 10^{17} \text{ cm}^{-3}$ ) GaAs bottom electrode, a 150 Å intrinsic GaAs spacer layer, a 152 Å (54 monolayer)  $\text{Al}_{0.3}\text{Ga}_{0.7}\text{As}$  tunnel barrier, a 150 Å quantum well, a 150 Å GaAs quantum well, a 150 Å undoped  $\text{Al}_{0.3}\text{Ga}_{0.7}\text{As}$  setback, a 350 Å  $n$  doped ( $\approx 6 \times 10^{17} \text{ cm}^{-3}$ )  $\text{Al}_{0.3}\text{Ga}_{0.7}\text{As}$  blocking barrier layer, and finally a 300 Å intrinsic GaAs cap layer.

Fig. 5.2 displays the sample after all processing has been completed. We will describe the details of the processing later. The finished sample consists of 300 Å tall pillars of GaAs, produced by etching the GaAs cap layer of the wafer, embedded in Cr metal. Cr metal contacts the surface of the semiconductor material surface everywhere. Between the GaAs pillars, the semiconductor material contacted by the Cr is  $\text{Al}_{0.3}\text{Ga}_{0.7}\text{As}$ . Everywhere along the chrome-semiconductor interface, a Schottky barrier is formed.

This Schottky barrier is responsible for producing the confinement. Fig. 5.3 is a band structure diagram of the sample underneath the center of a 300 nm diameter (round) pillar. The figure is shown with zero applied gate bias. At the top surface, the Fermi energy is pinned to a position of 0.8 eV below the conduction band edge, appropriate for a surface exposed to air prior to Cr evaporation.<sup>13</sup> The wafer was grown to have a large density of ionized donors



**Fig. 5.1** Layer structure of wafer used in quantum dot experiments.



**Fig. 5.2** A schematic cut-away of a completed quantum dot sample. The entire top surface of the sample is covered with chrome, creating a Schottky barrier everywhere along this surface.

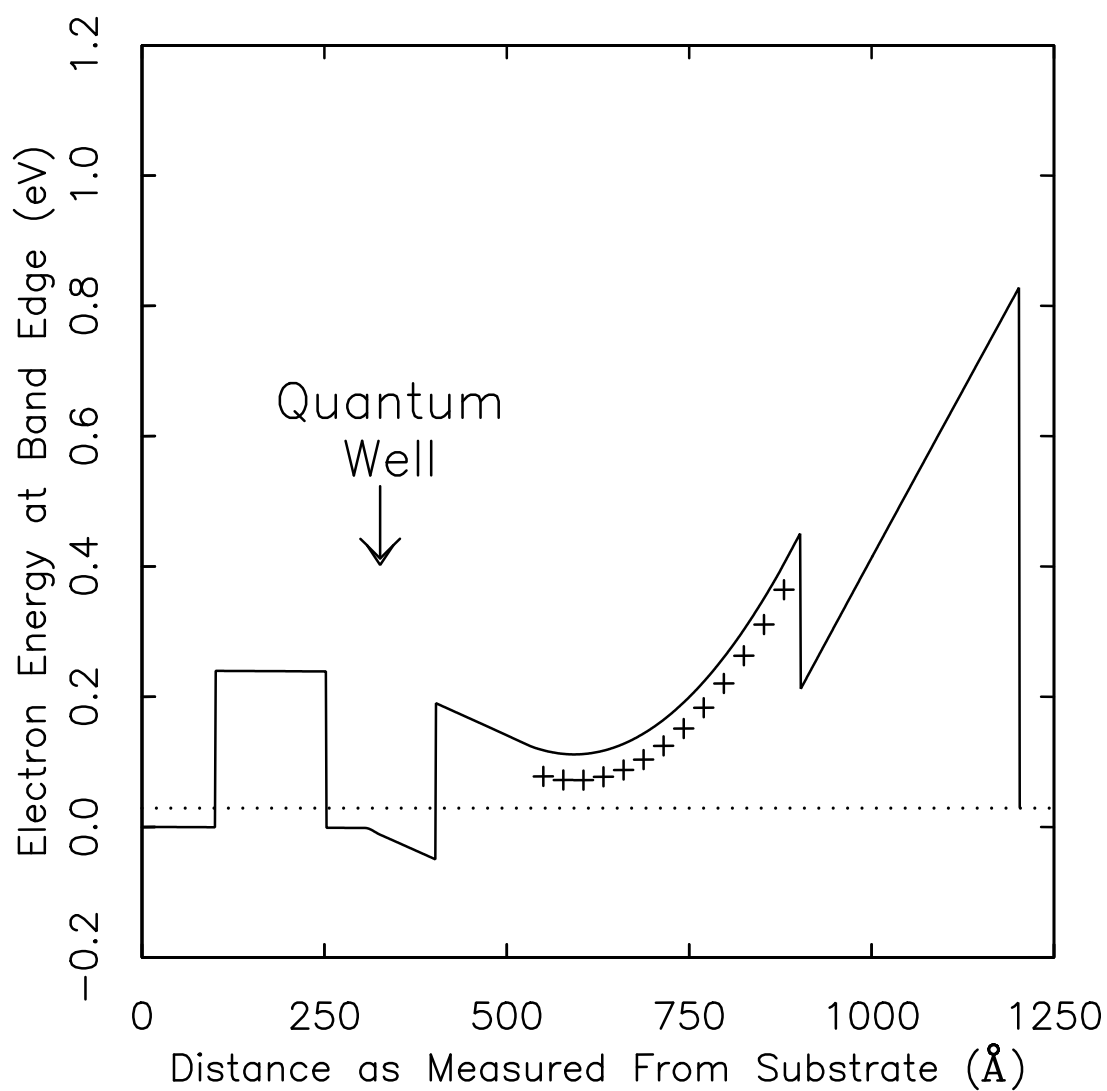


**Fig. 5.3** The band structure underneath a pillar etched on the surface as determined by computer calculation. The figure is shown at zero applied bias, and the dotted line is the Fermi energy. The “+” symbols represent unfilled energy levels of donors dispersed in the AlGaAs blocking barrier.

in the “blocking barrier”. Under a dot, the 0.8 V Schottky barrier is *far enough* away from these donors that the electric field caused by the donors multiplied by the distance to the Schottky barrier is larger than 0.8 V. This means that the electric field from the Schottky barrier is “terminated” at the donors, and the electric field just at the edge of the quantum well is one which, due to the positive donor charge, draws in electrons.

If the GaAs cap layer is etched away, the position of the Schottky barrier will be *too close* to the donors for the Schottky electric field to be terminated at the donors. This is the situation in Fig. 5.4 which shows the electrostatic configuration calculated under the region halfway between two 300 nm diameter pillars spaced with edges 340 nm apart and again at zero applied gate bias. The electric field at the edge of the well repels electrons from the well, and the well remains empty at this position. Hence by simply corrugating the surface, we can achieve lateral confinement of electrons in the well. The relaxation method calculations for solving Poisson’s equation (classically) that produced Figs. 5.3 & 5.4 is described elsewhere.<sup>5</sup> We will return to these calculations and compare them with capacitance data from the a dot sample after a brief discussion of the processing sequence which produces the dots.

### 5.3 Device Fabrication Sequence

There are five basic steps in our device fabrication. These are: 1) electron beam lithography and liftoff to produce CrAu metal pads on the sample surface, 2) photolithography to define mesas for capacitance measurements (masks for liftoff of step #4), 3)  $\text{CCl}_2\text{F}_2$  (freon) etch to produce 300 Å tall GaAs pillars on sample surface using the CrAu pads as an etch mask, 4) evaporation of Cr over the entire sample surface and liftoff of photoresist to leave large (200 μm) Cr

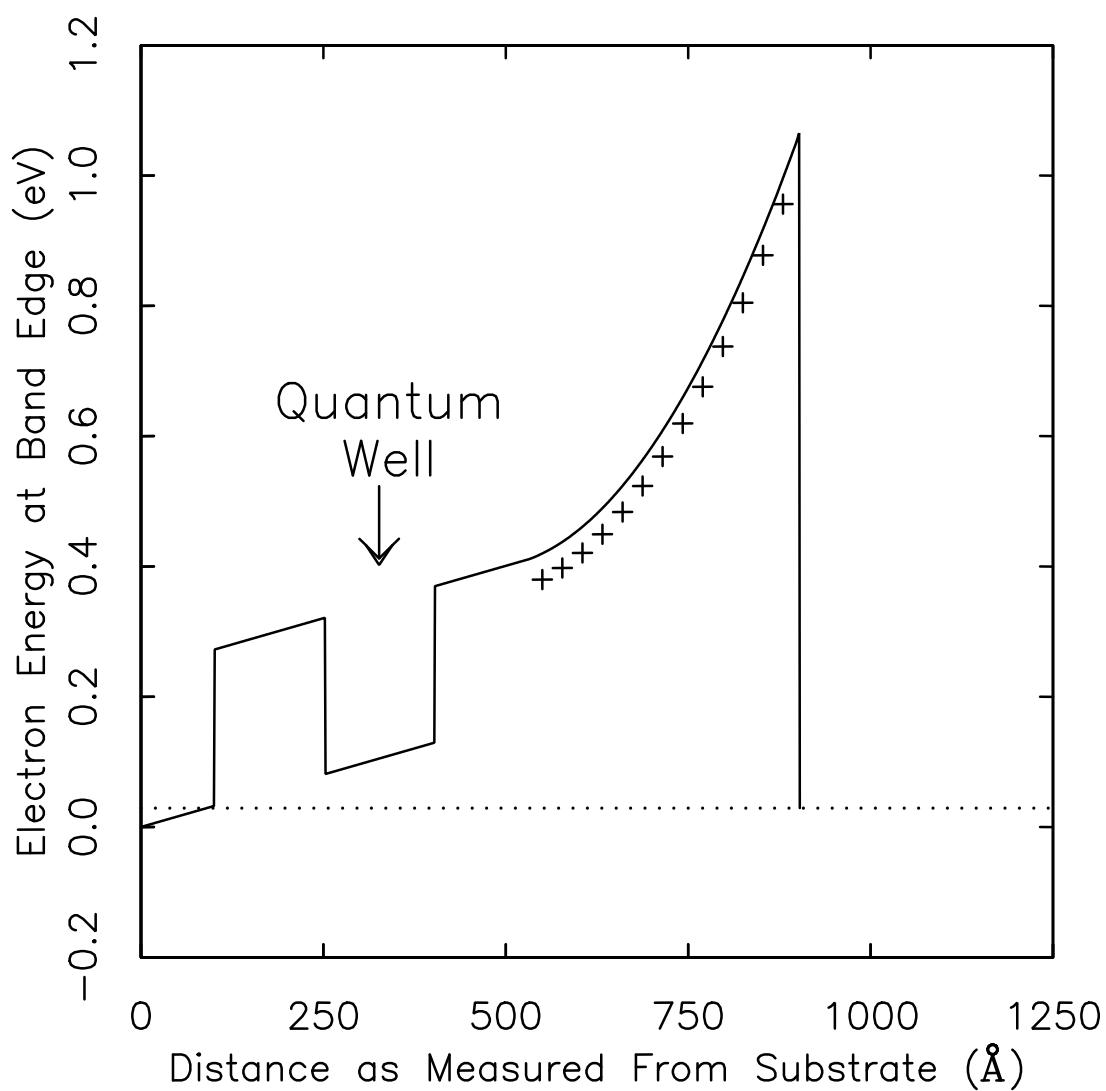


**Fig. 5.4** The band structure midway between two pillars obtained by computer calculation. Note that the cap layer has been etched away. The figure is shown at zero applied bias, and the dotted line is the Fermi energy. The “+” symbols represent unfilled energy levels of donors dispersed in the AlGaAs blocking barrier.

pads covering  $\approx 10^5$  GaAs pillars, and 5) a mesa isolation etch using the large Cr pads as a mask to produce separate devices for capacitance measurements.

We describe these process steps serially, starting with the steps just prior to electron beam lithography. A small piece of the wafer, with AuGeNi ohmic contact already made to the back side of the conducting substrate, is first cleansed thoroughly in organic solvents and then subjected to a “descumming” oxygen plasma. Extreme caution must be taken that the plasma potential is small enough so that the bombarding oxygen ions do not damage the sample. We use the Branson/IPC P2000 barrel etcher system at the National Nanofabrication Facility (NNF). In this system, oxygen ions are accelerated to  $< 10$  eV. Further, we use special shielding in the etcher known as an “etch tunnel” which effectively neutralizes a very large fraction of the oxygen ions.<sup>14</sup> The cleansing effect of the oxygen plasma occurs largely as neutral oxygen radicals diffuse to the surface and react with adsorbates.

We then spin on a bilayer resist. The top surface layer of the bilayer is a resist with lower sensitivity to the electron beam than the underlying layer. When this bilayer is exposed to the electron beam and developed, the surface layer produces an opening which is undercut in the underlying high sensitivity layer. This undercut is necessary for easy liftoff of metallization. We wet the sample surface with 3% solids copolymer (PMMA-MMA) solution and spin this at 5000 rpm. The sample is then baked for 1 hr at 170°C. This leaves about 700 Å of resist on the surface. Then a 2% solids mixture of PMMA is spun on at 6000 rpm. The sample is baked again for 1 hr, and this leaves a 1000 Å layer of PMMA. The sample is then loaded into the JEOL JBX5D11 electron beam lithography system at the NNF. 1 mm by 1 mm arrays, containing  $\approx 4 \times 10^6$  patterns of either hexagons or squares of particular sizes and spacings,



are exposed. Typically, 4 or more arrays are exposed, each containing different pattern shapes or sizes. We use a beam current of 300 pA which produces a spot size of around 20-30 nm<sup>15</sup> for high resolution of our patterns. Exposures vary from between 160  $\mu\text{Coul}/\text{cm}^2$  to 240  $\mu\text{Coul}/\text{cm}^2$  depending on the size and spacing of the patterns in the array. A hexagon, 300 nm across in its long dimension and center separation from nearest neighbors of 520 nm in a hexagonal close packed array consists of about 100 exposures per hexagon with a current density of 200  $\mu\text{Coul}/\text{cm}^2$ .

The resist is then developed in a 1:1 mixture of methyl isobutyl ketone and isopropyl alcohol at 21°C for 60 sec. This is followed by an 8 sec. rinse with isopropyl alcohol to wash away any excess resist still left in the patterns. As the alcohol causes some development of the underlying PMMA-MAA layer, care must be taken to standardize this rinse time.

After development, the sample is prepared for evaporation to produce small metal pads on the sample surface. The sample is again subjected to a short oxygen descum to clear away any residual resist. The sample is then dipped in a 1:5 dilution of hydrochloric acid to clear away any oxide that may have formed on the sample surface. From the acids hood, the sample is rushed to and quickly loaded in the electron beam evaporator at the NNF so that the oxide does not have time to reform. We evaporate 200 Å of chrome followed by 200 Å of gold. Liftoff is then performed in methylene chloride and acetone. Fig. 5.5 displays hexagonal patterns on the surface of a sample after liftoff. The resolution shown and the uniformity of the dots is typical for our samples.

At this point, the sample consists of several large arrays of metal pads on the surface of a piece of the M.B.E. grown wafer. These arrays are so large, that it is likely that there are several oval defects contained in a large array. Because

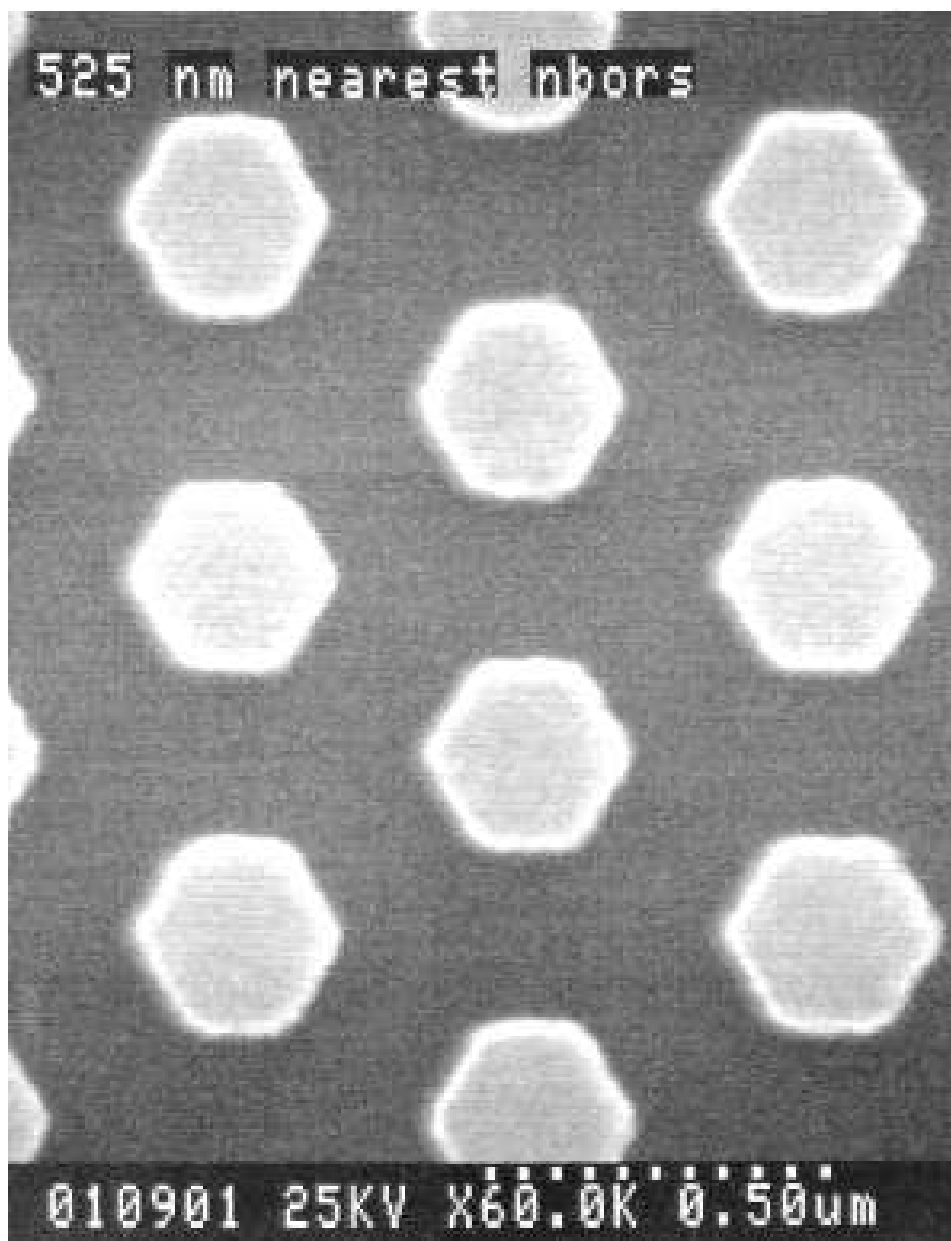


**Fig. 5.5** A scanning electron micrograph of an array of AuCr hexagonal patterns after metallization and liftoff.

these oval defects can create shorts in our devices, these must be avoided. To increase the chances for finding a non-short device, we divide the array into 16, 200 nm on a side, square pieces using photolithography. Photoresist (using no primer) is spun onto the sample and is exposed and developed so that each large array has 16 box regions free from resist, each separated by resist. Each box region contains between  $0.8 \times 10^5$  and  $2 \times 10^5$  patterns. Primer is not used before spinning on the photoresist as it is thought to leave more residue after development than photoresist when used alone.<sup>16</sup>

We now proceed to etch the metal patterns to produce pillars. Before loading into the reactive ion etcher, we do another oxygen descum to remove any remnant photoresist in the box regions and another hydrochloric acid dip to remove any oxide that might impede etching.<sup>5</sup> The  $\text{CCl}_2\text{F}_2$  etch<sup>17</sup> and the physical processes<sup>18</sup> which allow it to etch GaAs and not AlGaAs have been well characterized by others. In order to reduce etch damage from fast and light helium atoms,<sup>19</sup> we chose not to mix in helium with the freon. This has been done by others<sup>5,17</sup> remove carbon contaminants from the etch which induce poor surface morphology and to improve the directionality of the etch. For the short, 300 Å etching distance before the etch is stopped by an underlying AlGaAs layer in our samples here, carbon contaminant buildup and undercutting of the pillars occur only insignificantly. There was no observable difference in sample morphology with and without helium added to the etchant. The freon etch was run under conditions of a low D.C. self bias of 60 V (r.f. power was 0.2 W/cm<sup>2</sup>) and a pressure of 24 mT. The low self bias was again chosen to minimize etch damage. Etch times were typically around 10 sec., about one and a half to twice as long as needed to etch through 300 Å of GaAs.

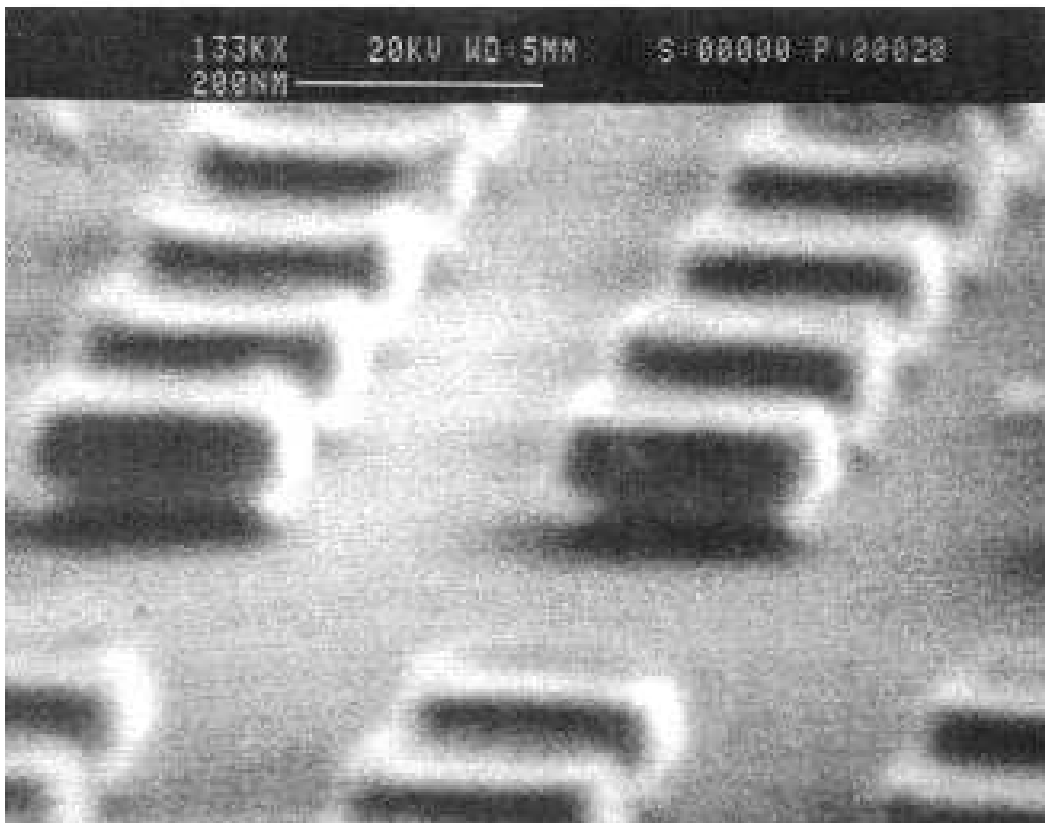


**Fig. 5.6** An SEM photo of 200 nm wide metallized patterns after the freon etch described in the text.

Fig. 5.6 displays a set of 200 nm square dots after etching. There is an obvious undercut, indicative that etching has taken place, underneath the square CrAu metal pads which form “hats” on top of the pillars. The smooth surfaced material between the pillars is AlGaAs.

Before doing the final chrome evaporation, we again descum the sample with oxygen and do another hydrochloric acid dip. The sample is loaded into the thermal evaporator and 2000 Å or more of Cr is evaporated on the surface. We then liftoff the Cr in acetone leaving 16 boxes per large array of pillars buried in chrome.

Finally, we use the Cr as an etch mask in a CAIBE etch to produce mesas for the device. This step was done with the assistance of George Porkolab in the Technics Plasma GmbH R.I.B.-etch 160 system at the NNF. A beam of 500 eV argon ions assists etching by a chlorine etch. The run parameters used were: argon flow of 3.5 mL/min, chlorine flow 9.0 mL/min, and 0.1 mA/cm<sup>2</sup> beam current. The etch ran for 15 minutes and etched to a depth of 1 μm. Fig. 5.7 is a picture of the edge of a mesa of 260 nm wide hexagons after this etch. The pillars off of the edge of the mesa arise from metal pads previously covered with photoresist and thus not protected by the large chrome boxes. The sample is now mounted and wirebonds are made to the mesas.

#### 5.4 Measurement of Dot Area

In this section, we look at the capacitance vs. gate bias characteristics of one of the device mesas. We interpret these results in terms of the area in the quantum well which contains electrons. This can then be compared with a computer model which predicts the area of the sample as a function of gate

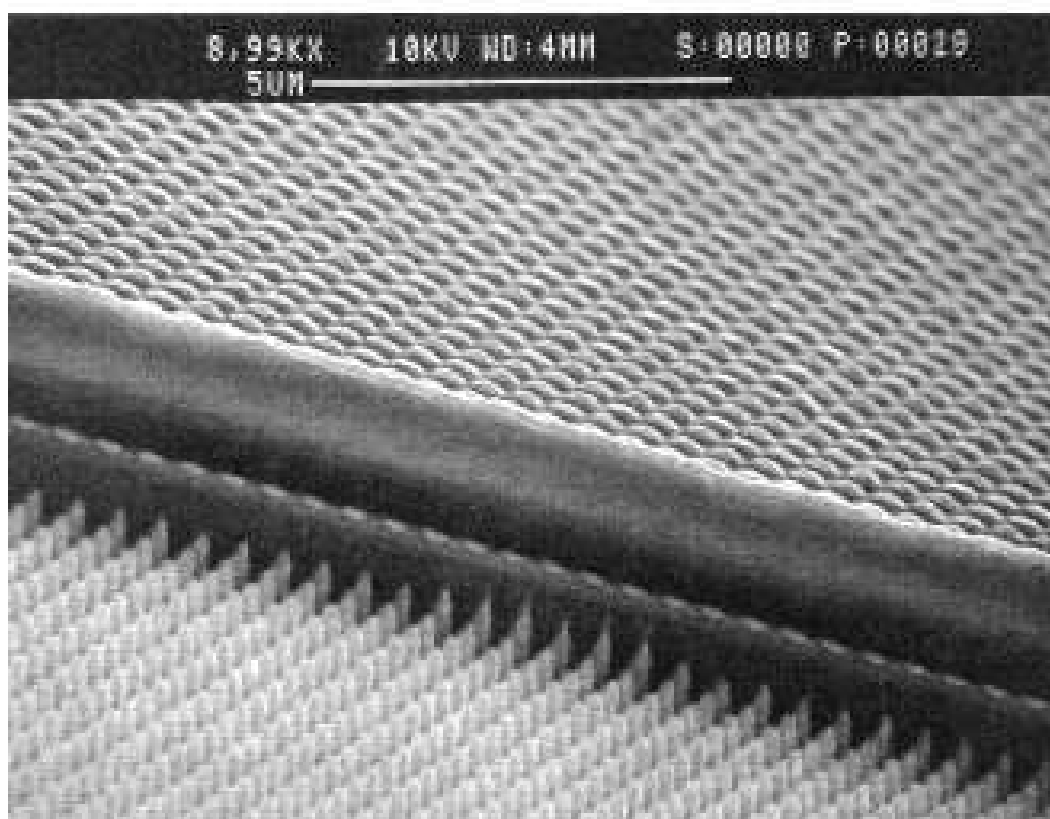


**Fig. 5.7** An SEM photo of a finished sample. Shown is the edge of a sample mesa after the CAIBE etch described in the text. The pillars shown in the lower part of the photograph are not used in the experiment. These have been etched in the final CAIBE step that defines the mesa.

bias. The detailed results of high resolution capacitance measurements, and our search for effects of the “Coulomb Blockade”<sup>20</sup> will be discussed in Chapter 6.

As discussed in Chapter 3, the capacitance of our devices is a function of frequency. The capacitance measured at low frequencies,  $C_{low}$ , measures the capacitance of the device including charge transfer to the quantum dots from the substrate. The distinction between low and high frequency arises from the  $RC$  equilibration time the quantum dots and the substrate. At high frequencies, there is insufficient time during one cycle of the measuring voltage for appreciable charge to be transferred between the electron density in the substrate and the quantum dots, and we call this capacitance  $C_{high}$ . The capacitance at low frequencies is thus larger than that measured at high frequencies. As described below, knowledge of the value of  $C_{low}/C_{high}$  in comparison to its value in broad area samples (no dots patterned) gives a measure of the size of the dots.

For the same wafer upon which the quantum dots were fabricated, we have made measurements on broad area samples of the low and high frequency capacitances. These are displayed in Fig. 5.8. At very low gate biases,  $C_{low}$  and  $C_{high}$  are the same; as the gate bias is increased beyond the threshold at which electrons begin to populate the well, the  $C_{low}$  increases to a value larger than  $C_{high}$ . In the broad area case in the absence of magnetic field, the ratio of low to high frequency capacitances is very nearly independent of the electronic density (gate bias) in the well. By measuring the ratio,  $C_{low}/C_{high}$  in the quantum dot experiment and comparing this with the ratio (about 1.36) obtained in the broad area experiment, we can determine the fraction of the area in the quantum well which is filled with electrons. Since we know the number of quantum dots in a sample and the total area of the sample, we can thus determine the area of a dot.

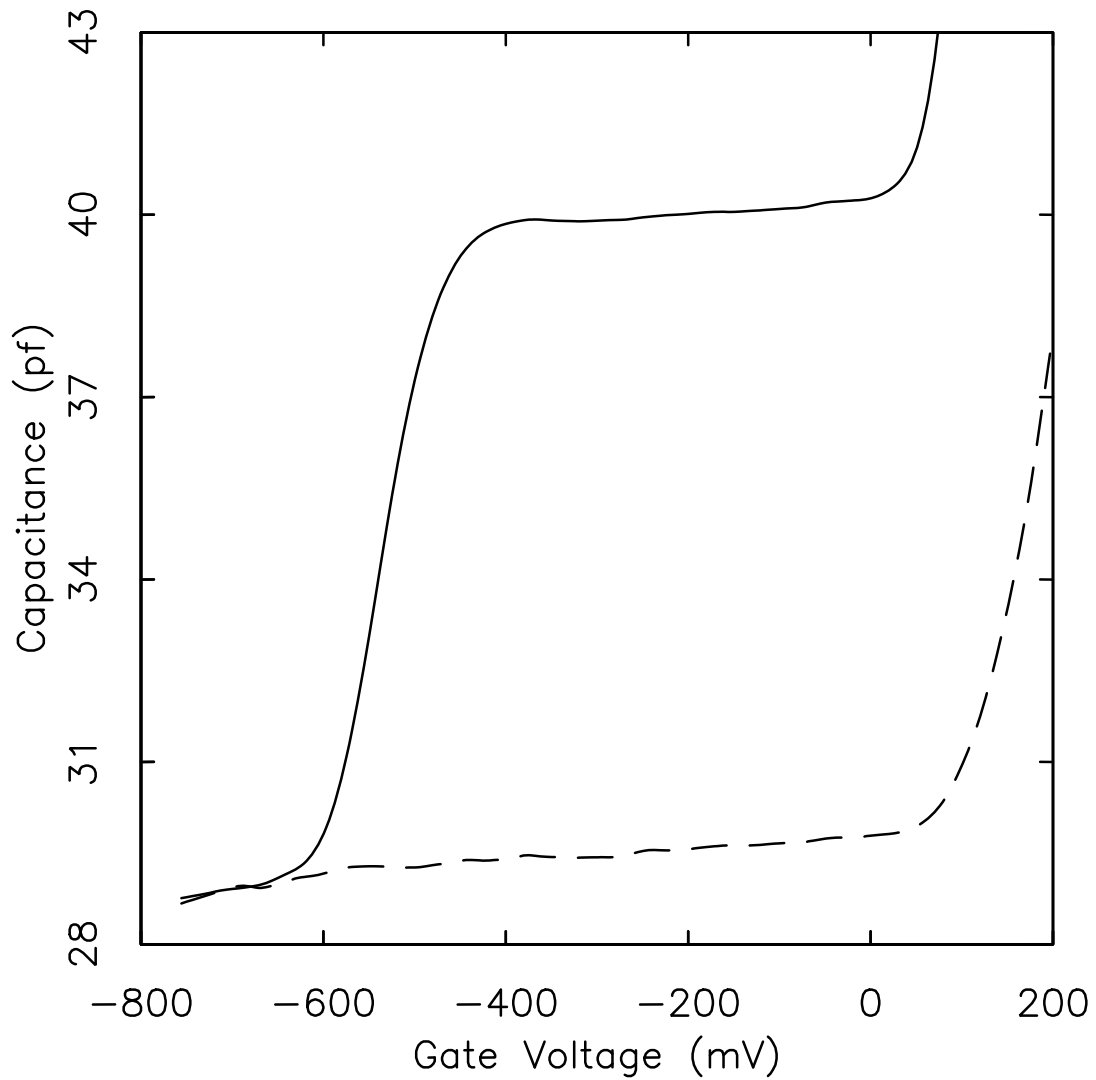


**Fig. 5.8** Low (solid) and high (dashed) frequency capacitance results from a  $200\ \mu\text{m}$  diameter broad area mesa with no patterning to produce quantum dots. The sharp rise in the low frequency capacitance occurs as the gate bias is increased beyond the threshold which allows electrons to enter the quantum well. The rise in both the low and high frequency capacitance at positive gate voltage occurs as electrons start to tunnel from the well to donors sites in the AlGaAs blocking barrier. These results were obtained from fits to data of the device capacitance vs. frequency.



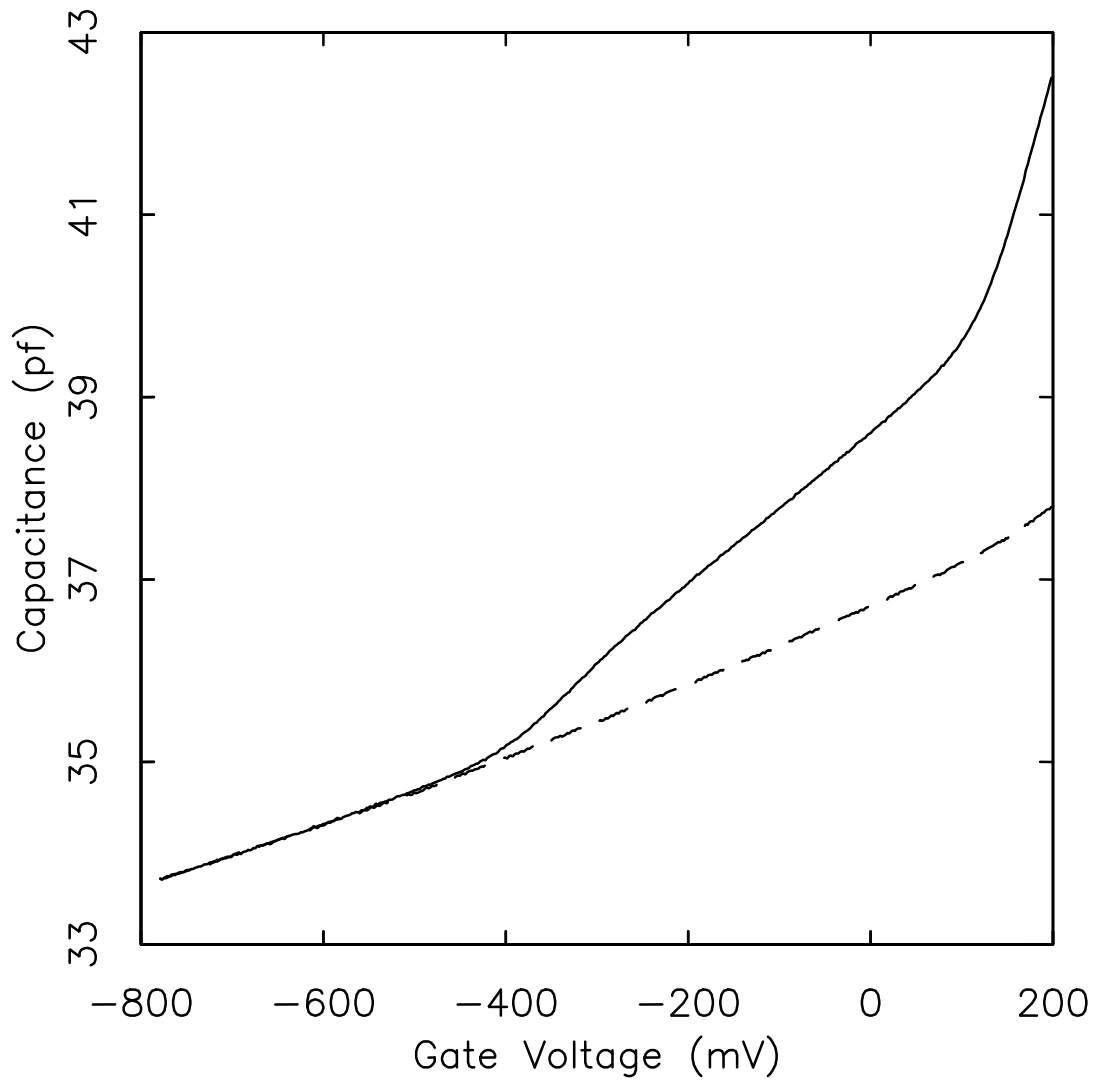


**Fig. 5.9** Low (solid) and high (dashed) frequency capacitances from a  $200\ \mu\text{m}$  wide square mesa of hexagonal patterns at 95 Hz and 25 kHz, frequencies low and high enough respectively so that the capacitance can be considered to be the low and high frequency limiting values. Notice the shift in the position of the bifurcation of the low and high frequency capacitances as compared to Fig. 5.8. The low frequency capacitance rises much more slowly at gate biases above this position in this sample than it does in the broad area mesa.

Figure 5.9 displays the low and high frequency capacitances from an array of dots produced using hexagonal shaped pillars (260 nm wide from edge to edge) in a hexagonal array (520 nm spacing between centers of nearest neighbors). Notice two striking differences between these results and the capacitances obtained for the broad area samples in Fig. 5.8. Firstly, the threshold gate voltage at which electrons begin to enter the well is significantly increased in the case of the quantum dot sample compared to the broad area sample. This is expected as a result of the extra repulsion of electrons away from the quantum well by the surface Schottky potential in etched regions of the sample surface. Secondly the increase of the  $C_{low}$  above  $C_{high}$  is much slower as the gate bias is increased compared to the broad area sample. This is a consequence of a slow increase of the area of a dot as the capacitance is increased.

Figure 5.10 graphically displays the model that we use to determine the area of a dot. Note that this figure is not drawn to scale. In reality the width of the pillars on top of the sample is several times larger than the distance from the metallic cap to the substrate. Our smallest pillar widths are 200 nm, whereas the pillars are 30 nm high. Also, the dot size is much larger than its spacing to the top metallic cap or the substrate for most of the operating range of the device. A main assumption in our model for the dot area determination is that electric field lines point only vertically through the sample structure. This assumption reasonable as long as the dot diameter is larger than around 50 nm (.002 square micron dot area). Using the model of Fig. 5.10 and neglecting fringing fields, it is easy to show that the fraction of the area occupied by electrons in the well,  $\alpha$  is given by:

$$\alpha = \left[ \frac{C_{low}}{C_{high}} - 1 \right] \left( \Upsilon - \frac{x_g - \delta}{x_g - D\delta} \right)^{-1}. \quad (5.1)$$

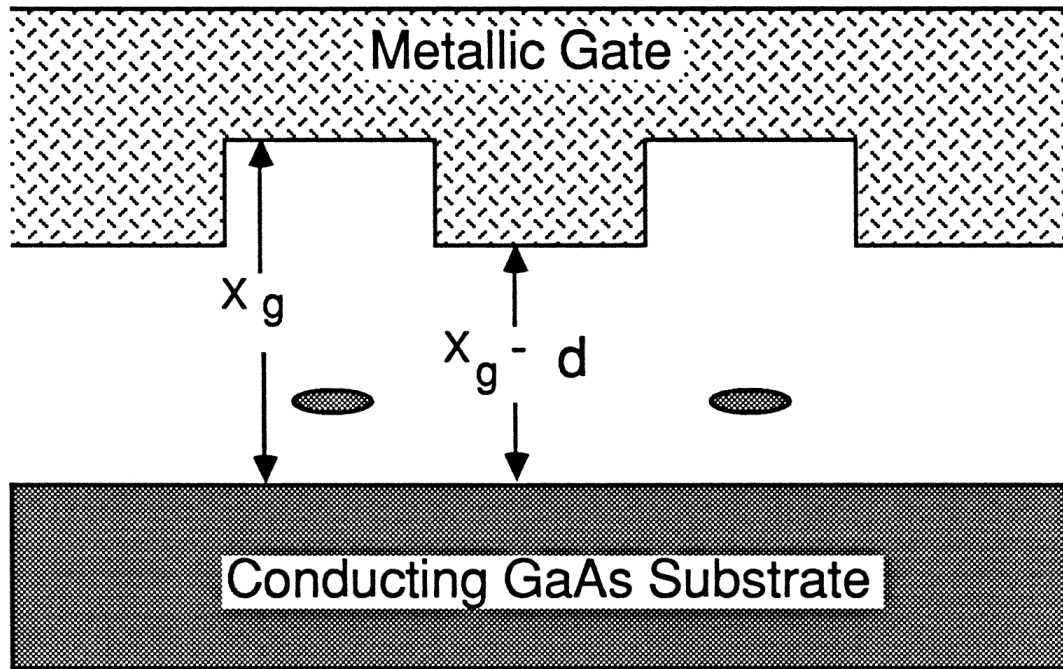


**Fig. 5.10** The figure shows the model of the quantum dot samples used to extract the area of electron packets from capacitance measurements. Note that the figure is not to scale. In actuality, the width of the pillars on top of the sample is several times larger than the distance from the metallic cap to the substrate, and the pillar is much wider than it is tall. Further, over much of operating range, the dot size is larger than its spacing to either the top metallic cap or the substrate.

Here we have denoted the distance from the conducting substrate to the top gate in unpatterned samples as  $x_g$ , the height of the pillars on the sample surface by  $\delta$ , the fractional area of the surface of the sample that is made up of pillars by  $D$ , and  $C_{low}/C_{high}$  for the broad area sample (in which  $D$  is effectively equal to one), with the quantum well occupied everywhere, by  $\Upsilon$ . Note that Eq. 5.1 is only correct when the area of the dot is smaller than the area of the pillar on the surface (true for all of our samples). We have assumed in the argument that led to Eq. 5.1 that the density of states per unit area and energy is the same for the broad area 2d electron gas as it is for the quantum dots. If this is indeed true, the density of states drops out of the equation for determining the occupied area entirely, as in Eq. 5.1. In any case level spacing in the well is an order of magnitude smaller than the electrostatic energy so errors due to any incorrectness of this assumption are likely to be very small.

The area of a dot is of course given by  $\alpha$  times the area of the entire sample divided by the number of pillars patterned onto the sample surface. Figure 5.11 displays the area determined from capacitance measurements on four samples with different size and shape patterned pillars. One obvious feature here is that smaller patterns produced on the sample surface create smaller sized dots whose threshold voltage for filling increases as the pattern size is made smaller. Results from above 0 mV gate bias in the figure should be ignored; the sharp rise in the plotted results here is an artifact caused by electrons tunneling from the well into donors in the doped region of the AlGaAs blocking barrier. Below 0 mV, it is clear that the size of the dot remains smaller than the size of the patterned pillar.

We can now compare these results with the computer calculation discussed earlier. Figure 5.12 shows the area from capacitance data for an array of

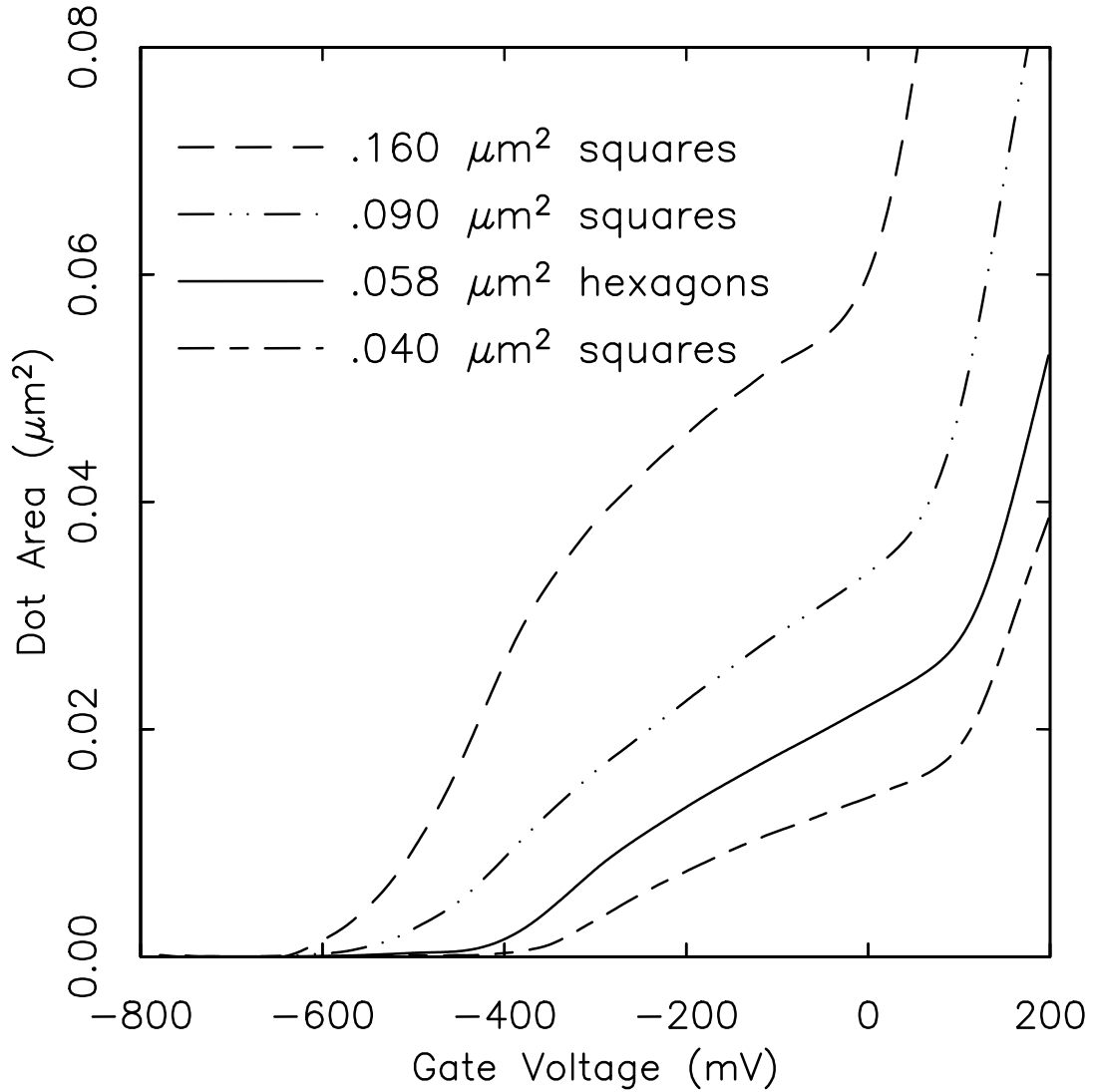


**Fig. 5.11** Areas of dots determined using Eq. 5.1 for various shapes and sizes of pillars on the sample surface. The top dashed line is from a sample with 400 nm wide square pillars spaced with centers 720 nm apart; the dashed-dotted line is from 300 nm square pillars with centers 600 nm apart; the solid line is from hexagonal shaped pillars with parallel sides 260 nm apart and with centers spaced 520 nm apart; the lower dashed curve is from 200 nm square pillars with centers spaced 450 nm apart. The actual pillar size may be slightly smaller due to undercutting during the freon RIE etching which produced the pillars. The sharp rise in the area of dots at positive gate biases should be ignored as this is an artifact caused by electrons tunneling to donor sites in the AlGaAs blocking barrier.

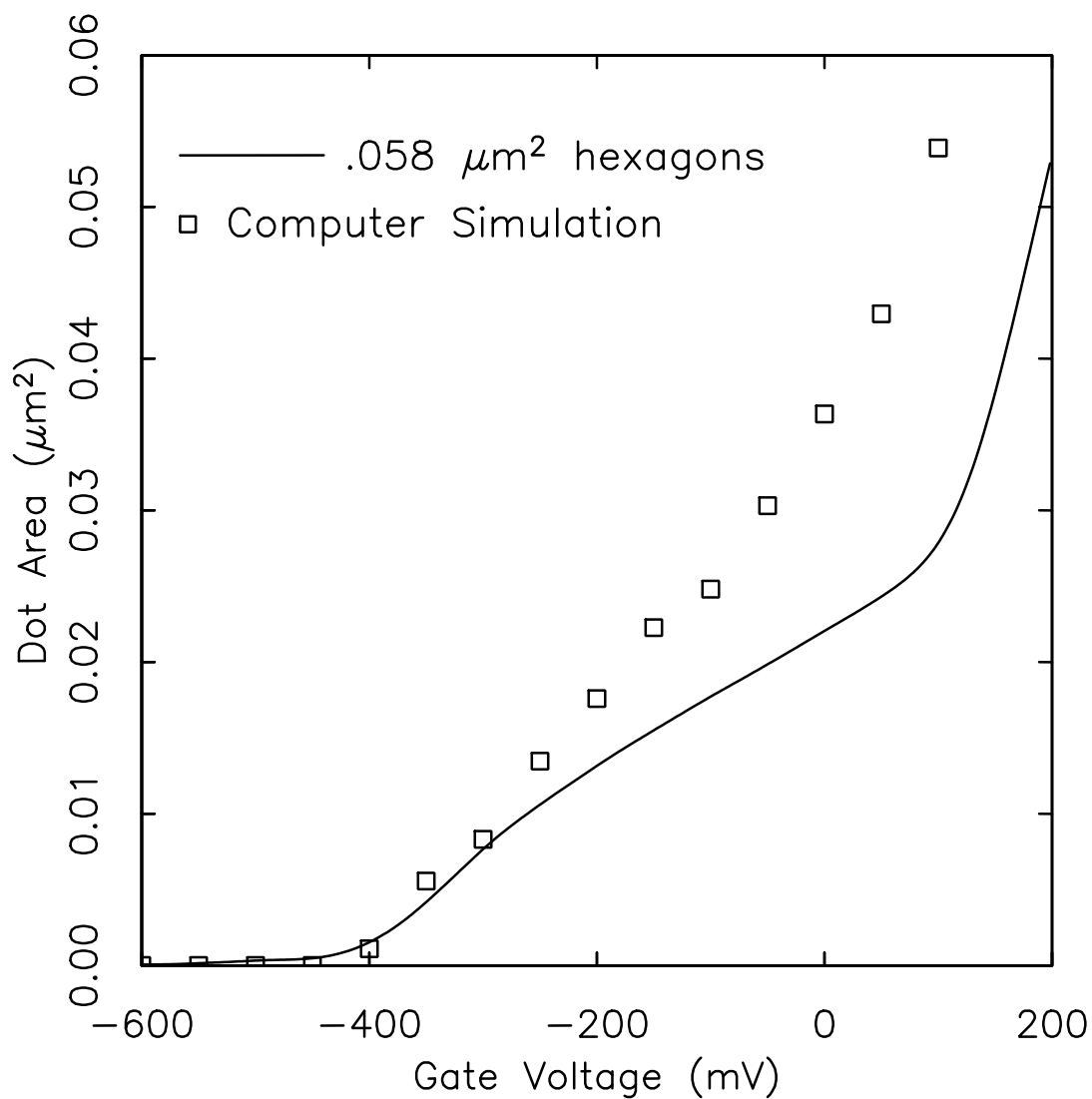


**Fig. 5.12** Area of dots underlying hexagonal pillars from capacitance data (solid) compared to computer calculation (boxes). The scatter in the calculation's results arises from digitization error. Note the horizontal and vertical scales are different here than in Fig. 5.11.

hexagonal dots compared with the calculated results. We make a few brief remarks on this calculation.<sup>5</sup> The calculation assumes a Schottky barrier height of 0.8 V on the sample surface. The doping density in the AlGaAs blocking barrier is adjusted so that the calculation correctly predicts the gate bias threshold for electrons to begin entering the quantum well in a broad area sample. A threshold in agreement with data is obtained if the doping density is adjusted to a value of  $5.75 \times 10^{17} \text{ cm}^{-3}$ , very close to the value estimated by the crystal grower<sup>21</sup> of  $6 \times 10^{17} \text{ cm}^{-3}$ . Particularly interesting in Fig. 5.12 is the fact that the computer calculation correctly predicts the gate bias threshold for filling the dots. This is true systematically for different size dots. The calculation does less well at predicting the size of the dot as it grows. The area from the calculation is, depending on gate bias, up to 50% larger than the area determined from capacitance data.

The disagreement in sample area between calculation and data in Fig. 5.12 may arise from several factors. The computer calculation is two-dimensional. It assumes cylindrical symmetry of potentials about the center of a dot. In the actual sample, neither the square or hexagonal pillars on the top surface or the positions of neighboring dots around a central dot have cylindrical symmetry. In the computer calculation, we simply adjust the radius of a cylindrical pillar so that it has the same area as the true square or hexagonal pillars. We also adjust the size of a “unit cell” in the calculation so that its area is the same as that of a unit cell in the actual sample configuration. A potentially important issue in the dot confinement is that of “etch damage”. The freon etch described above in the sample processing section which produced the pillars on the surface of the sample may, despite the very low bias voltage at which it was carried out, cause some etch damage. Similar etch damage has successfully been used by Scherer

and Roukes to produce confinement in a heterostructure with the 2d gas about 500 Å away from the sample surface with beams of 200 eV Ne ions.<sup>22</sup> These damage effects may confine our dots to a smaller area than would otherwise be expected from an electrostatics calculation alone.

Another effect, this time ignored in the determination of the dot area from the sample capacitance, is a contribution to the device capacitance due to the rate of increase of the dot area as the gate bias is increased. Back of the envelope calculations indicate that the actual dot area may, in a worse case picture of dots confined in lateral square well potentials, be as much as 50% smaller than the results indicated by Eq. 5.1. However, if the potential sidewalls of the dot are as gradual in slope as expected from computer calculations, this effect would increase the measured dot area by at most a few percent compared to the actual dot area. Correction for this effect would worsen agreement between the computer calculation for the dot size and the experimental results.

With the quantum dot system now reasonably well characterized, we now search in chapter 6 for new physics arising from the confinement of electrons in small packets.



## References

1. K. Kash, A. Scherer, J.M. Worlock, H.G. Craighead, and M.C. Tamargo, Appl. Phys. Lett. **49**, 1043 (1986)
2. W.E. Spicer, I. Lindau, P. Skeath, and C.Y. Su, J. Vac. Sci. Technol. **13**, 831 (1976)
3. M.H. Hecht, L.D. Bell, W.J. Kaiser, and F.J. Grunthaner, Appl. Phys. Lett. **55**, 780 (1989)
4. M.A. Reed, J.N. Randall, R.J. Aggarwal, R.J. Matyi, T.M. Moore, and A.E. Wetsel, Phys. Rev. Lett. **60**, 535 (1988)
5. J.A. Lebens, Ph.D. thesis, Cornell University (1988)
6. T.J. Thornton, M. Pepper, H. Ahmed, D. Andrews, and G.J. Davies, Phys. Rev. Lett. **56**, 1198 (1986)
7. K.F. Berggren, T.J. Thornton, D.J. Newson, and M. Pepper, Phys. Rev. Lett. **57**, 1769 (1986)
8. J. Alsmeier, E. Batke, and J.P. Kotthaus, Phys. Rev. B **41**, 1699 (1990)
9. N. Blanc, P. Guéret, P. Buchmann, K. Dätwyler, and P. Vettiger, Appl. Phys. Lett. **56**, 2216 (1990)
10. T.P. Smith, III, H. Arnot, J.M. Hong, C.M. Knoedler, S.E. Laux, and H. Schmid, Phys. Rev. Lett. **59**, 2802 (1987)
11. W. Hansen, T.P. Smith, III, K.Y. Lee, J.A. Brum, C.M. Knoedler, J.M. Hong, and D.P. Kern, Phys. Rev. Lett. **62**, 2168 (1989)
12. K.Y. Lee, T.P. Smith, III, H. Arnot, C.M. Knoedler, J.M. Hong, D.P. Kern, and S.E. Laux, J. Vac. Sci. Technol. B **6**, 1856 (1988)
13. Z. Lilental-Weber, N. Newman, J. Washburn, E.R. Weber, and W.E. Spicer, Appl. Phys. Lett. **54**, 356 (1989)
14. J. Coumeau, private communication
15. JEOL JB5DX11 users manual, unpublished
16. D. Woodard, private communication
17. K. Hikosaka, T. Mimura, and K. Joshin, Jpn. J. Appl. Phys. **20**, L847 (1981)
18. K.L. Seaward, N.J. Moll, and W.F. Stickle, J. Vac. Sci. Technol. B **6**, 1645 (1988)
19. M.L. Roukes, A. Scherer, and B.P. Van der Gaag, (unpublished)

20. John Lambe and R.C. Jaklevic, Phys. Rev. Lett. **22**, 1371 (1969)
21. L. Pfeiffer, private communication
22. A. Scherer and M.L. Roukes, Appl. Phys. Lett. **55**, 377 (1989)

## Chapter VI

### Observation of the Single Electron Addition Spectrum of Quantum Dots

#### 6.1 Introduction

In the last 25 years, technological advances have allowed the construction of “particles” so small that the addition or subtraction of an individual electron to them leads to experimentally observable effects. In a pioneering work, Giaver and Zeller<sup>1</sup> demonstrated the effects of the Coulomb repulsion of single electrons on the conductivity of a film of very small tin particles embedded in an oxide layer. The effects of this Coulomb repulsion of single electrons in small particles can be described by a “charging energy”,  $e^2/C$ , where  $C$  is the capacitance of the small particle to its environment. Manifestations of charging energy have been observed more recently by Fulton and Dolan<sup>2</sup> in a sample in which tunneling currents pass between two electrodes through a single small metal particle. The essential effect that they see is a lack of electric conduction through their device until the voltage across the device reaches a threshold beyond which electrons can overcome the Coulomb repulsion associated with tunneling to the particle. This effect has been dubbed the “Coulomb Blockade” in tunneling. The Coulomb blockade can also be observed in tunneling across small capacitors that do not contain a small particle under certain conditions depending on the impedance

of the the leads which transport charge to the capacitor.<sup>3</sup> Coulomb blockade effects have now been used to manipulate the motion of single electrons in multi-capacitor devices,<sup>4</sup> exposing the possibility that such devices may be used in “single electron logic” functions.

Aside from the Coulomb blockade, another more obvious effect in a small particle is the nonzero energy splitting of the quantized states of electrons in the small particle. Reed et. al.<sup>5</sup> believe to have observed the level splitting, associated with quantum confinement in all three dimensions, in tiny resonant tunneling diodes. Further, in an experiment in which electrons are added or subtracted from a small particle, these energies can be important as the Pauli principle forces newly added electrons into higher lying energy states.

This chapter focuses on the effects of both single electron charging energy and quantum level splitting in a large array of very small particles (quantum dots) coupled by tunneling to a metallic substrate. The dots were made by laterally confining electrons of a two dimensional electron gas using techniques described elsewhere.<sup>6</sup> The dots have an occupancy of electrons which can be varied by means of a gate bias. In a simple model, a single dot develops a spectrum of threshold gate voltages at which electrons are energetically allowed to tunnel into and out of the dot. The Coulomb blockade regulates the entrance of electrons into a dot, allowing them to be added only one at a time, with spacings between the electronic additions at intervals in gate bias as large as 30 mV.

The sizes of our dots increase as more electrons are added to them. In chapter 5, we determined the area of dots as a function of gate bias using capacitance measurements. Employing this, we develop a model which predicts a

spectrum of individual electronic additions. The spacing in gate voltage between electron additions to the dots decreases as the dot size increases.

We study the capacitance of these arrays to very high resolution as a function of gate bias and amplitude of measuring signal. Intriguing fluctuations, of amplitude on order 1 fF, are observed in the device capacitance. Some of these fluctuations consists of nearly periodic oscillations which can persist for many cycles. This periodic structure can be identified as a reflection of an almost regular spectrum of electron additions to the dots, with one oscillation occurring per electron addition to each of the dots in the array.

These experiments differ from previous experiments which studied coarse features in the capacitance spectra of quantum dots.<sup>7</sup> In our model for that work,<sup>8</sup> the capacitance fluctuations arise from statistical anomalies in the spectrum of electron additions to a single dot, on the scale of many electron additions. Here, we observe features in the capacitance arising from the addition of single electrons to the well.

Some of the work in this chapter has not been completed, and issues brought forth in the data have not been entirely resolved. A number of questions remain unanswered because further modeling of the system is required.

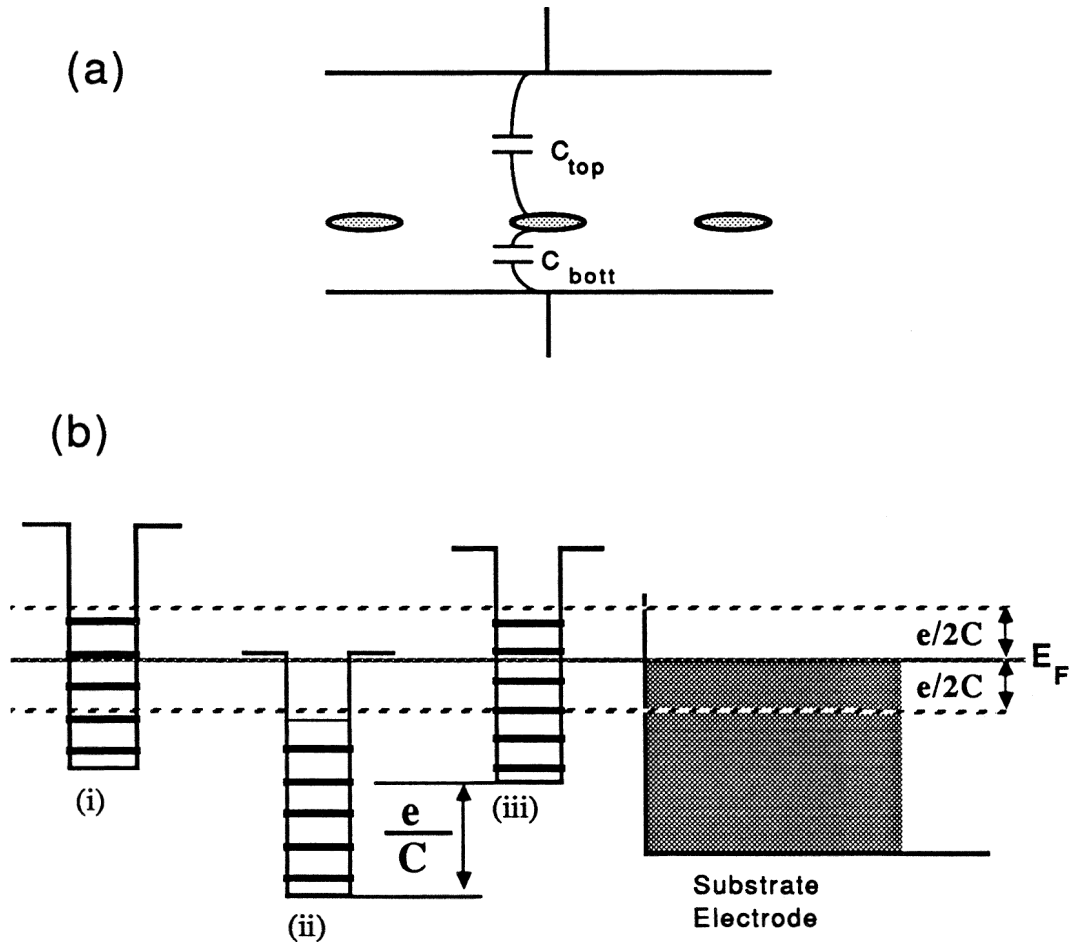
## 6.2 Equilibrium State of Quantum Dots

Figure 6.1a shows the basic schematic structure of our device. The device structure and fabrication were described in detail in chapter 5. Electrons, laterally confined in a GaAs quantum well, embedded in the dielectric of a semiconductor capacitor, can tunnel to an  $n^+$  GaAs conducting substrate (bottom capacitor plate) via an AlGaAs tunnel barrier. A gate bias applied between the two electrodes, a top metal gate and the conducting substrate,

of this capacitor varies the number of electrons in the dots. The dots were produced using electron beam lithographic techniques; the electron occupancy of those made with the smallest lithographic patterns (patterns of  $0.04 \mu\text{m}^2$  area) can be varied from 0 to about 60 electrons per dot by means of the gate bias. There are capacitances  $C_{top}$  and  $C_{bott}$  coupling the dot to the top gate and substrate electrodes respectively. We consider the capacitance of the dot to the surroundings to be  $C_{top} + C_{bott}$ , and refer to this sum as  $C$ . Our measurements involve both a conductance measurement of this tunneling, discussed later in this chapter, as well as measurements of the bulk device capacitance.

We briefly explore the energetics of electron transfer between the quantum dots and the substrate. In order to minimize the Gibbs free energy of the system, the Fermi energy in the well and the substrate tend to equalize. The nonzero Coulomb charging energy often makes exact alignment of Fermi energies impossible. Neglecting charging effects, an empty quantum level whose energy is less than the Fermi energy in the substrate would ordinarily be filled by tunneling from the substrate. Notice that, if charging effects are included, the addition of this one electron from the substrate increases the electrostatic potential of the dot. In fact, it may increase the dot potential so much so that the energy of the quantum level just filled may be greater than the Fermi energy in the substrate! The system is in a strange “pickle”, unable to equilibrate Fermi energies in the dot and in the substrate.

The solution to this problem is, of course, that the dot-substrate system minimizes its Gibbs free energy as well as it can without actually equilibrating the Fermi energies in the dot and in the substrate. Lambe and Jacklevic<sup>9</sup> first developed a model which was further elaborated by Cavicchi and Silsbee<sup>10</sup> to described tunneling of electrons between small metal particles, embedded in an



**Fig. 6.1** (a) schematically describes the structure of our devices. Small packets of electrons (dots) are embedded in a large capacitor. Tunneling of electrons is permitted between the dots and the bottom electrode of this capacitor; the dots are electrically insulated from the top electrode. Changing the voltage across the device (gate voltage) varies the electron occupancy within the dots from zero to as many as several hundred electrons. (b) depicts the “equilibrium zone” of width in energy  $e^2/C$  on either side of the substrate Fermi energy which develops as a manifestation of the “Coulomb blockade”. For simplicity, consider quantum levels in the dots to be nondegenerate. Dark bars in the wells shown to the left represent filled quantum levels. (i) depicts a dot in equilibrium even though its chemical potential is greater than that in the substrate. If this dot were to lose an electron, its chemical potential, due to the change in its electrostatic energy of  $e/C$  would fall below the lower edge of the equilibrium zone. In (ii), a nonequilibrium situation is shown with an unfilled level below the edge of the equilibrium zone. This level is filled in (iii) and the electrostatic energy of the dot increases by  $e/C$ .

oxide capacitor, to a metal electrode. The same models should be applicable to the GaAs quantum dot system, and we present them here. Figure 6.1b diagrams the energetics of transfer of electrons between the quantum dot and the substrate. An “equilibrium zone” within  $e^2/2C$  above and below the Fermi energy of the substrate develops, and dots with their Fermi energies within this zone do not gain or lose electrons. To induce a dot to take on another electron, its Fermi energy must first (by means of externally applied potentials) be made less than that in the substrate by an amount  $e^2/2C + \delta_n$ , where  $\delta_n$  is the quantum level spacing between the highest energy occupied state in the particle and that of the next one to be occupied when another electron is added to the dot. Once the electron tunnels into the dot, the Fermi energy of the dot rises by an amount  $e^2/C + \delta_n$ .

### 6.3 Spectrum of One Electron Additions to a Quantum Dot

The discussion of the last paragraph suggests, if the quantum level spacing in the dots is taken to be zero, that one electron will tunnel into a dot every time the electrostatic potential energy of a dot is decreased with respect to the substrate, by an amount of  $e^2/C$  (or  $\Delta$ ). These single electron additions would occur periodically as a function of the electrostatic potential energy of the dot if no changes were to take place in the capacitance of the dot to its surroundings as the electronic occupation of the dot varies. As discussed in chapter 5, the areas (lateral area in the quantum well) occupied by the quantum dots in our samples vary as the gate bias which controls the electron occupation of the dots is varied. This causes the dot capacitance to the surroundings and therefore the charging energy to also vary with gate bias.



As alluded to above, in our samples the quantum level splitting is actually a substantial fraction of the charging energy further complicating the spectrum of electron additions to the dot. The important parameter in the case of capacitance fluctuations is the mean energy splitting  $\delta$  between quantum levels, *not* including in the average the zero splitting of degenerate levels. We note that as the size of the dots increases both the charging energy,  $\Delta$ , and the mean quantum level splitting,  $\delta$ , decrease, but their ratio remains fixed. These arguments are detailed in chapter 7. In our samples,  $\Delta/\delta \approx 3$ .

We now describe a model calculation which determines a spectrum of electron additions to the quantum dots. The results here are calculated assuming a circular dot shape with infinite walls and with area equal to the area determined using the capacitance given in chapter 5. The procedure consisted of several steps. First the quantum level structure for a dot of constant area  $A_0$  appropriate to a given gate bias  $V_0$  is calculated. The levels are spin degenerate and most are (doubly) orbitally degenerate as well. For this model the mean level splitting  $\delta$  between sets of these degenerate levels is about four times the inverse of the DOS, or  $\delta \approx 4\pi\hbar^2/A_0m^*$ . The constant charging energy  $\Delta_0$  corresponding to a dot of area  $A_0$  is determined using knowledge of the dielectric constant and distances from the charge in the quantum well to the top gate and the substrate in our samples. This energy is added for each *electron* (not each level) in the quantum level structure. This results in a spectrum with initially two and four fold spin and orbitally degenerate levels spaced by an amount,  $\Delta_0$ , with spacings between electron additions from different degenerate levels equal to  $\Delta_0 + \delta_n$ , where  $\delta_n$  (the index  $n$  is number of electrons in the dot) is the quantum level splitting between the sets of degenerate levels. Because  $\Delta_0$  is

typically a factor of three larger than  $\delta_n$ , this spectrum is almost periodic, but with slight irregularities in moving between the degenerate levels.

This spectrum is now converted to the dot filling spectrum one would expect as a function of gate bias for this fictitious dot of constant area. This is accomplished by multiplying the spectrum by the inverse of a “geometric lever-arm”  $\kappa$  ( this inverse value is approximately given by  $[C_{bott}/C_{top}] + 1$ ) which describes the amount by which the electrostatic potential at the dot varies for changes in the gate bias. In our samples  $\kappa$  is about 0.28, as determined from low and high frequency capacitance measurements on unpatterned samples discussed in chapter 5. The results of this calculation for  $A_0 = 0.014 \mu\text{m}^2$  are shown in Fig. 6.2a.

At this point, a correction must be made for the variation of the dot area as the gate bias is varied. As both Coulomb energies and quantum level spacings both scale inversely with dot area, this simply amounts to transforming the voltage scale through dividing it by the ratio of the dot area to the constant area of the dots assumed in the calculations of the last paragraph. Conveniently, in chapter 5 we determined the area of our dots as a function of gate bias,  $A(V_b)$  from capacitance measurements. There is a subtlety here which involves the fact that the calculated spectrum is not yet in gate bias coordinates,  $V_b$ ; it is instead given in the coordinates of the model  $V_m$  for a dot of fixed area rather than for an area which depends on bias. Because all energies in the problem scale with area, the two coordinate systems are related by

$$V_b = \frac{A_0}{A(V_b)} V_m. \quad (6.1)$$

We start with a spectrum known in terms of  $V_m$  and must solve this implicit equation to obtain the area in model coordinates  $A^*(V_m)$  so that the translation

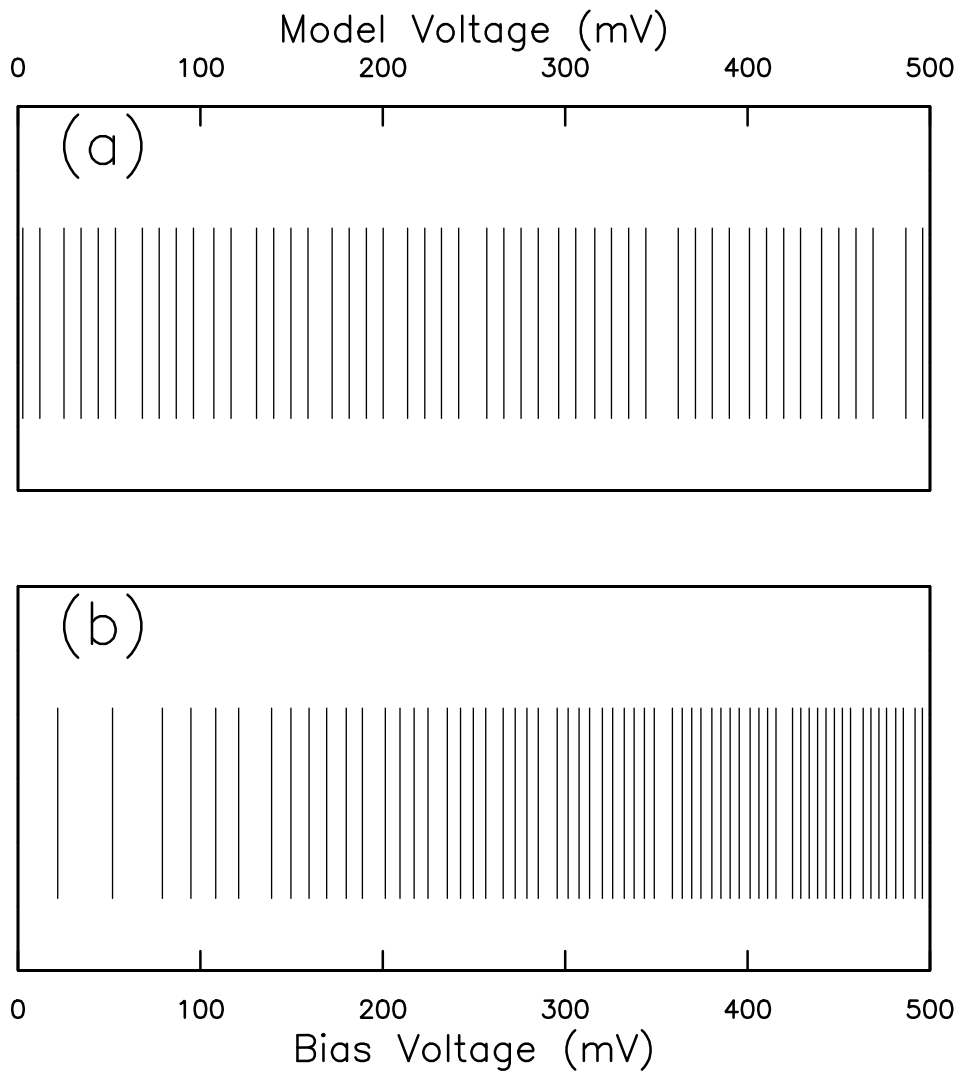


**Fig. 6.2** (a) portrays the electron addition spectrum for circular dots of area  $.014 \mu\text{m}^2$  after multiplication by the inverse of the geometric lever arm ( $\frac{1}{\kappa} \approx 3.6$ ) in this sample. (b) shows this spectrum after the area correction described in the text. The areas of the model before and after the varying area correction are the same at a gate bias of 355 mV. At this gate bias, both before and after the area correction the dots contain 34 electrons.

of the calculated spectrum into device (gate bias) coordinates can be accomplished. Once  $A^*(V_m)$  is known the mapping of the calculated results is made using

$$V_b = \frac{A_0}{A^*(V_m)} V_m. \quad (6.2)$$

We refer to the number of electrons in a dot as  $n$ . Reversing the statements given above relating the spacing between electron additions and the dot area given above, the following relation holds:

$$A(V_b) = K \frac{dn}{dV_b}.$$

Here  $K$  is a constant. Using the chain rule, we now write the area of the dot as

$$A = K \frac{dn}{dV_m} \frac{dV_m}{dV_b}. \quad (6.3)$$

Obviously, since the model was calculated for a dot of constant size,  $dn/dV_m$  is just a constant.

The problem is made easily solvable using the empirical fact that  $A(V_b)$  is fit well by a power law. The voltage,  $V_0$  at which the dot area is equal to  $A_0$  (by Eq. 6.1) is the same in both model and gate bias coordinates, so we write

$$A(V_b) = A_0 \left( \frac{V_b}{V_0} \right)^B. \quad (6.4)$$

Here  $B$  is the exponent in the power law determined from data of the area as a function of gate bias. It is simple to show using Eqs. 6.1 and 6.2 that if  $A(V_b)$  is given by a power law, so is  $A^*(V_m)$ . Hence we can write

$$A^*(V_m) = A_0 \left( \frac{V_m}{V_0} \right)^M. \quad (6.5)$$

Placing this expression for  $A^*(V_m)$  in Eq. 6.2, it follows that

$$V_b = V_0^M V_m^{1-M},$$

and

$$\frac{dV_m}{dV_b} = \frac{1}{1-M} \left( \frac{V_m}{V_0} \right)^M.$$

Equation 6.3 then gives

$$A = \frac{K}{1-M} \frac{dn}{dV_m} \left( \frac{V_m}{V_0} \right)^M = \frac{K}{1-M} \frac{dn}{dV_m} \left( \frac{V_b}{V_m} \right)^{\frac{M}{1-M}}.$$

Because  $dn/dV_m$  is a constant, we identify the exponent  $M/(1-M)$  as the exponent  $B$  in Eq. 6.4. Thus the exponent  $M$  is given by

$$M = \frac{B}{1+B}, \quad (6.6)$$

and  $A^*(V_m)$  is now determined.

The model spectrum abscissa is thus simply converted to gate bias using Eq. 6.2 with the dot area given by the power law in Eq. 6.5 with the exponent from Eq. 6.6. The resulting electron addition spectrum, after area correction using data of the area vs. gate bias from our smallest lithographically patterned dots, is plotted in Fig. 6.2b. These smallest dots were made using square patterns on the sample surface of area  $.04 \mu\text{m}^2$  as described in chapter 5. The exponent  $B$  in the power law fit to their area is 0.76.

## 6.4 Capacitance Fluctuations Expected in an Array of Quantum Dots

### *Capacitance Signal Due to Electron Transfer to Dots*

At particular gate biases at which one electron can enter a dot, a peak in the device capacitance occurs. This can be explained using the following simple argument. When an electron leaves or enters a single dot to or from the substrate, the charge on the entire device changes by an amount  $e\kappa$  because the electron traverses only part-way through the device. Consider the addition of

the  $n^{\text{th}}$  electron to only this one dot, which occurs at gate bias  $V_n$ . At zero temperature, the charge on the device, due to this transfer, as a time varying voltage  $V(t)$  is applied across the device is given by

$$Q = e\kappa\theta(V(t) - V_n),$$

where  $\theta$  is the Heaviside function (zero for argument less than zero, one for argument greater than zero). Taking the derivative with respect to time, we find

$$I = \frac{dQ}{dt} = e\kappa\delta(V(t) - V_n)\frac{dV(t)}{dt}.$$

The contribution of the electron transfer to the device capacitance (measured with infinitesimally small signals) is the term multiplying  $dV(t)/dt$  in this equation. At higher temperatures, this  $\delta$  function should be replaced by  $df(V - V_n)/dV_n$ , the derivative of the Fermi distribution function (replacing the energy in  $f$  with  $V$ , the chemical potential with  $V_n$ , and the temperature  $T$  with  $T/e$ ).

Consider next the addition of the  $n^{\text{th}}$  electron to each of the dots in a large array at zero temperature. Due to inhomogeneities in the device, the gate voltage of this transfer varies among the different dots. The transfers for the  $n^{\text{th}}$  electron are distributed according to some distribution function  $\rho_n(V)$  which, at zero temperature, is given by

$$\rho_n(V) = \sum_{d=1}^N \delta(V - V_{n,d}),$$

where the  $V_{n,d}$  are the voltages at which transfer of the  $n^{\text{th}}$  electron from the substrate to the  $d^{\text{th}}$  dot takes place, and  $N$  is the total number of dots. We define  $\rho_n(V)$  at finite temperatures to be given by

$$\rho_n(V) = \sum_{d=1}^N \frac{\partial f(V - V_{n,d})}{\partial V_{n,d}}.$$

The device capacitance due to the addition of the  $n^{\text{th}}$  electron to each of the dots is given by  $e\kappa\rho_n(V)$ .

For the rest of this chapter, we consider the electron addition spectra of different dots to be identical except for displacements of the origin (this model is justified somewhat by the results from measurements shown in section 6.6). In this case, for each electron added (for each value of  $n$ ),  $\rho_n(V)$  is identical, with only its origin shifted due to the voltage spacing between electron additions. We then define  $V_d$  to be the voltage at which the  $n^{\text{th}}$  electron is transferred to the  $d^{\text{th}}$  dot, measured from the mean voltage for the addition of the  $n^{\text{th}}$  electron  $\overline{V}_n$  to each of the dots in the array. Since the spectra of different dots just have their origins shifted,  $V_d$  is the same for a particular dot irrespective of the value of  $n$ . We define  $\rho(V)$  by

$$\rho(V) = \sum_{d=1}^N \frac{\partial f(V - V_d)}{\partial V_d}.$$

The device capacitance due to the transfer of the  $n^{\text{th}}$  electron to each of the dots in the device is given by  $e\kappa\rho(V - \overline{V}_n)$  independent of  $n$ . The total capacitance due to all electron transfers of any value of  $n$ ,  $C_{dots}$  is given by

$$C_{dots} = e\kappa \sum_{n=0}^{\infty} \rho(V - \overline{V}_n) \equiv e\kappa\gamma(V). \quad (6.7)$$

Here  $\gamma(V)$  is just the sum of  $\rho(V)$  repeated at the mean voltage  $\overline{V}_n$  for each electron addition.

### *Rough Arguments For Capacitance Fluctuation Size*

At the temperatures of our experiments ( $\approx 1.5$  K),  $k_B T$  is large enough, and the different  $V_d$ 's for the different dots closely spaced enough, that  $\rho$  is a smooth function of gate voltage. There are however, fluctuations in this shape

due statistical variations in the distribution of  $V_d$ 's. For simplicity, first consider the  $V_d$  to be randomly distributed with equal probability over a range  $V_t$  and with zero probability for all other voltages. Then the mean value of  $\rho$  is given by  $\bar{\rho}(V) = N/V_t$  in this voltage range and zero for all other voltages. We focus on  $\rho$  over a voltage range of width  $\Delta V$  within  $V_t$ . On average, within the range spanned by  $\Delta V$ ,  $N\Delta V/V_t$  different dots in the sample will have allowed electron transfers. Depending on the position in the span  $V_t$  at which we are looking, the fluctuations in the number of electron transfers to different dots over a range  $\Delta V_d$  are  $\sqrt{N\Delta V/V_t}$ .

Consider for this discussion the capacitance signal due to the  $n^{\text{th}}$  electron addition to each of the dots in the array. Given that  $\rho$  consists of  $\bar{\rho} + \delta\rho$ , where  $\delta\rho$  is the fluctuations in  $\rho$ , fluctuations will be seen in the device capacitance due to  $\delta\rho$ . Now take the voltage  $\Delta V$ , discussed in the last paragraph, to be the amplitude of the measuring voltage,  $V_{meas}$  used in capacitance measurements. Taking  $\Delta V = V_{meas}$  to be much larger than  $k_B T / e\kappa$ , the average capacitance signal from an electron transfer to a single dot is equal to  $e\kappa / \Delta V$ . The size of fluctuations in the device capacitance due to fluctuations in  $\rho$  is

$$\delta C \approx \frac{e\kappa}{\Delta V} \sqrt{\frac{N\Delta V}{V_t}} = \frac{e\kappa}{\sqrt{V_{meas}}} \sqrt{\frac{N}{V_t}}. \quad (6.8)$$

From Eq. 6.8, it is clear that the fluctuations in the device capacitance decrease as the measuring voltage is increased.

In the simplest picture in which the area of the dots is a constant and the quantum level spacing in the dots is so small that it can be ignored, the electron additions occur periodically in gate voltage for the dots, with period  $e/\kappa C$ . If  $e/\kappa C$  were larger than the spread in threshold voltages,  $V_t$ , then  $C_{dots}(V)$  would consist of a periodic reflection of  $\rho(V)$ , with capacitance fluctuations due to  $\delta\rho(V)$  also occurring periodically in gate voltage. In another case, with  $V_t$



larger than  $e/\kappa C$ ,  $C_{dots}$  is aperiodic for the voltage range over the first few electron additions, but for gate voltages larger than  $V_t$ , the spectrum again becomes periodic. This behavior is due to the overlapping of  $\rho(V - \overline{V}_n)$  for different electron additions in Eq. 6.7. The size of the capacitance fluctuations is now different from that given in Eq. 6.8. At gate voltages larger than  $V_t$ , it is assured that in any interval of gate voltage  $e/\kappa C$  there will be one electronic transfer to every dot in the system. In this case,  $V_t$  in Eq. 6.8 should be replaced by  $e/\kappa C$ . The fluctuations in the capacitance are now given by

$$\delta C_{dots} \approx \frac{e\kappa}{\sqrt{V_{meas}}} \sqrt{\frac{N}{(e/\kappa C)}}. \quad (6.9)$$

For a sample with 200,000 dots,  $\kappa$  of 0.28, and a 2.5 mV charging energy ( $e/C$ ), and measured with a 2.5 mV amplitude signal, Eq. 6.9 indicates that the fluctuations observed in the capacitance, due to statistical variation in the thresholds for accumulating electrons among the different dots, will be of rms magnitude 4 fF. As shown later, the observed capacitance fluctuations in our devices have nearly the same, but smaller, amplitude. The details of the capacitance measurement technique must be described for better comparison, as is done below. Our samples are made more complicated to understand by irregularities in the electron addition spectrum caused by the quantum level structure in the samples as well as the changing area of the quantum dots. Further below we discuss a model which includes these irregularities.

#### *Evaluation of the breadth of the $V_d$ distribution*

The width of the distribution of thresholds can be judged from the shape of the increase of the device capacitance as the first electrons begin to enter the dots. We determine the total capacitance due to electron transfer to the dots

$C_{dots}$  using Eq. 6.7 and the spectrum of electron additions shown in Fig. 6.2b. We consider the smooth part of distribution of thresholds,  $\overline{\rho}(V)$  to be given by a Gaussian shape and multiply this by  $e\kappa$  to give the capacitance signal (smooth part) from each electron addition to the array of dots. We neglect capacitance fluctuations caused by  $\delta\rho$  because they are too small to be of importance for our purposes here. This Gaussian is normalized so that its integral over gate voltage is equal to  $N$ , the number of dots in the sample. It is repeated at every electron addition in Fig. 6.2b as indicated by Eq. 6.7 to give the total device capacitance due to charge transfer to the dots.

In Fig. 6.3 shows the experimental capacitance signal due to transfer of electrons to dots in a sample of 200 nm wide square lithographic patterns on the sample surface (the same sample whose area as a function of gate bias was used to generate Fig. 6.2b). The capacitance of our device is a function of frequency. At frequencies low enough that equilibrating electron transfer between the dots and the substrate occurs in one cycle of the measuring voltage the capacitance  $C_{low}$  is measured; at high frequencies where no electron transfer occurs,  $C_{high}$  is measured.  $C_{low}$  contains both the background device capacitance and the capacitance due to electron transfer to the dots;  $C_{high}$  contains only the background capacitance.  $C_{low} - C_{high}$  is the capacitance signal due solely to electron transfer to the dots, and this is the solid curve of Fig. 6.3. Shown also in Fig. 6.3 is the device capacitance modeled using the above protocol with an rms width of  $\overline{\rho}(V)$  of 35 mV. Note that 355 mV has been subtracted from the abscissa of the model curve to match the device threshold. -355 mV was also used as the origin in the power law fit to the device area used in the calculation of the electron addition spectrum.

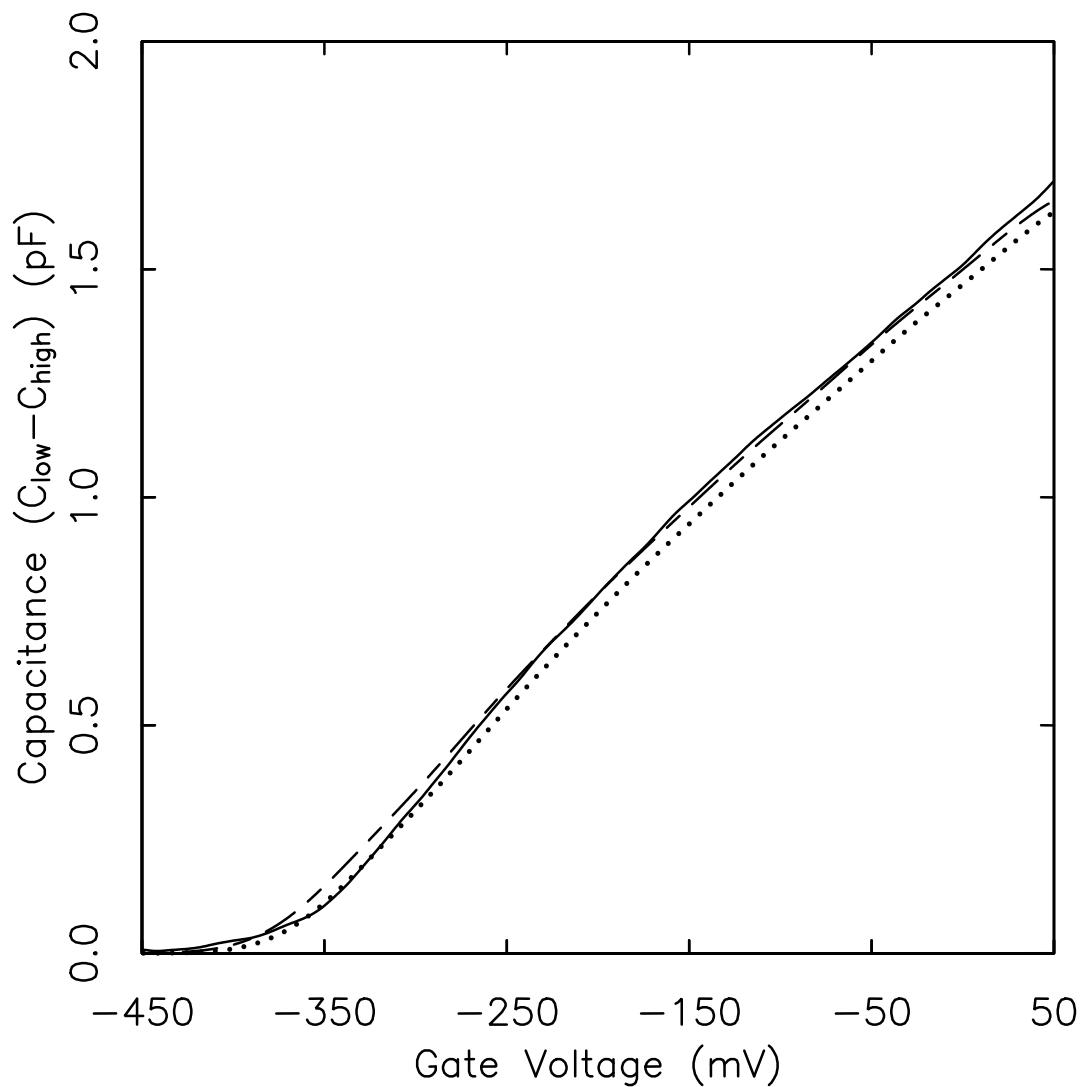


**Fig. 6.3** The solid curve is the device capacitance at low frequencies minus the high frequency capacitance. This signal is the capacitance resulting from electron transfer between the quantum dots and the substrate. The dashed curve is the capacitance obtained assuming a Gaussian distribution, of rms width 35 mV, of threshold voltages for the different quantum dots in the array and using the protocol for obtaining the device capacitance described in the text. The dotted curve is the same as the dashed curve except that it has been shifted by 10 mV.

We see the results from the model agree well with the measured capacitance of the device. This is not altogether surprising as the area of the dot used in determining the electron addition spectrum was initially obtained from these capacitance data.<sup>6</sup> However, the agreement also arises from a propitious choice of charging energy per unit area of the dot. In the calculation of the electron addition spectrum, we chose a value of  $\Delta_0$  of 2.6 meV based on a simple parallel plate capacitor argument for the capacitance of a  $0.014 \mu\text{m}^2$  area dot. Using a larger value for  $\Delta_0$  would cause the simulated results in Fig. 6.3 to fall below the capacitance data. The results confirm the validity of the method of section 6.3 for the determination of the electron addition spectrum. The region of importance for our purposes here is the device capacitance at the gate bias threshold where electrons begin to enter the dots. The device capacitance displays a tail, and at gate voltages above this tail the capacitance increases with a much steeper slope. This tailing arises from inhomogeneity in the thresholds for adding the first electron to each of the dots. We use this tail to estimate the spread in dot thresholds.

The model does not fit the data well at gate biases where electrons first begin to enter the dots. This is a difficult region to understand because the dots are so small that fringing fields are expected become important in determining the dot capacitance and the fact that there are only a few electrons in the dot may demand a rigorous quantum mechanical solution to the problem. We skirt these problems by assuming the breadth of the first electron addition among the different dots is responsible for the observed tail in the capacitance. We adjust the model results by shifting them by 10 mV towards positive gate bias, so that the capacitance at low bias for both the model and the data have substantial overlap. Then the breadth of the Gaussian distribution of thresholds is adjusted

to give the best fit of these two curves. The model curve adjusted this way is shown as the dotted curve in Fig. 6.3.

Notice that the tail in the capacitance appears slightly longer than that in the model. We have tried using different widths of the threshold distribution function to fit this curve better. We find that although wider (e.g. rms width of 45 mV) distributions fit the tail of the capacitance better, they match the region of high curvature (around -350 mV) less well. We find that the 35 mV rms wide Gaussian fits this region much better. Perhaps forms other than a Gaussian distribution should be examined. In any case, we determine through examination of the threshold for accumulation that the rms width of the distribution function is between 35 and 45 mV. Our models of the fluctuation spectrum of the capacitance are not sensitive to the precise width; we proceed assuming a width of 35 mV.

This 35 mV width (83 mV full width at half maximum) is larger than  $e/\kappa C$  over almost the full range of gate biases in the device. Further, this wide distribution is consistent with our lack of observation of large capacitance features associated with statistical anomalies (*not* in dot thresholds for accumulating electrons in different dots as characterized by  $\delta\rho$ ) in the spectrum of single electron additions in a single dot. In chapter 7, we show that a narrower threshold distribution (11 mV for the electron addition spectrum shown in chapter 7) allows observation of these fluctuations.

### *Sinusoidal Measuring Signals; More Formal Model*

In our experiment, the capacitance of samples is measured using sinusoidal signals. To understand better the capacitance spectra that are observed, we

briefly explore the implications of our capacitance measurement technique for the observed capacitance fluctuations.

A sinusoidal measuring voltage,  $V = \beta \sin(\omega_0 t)$  is applied across our samples, and the current through the device is observed by means of a lock-in amplifier. The current due to transfer of electrons to and from the dots is given by  $I = C_{dots} dV/dt$  or

$$I = e\kappa\gamma(V_0 + \beta \sin(\omega_0 t))\beta\omega_0 \cos(\omega_0 t). \quad (6.10)$$

Here  $V_0$  is the dc bias applied to the sample. Notice that the time varying voltage forces the value of  $\gamma$  to be time varying as well. The lock-in detects only the components of this signal at frequency  $\omega_0$  and not the harmonics generated by the time varying amplitude in this equation. The output of the lock-in channel out of phase with the reference signal  $\beta \sin(\omega_0 t)$  is given by the coefficient of the cosine component of a discrete Fourier transform of this signal at frequency  $\omega_0$ . This is given by

$$e\kappa \frac{\omega_0}{\pi} \int_0^{2\pi/\omega_0} \gamma(V_0 + \beta \sin(\omega_0 t))\beta\omega_0 \cos^2(\omega_0 t) dt.$$

Using a change of variables,  $U = V_0 + \beta \sin(\omega_0 t)$ , recognizing that this Fourier coefficient divided by  $\beta\omega_0$  is the capacitance that the lock-in measures,  $C_{lock}$ , and recalling that  $C_{dots} = e\kappa\gamma$  gives

$$C_{lock}(V_0) = \frac{2}{\pi\beta} \int_{V_0-\beta}^{V_0+\beta} C_{dots}(U) \sqrt{1 - \left(\frac{U - V_0}{\beta}\right)^2} dU. \quad (6.11)$$

In words, the capacitance spectrum measured by the lock-in is simply a convolution of the device capacitance for infinitesimal measuring voltage given in Eq. 6.7 by the “ellipse function” given by the square root in Eq 6.11 and normalized by multiplying the result by  $2/\pi\beta$ . This ellipse function is plotted in Fig 6.4.

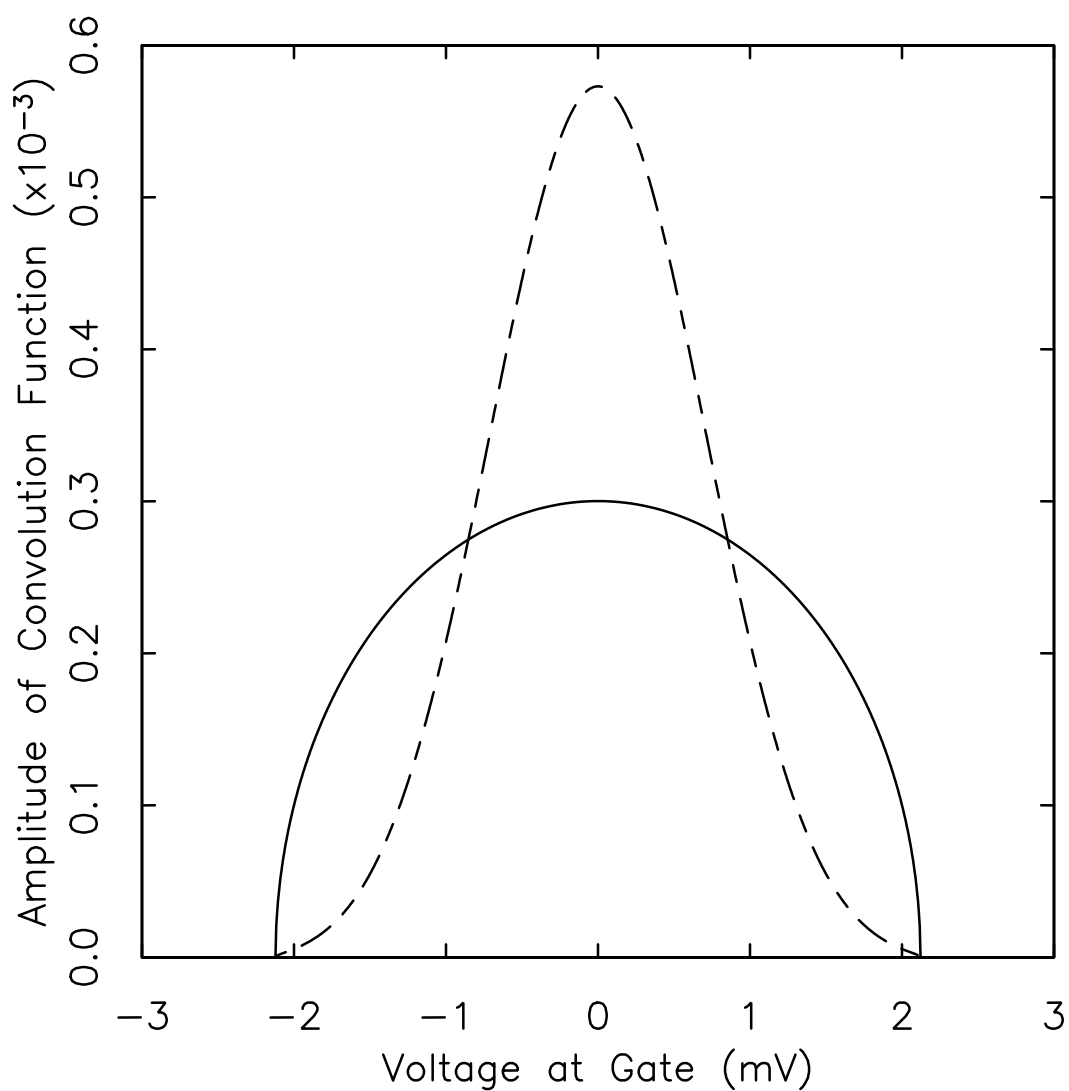


**Fig. 6.4** The solid curve plots the ellipse function described in the text which is convolved with the capacitance ideally measured at infinitesimal measuring voltage to give the capacitance indicated by the lock-in amplifier. The ellipse is for a 1.5 mV rms sinusoidal measuring voltage. The dashed curve shows the convolution function imagined for capacitance measurements made at higher frequencies where there is insufficient time in a half cycle of the measuring voltage for equilibration of the dots and substrate to occur. See section 6.5 for explanation.

### *Simulated Capacitance Spectrum*

We are now in a position to create a simulated capacitance spectrum using the ideas given above and to compare it, and fluctuations in it, with data that we have taken. A Gaussian form is assumed for  $\bar{\rho}(V)$  is assumed (the precise shape of  $\bar{\rho}(V)$  is irrelevant to our arguments).  $\rho$  is given by

$$\rho(V) = \frac{N}{\sqrt{2\pi}\Gamma} \exp\left[\frac{-V^2}{2\Gamma^2}\right] + \delta\rho(V). \quad (6.12)$$

Here  $\Gamma$  is the rms width of the distribution, and  $\delta\rho(V)$  gives the fluctuations in  $\rho$ . Consider that over an interval of gate bias  $\Delta V$  the number of particles allowing tunneling is, of course,  $\rho\Delta V$ . The rms size of the fluctuations in this number is given by  $\sqrt{\rho\Delta V}$ .  $\delta\rho$  is given the by fluctuation in number divided by the interval over which the number was obtained. The rms size of  $\delta\rho$  when measured over the interval  $\Delta V$  is equal to  $\sqrt{\rho/\Delta V}$ .

We now describe the method used to produce the simulated fluctuations in the device capacitance. We commence by modeling the capacitance fluctuations due to the  $n^{\text{th}}$  electron addition to each of the dots in the array. These fluctuations are obtained in our computer models by starting with a noise signal whose points are Gaussian distributed with an rms amplitude of one. There is a discrete spacing between points of  $\Delta V_p$ . This random noise signal is multiplied with the square root of the smooth part of  $\rho$  divided by the point spacing. The spacing  $\Delta V_p$  (typically 0.2 mV) is chosen to be much smaller than the amplitude of the measuring voltages used so as not to influence the final outcome of the simulation. These fluctuations are convolved with the derivative of the Fermi distribution function to account for the effects of nonzero temperature. A temperature of  $(1/\kappa)T$  is used to account for the effects of the geometric lever-arm. Given that most of our data was taken at 1.4 K, this distribution function



has a width of  $(1/\kappa)k_B T$  of about 0.4 mV. For modeling fluctuations, a replica of  $\delta\rho(V)$  is reproduced at every electron addition in the spectrum of Fig. 6.2b. These repeating fluctuations are then multiplied by  $e\kappa$  and lastly convolved with the ellipse function described above.

Shown in Fig. 6.5 is a computer generated version of  $e\kappa\delta\rho(V)$ , the capacitance fluctuations due to the  $n^{\text{th}}$  electron addition to the dots, after convolution with the ellipse function. We have used  $\Gamma$  in Eq. 6.12 equal to 35 mV, a measuring voltage of 2.4 mV rms ( $\beta = 3.4$  mV), and a temperature of 1.4 K. Note that the effect of the temperature, which is smaller than the measuring voltage in this case, is mostly to smooth jagged edges in the fluctuations shown in Fig. 6.5.

To produce the capacitance fluctuations expected for all electron additions, this curve is repeated at every electron addition shown in Fig 6.2b. (We note that this addition of convolved curves gives the same result as adding unconvolved curves and convolving the entire capacitance spectrum.) The smooth background is subtracted, and the results are plotted in Fig. 6.6 and 6.7. The two figures are for different ranges of the gate bias. At the base of these figures is replotted the spectrum from Fig. 6.2b. 355 mV (the same voltage used as the device threshold in power law fit to the dot area used in the model spectrum calculation) has been subtracted from the abscissa of this curve so that the device threshold for the model curves corresponds with the experimental thresholds on actual samples.

We mention several features of this artificial spectrum before comparing it to our experimental results. Notice that the breadth of peaks in Fig. 6.5 is two or three times  $\beta$ . In Fig. 6.6, where the spacing between electron additions is several times this breadth, several peaks are seen in the capacitance spectrum

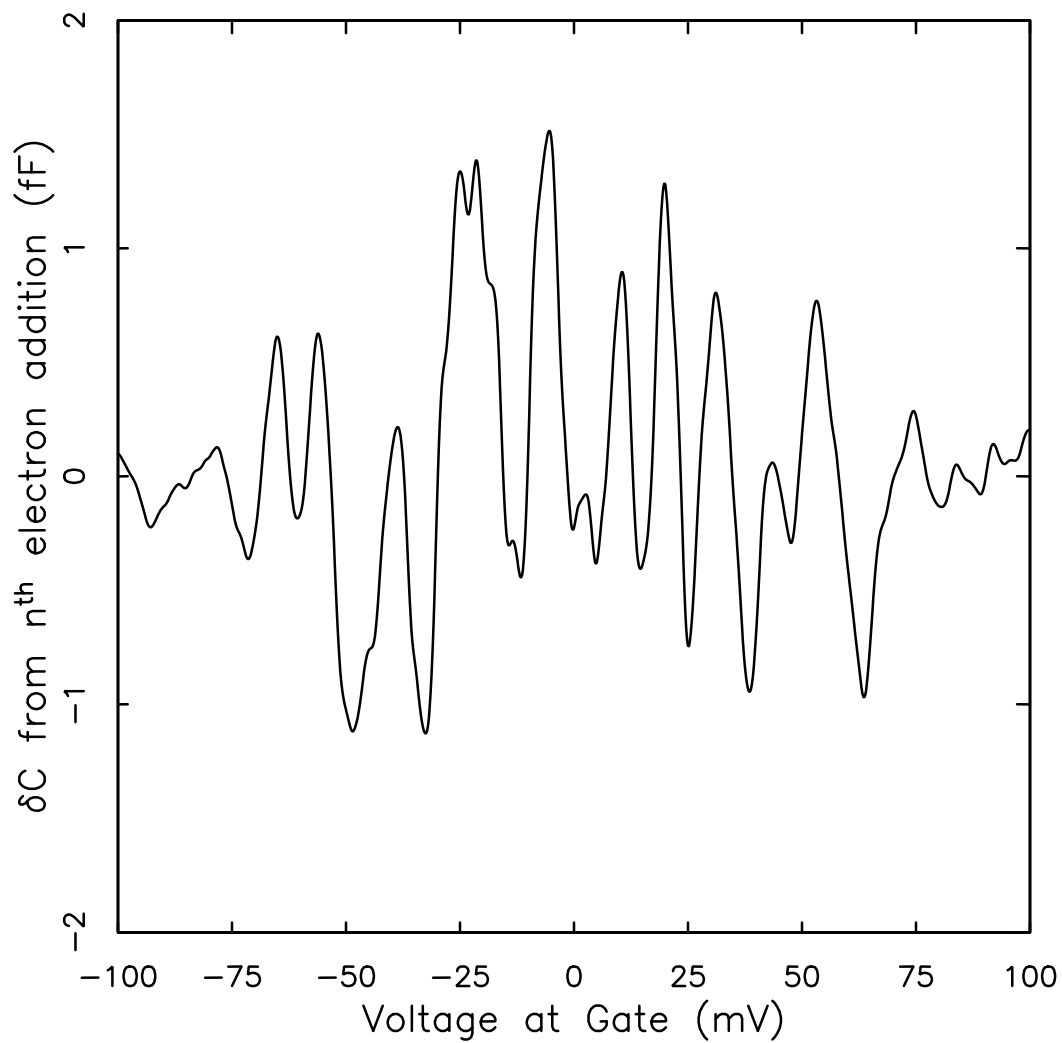


**Fig. 6.5** The figure displays a typical capacitance fluctuation spectrum for the addition of the  $n^{\text{th}}$  electron to each dot in the quantum dot array. The spectrum was developed using the protocol described in the text using a 2.44 mV rms sinusoidal measuring voltage. The results were obtained assuming a  $\bar{\rho}(V)$  described by a Gaussian distribution of rms width 35 mV.

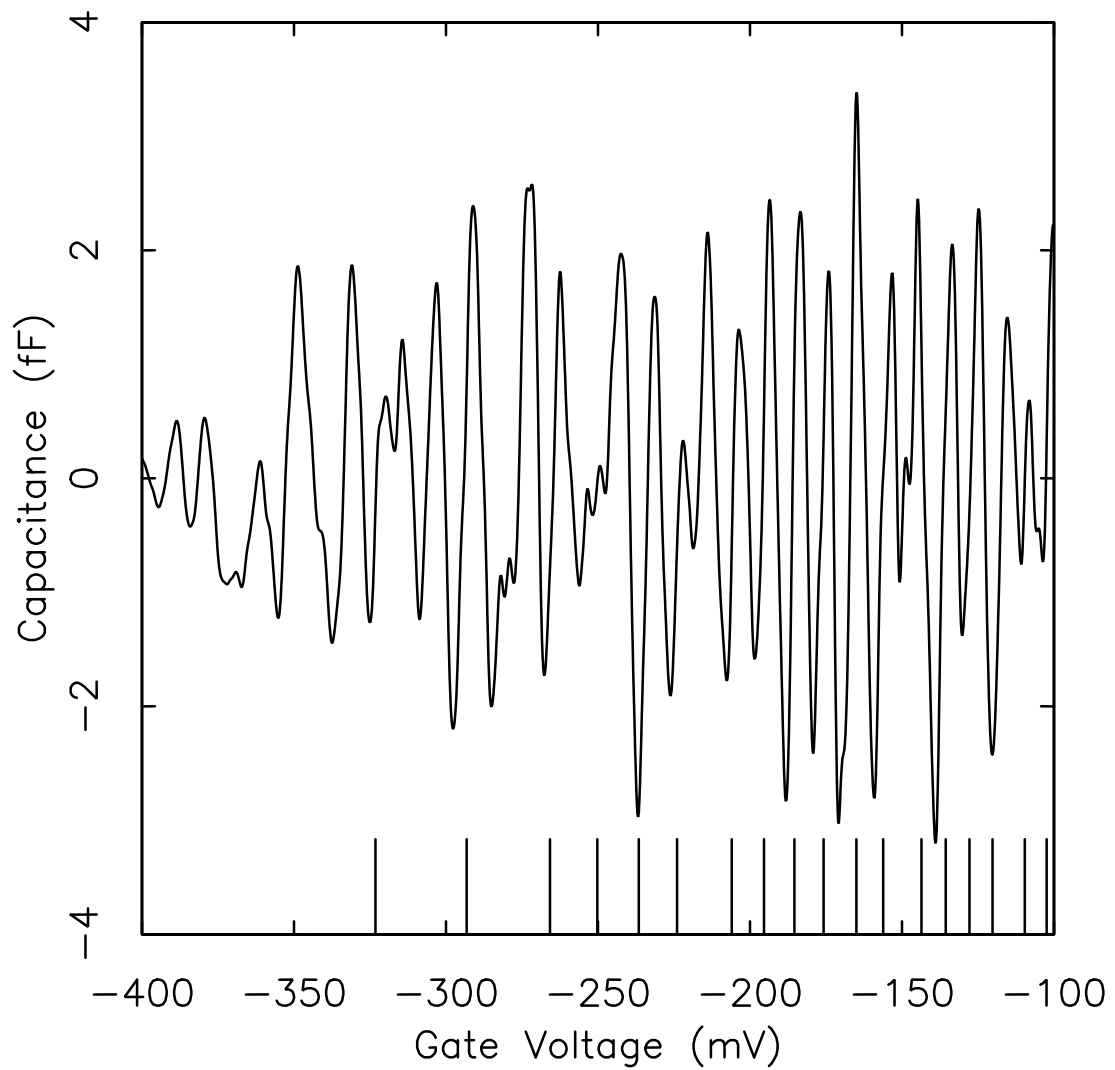


**Fig. 6.6** The figure displays a simulated capacitance fluctuation spectrum developed from our model by repeating the fluctuation shown in Fig. 6.5 at every electron addition (shown by the sticks in the bottom portion of the figure). The smooth background has been subtracted.

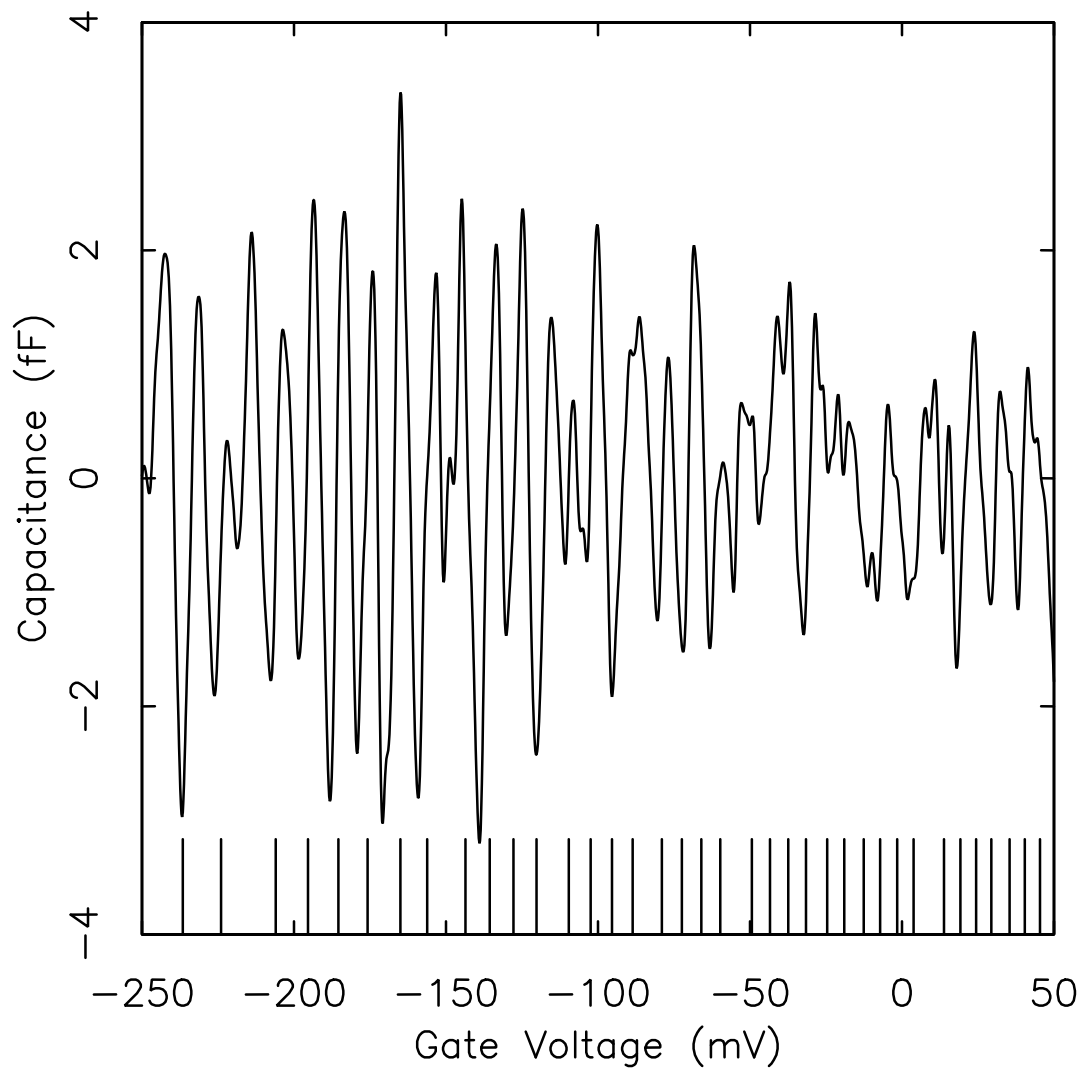


**Fig. 6.7** The figure displays a capacitance fluctuation spectrum developed from our model by repeating the fluctuation shown in Fig. 6.5 at every electron addition (shown by the sticks in the bottom portion of the figure). This is the result of the same calculation used in Fig. 6.6. This plot shows a different region of gate bias.

between electron additions. Conversely, beyond about 150 mV (-220 mV on the plot) above the device threshold where the spacing between electron additions is less than 10 mV, typically only one peak per electron addition is seen. In this region, there is significant variation of the amplitude of peaks in the capacitance spectrum and the phase of the peaks varies somewhat with respect to the electron addition spectrum. Despite these observations, the spacing between successive peaks in the capacitance spectrum is nearly equal (to within about 30%) to the spacing of individual electron additions in a single dot. Put another way, the density of peaks in the capacitance spectrum is very nearly the same as the density of electron additions in the spectrum for one particle.

We make a few statements based on observations of changes to calculated capacitance spectra as the measuring voltage amplitude is varied using several different sets noise fluctuations,  $\delta\rho$ . Though the different noise fluctuations give very different looking capacitance spectra, some generalizations can be drawn. All of these observations are made for  $V_t$ , the width of the distribution of electron addition spectra among the different dots, larger than  $e/\kappa C$  anywhere in the electron addition spectrum. We notice that the peak structure of the fluctuations in the final capacitance spectrum is rather insensitive to the shape of the  $V_d$  distribution. Using Gaussian or “flat” (boxcar) distributions with the same rms width and starting with the same noise spectrum give nearly identical capacitance fluctuation spectra. The rest of our observations detail results from using a Gaussian distribution with rms width of 35 mV.

There are three limiting cases. **1)** The amplitude of the measuring voltage,  $\beta$ , is less than about 25% of  $e/\kappa C$ . In this case, typically more than one peak in the capacitance fluctuation spectrum is seen for each electron addition. This structure is a consequence of the random peak structure such as that seen in

Fig. 6.5. Depending on the structure of the fluctuations in the dot thresholds, the capacitance fluctuations may or may not appear to have regions of quasi-periodic oscillations. **2)** The next case roughly occurs when

$$0.25e/\kappa C < \beta < 0.6e/\kappa C.$$

In this regime, the capacitance spectrum displays, over portions of the spectrum, almost regular oscillations. Depending on the noise fluctuations used, these may continue for many cycles or may have a coherence of only a few cycles. The density of peaks in the capacitance in these portions is nearly the same (it can be accurate to better than 10% over a 100 mV interval) as the density of electronic additions. In the other portions of the spectrum, the capacitance appears to be random with few clear peaks defined, and the density of these peaks bears no apparent relation to the density of electron additions. The important point is that in this regime, where clear oscillations are seen, our simulations indicate that their spacing *is* nearly equal that of the underlying electron addition spectrum. **3)** The measuring voltage amplitude approaches or becomes larger than the spacing of electron additions or

$$0.6e/\kappa C < \beta.$$

In this case, fluctuations in the capacitance appear to be random, with no obvious relation to the electron addition spectrum.

We remark briefly on the reasons for this behavior in the capacitance spectrum. Consider two peaks in the capacitance fluctuations shown in Fig. 6.5 due to the addition of the  $n^{\text{th}}$  electron to each of the dots. If these peaks are separated by an amount equal to the spacing between successive electron additions in the dots, then they reinforce one another in the capacitance fluctuation spectrum for the sample. Peaks separated by voltages different the underlying

spacing between electron additions do not undergo this reinforcement. In this way, the capacitance spectrum tends to display peaks separated by the spacings of the electron addition spectrum.

For comparison, we also repeat the spectrum in Fig. 6.5 at each of the random electron additions shown in Fig. 6.8. This random spectrum was developed by considering the spacing between successive electron additions to be Gaussian distributed with the mean spacing between additions given by  $(e/\kappa C) + (\delta_{mean}/\kappa)$ , for a particular sized dot, where  $\delta_{mean}$  is the inverse of the electronic density of states in the dot (not the  $\delta$  defined earlier). We then correct the spectrum for the variable area of the dot using the method described in section 6.3 above. Clearly, the repetition of the fluctuations of Fig. 6.5 at random intervals produces a qualitatively different final capacitance fluctuation spectrum than repetition at the regular intervals of Fig. 6.2b. We conclude that if regular oscillations are seen in the capacitance fluctuation spectrum of our quantum dot array, they are likely indicative of an underlying regular spectrum of electron additions such as that in Fig. 6.2b. We start off looking at capacitance data in the absence of magnetic field first to gain some feel for the problem and then turn to results taken in a magnetic field where the connection between the capacitance fluctuations and the underlying spectrum is much more clear.

## 6.5 Comparison of Simulation to Observed Capacitance Spectra

We turn now to actual data. Most of our data has been taken on a sample of dots made using  $0.04 \mu\text{m}^2$  square patterns. This sample contains about 200,000 dots. We have also taken data on other samples with larger pattern sizes and for hexagonal pattern shapes as well. Although these samples show similar results, we concentrate here on the sample with  $0.04 \mu\text{m}^2$  patterns because this sample

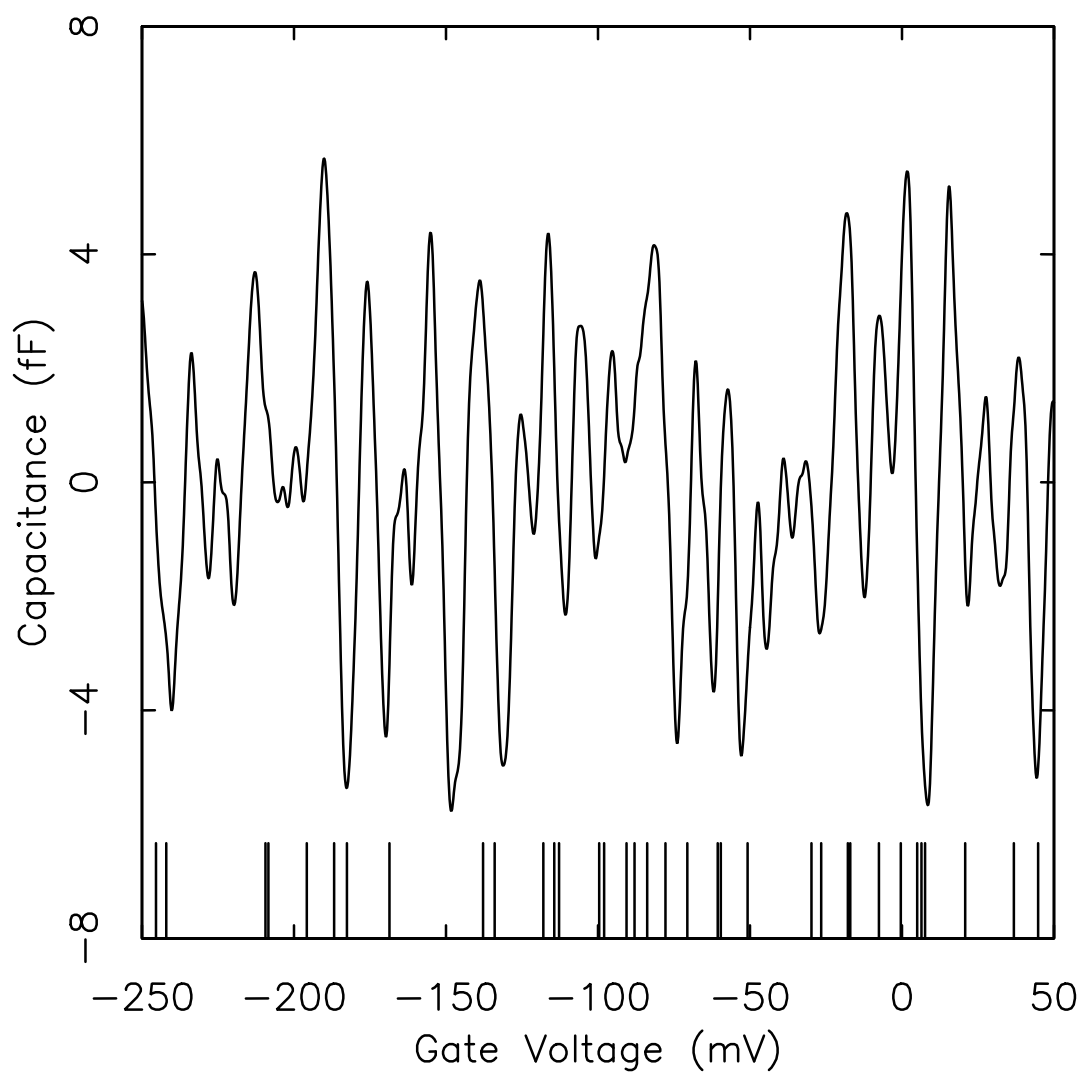


**Fig. 6.8** Displayed is the result of repeating the capacitance fluctuation spectrum of Fig. 6.5 at for a random electron addition spectrum.



contains the most dots, giving the largest capacitance fluctuations, and the dots are smaller than in other samples, leading the energies of interest to be larger.

We measure the capacitance of our samples to a noise resolution of  $\approx 0.1$  fF as the gate bias is varied. The smooth variation in capacitance curves is removed by fitting the capacitance to a polynomial (at most ninth order) and subtracting off this fit. The order of this polynomial is always kept small enough so that any fluctuations induced by the subtraction of these fits would be of much longer period than the fluctuations of interest.

Fig. 6.9 shows capacitance results, obtained using the procedure outlined above. These data were taken with an rms signal amplitude of 2.4 mV rms at a temperature of 1.4 K (smaller than the signal amplitude as seen at the well) and a frequency of 615 Hz. The results are in many ways similar to those of Fig. 6.7. Firstly, both the simulated and the actual show regions between -250 mV and between -100 mV to -50 mV where there are almost periodic oscillations in the device capacitance. These oscillations have nearly the same amplitude and periodicity. Additionally, both spectra show some hint of a “chirp” in the oscillations with decreasing period as the gate bias is increased. Secondly, the fluctuations in the device capacitance become aperiodic for voltages greater than -50 mV and the simulations of Fig. 6.7 show a similar behavior at voltages greater than -100 mV.

We underscore that these fluctuations observed in the device capacitance are reproducible; the statistical error bars (around 0.15 fF) from the signal averaging used in these measurements is minute on the scale shown. These fluctuations change when the device is biased so that leakage currents pass through the thick AlGaAs barrier separating the top gate and the dots. They also change for warm up and subsequent cool down of the device. Both of these occurrences

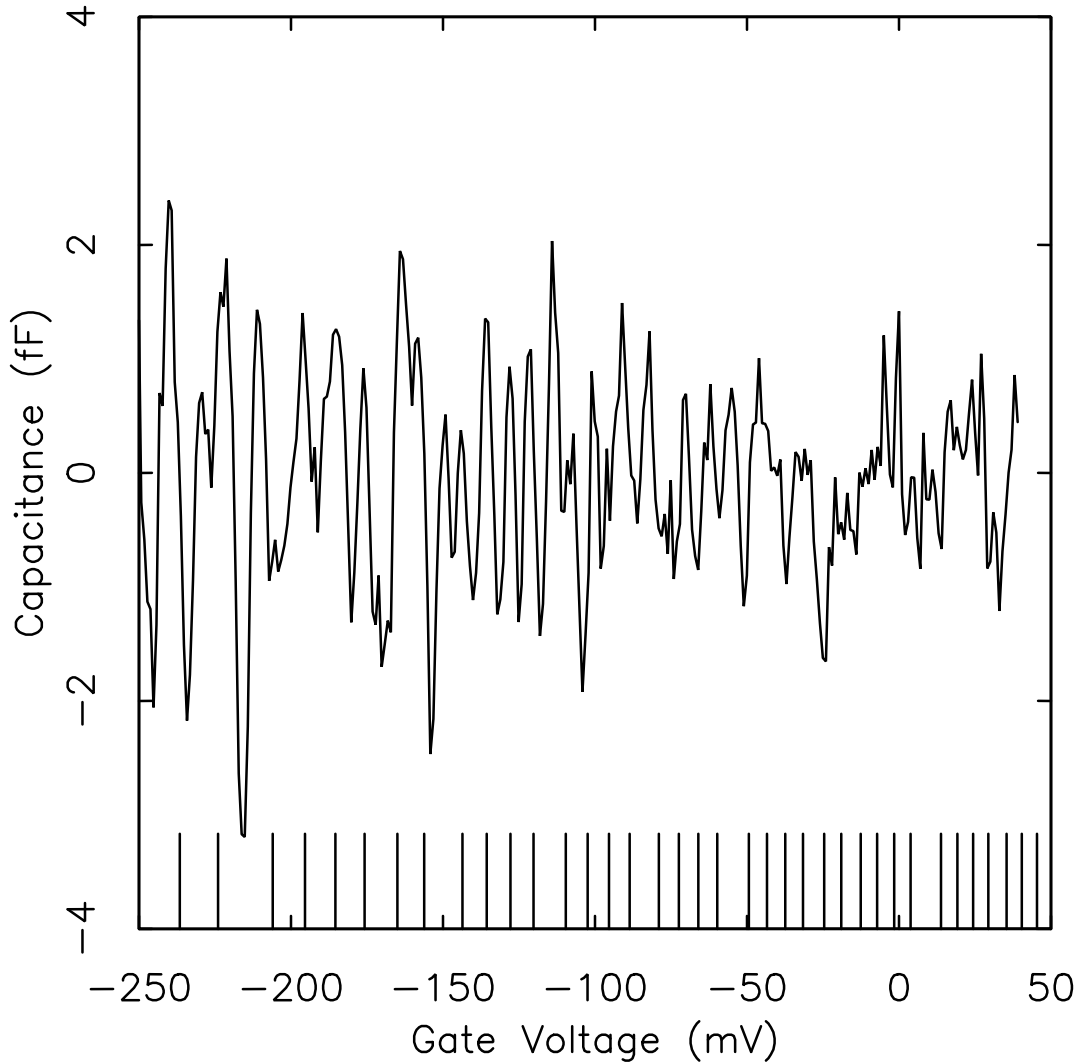


**Fig. 6.9** The figure shows the sample capacitance (measured at 615 Hz with a 2.44 mV rms measuring signal) with the smooth background subtracted off. The quasi-periodic peaks in the fluctuations in the capacitance for gate voltages between  $-250$  mV and  $-50$  mV are thought to occur with the nearly the same frequency as the electron additions to the dots. For gate voltages above  $-50$  mV, where the spacing between successive electron additions in our model is smaller than the peak to peak amplitude of the measuring voltage, the fluctuations have a more random character. Plotted on the abscissa are the electron additions from the model spectrum. (All experimental results in this and other figures in this chapter are from the same array of 197,500 quantum dots made from  $0.04 \mu\text{m}^2$  square patterns.)

are thought to change the occupation of donor sites in the AlGaAs barrier, and thus change the distribution of thresholds for adding electrons into the dots.

It is not always obvious in observation of our data where “regular” oscillations begin and end. Further, as discussed above, even a random spectrum of electronic additions may produce fluctuations such as those in Fig. 6.9 which appear regular. We cannot yet conclude that the oscillations seen in the data of Fig. 6.9 arise from the near periodicity of the electron addition spectrum.

### *Measurements Involving the Real Part of the Device Admittance*

Before proceeding, we make a few remarks on the methods used to take the data. As with the broad area 2d electron gas samples discussed in chapters 3 and 4, the capacitance and loss tangent of our samples (not patterned to produce dots) display a relaxation behavior. The capacitance decreases on moving from low to high frequencies over a certain range in frequencies, governed by the characteristic charging time of a dot, and the loss tangent has a peak in this range of frequencies. It is a simple matter to show, using the equations of chapter 4, for our 2d electron gas samples that any fluctuations in the low frequency capacitance  $C_{low}$  will lead to fluctuations of the same size in the device conductance divided by the frequency (in radians per second) when measured at the frequency of the relaxation peak. Also, the size of fluctuations in the capacitance steadily decrease as the frequency is increased. At the relaxation peak frequency, the size in the fluctuations in the capacitance should be half that measured in the device conductance divided by frequency.

The only electron transfer in our devices which occurs at the frequencies of the observed relaxation peak is electron tunneling between the dots and the substrate. Fluctuations in the conductance signal occur due to changes in

the height of the relaxation peak. The conductance measurements are only sensitive to these fluctuations at frequencies around the relaxation peak. This is not true of fluctuations in the capacitance signal which depends on electron transfer for all frequencies faster than the measuring frequency. Fast transfer of electrons in other regions of the sample (perhaps between donors in the AlGaAs barrier between the quantum well and the top electrode) can contribute to this signal. In measurements at frequencies around the relaxation peak, both the capacitance and the conductance (divided by the measuring frequency) show similar fluctuations, with peaks in the capacitance and the conductance occurring at the same gate bias voltages.

Sometimes the capacitance displays fluctuation which is not seen in the conductance. Measuring the conductance allows us to reject spurious fluctuations. The other feature of making measurements at the loss peak frequency, for our particular device, is that it allows us to work at higher frequencies (1.7 kHz) avoiding  $1/f$  noise in low frequency capacitance measurements (such as those in Fig. 6.9 taken at 615 Hz) which makes measurements more difficult. In all of this “high” frequency work, both the device capacitance and conductance are measured simultaneously.

The convolution used to describe the effect of the measuring voltage discussed in section 6.4 must be changed at higher frequencies. This is because Eq. 6.10 considers electron transfer to occur quickly on the scale of the period of the measuring voltage. If the relaxation time is not fast compared to the period of the measuring voltage, a different convolving function must be used. As shown in Fig. 6.4 at measuring frequencies which are not small compared to the relaxation peak frequency the convolving function for capacitance fluctuations will to narrow. This shape is different at higher frequencies because, as will

be discussed below, the tunneling rate from a dot depends on the position in gate bias at which a dot's threshold (such as any particular stick in Fig. 6.2b) lies for exchanging an electron with the substrate. We expect that dots whose thresholds lie further from the setting of the gate bias to have slower tunneling rates. At measuring frequencies comparable to the tunneling rate, some of the dots do not undergo a tunneling event in a half cycle of the measuring voltage and hence do not contribute to the device capacitance. Because dots with thresholds near the position of the gate voltage are more likely have tunneling events in a half cycle compared to those with thresholds far from this gate voltage position, the convolving function narrows. This model is difficult to solve for sinusoidal measuring signals and the dashed curve in Fig. 6.4 is an imagined form for the shape.

Now we refer to Fig. 6.10 which shows the fluctuations in the real part of the device admittance (conductance) of the same device from which data of Fig. 6.9 was obtained. (Note these data were taken at about two weeks after those in Fig. 6.9, and leakage currents had been passed through the device, changing the fluctuation spectrum; so we do not expect these two spectra to have features in common.) It is difficult to distinguish where in this spectrum fluctuations which have obvious correlation with the supposed spectrum of electron additions commence. While above -150 mV there are some regular oscillations that might be associated with the addition spectrum, at lower gate voltages there are also regions where almost periodic oscillations persist.

For comparison, we also show the capacitance signal from the same data run in Fig. 6.11. Comparing this carefully with the results of Fig. 6.10, it is clear that almost all of the peaks in the two figures agree. However, the detailed shapes of peaks in the two curves are different, with peaks having different amplitudes

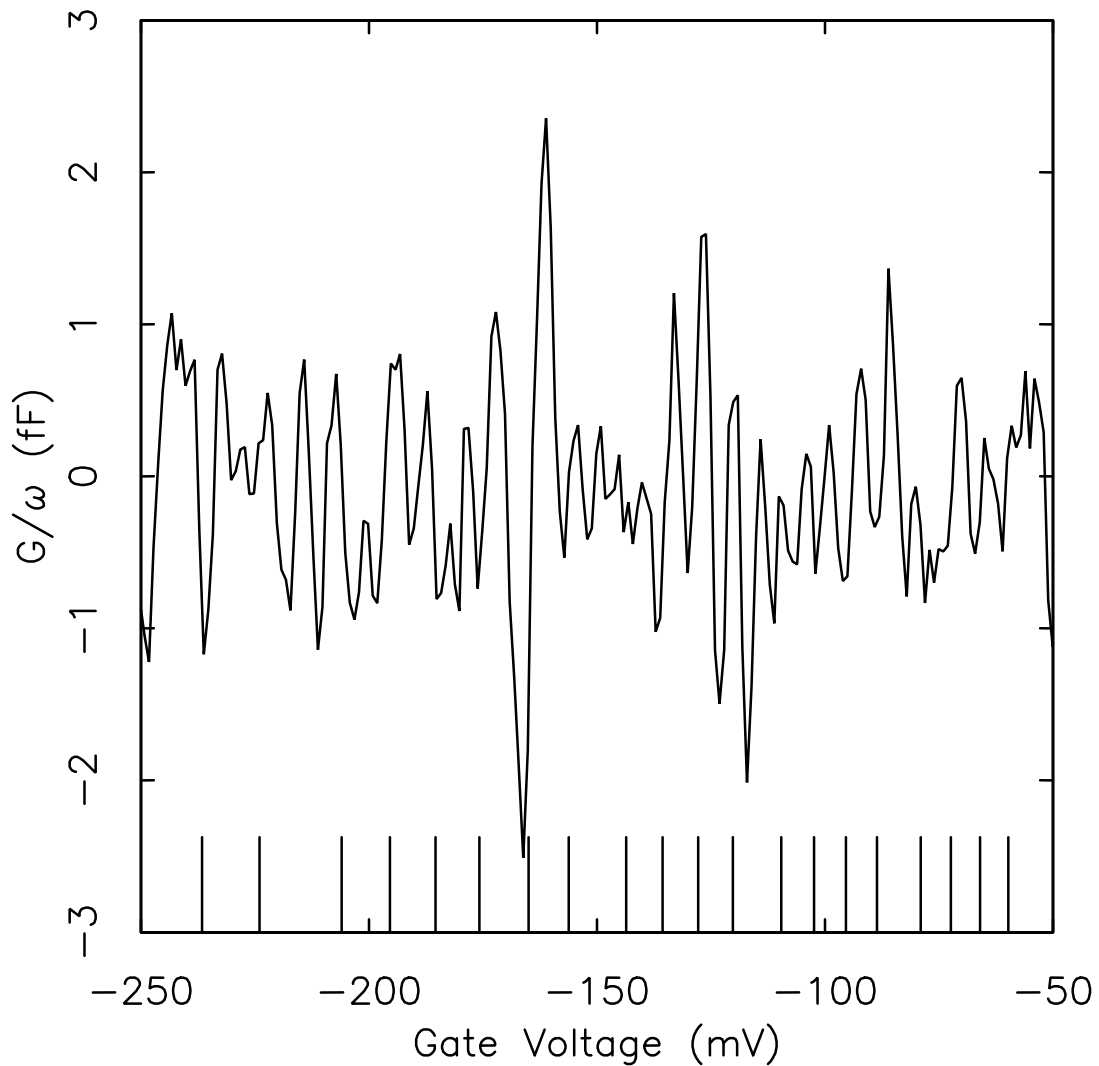


**Fig. 6.10** The figure shows the fluctuations in the device conductance (at 1.7 kHz and with a 2 mV rms measuring voltage). It illustrates the difficulty in distinguishing fluctuations associated with the electron addition spectrum and those, unrelated to the addition spectrum, which occur with the measuring voltage much smaller than the spacing between electron additions. Peaks in the fluctuations in the lower gate bias region of the graph have a periodicity shorter than the electron additions given by the model spectrum, whereas at higher gate biases the periodicities are about the same. However without the model spectrum as a guide, it is difficult to judge where the fluctuations become “regular” and associated with the addition spectrum.

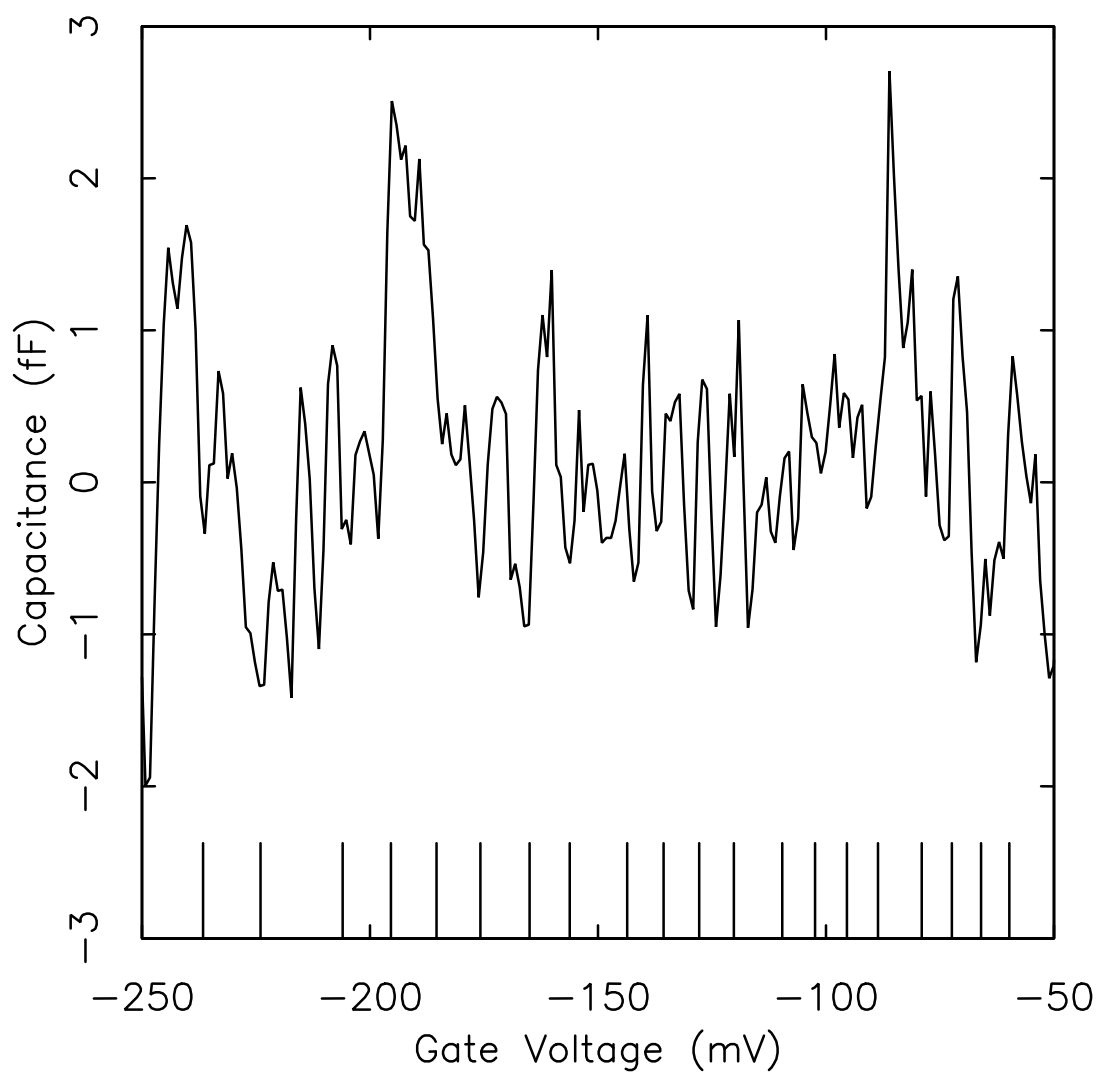


**Fig. 6.11** The capacitance from the same run which produced Fig. 6.10 is displayed. While most all of the peaks in both figures occur at the same gate bias values, the capacitance contains additional fluctuations, such as those around -190 mV and -80 mV, which are confined to a narrow enough range that they are not subtracted off in the smooth background subtraction.

in some cases, and the capacitance containing some large deviations (the ones at -190 and -80 mV being most obvious) which are not seen in the conductance. These extra fluctuations in the capacitance are typical of our results.

## 6.6 Capacitance Spectra in Magnetic Field

With the data shown so far, it is not entirely certain that the model which we have developed is actually applicable. Fortunately, the fluctuation spectrum with magnetic field shows features which are far clearer.

At 4.3 T, the magnetic length is about  $150\text{\AA}$  and is much smaller than the diameter of our dots for almost the full range of gate biases. The dots are big enough that it is appropriate to think of the electronic states in the dot in terms of Landau levels. For a magnetic field of 4.3 T, the Landau level degeneracy (including spin degeneracy) in a dot of area  $0.01\text{ }\mu\text{m}^2$  (the size of the dot sample produced with  $0.04\text{ }\mu\text{m}^2$  lithographic patterns at -130 mV gate bias) is about 21 electrons. This is larger than the number of electrons in the dot (about 16 from our calculated electron addition spectrum) at the same gate bias.

We examine the simplest picture with no broadening of the Landau levels. As the gate voltage is scanned and electrons are added to a particular Landau level, the change in gate voltage needed to added consecutive electrons is only  $e/\kappa C$  with no additional energy from quantum level splittings. The electron addition spectrum is now much more regular than without magnetic field; the variable energy level splittings in zero field (which appeared in the addition spectrum after every second or forth electron) have been removed.

For the only sample on which we have taken capacitance fluctuation measurements in magnetic field (the sample made from  $0.04\text{ }\mu\text{m}^2$  lithographic patterns), the model calculations indicate that only the lowest Landau level



is filled up to a gate voltage of -60 mV at which there are 25 electrons in the dots. Above this gate voltage, the second level begins to fill as well as the first Landau level orbits as the dot area increases. In a picture where the dot area is not changing, electrons begin to enter the second level after a gap of  $\hbar\omega_c/\kappa$  (plus the charging energy for one electron) in gate bias after the first level is completely full. In the real sample in which the area changes, we find that one Landau orbit is added, due to increase in the area of the dot, for a change in gate voltage (at the gate voltage at which there are 25 electrons in a dot) slightly larger than  $\hbar\omega_c/\kappa$ . We have not well understood the complications arising from the changing area of the dot as they concern these gaps. Some arguments dictate that a wide gap remains between the Landau levels while others indicate that the gap may contain electron additions from newly added Landau orbits in the dot. For simplicity we proceed with simulations ignoring any gaps, which after all appear relatively infrequently after many electron additions to the dot, and adding electrons to the dot for every  $e/\kappa C$  interval in gate bias.

Fig. 6.12 shows both the calculated electron addition spectrum as well as a simulated fluctuation spectrum considering electron additions to be spaced only by  $e/\kappa C$ . The same “noise” used to generate Fig. 6.5 was used, this time (for comparison to data taken at frequencies near the relaxation peak frequency) convolved with an ellipse function corresponding to a measuring voltage of 1.0 mV. The simulation shows much more regular oscillations than previous simulations. The removal of the quantum level spacings has enhanced the periodic nature of the fluctuations. We note even that when a gap of width  $\hbar\omega_c/\kappa$  (about 27 mV or about 4 times  $e/\kappa C$  at -60 mV) is placed in this electron addition spectrum at a voltage of -60 mV, the simulation continues to show a strong periodic behavior with oscillations occurring for each electron addition

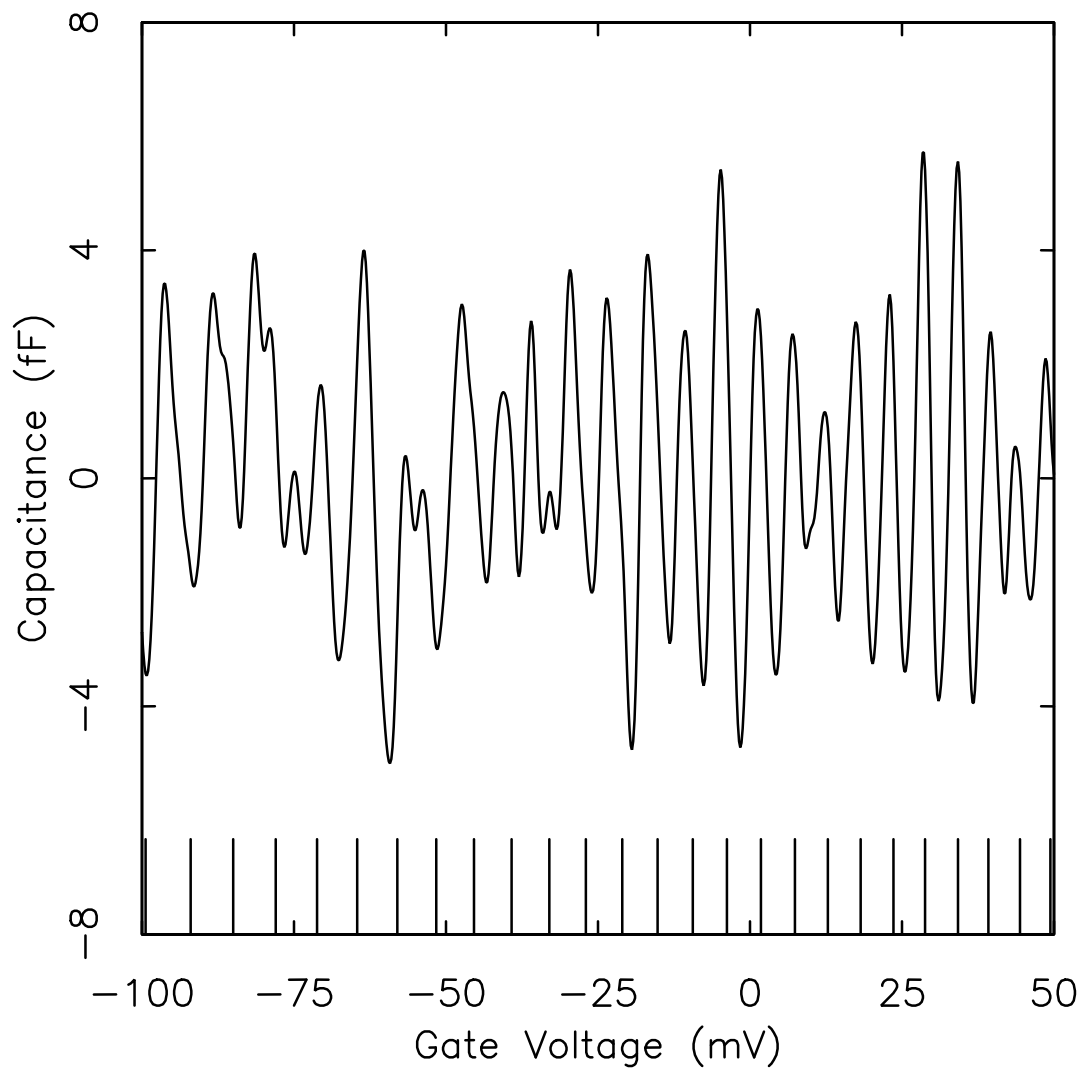


**Fig. 6.12** The results of repeating the fluctuations from Fig. 6.5 (except that a 1 mV rms measuring voltage is used in the convolution of Eq. 6.11) on a spectrum calculated with all states considered to be completely degenerate. Note that the removal of the quantum level splittings causes the capacitance spectrum to contain much more regular oscillations than those seen in Fig. 6.7

(depending on the noise fluctuations  $\delta\rho$  used the oscillations may persist even through the region of the gap).

We compare this simulation (created without the  $\hbar\omega_c$  gap) to capacitance fluctuation data taken at 4.3 T and 1.8 K shown in Fig. 6.13. This spectrum (taken again at frequencies near the relaxation peak for the sample) shows oscillations remarkably similar to those shown in Fig. 6.12. The ticks on the bottom of Fig. 6.13 show the same electron addition spectrum as that used in Fig. 6.12. The oscillations in the data, like those in the simulation, occur with nearly the same period as the separation between electron additions in the model spectrum. The small amplitude of the oscillations in the sample conductance relative to the model spectrum may arise because the measuring frequency is not exactly tuned to the relaxation peak frequency; also, the shape of the relaxation peak, as discussed below, is somewhat broadened which would decrease the amplitude of oscillations. The data also more clearly show the expected chirp in the oscillations arising from the decrease in spacing between electron additions as the gate bias is increased. For completeness, we also show in Fig. 6.14 a different portion of the same gate bias sweep (lower voltages). The oscillations again display good agreement with electron addition spectrum.

We have a limited data set from measuring capacitance fluctuations. We have taken only one other spectrum, at lower gate biases (from -350 to -100 mV) on the same sample, in magnetic field (also at 4.3 T). It shows fluctuations which develop, as the gate bias is increased into the range above -200 mV, into similar quality oscillations as to those of Figs 6.13 and 6.14. Though the quantity of the data is limited, we find broad agreement with the model capacitance spectrum in spacing and chirp of oscillations. We believe this to be a convincing argument

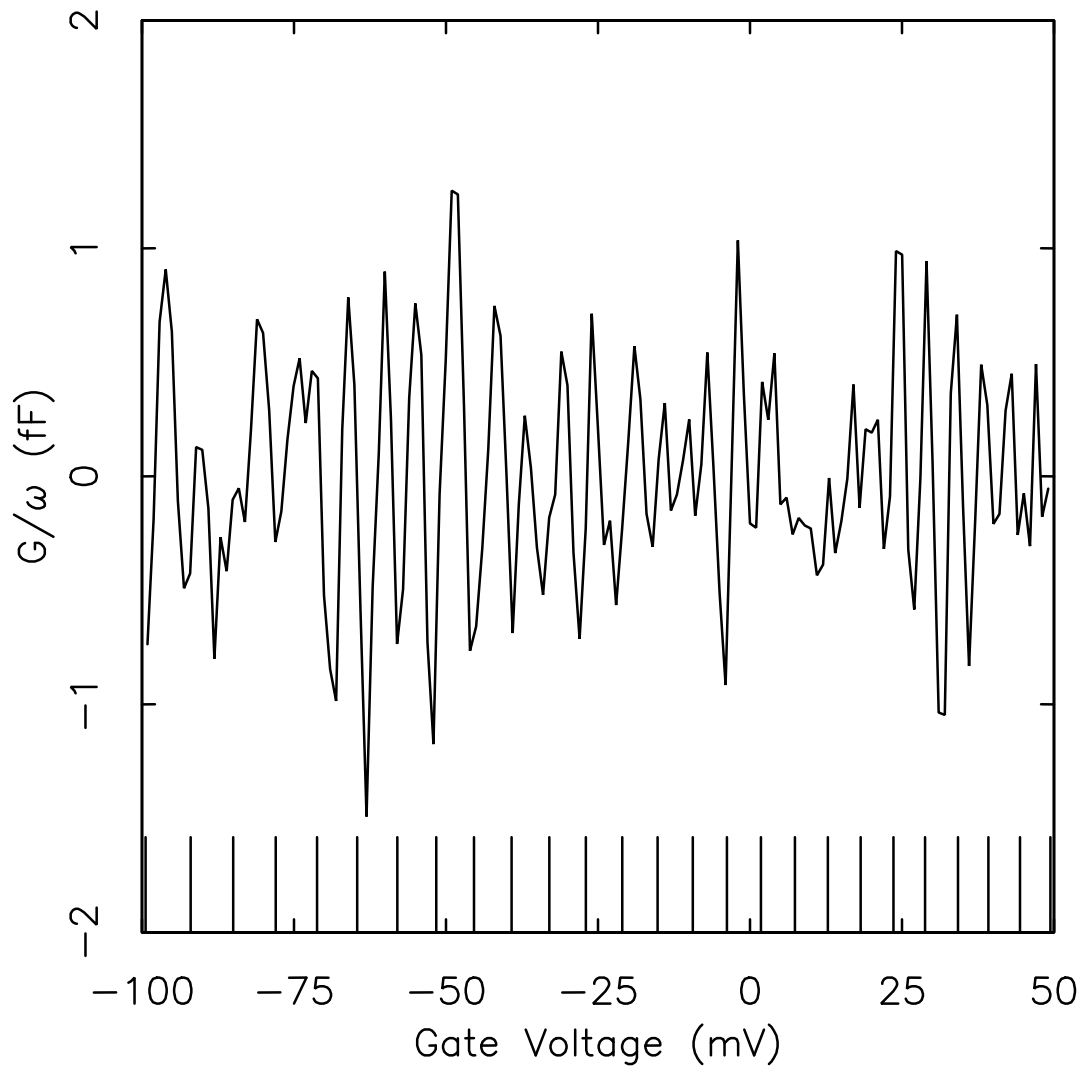


**Fig. 6.13** The figure shows the fluctuations in the device conductance (measured at 1.7 kHz) in a magnetic field of 4.3 T. Note the long coherence of the oscillations.

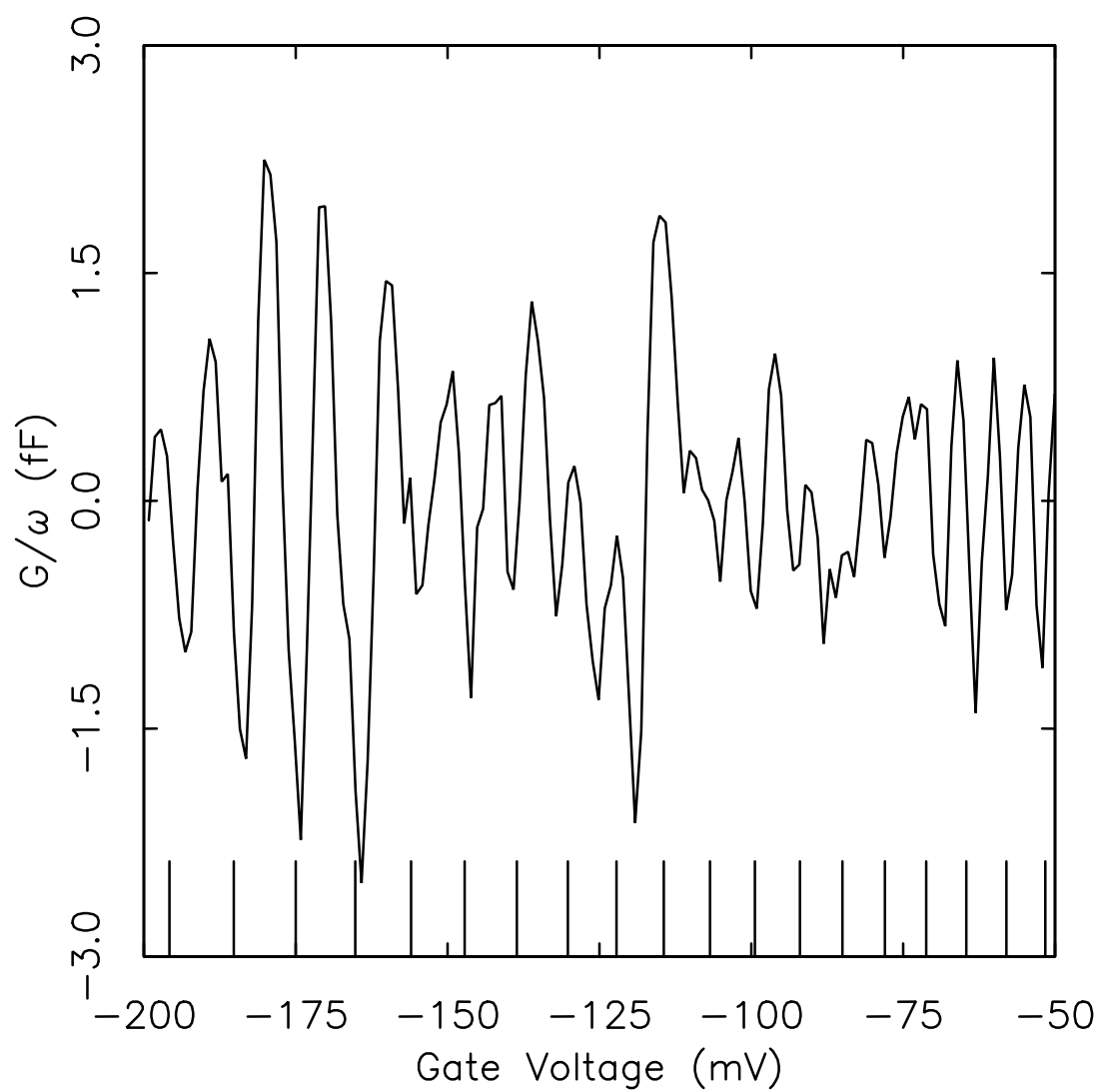


**Fig. 6.14** The figure displays conductance fluctuations from the same data run which was used to produce Fig. 6.13 at a lower region of gate biases.

that the observed fluctuations in the capacitance spectrum in magnetic field do indeed occur at intervals given by the Coulomb charging energy of the dots.

To close these sections on the capacitance fluctuations, we note that the results in magnetic field also make a statement on the uniformity of the dots. The obvious correlation seen in the capacitance fluctuations over many cycles indicates that electrons are added to the different dots with nearly the same periodicity. We expect the periods of electron addition in different dots to be the same if the dots are the same size (so that they have the same charging energies). Electron beam lithography produced very uniform patterns for creating the dots, but this may not be the only factor influencing the uniformity of the size of the electron packets. Any quantitative statement to be derived from the data on the uniformity of dot sizes requires further analysis. We expect the autocorrelation function of the fluctuation spectra to be useful in making these determinations. Our model, of identical electron addition spectra in the dots but with varying origins (thresholds), works well in simulating the fluctuation data.

## 6.7 Tunneling Rate Measurements

Tunneling of electrons from small metal particles to a metallic electrode has been studied in detail in our lab previously. Cavicchi and Silsbee<sup>11</sup> developed a model which describes the effects of the charging energy on tunneling. One of their essential results, of importance to the work presented here, determines that the average tunneling rate for an array small particles becomes dependent on the amplitude of the signal used to make measurements on the sample. In this section, we give a brief review of these ideas and examine their applicability to tunneling measurements done on our quantum dot arrays.

We examine the tunneling in our quantum dot sample at fixed gate bias, focusing on a particular dot whose Fermi energy at this gate bias differs from that in the sample substrate by an amount  $eV_k$ . Of course the Fermi energy of this dot lies somewhere within the equilibrium zone shown in Fig. 6.1b. Now imagine that a square wave measuring voltage,  $\beta\text{sq}(\omega t)$  is applied to the sample. Here  $\text{sq}(x)$  is a square wave of unit amplitude which repeats every time its argument passes thorough  $2\pi$ . For argument between 0 and  $\pi$ ,  $\text{sq}(x)$  is equal to one, and in the other half cycle it is equal to negative one. The voltage which appears between the quantum dot and the substrate due to this measuring signal is given by  $\kappa\beta\text{sq}(\omega t)$ . Thinking just of the tunneling response of this particular dot during the first half cycle of the square wave, it is clear that no tunneling of electrons from the particle to the substrate occurs unless  $V_k + \kappa\beta > e/2C$ . This is the requirement that the measuring voltage amplitude be large enough so as to move the (quasi) Fermi energy of the dot out of the equilibrium zone.

Consider the square wave amplitude to be within the correct range so that just one filled quantum level in the dot is exposed over the top edge of the equilibrium zone during the first half cycle of the square wave. We ignore degeneracies of levels for the present discussion. We refer to the tunneling rate (which can be determined in a WKB approximation) from a single nondegenerate level as  $1/\tau_0$ . Now, if the amplitude of the square wave is increased so that  $n$  filled levels are exposed outside of the equilibrium zone, the rate for tunneling will be  $n/\tau_0$ . If the spacing between nondegenerate levels is equal to  $\delta$ , the tunneling rate,  $1/\tau$  is given as follows:

$$\frac{1}{\tau} = \begin{cases} \frac{V_k + \kappa\beta - e/2C}{\delta} \frac{1}{\tau_0} & \left( V_k + \kappa\beta \geq \frac{e}{2C} \right) \\ 0 & \left( V_k + \kappa\beta < \frac{e}{2C} \right). \end{cases}$$

In words, the tunneling rate for electrons moving from the dots to the substrate is zero until measuring voltage is increased to some threshold value. Beyond this threshold the rate increases linearly with gate bias. These arguments are mirrored for the second half of the square wave where the square wave amplitude threshold for a dot to accept an electron (for moving the quasi-Fermi energy an amount  $\delta$  below the edge of the equilibrium zone so that an electron can tunnel into the dot from the substrate) is given by

$$V_k - \kappa\beta < -\frac{e}{2C} - \delta$$

Again, the tunneling rate from the particle increases linearly with voltage beyond this threshold.

In our experiment, the tunneling current is measured. For a single particle with square wave excitation, this current is zero for the square wave amplitude below the thresholds described above and rises linearly with amplitude as these thresholds are surpassed. The tunneling current,  $I_{dot}$  for a single dot, initially in equilibrium (square wave measuring voltage just turned on) just after an upward step in the square wave voltage with amplitude large enough to surpass the conductance threshold, is

$$I_{dot} = \frac{V_k + \kappa\beta - e/2C}{\delta} \frac{e}{\tau_0}.$$

Beyond threshold, the differential conductance associated with electron tunneling is a constant.

Consider now a uniform distribution of  $V_k$ 's for the array of dots. As the measuring voltage amplitude,  $\beta$  is increased between 0 and  $e/\kappa C$  there is a linear increase in the number dots (initially in equilibrium for zero measuring voltage applied) from which tunneling events can occur during the first half cycle. Recall that beyond threshold, the differential conductance of conductance



of any one dot is a constant. Since the currents from the different dots in the array are summed in a measurement of the sample current, we expect a linear increase in the differential tunneling conductance as the measuring voltage amplitude is increased. Put in other words, two factors are involved in the sample current. The current from the dots which allow tunneling increases linearly with measuring voltage beyond a threshold. Also, the number of dots which allow tunneling increases linearly with the gate voltage. The combination of these two factors causes a quadratic increase in the sample current with voltage.

There are limits to this linear increase in sample conductance. If the measuring voltage amplitude is increased so that  $\beta > e/\kappa C$  then tunneling is allowed (during both half cycles of the square wave) from all of the dots, at which point the increase in the sample current from adding more dots to the tunneling process ceases. The conductance becomes a constant. The tunneling current also becomes a constant for measuring voltages so small that  $\beta < \delta/\kappa$ , where  $\delta$  is the quantum level splitting. In this case, only very few of the dots allow tunneling and the tunneling rate for each of these dots is fixed at  $1/\tau_0$  (for nondegenerate levels) because at most only one level can contribute to the tunneling current. In the case of degenerate levels, we must consider  $\delta$  to be the energy spacing between sets of degenerate levels. The tunneling rate at very low voltages, for those dots from which tunneling is allowed, is the level of degeneracy of the exposed level times  $1/\tau_0$ . The irregularity of the spacings between degenerate levels in our samples should perhaps wash out this low amplitude cut-off.

As stated earlier, the ratio of the charging energy  $\Delta$  to the level splitting between degenerate levels is about 3 in our samples. We thus expect the observed sample tunneling conductance to be level at low measuring voltages, start a

linear increase at a particular measuring voltage and continue to rise for voltages to about 3 times this voltage and then level off once again.

Figure 6.15 displays the relaxation peak frequency, measured using *sinusoidal* signals as a function of the rms amplitude of measuring signals. The gate bias here is set to zero, corresponding to a charging energy ( $e/\kappa C$ ) of about 9 mV in our model. The peak frequency, as discussed in chapter 4, is proportional to the tunneling conductivity (which in turn is proportional to the mean tunneling rate from the dots) between the quantum well and the substrate. The curve shows some of the expected features. There appears to be a leveling off of the conductivity both at low and at high amplitudes. Moreover, the high amplitude plateau occurs at around the value of  $e/\kappa C$  and the low amplitude plateau, much less well defined, begins to set in at a fraction of something near the expected 1/3 of the voltage of the high amplitude plateau. The conductivity, however, does not increase nearly fast enough in the region between the plateaus to agree with our model; the conductivity in Fig. 6.15 rises with an exponent much less than unity.

One explanation for this less than dramatic rise in the conductivity is derived from the fact that sinusoids and not square waves were used in the measurement. The calculation of the system response to sinusoidal signals is complicated, and we have not solved this problem. We suspect though, that the sinusoid should blur the three sharply defined regions described in the square wave model, rounding the transitions between them as a function of measuring voltage.

We also know, from our work in chapter 4, that for low densities of the 2d electron gas a temperature dependent tunneling suppression arises, likely the result of collective effects. These effects may influence the behavior of quantum

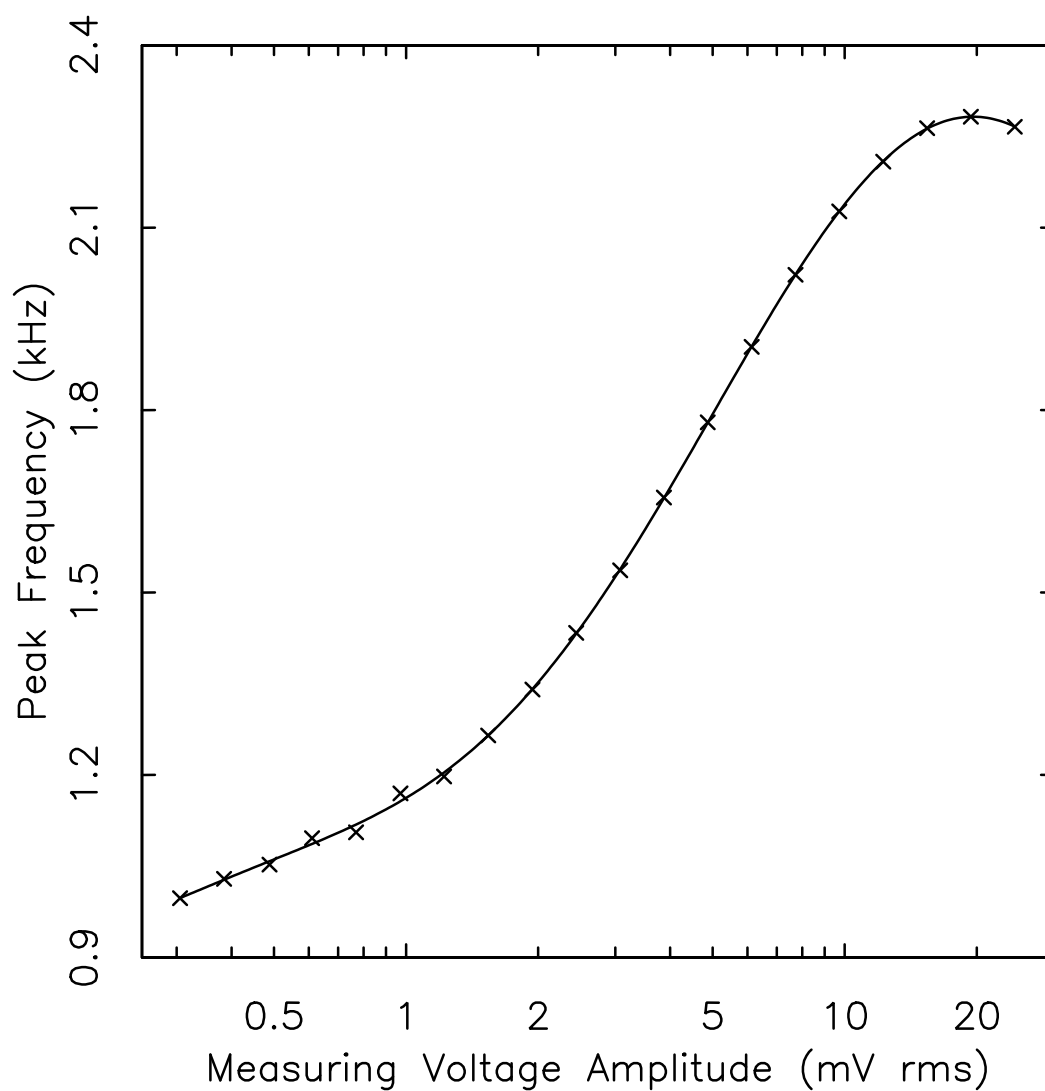


**Fig. 6.15** Shown is the frequency of the relaxation peak of a quantum dot array, determined from fits, plotted as a function of the rms amplitude of the sinusoidal voltage used to make the measurements. The gate bias voltage is set to zero. The solid curve is a guide to the eye.

dots. The suppression seen in chapter 4, while occurring at a lower temperature scale than the corresponding amplitude dependence of the conductance in the dots, shows a similar range of increase (factor of 2 or 3) of the tunneling conductivity. Further characterization of the dots is required to discern the cause of the observed variation of the conductivity with measuring voltage amplitude. Specifically a series of curves at different gate biases would be useful to view the effects different charging energies on the conductivity vs. measuring voltage amplitude curve. Also, the use of square wave measuring signals may give clues to whether collective or single particle effects cause the observed behavior.

## 6.8 Shape of the Relaxation Peak

It is clear from the discussion above that tunneling rates from the different quantum dots in the array vary widely. Depending on the measuring voltage amplitude, some dots do not allow tunneling at all while those that allow tunneling do so with rates proportional to the number of quantum levels exposed by the measuring voltage.

In this situation, we must combine models used in chapters 3 and 4 to fit capacitance and loss tangent vs. frequency curves. In section 3.7.2, we described a model used for the samples composed of isolated domains each with different tunneling times. This model gave broadened loss peaks described by a “broadening” parameter  $\chi$ . The model though, was for a quantum well whose area is fully occupied with electrons and not directly applicable to our results here for quantum dots with large portions of the quantum well empty. We invoke the “puddling” model used in section 4.7 to describe a well where a fraction  $\alpha$  is filled. We assume in this model that the density of states in the occupied

portions of the well is the same as the constant 2d DOS in the well for a broad area sample.

We describe fits to the capacitance. For samples with the well partially filled, the “puddling” model of section 4.7 gave the device capacitance by

$$C(f) = \alpha C_p(f) + (1 - \alpha) C_{high}.$$

$C_p(f)$  is defined as

$$C_p(f) = \frac{C_{high} C_x [1 + (f/f_{peak})^2]}{C_{high} + C_x (f/f_{peak})^2}.$$

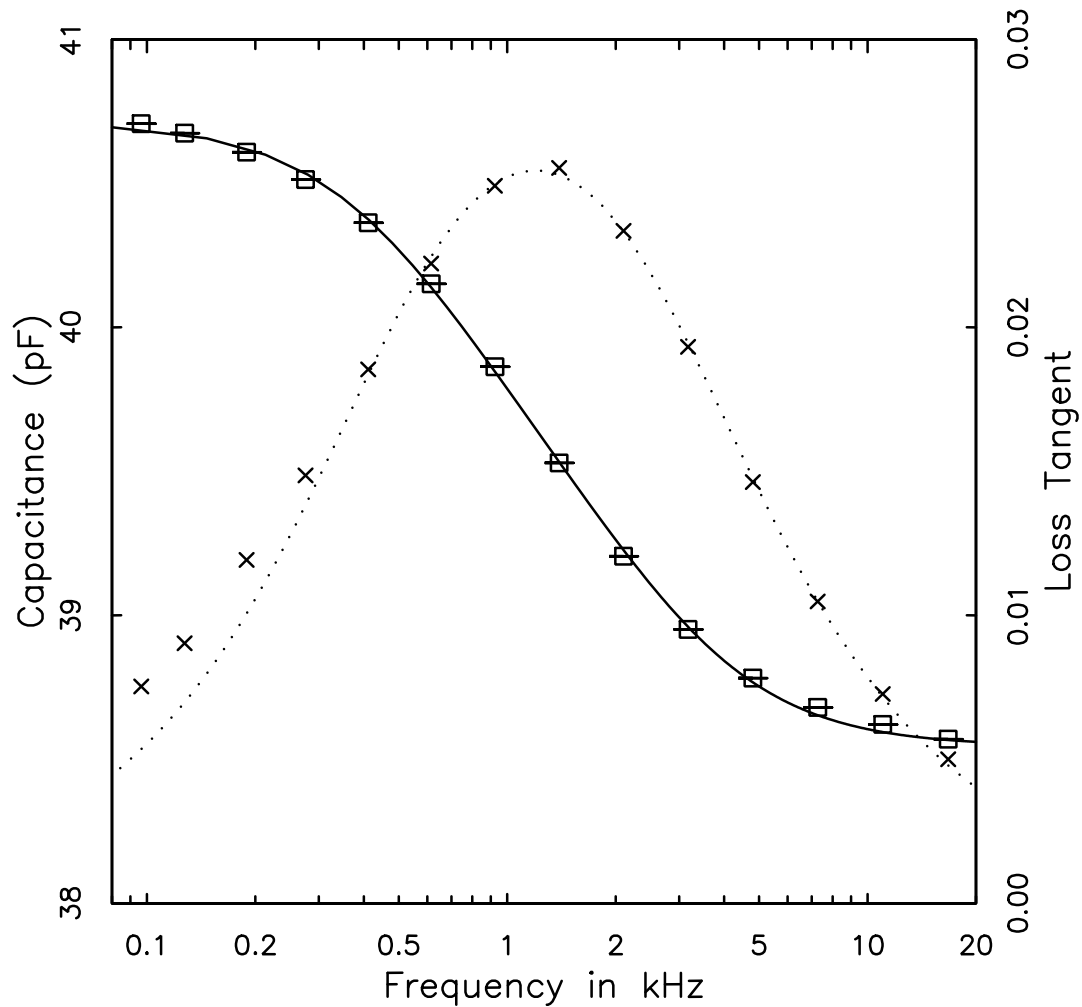
Here  $C_{high}$  is the high frequency capacitance of the device,  $C_x$  is the capacitance  $C_{low}$  that *would* be measured at low frequencies if the well were full and the DOS in the well were the constant 2d DOS, and  $f_{peak}$  is the relaxation peak frequency. Combining this model with the model for the broadening parameter given in section 3.7.2, we get

$$C(f) = \alpha [.2C_p(f; f_{peak}) + .4C_p(f; \chi f_{peak}) + .4C_p(f; f_{peak}/\chi)] + (1 - \alpha) C_{high}.$$

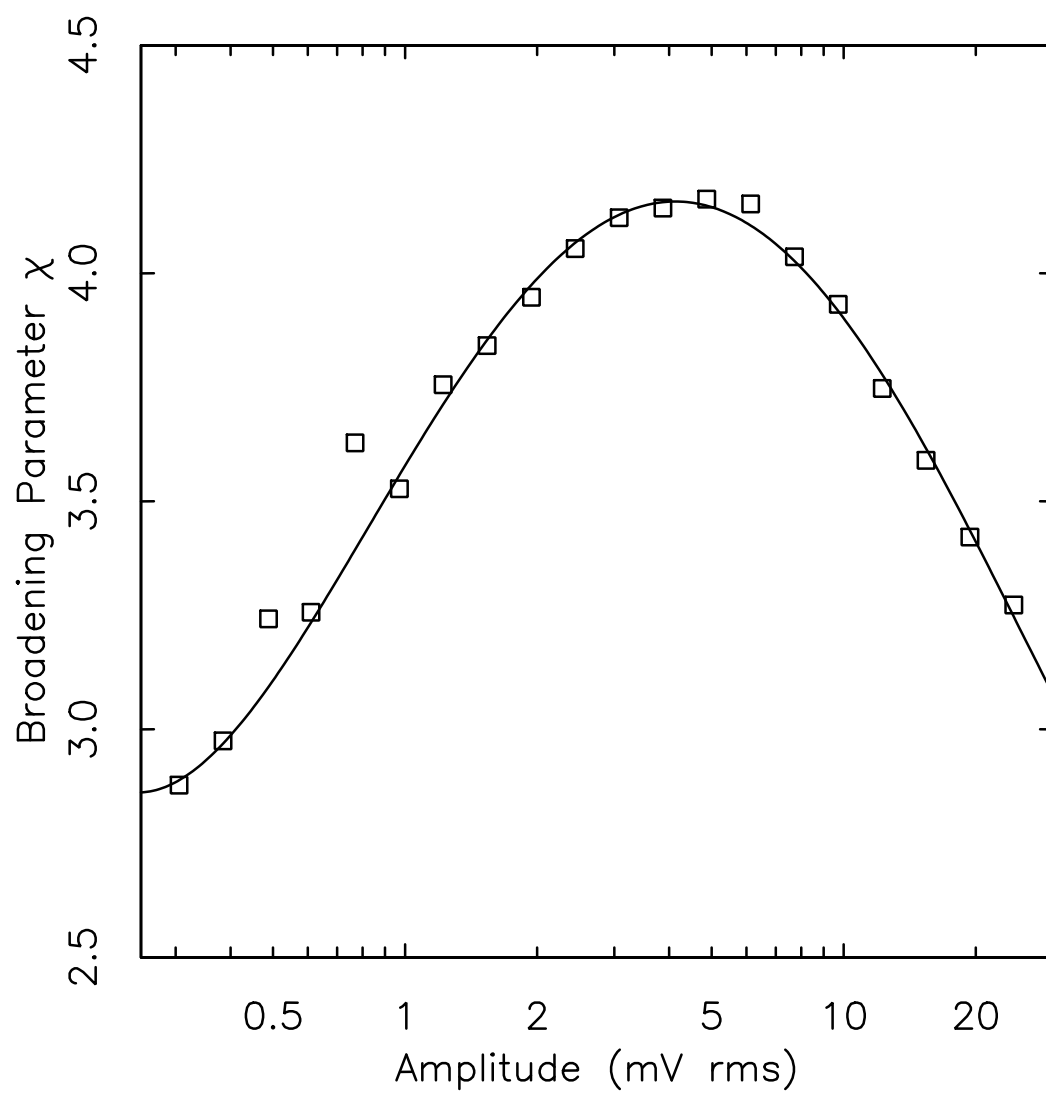
In fits, the free parameters are  $f_{peak}$ ,  $C_{high}$ ,  $\alpha$ , and  $\chi$ . The value of  $C_x$  is fixed (with respect to  $C_{high}$ ), and we set this value to  $1.36C_{high}$  from measurements of the ratio  $C_{low}/C_{high}$  on broad area samples from the same wafer on which the quantum dot sample was produced.

Figure 6.16 displays the capacitance and loss tangent of the quantum dot sample (same device as in previous figures) as a function of frequency. The gate bias is set to zero, and the sinusoidal signal amplitude is 2.4 mV rms. The “broadened” fits from the puddling model were used to fit to the capacitance data in Fig. 6.15.

We have measured the broadening parameter as a function of signal amplitude for gate bias set to zero. This is plotted in Fig. 6.17. Interestingly, the



**Fig. 6.16** The figure displays the capacitance and loss tangent of the quantum dot sample as a function of frequency for gate bias set to zero and using a 2.4 mV rms measuring signal along with fits to them as described in the text. The parameters for the capacitance fit are as follows:  $f_{peak} = 1.43$  kHz,  $C_{high} = 38.54$  pf,  $\kappa = .156$ , and  $\chi = 4.05$ .



**Fig. 6.17** Plotted is the broadening parameter  $\chi$  obtained from fits as a function of the amplitude of the measuring voltage. The smooth curve is a guide to the eye.

broadening parameter increases as the signal amplitude is increased, reaching a maximum at around 7 mV rms, and then decreases again as the signal level is further increased.

This behavior is consistent with the ideas about tunneling from quantum dots given above. For simplicity, consider all quantum levels in a dot to be nondegenerate with constant energy spacing between levels given by  $\delta_{mean}$ . For a square wave measuring voltage of amplitude  $\beta$  (smaller than  $e/\kappa C$ ), for those dots from which tunneling is allowed, tunneling rates range from  $1/\tau_0$  to  $\beta/\delta_{mean}\tau_0$ . As  $\beta$  is increased, this range of rates is obviously increased. The range reaches a maximum when  $\beta = e/\kappa C$ . Beyond this, all dots allow tunneling and the slowest dots have a rate given by  $(\beta - (e/\kappa C))/\delta_{mean}\tau_0$  while the fastest dots have a rate of  $\beta/\delta_{mean}\tau_0$ . Clearly, the ratio of the fastest to slowest tunneling times decreases as  $\beta$  is increased in this regime. Again, issues are confused by our use of a sinusoidal measuring voltage and the level degeneracies. However, the qualitative behavior is still apparent in Fig. 6.17.

Finally, we do not necessarily expect  $\chi$  to approach one even in the extremes of high and low measuring voltage amplitude. Inhomogeneity in the tunnel barrier or in the shapes of the dots may cause them to have different tunneling rates even if the Coulomb blockade were not present. In our model, at very low measuring voltages with amplitude smaller than  $\delta_{mean}/\kappa$  the tunneling rate from all of the dots which allow tunneling is  $1/\tau_0$ . The fact that  $\chi$  retains a value between two and three as the measuring voltage amplitude is decreased to values (the lowest amplitudes plotted) around  $\delta_{mean}/\kappa$  may indicate some intrinsic broadening.

An intriguing behavior is seen in the high frequency capacitance  $C_{high}$  obtained from fits. This is plotted in Fig. 6.18.  $C_{high}$  decreases as the measuring voltage amplitude is increased, reaches a minimum at around the same amplitude



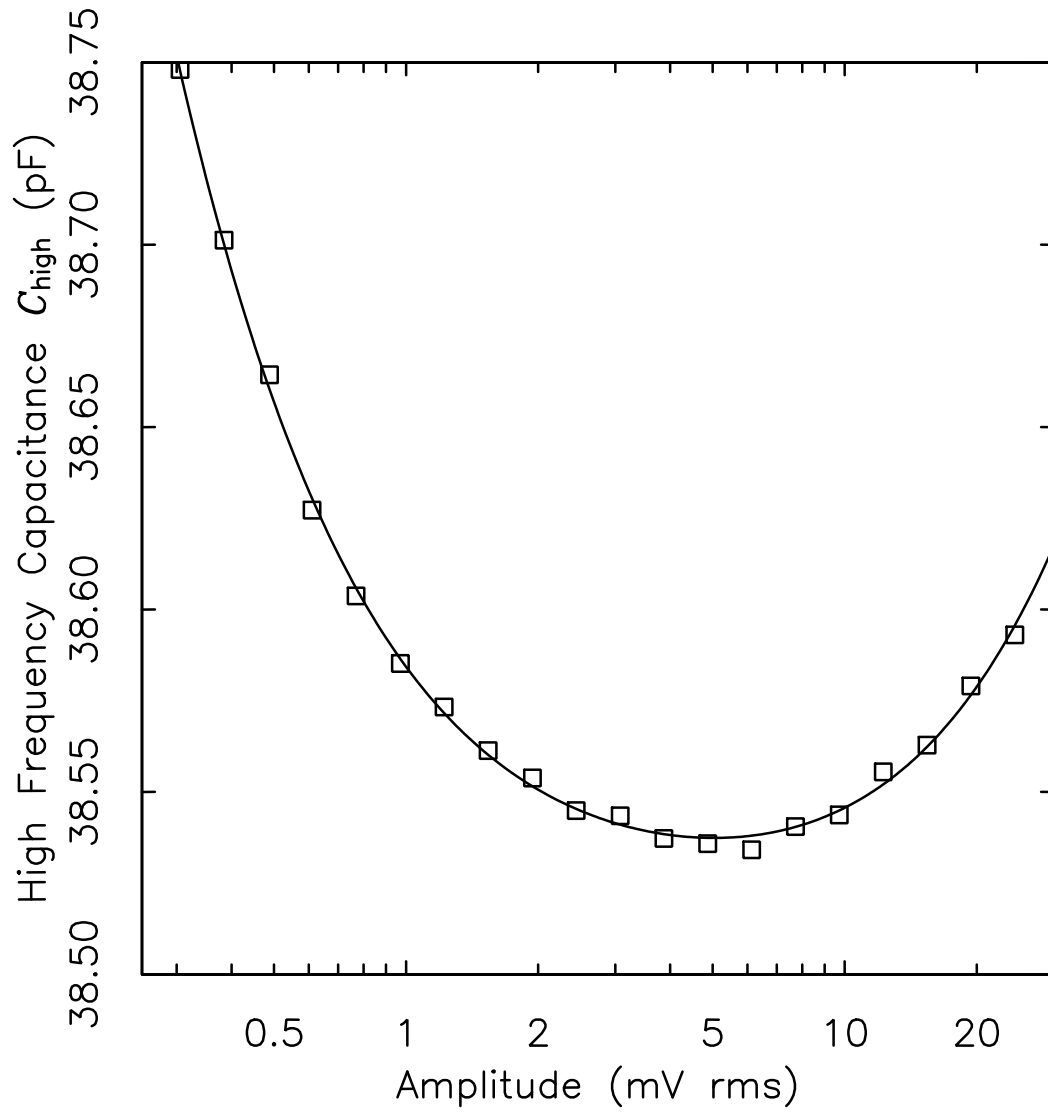


**Fig. 6.18** The figure shows the high frequency capacitance  $C_{high}$  plotted as a function of the amplitude of the measuring voltage. The smooth line is a guide to the eye.

at which the broadening parameter reaches a maximum, and then starts to increase again. Observation of capacitance vs. frequency curves at different amplitude, such as those shown in Fig. 6.19, indicates that these results are *not* an artifact of the fitting procedure. In our model, the high frequency capacitance (the capacitance measured at time scales so fast that no charge can be transferred to the dots) should not depend on measuring voltage amplitude. The results may possibly be explained by a few dots which transfer electrons for very small measuring voltages and do so at an enormous tunneling rate (compared to tunneling rates for other dots) and thus contribute to the device capacitance even at the highest measuring frequencies. As at most one electron is transferred to these dots per half cycle of the measuring voltage, the contribution of these dots to the device capacitance decreases as the measuring voltage is increased (i.e.  $e/V$  decreases as  $V$  is increased). This is a highly speculative picture, and we have no explanation why fast transfer should exist only for a few dots which transfer electrons at very low voltages. This aspect of the high frequency capacitance data is at present a mystery.

Finally we note, as discussed elsewhere,<sup>12</sup> that the low frequency capacitance in our model should not (and experimentally does not) depend on the amplitude of the measuring voltage. While many dots do not contribute to the tunneling at low amplitude, those that do contribute transfer a disproportionately large amount of charge (a whole electron) for the size of the measuring voltage used.

## 6.9 Summary

We have made a series of capacitance measurements on quantum dot arrays. High precision measurements have revealed reproducible capacitance

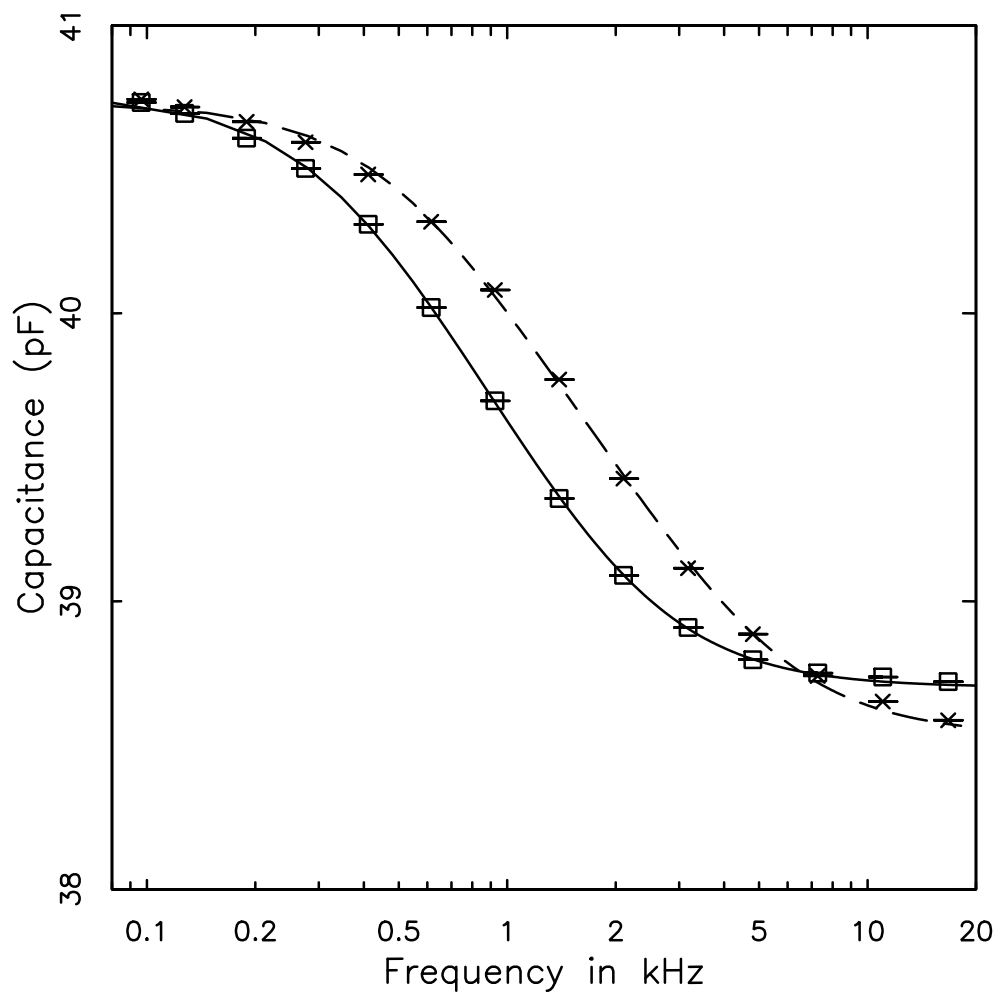


**Fig. 6.19** The device capacitance is plotted as a function of frequency for two different amplitudes of the measuring voltage. The boxes are for a voltage of 0.39 mV rms and the crosses are for 6.1 mV rms. The capacitance at high frequencies for the two curves appears to be approaching different limits.

fluctuations which develop in the capacitance spectrum of the dots as a function of gate bias. A model for the dots, involving a spectrum of individual electron additions to the dot which occur as the gate bias is increased produces simulated results which have qualitative features of the data. In magnetic field, with highly degenerate Landau levels, the fluctuations seen in the data appear as regular oscillations with period thought to be given by the gate voltage change necessary to add one electron onto a dot.

Tunneling measurements have also been made on the dot array. Some of these results are in qualitative agreement with models while others remain unexplained. More data and analysis are required.

## References

1. I. Giaever and H.R. Zeller, Phys. Rev. Lett. **20**, 1504 (1968)
2. T.A. Fulton and G.J. Dolan, Phys. Rev. Lett. **59**, 109 (1987)
3. P. Delsing, K.K. Likharev, L.S. Kusmin, and T. Claeson, Phys. Rev. Lett. **63**, 1180 (1989) and Phys. Rev. Lett. **63**, 1861 (1989)
4. L.J. Geerligs, V.F. Anderegg, P.A.M. Holweg, J.E. Mooij, H. Pothier, D. Esteve, C. Urbina, and M.H. Devoret, Phys. Rev. Lett. **64**, 2691 (1990)
5. M.A. Reed, J.N. Randall, R.J. Aggarwal, R.J. Matyi, T.M. Moore, and A.E. Wetsel, Phys. Rev. Lett. **60**, 535 (1988)
6. *See Chapter 5*
7. W. Hansen, T.P. Smith, III, K.Y. Lee, J.A. Brum, C.M. Knoedler, J.M. Hong, and D.P. Kern, Phys. Rev. Lett. **62**, 2168 (1989)
8. *See Chapter 7*
9. John Lambe and R.C. Jaklevic, Phys. Rev. Lett. **22**, 1371 (1969)
10. R.E. Cavicchi and R.H. Silsbee, Phys. Rev. Lett. **52**, 1453 (1984)
11. R.E. Cavicchi and R.H. Silsbee, Phys. Rev. B **37**, 706 (1988)
12. R.E. Cavicchi, Ph.D. Thesis, Chapter 4, Cornell University (1987)

## Chapter VII

### Computer Simulation of Quantum Dot Capacitance

Hansen et al. have interpreted the magnetic field dependence of capacitance spectra of quantum dot arrays as reflecting the evolution of individual electron states. They model the system as a two-dimensional quantum well with lateral confinement on the scale, independent of bias, of 120 nm.<sup>1</sup> We question whether the experiment has adequate resolution to reveal structure associated with individual levels.

In a circular dot of diameter  $D$ , two energies are important, the typical splitting  $\delta \approx 16\hbar^2/m^*D^2$  of the one electron energy levels, usually both orbitally and spin degenerate, and a charging energy  $\Delta \equiv e^2/C \approx 16e^2d_e/\epsilon D^2$  (*cgs* units).  $C$  is the capacitance of the dot to its surroundings,  $\epsilon$  is the dielectric constant of the medium, and  $d_e$  is a length of the order of the distance from the dot to the substrate or gate structure. The ratio of the charging energy to the quantum splitting is  $\Delta/\delta \approx e^2d_em^*/\epsilon\hbar^2 \approx 5$  for the configuration of the Hansen experiment and is independent of the size of the dot.

If the experiment can be carried out with adequate resolution, each successive electron transfer will contribute a distinct peak to the capacitance spectrum.<sup>2</sup> With  $\Delta \gg \delta$ , the spacing between peaks will be determined principally by the charging energy  $\Delta$ , not by the level splitting  $\delta$ .

Fig.7.1a illustrates a model calculation for a dot with a square well confining potential (infinite walls) with circular symmetry. Individual energy levels were calculated for the dot whose diameter was taken to be proportional to the square root of the dot capacitance deduced from Ref.1 by integration of  $dC/dV_{gate}$ . A maximum value of 270 nm was chosen for the dot diameter, nearly equal to the lithographically defined size of 300 nm. The one electron spectrum for the dot was converted to a capacitance spectrum by adding  $\Delta$  for each electron added to the dot and converting to gate voltage from well voltage using a geometric lever-arm of 2 for this structure. This scheme gives an areal density of electrons in the dot equal to that implied by the interpretation of the strong maxima in the 2 T data of Ref.1 as spin degenerate Landau maxima. The increase in level density with increasing gate voltage in fig.7.1a results from the increase in the diameter of the dot as it is filled and the consequent decrease of both  $\Delta$  and  $\delta$ .

To simulate the experiment, this spectrum is convolved with a Gaussian with rms width of 11 meV at the gate (or  $\sim 0.3$  meV at the well) to destroy resolution on the scale of individual energy levels, giving the density of states (DOS) of fig.7.1b. For comparison fig.7.1c shows the normalized DOS, obtained from the integration of  $dC/dV_{gate}$  of the zero magnetic field data of Ref.1.

The two curves show the same qualitative behavior. Comparison with the unbroadened spectrum shows that the first two or three peaks may indeed be associated with filling of the first doublet and the next one or two quartets of the single particle spectrum, but structure at higher filling is the consequence of fluctuations in the density of states. Each peak is associated, at the highest gate voltages, with about 20-30 electrons. The results of this simulation indicate: over most of the range of gate voltage, the experiment does not resolve individual

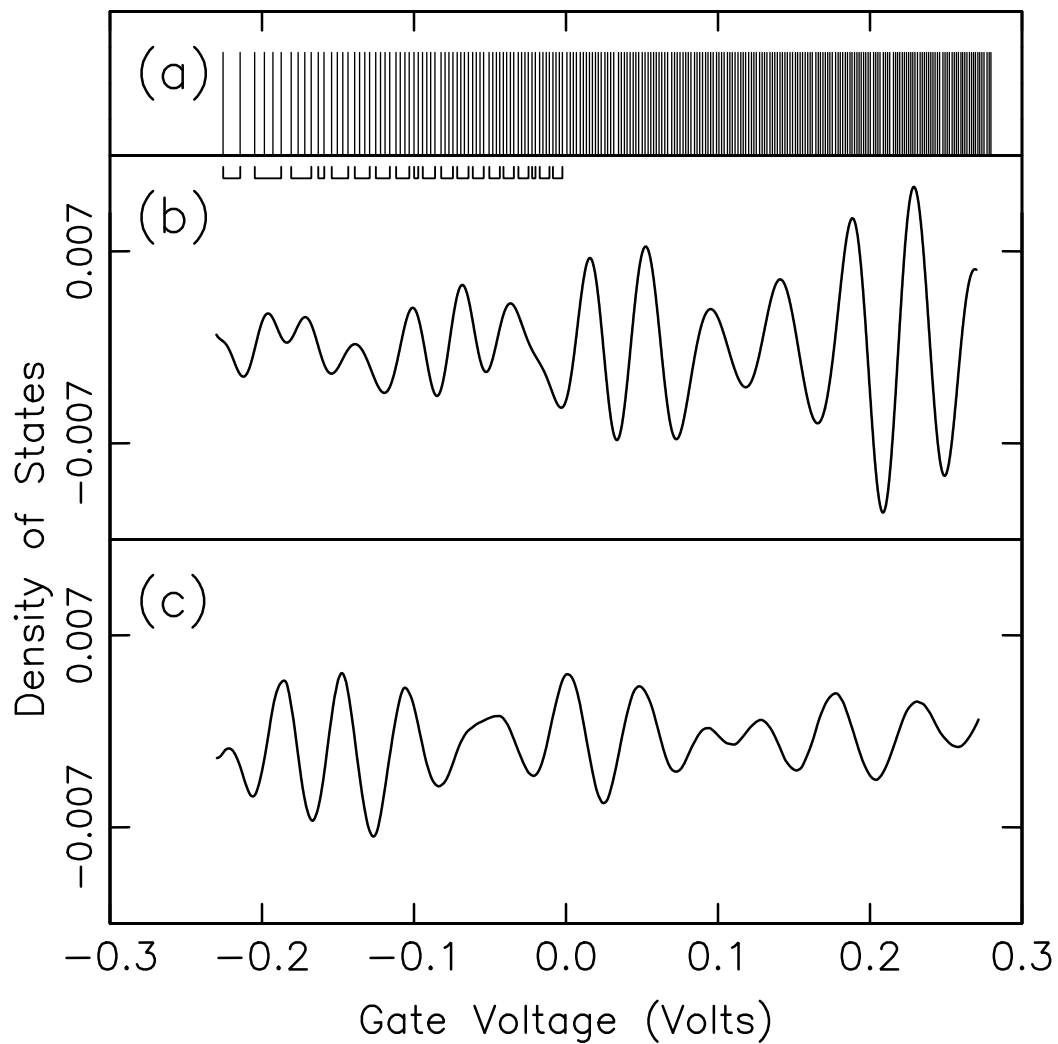


**Fig. 7.1** (a) Each bar represents the gate voltage at which one electron may enter a dot, from model described in text. Brackets at low gate bias demarcate quantum levels. (b) DOS determined from (a) after convolution with a Gaussian rms width 11 mV. (c) DOS from the data of Ref.1. In both (b) and (c), the smooth variation has been subtracted, and the results have been normalized to the DOS at .26 volts.



quantum levels, and changes in structure induced by a magnetic field are not simply interpretable in terms of the behavior of the individual quantum levels.

### References

1. W. Hansen, T.P. Smith, III, K.Y. Lee, J.A. Brum, C.M. Knoedler, J.M. Hong, and D.P. Kern, Phys. Rev. Lett. **62**, 2168 (1989)
2. John Lambe and R.C. Jaklevic, Phys. Rev. Lett. **22**, 1371 (1969)